

Lecture Notes in Mechanical Engineering

Shriram Hegde
Abhishek Mishra
D. K. Singh *Editors*

Recent Developments in Mechanics and Design

Select Proceedings of INCOME 2021

 Springer

Lecture Notes in Mechanical Engineering


Series Editors

Fakher Chaari, National School of Engineers, University of Sfax, Sfax, Tunisia

Francesco Gherardini , Dipartimento di Ingegneria “Enzo Ferrari”, Università di Modena e Reggio Emilia, Modena, Italy

Vitalii Ivanov, Department of Manufacturing Engineering, Machines and Tools, Sumy State University, Sumy, Ukraine

Editorial Board

Francisco Cavas-Martínez , Departamento de Estructuras, Construcción y Expresión Gráfica Universidad Politécnica de Cartagena, Cartagena, Murcia, Spain

Francesca di Mare, Institute of Energy Technology, Ruhr-Universität Bochum, Bochum, Nordrhein-Westfalen, Germany

Mohamed Haddar, National School of Engineers of Sfax (ENIS), Sfax, Tunisia

Young W. Kwon, Department of Manufacturing Engineering and Aerospace Engineering, Graduate School of Engineering and Applied Science, Monterey, CA, USA

Justyna Trojanowska, Poznan University of Technology, Poznan, Poland

Lecture Notes in Mechanical Engineering (LNME) publishes the latest developments in Mechanical Engineering—quickly, informally and with high quality. Original research reported in proceedings and post-proceedings represents the core of LNME. Volumes published in LNME embrace all aspects, subfields and new challenges of mechanical engineering. Topics in the series include:

- Engineering Design
- Machinery and Machine Elements
- Mechanical Structures and Stress Analysis
- Automotive Engineering
- Engine Technology
- Aerospace Technology and Astronautics
- Nanotechnology and Microengineering
- Control, Robotics, Mechatronics
- MEMS
- Theoretical and Applied Mechanics
- Dynamical Systems, Control
- Fluid Mechanics
- Engineering Thermodynamics, Heat and Mass Transfer
- Manufacturing
- Precision Engineering, Instrumentation, Measurement
- Materials Engineering
- Tribology and Surface Technology

To submit a proposal or request further information, please contact the Springer Editor of your location:

China: Ms. Ella Zhang at ella.zhang@springer.com

India: Priya Vyas at priya.vyas@springer.com

Rest of Asia, Australia, New Zealand: Swati Meherishi at swati.meherishi@springer.com

All other countries: Dr. Leontina Di Cecco at Leontina.dicecco@springer.com

To submit a proposal for a monograph, please check our Springer Tracts in Mechanical Engineering at <https://link.springer.com/bookseries/11693> or contact Leontina.dicecco@springer.com

Indexed by SCOPUS. All books published in the series are submitted for consideration in Web of Science.

Shriram Hegde · Abhishek Mishra · D. K. Singh
Editors

Recent Developments in Mechanics and Design

Select Proceedings of INCOME 2021

 Springer

Editors

Shriram Hegde
Department of Applied Mechanics
Indian Institute of Technology Delhi
New Delhi, Delhi, India

Abhishek Mishra
Department of Mechanical Engineering
National Institute of Technology Delhi
New Delhi, Delhi, India

D. K. Singh
Department of Mechanical Engineering
Netaji Subhas University of Technology
New Delhi, Delhi, India

ISSN 2195-4356

ISSN 2195-4364 (electronic)

Lecture Notes in Mechanical Engineering

ISBN 978-981-19-4139-9

ISBN 978-981-19-4140-5 (eBook)

<https://doi.org/10.1007/978-981-19-4140-5>

© The Editor(s) (if applicable) and The Author(s), under exclusive license to Springer Nature Singapore Pte Ltd. 2023

This work is subject to copyright. All rights are solely and exclusively licensed by the Publisher, whether the whole or part of the material is concerned, specifically the rights of translation, reprinting, reuse of illustrations, recitation, broadcasting, reproduction on microfilms or in any other physical way, and transmission or information storage and retrieval, electronic adaptation, computer software, or by similar or dissimilar methodology now known or hereafter developed.

The use of general descriptive names, registered names, trademarks, service marks, etc. in this publication does not imply, even in the absence of a specific statement, that such names are exempt from the relevant protective laws and regulations and therefore free for general use.

The publisher, the authors, and the editors are safe to assume that the advice and information in this book are believed to be true and accurate at the date of publication. Neither the publisher nor the authors or the editors give a warranty, expressed or implied, with respect to the material contained herein or for any errors or omissions that may have been made. The publisher remains neutral with regard to jurisdictional claims in published maps and institutional affiliations.

This Springer imprint is published by the registered company Springer Nature Singapore Pte Ltd. The registered company address is: 152 Beach Road, #21-01/04 Gateway East, Singapore 189721, Singapore

Preface

Mechanical engineering is the application of scientific principles, mathematical knowledge, and various techniques from designing to manufacturing of a highly innovative product, process or a system. The principles of mechanics help us to analyse the transmission of force, motion, and power in mechanisms and machines. The application of mechanical engineering design principles not only enables the product to be functional and safe, but also enables it to be reliable, competitive, usable, manufacturable, and marketable.

It is our immense pleasure to present the academicians, practicing engineers and scholars, the proceedings of 1st International Conference “International Conference on Mechanical Engineering (INCOME 2021)” held during 25–26 November 2021, which was organized by the Department of Mechanical Engineering, Netaji Subhas University of Technology (NSUT), New Delhi. This conference is the start for the series envisioned on recent developments and advances in field of Mechanical Engineering. The papers written by renowned and recognized experts in their fields serve as a reference and guide for future research. The conference was well received by the industrial personals, academicians and research scholars.

The proceeding consists of papers contributed by leading academicians, research scholars and industrial experts. The conference papers focus on contemporary research in numerical and experimental simulation of Mechanics and Design domain. The papers are a blend of research contribution from industry and academia, and are subdivided into the following three categories:

- Design and Optimization
- Mechanics of Composite
- Modelling and Simulation

The technical advisory committee is pleased to mention that the papers have been received on all these topics. A total of 130 papers were received by the Reviewing Committee. Following a qualitative peer-review of all papers, 29 papers were accepted for Mechanics and Design domain and 30 papers were accepted for Thermal and Fluids domain. Around 250+ academicians, research scholars and industrial experts attended the conference in the online and offline mode. In all,

papers with quality research with contemporary trends in Mechanical Engineering were presented during the conference.

Such voluminous proceedings were not possible without the generous support received from various quarters. The Organizing Committee would like to put on record its deep appreciation for the persistent efforts of all the reviewers, whose efforts positively influenced the quality of the final papers presented at the conference. We are grateful to all the authors for their contributions to enrich this international conference. We also express our gratitude to the members of the different committees for their support, collaboration and hard work.

It is our immense pleasure to express our heartfelt gratitude to Prof. P. K. Desai, President ISTE; Prof. Y. K. D. K. Prasad, Queensland University of Technology, Brisbane, Australia; Prof. Amit Swamy, Emirates College of Technology, UAE; Prof. N. Zoyimovich, School of Robotics, XJTU, China and other colleagues from India and abroad. Special acknowledgement to the keynote lecture by Prof. R. K. Yadav, ADM, Pragati Power Plant, Delhi. We also acknowledge the generous support received from Mr. Priyank Garg, Jt. Managing Director, Advance Valves Pvt. Ltd., Noida, India. We wish to thank the sponsoring/collaborating companies and other institutions for their supports and grants. And finally, thanks to all the participants of INCOME 2021.

New Delhi, India
January 2022

Shriram Hegde
Abhishek Mishra
D. K. Singh

Contents

Analysis of Single Overload Effect on Fatigue Crack Propagation Using Modified Virtual Crack Annealing Model	1
Chandra Kant and G. A. Harmain	
Design of Experiments Technique for Evaluation of Material Removal and Surface Quality of Ductile Material	9
Palwinder Singh, Lakhvir Singh, and Sehijpal Singh	
4D Printing—A Smart Way of 3D Printing: A Brief Review	25
Pretesh John, Venkateswara Rao Komma, and Skylab Paulas Bhore	
Stabilization and Trajectory Control of High-Altitude Balloons for Rockoons—A Review	35
A. A. Mandal	
A Review on “Designs and Fabrication” for the Next Generation of Organic Solar Cells Technology	45
Neeraj Kant and Pushpendra Singh	
Parametric Study of Stiffened Composite Structures Using Design of Experiments	59
Nagaraj Kishor Kelageri, Deepak C. Patil, and Santosh Nandurkar	
Design and Optimization of Trestle Jack	69
M. Sadiq A. Pachapuri, R. G. Lingannavar, Nagaraj K. Kelageri, and Sudarshan Kasar	
Simulation of a Vision-Based Model of a Robotic Work Cell (6-Axis) ...	83
Mitul Milind Gajbhiye, Amol Chaudhary, and Sangharatna Ramteke	
Numerical Simulations of an Interaction of a Blast Wave Produced from a Shock Tube with an Object Placed at Various Positions	93
Datti Ganapathi and Abhishek Kundu	

The Influence of Notch-Width Ratio on Mechanical and Electromagnetic Radiation Parameters During Tensile Deformation in FCC Metals	101
Anu Anand and Rajeev Kumar	
Comparison of In-Vitro Corrosion Behavior for Polished and WEDM Machined ZM21 Magnesium Alloy Used as Biodegradable Orthopedic Implants	115
Sarbjeeet Singh	
Investigation of Angular Distortion Using Mathematical Modelling in TIG Welded Dissimilar Stainless Steel 304 and 316 Grades	131
Deeksha Narwariya, Aditya Kumar Rathi, and Pradeep Khanna	
Development of Probe for Arsenic and Fluoride Detection in Drinking Water	145
Shivani Pandey, Satanand Mishra, H. N. Bhargaw, and Archana Singh	
Study of Smart Sensor Designing Parameters for Water Resources Management	161
Tanmay Sardar, Satanand Mishra, and Shivani Pandey	
Redesign of Assembly Line for Productivity Enhance in an Automotive Industry Using Line Balancing Technique	173
S. Karthik, S. Palani, and Ganapathy Srinivasan	
Experimental Characterization and FEA Comparison Between Wave and Helical Springs	185
S. Balodi and P. Pratim	
Mechanical Properties Enrichment of Glass Fiber Epoxy by Sugarcane Baggage	203
Punita Kumari, Ashraf Alam, and Saahil	
A Neural Network Based Approach to Determine Chatter Stability in Milling for a Variable Pitch Cutter	213
Pritam Ghoshal	
Effect of Chromium on Mechanical and Corrosion Behaviour of Ferrous Metal Matrix Composites by Using Powder Metallurgy Route	225
K. R. Varadaraj, Sanjay Kumar, H. R. Vitala, M. K. Ravishankar, and B. P. Dileep	
Study of Effect of Protrusions on Cones in Hypersonic Flow	235
V. C. Mithun Chandrakumar and S. R. Nagaraja	

Design and Analysis of Multifacility Splint for Children with Congenital Clubfoot Deformities 243
Mahavir Kantilal Beldar, Aditya Kumar Manethia, Mallika Joka, and Ayush Murarka

Experimental Validation of End Effector Position and Orientation for a 5 DoF Robotic Manipulator 257
Uday R. Walke, Raunak V. Wasnik, Rohit M. Pal, Ashutosh S. Borkar, Parag M. Kowe, Aniket R. Buchunde, Palak N. Ukey, and Vinit Gupta

Effect of Printing Parameters on Tensile Strength of 3D Printed PLA + Carbon Fiber Samples—A Taguchi Approach 265
T. S. Sachit, Mukul Ramnirajan Saini, and D. Vinaykumar

Modelling of Manganese and Nickel Transfer in Terms of Flux Ingredients in SAW 275
Brijpal Singh and Narender Singh

About the Editors

Dr. Shriram Hegde is currently a faculty member at the Department of Applied Mechanics, Indian Institute of Technology (IIT) Delhi. He obtained his B.E. (Mechanical) from University of Mysore, and M.E. from BITS, Pilani and Ph.D. from IIT Delhi. His major areas of research interests include flow instability studies in compliant-wall flows, computational mechanics, finite element methods, computational fluid dynamics and CAD/CAM. He has published about 65 papers in respected international journals. Dr. Hegde is currently serving as the treasurer and executive committee member of Indian Society of Mechanical Engineers (ISME). He is a life member of ISME and National Society of Fluid Mechanics and Fluid Power.

Dr. Abhishek Mishra is currently working as Assistant Professor in the Department of Mechanical Engineering, National Institute of Technology (NIT) Delhi. He obtained his M.Tech. degree in CAD/CAM from VIT University Vellore and wrote M.Tech. thesis at the University of Technology Compiègne, France on the topic “Numerical simulation of laser welding process” in collaboration with Arcelor Mittal Company, Montataire, France. He did Docteur Sciences pour l’Ingenieur from the University of South-Brittany France on “Experimental investigation and numerical prediction of rupture in bending of metallic sheets”. This work was part of SIMENDO project, which was financially supported by the French National Agency for Research (ANR). Currently, he is guiding research in the field of numerical modelling and simulation using finite element method (FEM): applications in metal forming process, mechanics of materials, design engineering and artificial joint implants. He had been awarded for Education Excellence and Swachh Bharat by different organizations. He has authored more than 20 research papers and book chapters in various international/national journals and conferences. He has extended his services in the capacity of Advisor/Expert in various government departments, universities and organizations.

Dr. D. K. Singh is Professor and founder Head of Mechanical Engineering Department, Netaji Subhas University of Technology (NSUT) New Delhi, India. He obtained his B.Tech. degree from NIT Patna, M.Tech. degree from Birla Institute of

Technology (BIT) Mesra, Ranchi and Ph.D. from Uttarakhand Technical University (UTU), Dehradun, India. His major areas of research include design and manufacturing, operations management, and supply chain management. He has published over 50 research papers in various national and international journals and conferences and has authored 12 books. He is a life member of Indian Society for Technical Education (ISTE), New Delhi.

Analysis of Single Overload Effect on Fatigue Crack Propagation Using Modified Virtual Crack Annealing Model



Chandra Kant and G. A. Harmain

Abstract A systematic study of overload-induced effect on fatigue crack propagation is presented. Effect of interspersed overload under constant amplitude load is simulated via modified virtual crack annealing (MVCA) model, which is based on crack closure phenomena. Study is performed on 304LSS (stainless steel) for various overload ratio and crack length. MVCA model prediction is validated using experimental data. Error analysis for studied cases has been presented.

Keywords Crack closure · Single overload · 304LSS · Virtual crack annealing model

1 Introduction

Overloads and underloads in loading pattern of aircraft, automobile, and power plant have been of interest and have been analyzed in [1]. In service condition of aircraft, very frequent overloads come usually during landing and takeoff due to atmospheric turbulences. Effect of distributed overloads in loading spectrum was reported in [2]. In service, aircraft experiences gust cycles and overloads during landing and takeoff and jerks due to atmospheric turmoil [3]. Reported that dispersed overload in constant amplitude spectrum is inflating the strength of structure hence used as remedy for structural health intensification [4]. Significant research has been reported for overload-induced fatigue crack propagation (FCP) retardation consequence for steel [5–8], aluminum [9–12], titanium alloy [13], and a critical review was presented in [14].

Consequence of overload-induced retardation is described by crack tip blunting [15], strain hardening [16], induced residual stress [17], crack branching [18], and plasticity induced crack closure [19], and a study on crack closure models was

C. Kant · G. A. Harmain (✉)
NIT Srinagar, Srinagar, Jammu and Kashmir, India
e-mail: gharmain@nitsri.net

C. Kant
e-mail: chandra07phd17@nitsri.net

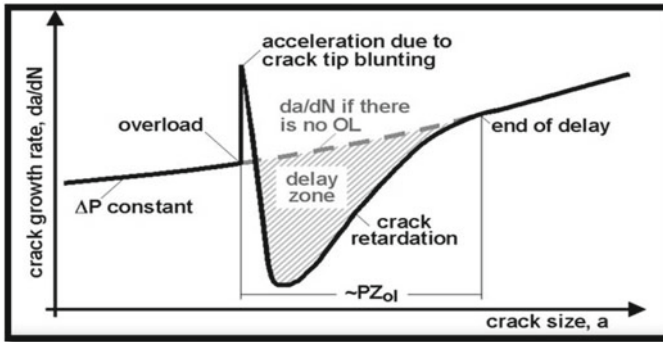


Fig. 1 Tensile overload induced retardation [22]

presented in [20]. A detailed description of overload brought on blunting of crack tip was reported by [21]. Overload reshapes the crack tip geometry (blunt). Hence stress field on crack tip vicinity changes and due to this intensity of crack driving force decreases. Hence crack propagation per cycle brings down till the crack tip sharpens again.

Effect of overload-induced retardation is still not fully understood categorically therefore more investigation is required to explain the phenomena and felicitous mechanism to the rear of.

Consequence of disseminated tensile overload in constant amplitude loading spectrum was reported in [23–27]. Crack propagation behavior after tensile overload has three sequence increase in crack propagation then decrease and finally comes up to constant amplitude fatigue crack propagation rate usually as shown in Fig. 1. First decrease in FCP and then increase is termed as delayed retardation as shown in Fig. 1.

Delayed retardation is elucidated by overload induce residual stress. Compressive residual stress decreases the applied crack driving force hence effective crack driving force is reduced to a certain amount due to this crack propagation retardation [28], presence of residual compressive stress near crack tip.

Meggiolaro et al. [29] reported the influence of tensile overload on SAE4340 steel and illustrate based on crack branching although [30] proposed that crack branching influence zone is smaller than the actual retardation region so phenomena cannot explain the retardation completely.

Crack closure-based models explained the delayed retardation due to overload via crack closure phenomena given by [19], and computability and predictability of crack closure models were presented by [31–33]. Antunes et al. [33] studied the effect of overload considering nonlinear parameter-based crack closure models, nonlinearity comes due to overload-induced large plastic zone, model is able to capture increasing and decreasing fatigue crack behavior. Post-overload, crack closure level decreases then increases which elucidates the post-overload FCP behavior.

Plasticity-induced crack closure is a phenomenon which comes in picture in constant amplitude loading (CAL) and in single overload. In case of interspersed

single overload where both overload-induced plasticity-induced crack closure and CAL-induced crack closure are observed, superposition model for crack closure was presented by [34] where separate crack closure for CAL and overload is evaluated and used for prediction.

This article presents the effect of single overload on fatigue crack propagation using MVCA model by discussing the modified virtual crack annealing model in the next section. Then material and methodology are discussed which are followed by results and discussions. The last section concludes this study and highlights the key points.

2 Modified Virtual Crack Annealing (MVCA) Model

MVCA model is based on crack annealing due to reversed plastic zone in cycling loading condition. Modified virtual crack annealing model assumes linear increase in crack propagation rate after immediate drop of crack propagation rate. Mathematical arrangement of parameters for simulating the overload-induced retardation is given by Eq. (1) for overload influence zone which is described by plastic zone due to overload in [31].

$$K_{op} = \left[\left(\frac{2}{1 + 4\gamma^2} + R * \frac{4\gamma^2 - 1}{1 + 4\gamma^2} \right) + \left(\frac{\left(\frac{4\gamma^2 - 1}{4\gamma^2 + 1} \right) \left(\frac{R}{OLR} - R \right) \left(a_i - \sum_{POL_i}^{rp_{OLf}} da \right)}{(-rp_{OL})} \right) \right] [K_{max}] \quad (1)$$

where γ is parameter which depends on hardening behavior of material, R is stress ratio, OLR stands for overload ratio = $\frac{p_{max,ol}}{p_{max,cal}}$, a_i is current crack length, rp_{OLf} is range of overload-induced plastic zone and p_{OLi} is crack length at overload is applied, rp_{OL} is overload-induced plastic zone. Using Eq. (1), the value of opening stress intensity factor can be determined which will be input parameter to find out the effective stress intensity factor. Effective stress intensity factor will be used in fatigue propagation model as shown in Eq. (2)

$$da/dn = c\Delta K_{eff}^m \quad (2)$$

$$\Delta K_{eff} = K_{max} - K_{op} \quad (3)$$

3 Material and Methodology

Modified virtual crack annealing model [35] is used for this analytical study which is a crack closure-based model. 304LSS is identified as the candidate material for the current study which is a widely used material and serves under multifarious loadings. The loading condition has been taken from experimental data of [32]; however, the parameters in the Paris model namely C and m have been obtained as per ASTM 647 [36]. Using all input loading conditions and hardening parameter γ crack opening stress intensity factor (K_{op}) is determined from Eq. (1) and from Eq. (2) post-overload crack propagation rate has been determined, cycle by cycle approach has been used. The Predicted results are verified with experimental data reported in [37] for 304LSS. Using MVCA model, corrected stress intensity factor is determined and used to predict fatigue crack propagation rate and life expectancy of structure. MVCA model parameter γ is varying with loading parameters. Simulation is conducted from the point of overload to the final failure of the material, and the crack propagation rate is determined for each cycle. Overload-induced delayed failure cycle prediction is compared with experimental data.

4 Result and Discussion

Four different overload ratios are analyzed, and single overload induce retardation is taken care using crack closure phenomena.

For Fig. 2a, the γ is 1.7; for Fig. 2b, the γ is 1.35; for Fig. 2c, the γ is 1.11; and for Fig. 2d, the γ is 1.11. The value of γ is determined from experimental data.

The model prediction for consumed cycle is in good agreement with experimental data. Crack propagation rate trend is not in coherence with experimental data.

FCPR is a complex phenomenon that depends on various intrinsic (microstructure, microscopic strength distribution, grain boundary, residual stress) strain hardening, and extrinsic parameters (nominal load, stress state, initial crack length). Discrepancy in predicted and experimental result might be due to overload-induced bigger plastic zone where linear elastic fracture mechanics is not applicable. Another cause of discrepancy might be involvement of post-overload, extra variable such as compressive residual stress, strain hardening, strain induce phase transformation influence post-overload fatigue crack propagation rate where Paris fatigue crack propagation model is not able to predict due overload induce plastic zone (excessive plasticity) makes FCPR tedious and process might be multivariate hence Fatigue crack propagation is still not modeled properly. Most of the model is based on regression, and modification is needed to make the model more efficient.

Further experimental and computational analysis is required to find the mechanism and formulate more efficient model.

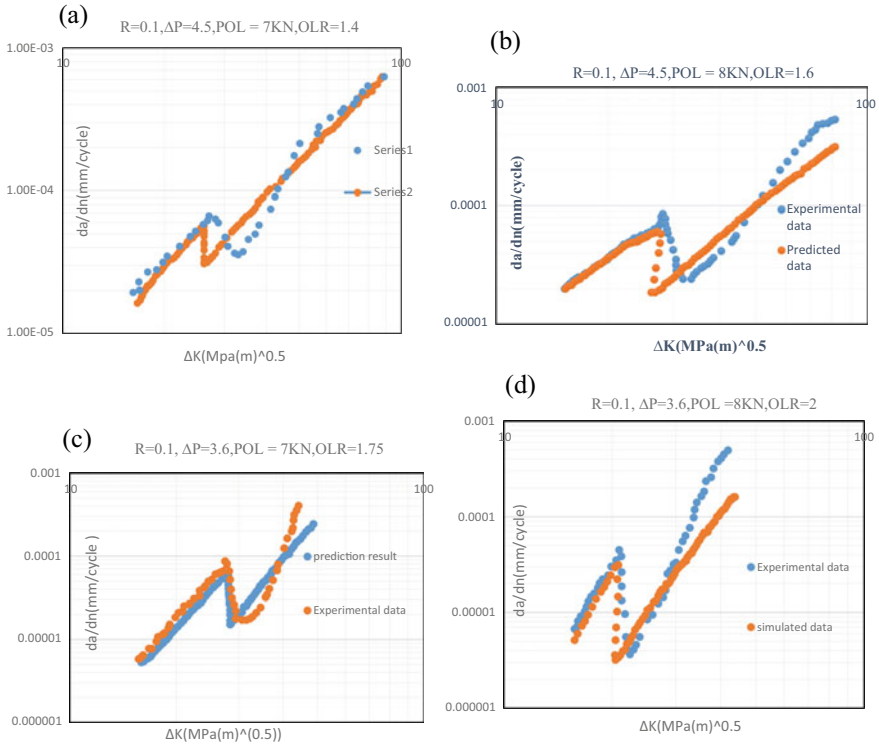


Fig. 2 a Fatigue crack propagation for OLR = 1.4. Curve fitting parameters are $c = 1.9e-11$, $m = 4.7$. b Fatigue crack propagation for OLR = 1.6. c Fatigue crack propagation for OLR = 1.75. d Fatigue crack propagation for OLR = 2.

5 Conclusion

The article shows performance of modified virtual crack annealing model for 304LSS under inter-spread single overload in constant amplitude loading. The model is based on the physical phenomenon of crack closure rather empirical mathematical relation which shows more insights about the failure of material.

MVCA model prediction is in good agreement for overload-induced delayed cycle as can be seen in Table 1. Crack growth rate trend is observed to have some discrepancy with experimental data. The model's Prediction is highly dependent on parameter γ and plastic zone size which can be determined through experimental analysis while plastic zone measurement is a complex process.

The model is not simulating overload-induced gradual crack growth decrement section. Overload-induced excess plastic zone is a suitable explanation for retarded rate of crack propagation.

Table 1 Results of MVCA model

OLR	ΔP (KN)	P_{ol} (KN)	Experimental consumed cycles	Prediction consumed cycles	Error percentage	$a_{ol}-a_{failure}$
1.4	4.5	7	62,526	62,491	0.0559	5.3365–11.5825
1.6	4.5	8	98,768	97,628	1.1542	5.4585–11.2585
1.75	3.6	7	161,183	148,214	8.046	8.2975–14.4395
2.0	3.6	8	591,941	591,973	0.0054	5.377–13.501

References

- Lee EU, Glinka G, Vasudevan AK, Iyyer N, Phan ND (2009) Fatigue of 7075–T651 aluminum alloy under constant and variable amplitude loadings. *Int J Fatigue* 31:1858–1864. <https://doi.org/10.1016/j.ijfatigue.2008.11.013>
- De Jong JB, Schütz D, Lowak H, Schijve J (1973) A standardized load sequence for flight simulation tests on transport aircraft wing structures. NLR-TR 73029 U, LBF Bericht FB-106
- Wahab MA, Rohrsheim GR, Park JH (2004) Experimental study on the influence of overload induced residual stress field on fatigue crack growth in aluminium alloy. *J Mater Process Technol* 153–154:945–951. <https://doi.org/10.1016/j.jmatprotec.2004.04.348>
- Kant C, Harmain GA (2021) An investigation of constant amplitude loaded fatigue crack propagation of virgin and pre- strained aluminium alloy. In: International conference on advanced manufacturing and materials processing, pp 1–14
- Wheeler OE (1972) Spectrum loading and crack growth. *J Fluids Eng Trans ASME* 94:181–186. <https://doi.org/10.1115/1.3425362>
- Rice RC, Stephens RI (1972) Overload effects on subcritical crack growth in austenitic manganese steel. In: ASTM special technical publication, pp 95–114. ASTM International. <https://doi.org/10.1520/stp49639s>
- Petrak GJ, Gallagher JP (1975) Predictions of the effect of yield strength on fatigue crack growth Retardation in HP-9Ni-4Co-30C steel. *J Eng Mater Technol Trans ASME* 97:206–213. <https://doi.org/10.1115/1.3443287>
- Matsuoka S, Tanaka K, Kawahara M (1976) The retardation phenomenon of fatigue crack growth in HT80 steel. *Eng Fract Mech* 8:507–523. [https://doi.org/10.1016/0013-7944\(76\)90005-9](https://doi.org/10.1016/0013-7944(76)90005-9)
- von Euw EFJ, Hertzberg RW, Roberts R (1972) Delay effects in fatigue crack propagation. ASTM special technical publication, pp 230–259. <https://doi.org/10.1520/stp34123s>
- Shih TT, Wei RP (1975) Effect of specimen thickness on delay in fatigue crack growth. *J Test Eval* 3:46–47. <https://doi.org/10.1520/JTE10131J>
- Mills WJ, Hertzberg RW (1975) The effect of sheet thickness on fatigue crack retardation in 2024–T3 aluminum alloy. *Eng Fract Mech* 7:705–711. [https://doi.org/10.1016/0013-7944\(75\)90026-0](https://doi.org/10.1016/0013-7944(75)90026-0)
- Himmelein MK, Hillberry BM (1976) Effect of stress ratio and overload ratio on fatigue crack delay and arrest behavior due to single peak overloads. In: Rice JR, Paris PC (eds) *Mechanics of crack growth*, pp 321–330. ASTM International, West Conshohocken, PA. <https://doi.org/10.1520/STP33954S>
- Gray TD, Gallagher JP (1976) Predicting fatigue crack retardation following a single overload using a modified wheeler model. In: Rice JR, Paris PC (eds) *Mechanics of crack growth*, pp 331–344. ASTM International, West Conshohocken, PA. <https://doi.org/10.1520/STP33955S>
- Kant C, Harmain GA (2021) A model based study of fatigue life prediction for multifarious loadings. In: *Advances in material science*, pp 296–327. Trans Tech Publications Ltd. <https://doi.org/10.4028/www.scientific.net/KEM.882.296>

15. Christensen RH (1959) Fatigue crack, fatigue damage and their detection. Metal fatigue. McGraw-Hill, New York
16. Jones RE (1973) Fatigue crack growth retardation after single-cycle peak overload in Ti-6Al-4V titanium alloy. *Eng Fract Mech* 5:585–604. [https://doi.org/10.1016/0013-7944\(73\)90042-8](https://doi.org/10.1016/0013-7944(73)90042-8)
17. Schijve J, Broek D (1962) Crack propagation: the results of a test programme based on a gust spectrum with variable amplitude loading. <https://doi.org/10.1108/eb033633>
18. Suresh S (1983) Micromechanisms of fatigue crack growth retardation following overloads. *Eng Fract Mech* 18:577–593. [https://doi.org/10.1016/0013-7944\(83\)90051-6](https://doi.org/10.1016/0013-7944(83)90051-6)
19. Elber W (1971) The significance of fatigue crack closure. ASTM special technical publication, pp 230–242. <https://doi.org/10.1520/stp26680s>
20. Kant C, Harmain GA (2021) An investigation of fatigue crack closure on 304LSS & 7020-T7 aluminium alloy. In: International conference on progressive research in industrial & mechanical engineering (PRIME—2021), pp 1–10
21. Schijve J (2015) The application of small overloads for fractography of small fatigue cracks initiated under constant-amplitude loading. *Int J Fatigue* 70:63–72. <https://doi.org/10.1016/j.ijfatigue.2014.09.001>
22. De Castro JTP, Meggiolaro MA, De Oliveira Miranda AC (2005) Singular and non-singular approaches for predicting fatigue crack growth behavior. *Int J Fatigue* 1366–1388. Elsevier. <https://doi.org/10.1016/j.ijfatigue.2005.07.018>
23. Brog TK, Jones JW, Was GS (1984) Fatigue crack growth retardation inconel 600. *Eng Fract Mech* 20:313–320. [https://doi.org/10.1016/0013-7944\(84\)90136-X](https://doi.org/10.1016/0013-7944(84)90136-X)
24. Skorupa M, Skorupa A (2005) Experimental results and predictions on fatigue crack growth in structural steel. *Int J Fatigue* 1016–1028. Elsevier. <https://doi.org/10.1016/j.ijfatigue.2004.11.011>
25. Lee SY, Liaw PK, Choo H, Rogge RB (2011) A study on fatigue crack growth behavior subjected to a single tensile overload: Part I. An overload-induced transient crack growth micromechanism. *Acta Mater* 59:485–494. <https://doi.org/10.1016/j.actamat.2010.09.049>
26. Lopez-crespo P, Withers PJ, Yusof F, Dai H, Steuwer A, Kelleher JF, Buslaps T (2013) Overload effects on fatigue crack-tip fields under plane stress conditions: surface and bulk analysis. *Fatigue Fract Eng Mater Struct* 36:75–84. <https://doi.org/10.1111/j.1460-2695.2012.01670.x>
27. Mehrzadi M, Taheri F (2014) Influence of an overload applied within compressive baseline loading on crack propagation retardation in AM60B magnesium alloy. *Mater Sci Eng A* 595:213–223. <https://doi.org/10.1016/j.msea.2013.12.009>
28. Kant C, Harmain GA (2021) Fatigue life prediction under interspersed overload in constant amplitude loading spectrum via crack closure and plastic zone interaction models—a Comparative Study. In: 9th International Conference on Fracture Fatigue and Wear (FFW 2021). Springer (Lecture Notes in Mechanical Engineering), Ghent, Belgium
29. Meggiolaro MA, Miranda ACO, Castro JTP, Martha LF (2005) Crack retardation equations for the propagation of branched fatigue cracks. *Int J Fatigue* 1398–1407. Elsevier. <https://doi.org/10.1016/j.ijfatigue.2005.07.016>
30. Espinosa AA, Fellows NA, Durodola JF (2013) Experimental measurement of crack opening and closure loads for 6082–T6 aluminium subjected to periodic single and block overloads and underloads. *Int J Fatigue* 47:71–82. <https://doi.org/10.1016/j.ijfatigue.2012.07.010>
31. Ishihara S, McEvily AJ, Goshima T, Nishino S, Sato M (2008) The effect of the R value on the number of delay cycles following an overload. *Int J Fatigue* 30:1737–1742. <https://doi.org/10.1016/j.ijfatigue.2008.02.011>
32. Shin CS, Hsu SH (1993) On the mechanisms and behaviour of overload retardation in AISI 304 stainless steel. *Int J Fatigue* 15:181–192. [https://doi.org/10.1016/0142-1123\(93\)90175-P](https://doi.org/10.1016/0142-1123(93)90175-P)
33. Antunes FV, Castanheira FA, Branco R (2016) A numerical analysis of the mechanisms behind plasticity induced crack closure: application to variable amplitude loadings. *Int J Fatigue* 89:43–52. <https://doi.org/10.1016/j.ijfatigue.2015.12.006>
34. Harmain GA (2005) An investigation on single overload fatigue crack growth retardation, Part-2 (Crack closure decomposition). *J Metall Mater Sci* 47:189–197

35. Jiang S, Zhang W, Li X, Sun F (2014) An analytical model for fatigue crack propagation prediction with overload effect. *Math Prob Eng* 2014. <https://doi.org/10.1155/2014/713678>
36. American Society for Testing and Materials (ASTM) (1999) ASTM E647: standard test method for measurement of fatigue crack growth rates. Annual Book of ASTM Standards, West Conshohocken, Pa, USA
37. Kalnaus S, Fan F, Jiang Y, Vasudevan AK (2009) An experimental investigation of fatigue crack growth of stainless steel 304L. *Int J Fatigue* 31:840–849. <https://doi.org/10.1016/j.ijfatigue.2008.11.004>

Design of Experiments Technique for Evaluation of Material Removal and Surface Quality of Ductile Material



Palwinder Singh, Lakhvir Singh, and Sehijpal Singh

Abstract Magnetic field assisted abrasive flow machining (MFA-AFM) is a realistic precision finishing process used for part finishing. The process has applicability in a wide scope of industries such as aerospace, automobile, prosthetic, and tool and die manufacturing. This article primarily emphasizes on the machining mechanism of MFA-AFM intending to understand the relationships among the machining parameters, the material removal rate (MRR), and the surface quality of soft, ductile aluminum tubes. Hydraulic pressure, magnetic flux, abrasive mesh size, no. of cycles, and media are the major machining parameters that influence the machining characteristics. The experiments have been organized and conducted by employing the design of the experiment technique. The analysis of variance (ANOVA) was presented to find the contribution of all model terms influencing the MRR, and percentage change in the surface roughness ($\% \Delta Ra$). The experimental results disclose that the key contributor parameters to enhance MRR and $\% \Delta Ra$ are hydraulic pressure and magnetic flux followed by the no. of cycles. Higher-order response models for the prediction of MRR and $\% \Delta Ra$ have also been presented. The optimum machining conditions have been found from numerical optimization. Surface analysis was employed to characterize the surface integrity.

Keywords MFA-AFM · Magnetic flux · ANOVA · Material removal rate (MRR) · SEM

P. Singh (✉) · L. Singh
Mechanical Engineering Department, Baba Banda Singh Bahadur Engineering College, Fatehgarh Sahib, India
e-mail: palwindergill13@gmail.com

S. Singh
Mechanical Engineering Department, Guru Nanak Dev Engineering College, Ludhiana, India

1 Introduction

Magnetic field assisted abrasive flow machining (MFA-AFM) is an unconventional machining process. In MFA-AFM, the flexible machining tool called media has some special properties. Abrasion occurs when the media goes through a very limited path. So, material removal occurs by the flow of polymeric abrasive media across or through the surfaces to be machined. Singh et al. [1, 2] machined brass and aluminum by magneto AFM and found that material removal rate (MRR) was improved lesser in aluminum than in brass. Kim [3] processed “chrome-molybdenum spring collects” and performed a deburring test utilizing AFM. Ling et al. [4] polished micro-bores of metal and ceramics utilizing AFM. Das et al. [5] proposed magneto-rheological abrasive flow finishing (MRAFF) process for nano-finishing of parts. Jung et al. [6] processed injectors using the AFM process and reported that engine performance can be improved by the machining results. Singh et al. [7] worked on aluminum and brass as workpieces. They found that the MRR of brass was more in comparison to aluminum. Das et al. [8] developed a “Rotational–MRAFF (R-MRAFF)” process for examining the improvement in “out-of-roundness (OOR)” of stainless steel tubes. The design of the experiment technique was proposed. Singh et al. [9] processed brass work specimens. They reported that improvement in surface finish acquired up to 0.6 T of magnetic flux. Pusavec et al. [10] proposed a movable mandrel-based AFM for improving AFM performance. Kathiresan and Mohan [11] employed the design of experiments for the processing of AISI stainless steel 316L using the MRAFF process. Butola et al. [12] described the optimal parameters for surface roughness. Singh et al. [13] reported that magnetic AFM showed more improvement in surface finish than AFM. Amir et al. [14] worked on stainless steel 304 with SiC abrasive particles-based media and described that with slowly increased magnetic flux from 0.2 T to 1 T, the surface finish decreases. Bahre et al. [15] machined AISI 4140 steel by AFM utilizing Al_2O_3 abrasives-based media and found that a high value of pressure resulted in the desired surface finish. Yadav et al. [16] machined aluminum and brass workpieces and concluded that AFM was able to deburr very small holes and radius small edges. Singh et al. [17–19] reported only the improvement in surface finish not MRR for aluminum tubes by the magnetic AFM process.

As noticed from the literature that very few studies are available regarding the processing of ductile materials like aluminum with bonded magnetic abrasives particles (MAPs) up till now. Also, simple trial-and-error techniques used to obtain an empirical relationship and optimization are time-consuming and result in decreased production, resulting in high rejections and costs. Therefore, the necessity of the design of experiment techniques emerges. The goal of the present work is to assess the influence of machining parameters on improving the rate of material removal and surface finish in the MFA-AFM process by the design of experiment techniques.

2 Experimental Work

2.1 Workpiece Preparation

Aluminum material has been selected due to its versatility and usefulness, in a more extensive scope of items, structures, and finishes than any other. The Aluminum rod for making work specimens (tubular type) is commercially available. Aluminum tubes were prepared to the required size of $\text{Ø}16 \text{ mm} \times \text{Ø}8 \text{ mm} \times 25 \text{ mm}$. The weight of these tubes was measured by a weighing balance (Least Count = 0.1 mg) and the surface roughness was measured by a Mitutoyo tester (Least Count = 0.001 μm).

2.2 Aluminum Tubes Processing by MFA-AFM Machine

The main components of the MFA-AFM machine are two hydraulic cylinders, two media cylinders, an electromagnet (Magnetic flux of 8000 Gauss), a cooling mechanism to maintain the media temperature within a specified range, and a fixture as shown in Fig. 1. The polymeric-laden medium was produced by mixing diamond-based mechanically alloyed bonded MAPs [20, 21] (average: 275 mesh) with a medium. Mcgregor [22] reported in a patent that the medium mainly consists of typical chemicals in specific amounts. In the MFA-AFM setup, the aluminum tube was clamped with a fixture [23] in such a way that the flow of media is axial.

3 Design of Experiments

“Response surface methodology (RSM)” has been employed for designing, performing, and optimizing the experimentation data. A Central Composite Design (CCD) and statistical analysis have been used in which twenty experiments have been conducted at the levels as illustrated in Table 2 according to the design matrix generated by the statistical “Design-Expert 13.0.0” software. This software has also been utilized for the regression analysis of experimental data, to plot various graphs and contour plots. Montgomery [24] stated that “RSM is a combination of mathematical and critical approaches to building a test model structure, improving and improving process parameters, and can be used equally to find connections to various influential factors”.

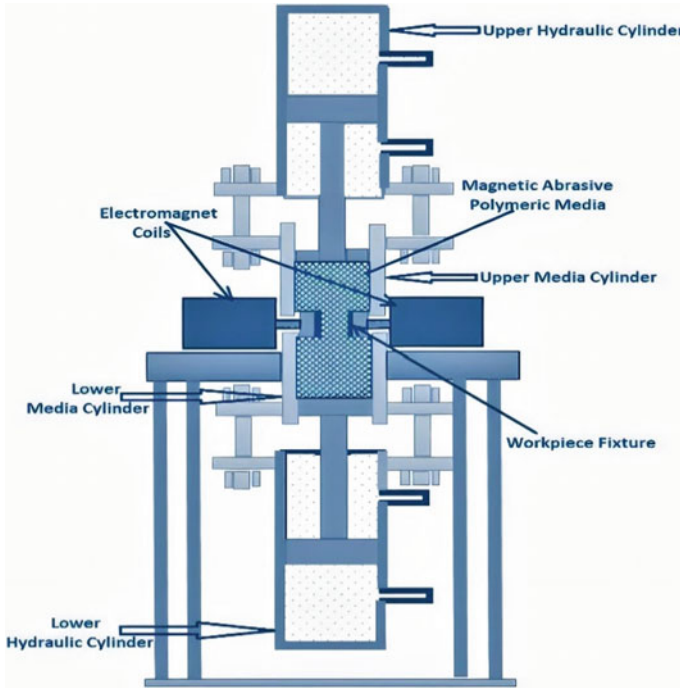


Fig. 1 Schematic view of MFA-AFM setup

The response function (Y) is divided into “linear, quadratic, and interactive components”. The data of experimentation is fitted to the 2nd-order regression equation [25]:

$$Y = X_0 + X_1A + X_2B + X_3C + X_{12}AB + X_{13}AC + X_{23}BC + X_{11}A^2 + X_{22}B^2 + X_{33}C^2 \quad (1)$$

where “ X_0 is the intercept; X_1 , X_2 , and X_3 are the linear coefficients; X_{12} , X_{13} , and X_{23} are the interaction coefficients; X_{11} , X_{22} , and X_{33} are the squared coefficients”.

The adequacies of the model were checked with respect to adjusted values. The ANOVA was utilized to decide the significance of the model and for the calculation of the statistical parameters. The statistical significance was checked by the F-test. Optimized conditions and estimated values are verified to confirm the validity of the model.

The coded and actual levels of considered independent machining parameters are given in Table 1. The experiments were performed keeping some parameters constant and varying other parameters like magnetic flux (A , Gauss), no. of cycles (B), and hydraulic pressure (C , bar) as given in Table 1. MRR and $\% \Delta Ra$ was used as a measure of performance evaluation of the MFA-AFM process. MRR is the

Table 1 Machining parameters and their levels

Coded levels	Magnetic flux (Gauss)	No. of cycles	Hydraulic pressure (bar)	Response parameters
-α	1500	10	15	1. Material removal rate (MRR) 2. Percentage change in surface roughness (%ΔRa)
-1	3000	15	30	
0	4500	20	45	
+1	6000	25	60	
+α	7500	30	75	

Constant parameters:
 MAPs of 275 mesh size
 Media temp., “32 ± 2 °C”
 Initial Ra, 1.05–1.45 μm

difference between “the initial weight and the final weight of the workpiece divided by the no. of cycles”. %ΔRa is “the ratio of (ΔRa × 100) and the initial Ra value where ΔRa is the difference between Ra values” before and after MFA-AFM. The experimental results for MRR and %ΔRa are tabulated in Table 2.

4 Results and Discussion

4.1 Generation of the Models

The regression analysis of the experimental data has been studied and contour plots have been generated. The quadratic models of both the responses (MRR and %ΔRa) in terms of coded parameters are given beneath:

$$\begin{aligned}
 \text{MRR (mg/cycle)} = & -0.704 + 0.0002 \times \text{Magnetic Flux(Gauss)} + 0.086 \\
 & \times \text{No. of Cycles} + 0.0125 \times \text{HydraulicPressure(bar)} \\
 & -0.000000 \times \text{Magnetic Flux(Gauss)} \times \text{Magnetic Flux(Gauss)} \\
 & -0.00154 \times \text{No. of Cycles} \times \text{No. of Cycles} - 0.000165 \\
 & \times \text{HydraulicPressure(bar)} \times \text{HydraulicPressure(bar)} \tag{2} \\
 & -0.000006 \times \text{Magnetic Flux(Gauss)} \times \text{No. of Cycles} \\
 & +0.000001 \times \text{Magnetic FLux(Gauss)} \\
 & \times \text{Hydrauli cPressure (bar)} + 0.00014 \times \text{No. of Cycles} \\
 & \times \text{Hydraulic Pressure (bar)}
 \end{aligned}$$

Table 2 Central composite design presentation and responses along with the errors

Exp. no.	A: Magnetic flux	B: No. of cycles	C: Hydraulic pressure	Exp. MRR (mg/cycle)	Pred. MRR(mg/cycle)	Error, MRR	Exp % Δ Ra (%)	Pred % Δ Ra (%)	Error, % Δ Ra
1	5000	20	45	1.07	1.09	-0.0187	69.37	69.61	-0.2380
2	5000	20	45	1.09	1.0913	-0.0013	70.62	69.61	1.010
3	3500	25	30	0.9570	0.9598	-0.0028	46.38	46.94	-0.5624
4	6500	15	30	0.9470	0.9553	-0.0083	66.67	66.70	-0.0299
5	5000	20	45	1.10	1.09	0.0113	70.30	69.61	0.6920
6	5000	20	75	1.09	1.10	-0.0038	72.18	72.34	-0.1639
7	5000	20	45	1.08	1.09	-0.0087	68.95	69.61	-0.6580
8	6500	15	60	1.13	1.135	-0.005	69.10	69.18	-0.0799
9	5000	20	45	1.11	1.09	0.0223	68.85	69.61	-0.7580
10	5000	20	45	1.08	1.09	-0.0097	70.20	69.61	0.5920
11	2000	20	45	0.9560	0.9598	-0.0038	57.30	56.54	0.7561
12	6500	25	30	0.8630	0.8581	0.0049	45.97	46.63	-0.6624
13	5000	30	45	0.9460	0.9498	-0.0038	56.68	56.26	0.4186
14	3500	15	60	0.9670	0.9698	-0.0028	57.51	57.49	0.0201
15	8000	20	45	1.02	1.02	0.0017	67.81	67.92	-0.1139
16	5000	10	45	0.9260	0.9243	0.0017	58.97	58.75	0.2236
17	6500	25	60	1.07	1.07	-0.0028	75.61	75.25	0.3576
18	3500	15	30	0.8840	0.8791	0.0049	54.50	55.50	-0.9999
19	3500	25	60	1.10	1.09	0.0104	74.46	75.07	-0.6124
20	5000	20	15	0.7910	0.7893	0.0017	42.54	41.73	0.8061

$$\begin{aligned}
 \% \Delta Ra (\%) = & -16.25 + 0.0175 \times \text{Magnetic Flux(Gauss)} + 2.715 \times \text{No. of Cycles} \\
 & -0.003 \times \text{Hydraulic Pressure (bar)} - 0.000001 \times \text{Magnetic Flux} \\
 & \times (\text{Gauss}) \times \text{Magnetic Flux(Gauss)} - 0.121 \times \text{No. of Cycles} \\
 & \times \text{No. of Cycles} - 0.014 \times \text{Hydraulic Pressure (bar)} \\
 & \times \text{Hydraulic Pressure (bar)} - 0.00038 \times \text{Magnetic Flux(Gauss)} \\
 & \times \text{No. of Cycles} + 0.000005 \times \text{Magnetic Flux(Gauss)} \\
 & \times \text{Hydraulic Pressure (bar)} + 0.0871 \times \text{No. of Cycles} \\
 & \times \text{Hydraulic Pressure (bar)}
 \end{aligned}
 \tag{3}$$

4.2 Analysis of the Models

The ANOVA was carried out at a 5% significance and 95% confidence level for MRR and $\% \Delta Ra$. The quadratic model is suitable for both $\% \Delta Ra$ and MRR. The complete ANOVA results for MRR and $\% \Delta Ra$ are stated in Table 3.

The models for both the responses are highly significant and the lack of fit is not significant which is good for the fitness and adequacies of the models. There is a decent agreement between “**Predicted R²**” and “**Adjusted R²**” for both the models due to the negligible difference. So, the generated models are acceptable for both MRR and $\% \Delta Ra$. The “adjusted R²” values for MRR and $\% \Delta Ra$ were 0.9847 and, 0.9933 respectively, which were also high and state a high correlation between the experimental and the predicted values. **Adequacy precision** > 4 for both models shows the adequacy of the models. The predicted and actual (experimental) values for both the responses are in near agreement as they are following the fitted-line as revealed in Fig. 2a and b. This represents that the models are acceptable and can be applied on the shop floor directly.

4.3 Evaluation of Material Removal Rate (MRR)

The main effect graphs of parameters for MRR generated with the aid of Minitab 17 software are illustrated in Fig. 3a–c. It can be seen that under a strong magnetic field, there is a significantly improved MRR. Figure 3a–c demonstrates the effect of parameters such as “magnetic flux, no. of cycles, and hydraulic pressure” on the MRR. The MRR will increase significantly by increasing magnetic flux from 1500 to 4500 Gauss. Graphically the MRR has increased when the no. of cycles has increased. The workpiece abrasion is caused by the magnetic flux, resulting in a change in the scatter pattern of the MAPs on the inner hollow surface of the workpiece, resulting in the MAPs gradually participating in the abrasion zone and the axial MAPs strike the working surface at smaller angles. The enhanced MRR may be due to the cumulative

Table 3 ANOVA for the quadratic model of responses

Source	SSq	DOF	MSq	F-Value	p-value	Significance
<i>Material removal rate (MRR)</i>						
Model	0.1811	9	0.0201	136.63	<0.0001	Yes
A	0.0033	1	0.0033	22.45	0.0008	Yes
B	0.0007	1	0.0007	4.42	0.0619	No
C	0.0939	1	0.0939	637.93	<0.0001	Yes
AB	0.0158	1	0.0158	107.58	<0.0001	Yes
AC	0.0034	1	0.0034	23.39	0.0007	Yes
BC	0.0009	1	0.0009	5.99	0.0344	Yes
A ²	0.0164	1	0.0164	111.32	<0.0001	Yes
B ²	0.0371	1	0.0371	251.88	<0.0001	Yes
C ²	0.0345	1	0.0345	234.17	<0.0001	Yes
“Residual”	0.0015	10	0.0001			
“LOF”	0.0003	5	0.0001	0.2858	0.9023	No
“Pure Error”	0.0011	5	0.0002		R ² = 0.9919	Pred. R ² = 0.9779
Correlation Total	0.1826	19			Adj. R ² = 0.9847	Adeq. Prec. = 39.60
<i>Percentage Change in Surface Roughness (%ΔRa)</i>						
Model	1890.29	9	210.03	314.90	<0.0001	Yes
A	129.50	1	129.50	194.17	<0.0001	Yes
B	6.18	1	6.18	9.26	0.0124	Yes
C	936.97	1	936.97	1404.80	<0.0001	Yes
AB	66.24	1	66.24	99.31	<0.0001	Yes
AC	0.1200	1	0.1200	0.1800	0.6804	No
BC	341.65	1	341.65	512.24	<0.0001	Yes
A ²	85.45	1	85.45	128.12	<0.0001	Yes
B ²	230.23	1	230.23	345.18	<0.0001	Yes
C ²	248.26	1	248.26	372.21	<0.0001	Yes
“Residual”	6.67	10	0.6670			
“LOF”	3.82	5	0.7642	1.34	0.3776	No
“Pure Error”	2.85	5	0.5698		R ² = 0.9965	Pred. R ² = 0.9818
Correlation Total	1896.96	19			Adj. R ² = 0.9933	Adeq. Prec. = 58.04

Notes SSq—Sum of Squares; DOF—Degree of Freedom; MSq—Mean Square; LOF—Lack of Fit

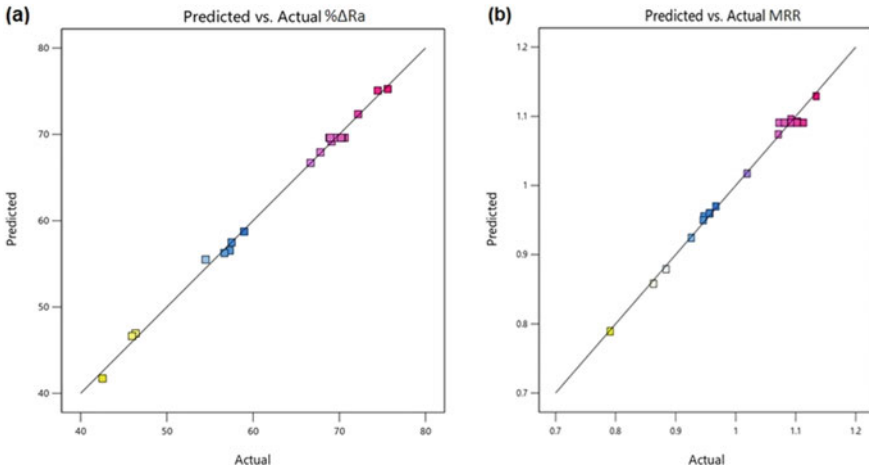


Fig. 2 Predicted versus actual plot for **a** %ΔRa and **b** MRR

effect of the above-mentioned reasons [2]. Interaction of magnetic flux and the no. of cycles is also significant and can also be seen in Table 3. Since aluminum is softer and more ductile, MAPs that hit the surface at an angle will plough the material and create pits, resulting in a higher MRR.

The data in Table 3 exhibited that, for the MRR model, every linear component is significant (<0.05) with hydraulic pressure having the dominant influence on MRR followed by magnetic flux and no. of cycles. Figure 4a–c represents the contour

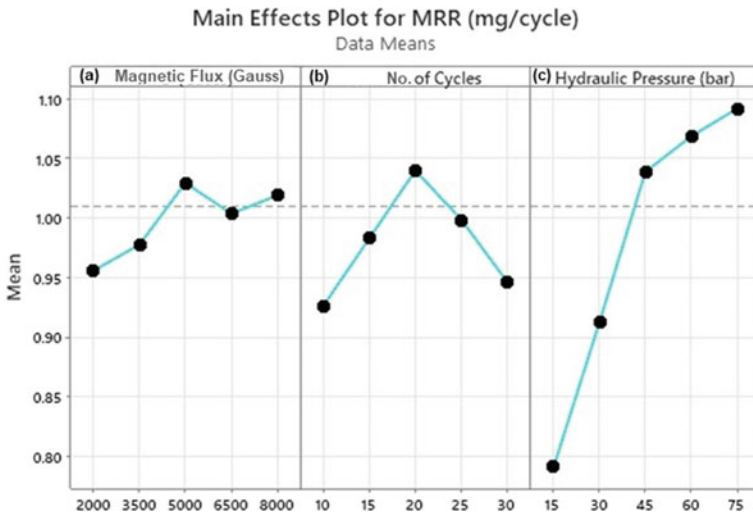


Fig. 3 a–c Main effect graphs for MRR

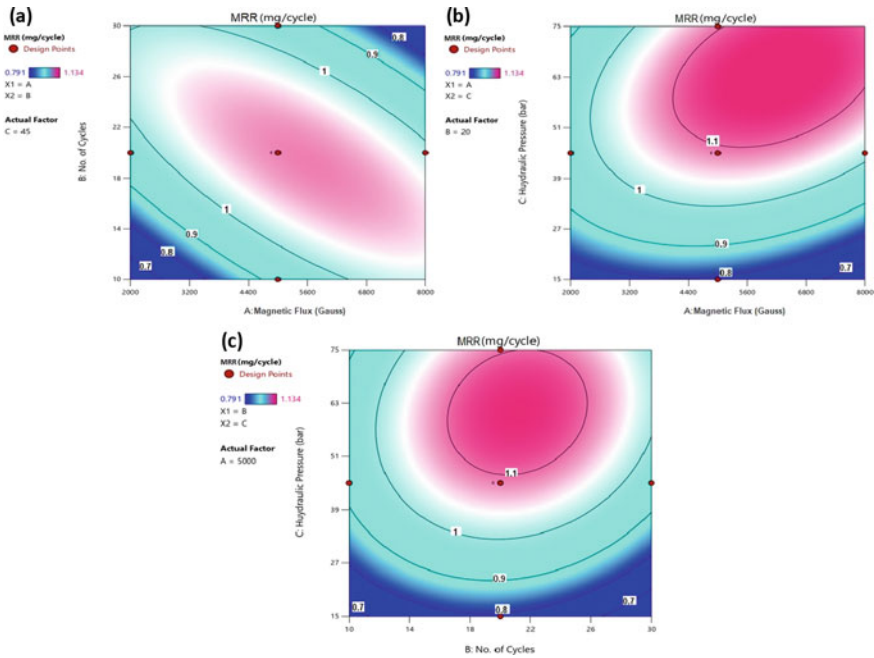


Fig. 4 a–c Contour plots for MRR

plots representing the influence of machining parameters on MRR. Figures 4a and c revealed that the increased hydraulic pressure and magnetic flux will increase the value of MRR with the increasing no. of cycles up to a definite limit of the tried range. But, further increasing no. of cycles did not result in significant improvement in the MRR. Moreover, from an industrial point of view, a higher no. of cycles means low efficacy of the MFA-AFM process. The MRR value can be improved with the increment of hydraulic pressure as depicted in Fig. 4b. The positive linear effect (<0.01) and significant quadratic effect (<0.05) of hydraulic pressure have brought about a curvilinear increment in MRR for all estimations of magnetic flux. The effects of the hydraulic pressure and magnetic flux on MRR are shown in Fig. 4b. Because both of the parameters played a more vital role in improving MRR, by increasing hydraulic pressure and magnetic flux, the MRR increases significantly.

4.4 Evaluation of Percentage Change in Surface Roughness ($\% \Delta Ra$)

The main effect graphs of parameters for $\% \Delta Ra$ are illustrated in Fig. 5a–c. It is seen that with the increased magnetic flux, the $\% \Delta Ra$ increased because the magnetic flux increases the polishing pressure which further increased the indentation force to

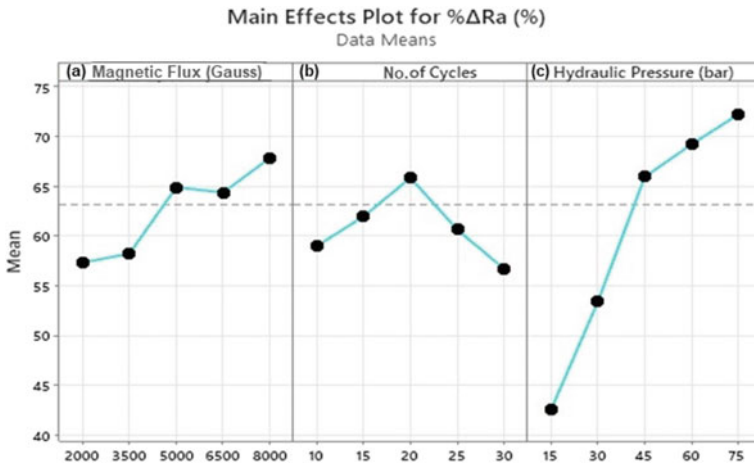


Fig. 5 a–c Main effect graphs for %ΔRa

increase the material removal and accelerate the finishing [25]. Figure 5b illustrates that %ΔRa increases sharply for the initial no. of cycles, and a further decrease in the value of %ΔRa, as the edges of the sharp MAPs, become blunt, results in only a slight change in the surface roughness on continuous machining [25]. It is also clear from Fig. 5c, that with increased hydraulic pressure, %ΔRa goes on increasing but the change in the surface roughness is more up to 45 bar and there is marginal improvement after 45 bar of hydraulic pressure. This is because an increased hydraulic pressure up to 45 bar prompts an increased axial force that results in increasing %ΔRa values. Furthermore, with increased hydraulic pressure from 45 to 75 bar, the change in the surface roughness is very small. This is because at high values of hydraulic pressure, as the highly viscous medium hardens, the no. of active abrasive particles decreases.

Figure 6a–c represents the contour plots representing the influence of machining parameters on %ΔRa. It could be seen in Fig. 6a and b that an enhancement of magnetic flux past a specific limit of the tried range has brought about the increment of the %ΔRa. As hydraulic pressure and magnetic flux have a dominant influence compared to the no. of cycles for %ΔRa, an increased no. of cycles may not be useful for the MFA-AFM process. Also, from an industrial point of view, a higher no. of cycles means low efficacy of the MFA-AFM process. The %ΔRa value can be improved with the increment of hydraulic pressure as depicted in Fig. 6b. Figure 6c exhibited that at a fixed magnetic flux of 5000 Gauss and by enhancing the hydraulic pressure the outcome is approximately equal as increasing the no. of cycles.

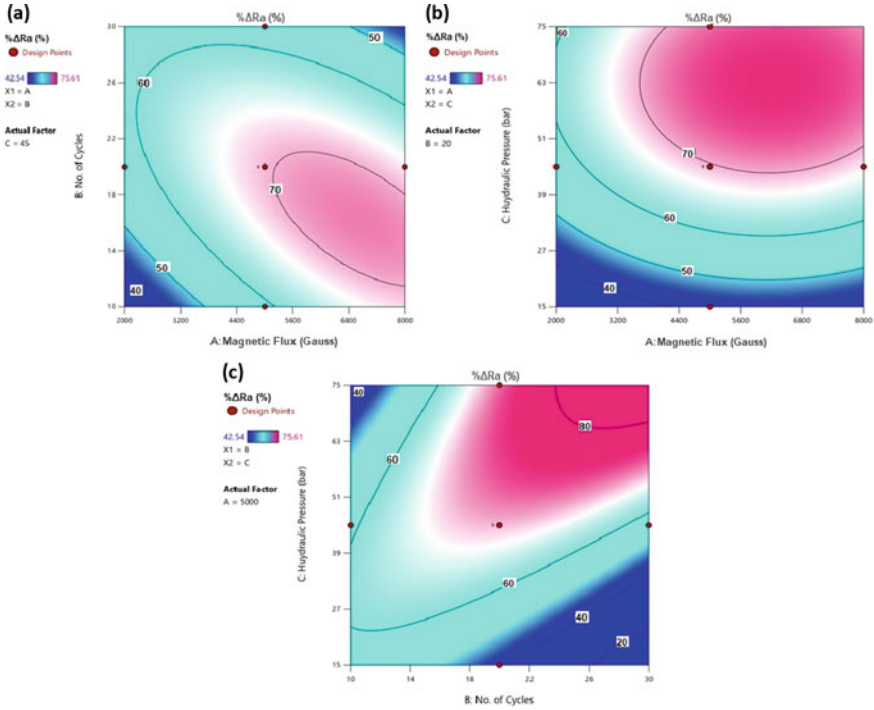


Fig. 6 a–c Contour plots for %ΔRa

4.5 Response and Input Parametric Optimization

Optimization of the MFA-AFM parameters is achieved by the numerical optimization method in which the optimum MFA-AFM conditions are decided where the highest MRR and %ΔRa can be achieved. The optimum operating conditions for MRR and %ΔRa by the MFA-AFM process are given in Table 4. Results show that experimental and predicted values are in close conformity in terms of a relative error of MRR = -0.442% and %ΔRa = 0.476%. This indicates that the proposed models could accurately estimate MRR and %ΔRa. So, the generated mathematical models are helpful to determine the process performance. The minimum Ra (highest surface finish) value was found to be 200 nm at optimum conditions.

4.6 Surface Analysis

“Scanning electron microscopy (SEM)” was utilized to study the surface integrity of the workpiece.

Table 4 Optimum conditions and model validation of % Δ Ra and MRR

Optimal levels	$Y_{\text{predicted}}$	$Y_{\text{experimental}}$	Relative error (%)
Material removal rate (MRR), mg/cycle A = 6500 Gauss, B = 15, C = 60 bar	1.135	1.13	-0.442
Percentage change in surface roughness (% Δ Ra), % A = 6500 Gauss, B = 25, C = 60 bar	75.25	75.61	0.476

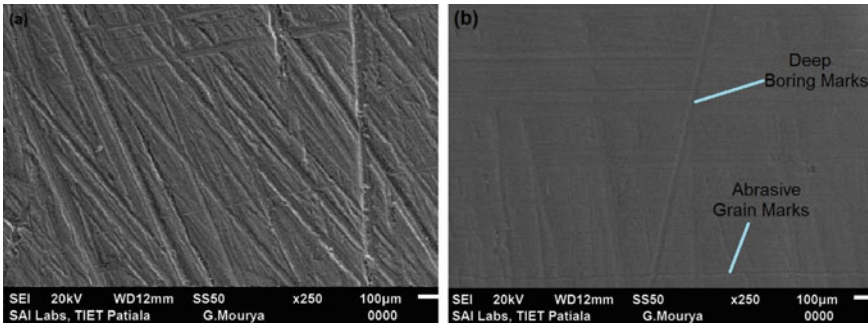


Fig. 7 SEM images for aluminum workpiece surface **a** before MFA-AFM, **b** after MFA-AFM

Figures 7a and b show the surface of the aluminum tube workpiece before and after MFA-AFM, respectively. SEM images represent that during MFA-AFM, cavity peaks got removed and the topography changes significantly finer. Therefore, the anomalies were significantly reduced, with only some abrasive grain marks and boring tool marks visible as shown in Fig. 7b. Therefore, such aluminum tubes are more useful in applications such as bio and micro-fluids applications.

5 Conclusions

The experiments were executed according to the design of experiments technique to investigate the performance of the MFA-AFM process in terms of material removal rate (MRR) and percentage change in surface roughness (% Δ Ra) of ductile material i.e., aluminum tubes. The magnetic flux, no. of cycles, and hydraulic pressure were the machining parameters. The diamond abrasive-based media was utilized, which works on the principle of extrusion and material removal which is in the type of minute chips owing to the abrasive-asperity interactions during the extrusion under applied pressure. The experimentation yielded the following main conclusions:

1. The hydraulic pressure and magnetic flux have the largest significant effect on material removal and surface roughness.

2. The combined effect of all considered machining parameters has a significant influence on MRR.
3. The magnetic flux, no. of cycles, and hydraulic pressure showed a significant quadratic effect in the central composite design experiment.
4. High-order non-linear response models were generated to indicate the influence of machining parameters on MRR and $\% \Delta Ra$.
5. A significant material removal rate (up to 1.135 mg/cycle) and change in the surface roughness (75.25%) were obtained at the optimum conditions in this work. Accordingly, the Ra value obtained was 200 nm.
6. This process can remove cavity peaks and the topography changes significantly finer as shown in the SEM images.

Acknowledgements The authors wish to thank the mechanical engineering department of Baba Banda Singh Bahadur Engineering College, Fatehgarh Sahib, India, for providing the necessary facilities for experimentation on the MFA-AFM setup.

References

1. Singh S, Shan HS (2002) Development of magneto-abrasive flow machining process. *Int J Mach Tools Manuf* 42:953–959
2. Singh S, Shan HS, Kumar P (2002) Wear behavior of materials in magnetically assisted abrasive flow machining. *J Mater Process Technol* 128:155–161
3. Kim JD, Kim KD (2004) Deburring of burrs in spring collets by abrasive flow machining. *Int J Adv Manuf Technol* 24:469–473
4. Das M, Jain VK (2008) Ghoshdastidar PS. Fluid flow analysis of magnetorheological abrasive flow finishing (MRAFF) process. *Int J Mach Tools Manuf* 48:415–426
5. Abrasive Flow Polishing of Micro Bores (2004) Ling., Y., Kuppuswamy, R., Stephen, W., Xiang, D.L., Han, H., Yu, C.L. *Mater Manuf Processes* 19:187–207
6. Jung D, Wang WL, Knaf A, Jacobs TJ, Hu SJ, Assanis DN (2008) Experimental investigation of abrasive flow machining effects on injector nozzle geometries, engine performance, and emissions in a DI diesel engine. *Int J Autom Technol* 9(1):9–15
7. Singh S, Shan HS, Kumar P (2008) Experimental studies on mechanism of material removal in abrasive flow machining process. *Mater Manuf Processes* 23(7):714–718
8. Das M, Jain VK, Ghoshdastidar PS (2011) The out-of-roundness of the internal surfaces of stainless-steel tubes finished by the rotational-Magnetorheological abrasive flow finishing process. *Mater Manuf Processes* 26(8):1073–1084
9. Singh R, Walia RS, Suri NM (2013) Study of parameters for magnetic force assisted abrasive flow machining process. *J Eng Technol Educ* 7:44–48
10. Pusavec F, Kenda J (2014) The transition to a clean, dry, and energy efficient polishing process: an innovative upgrade of abrasive flow machining for simultaneous generation of micro-geometry and polishing in the tooling industry. *J Clean Prod* 76:180–189
11. Kathiresan S, Mohan B (2017) Experimental analysis of magneto rheological abrasive flow finishing process on AISI stainless steel 316L. *Mater Manuf Processes* 33(4):422–432
12. Butola R, Jain R, Bhangadia P, Bandhu A, Walia RS, Murtaza Q (2018) Optimization to the parameters of abrasive flow machining by Taguchi method. *Mater Today Proc* 5:4720–4729
13. Singh P, Singh L, Singh S (2018) Experimental comparison of abrasive flow machining and magnetic abrasive flow machining for aluminum tubes. *Int J Res Eng Appl Manage* 4(3):714–720

14. Dehghanghadikolaei A, Fotovvati B, Mohammadian B, Namdari N (2018) Abrasive flow finishing of stainless steel 304 biomedical devices. *Res Dev Mater Sci* 8(2):1–8
15. Bahre D, Brunnet H, Swat M (2012) Investigation of one-way abrasive flow machining and in-process measurement of axial forces. In: 5th CIRP Conference on high performance cutting, vol 1, pp 419–424
16. Yadav SK, Singh MK, Singh BR (2015) Effect of unconventional machining on surface roughness of metal: aluminum and brass—a case study of abrasive flow. *SAMRIDDHI: J Phys Sci Eng Technol* 2:53–60
17. Singh P, Singh L, Singh S (2020) Analysing process parameters for finishing of small holes using magnetically assisted abrasive flow machining process. *J Bio- Tribo- Corrosion* 6:1–10
18. Singh P, Singh L, Singh S (2020) Manufacturing and performance analysis of mechanically alloyed magnetic abrasives for magneto abrasive flow finishing. *J Manuf Process* 50:161–169
19. Singh P, Singh L, Singh S (2020) Experimental investigation and design optimisation for magnetic abrasive flow machining using response surface methodology. *Int J Mater Prod Technol* 61(2–4):244–261
20. Singh P, Singh L, Singh S (2019) Preparation, microstructure evaluation and performance analysis of diamond-iron bonded magnetic abrasive powder. *Powder Metall Progr* 19(2):82–89
21. Singh P, Singh L, Singh S (2020) Preparation, microstructure analysis and performance evaluation of bonded magnetic abrasives. *Int J Abras Technol* 10(1):32–43
22. Mcgregor RR (1975) United states pat. 2431878, Corning Glass Works, Corning, New York
23. Walia RS, Shan HS, Kumar P (2009) Enhancing AFM process productivity through improved fixturing. *Int J Adv Manuf Technol* 44:700–709
24. Montgomery DC (2004) Design and analysis of experiment. Wiley, New York
25. Sihag N, Kala P, Pandey PM (2017) Analysis of surface improvement during ultrasonic assisted magnetic abrasive finishing on chemically treated tungsten substrate. *Proc Manuf* 10:136–146

4D Printing—A Smart Way of 3D Printing: A Brief Review



Pretesh John, Venkateswara Rao Komma, and Skylab Paulas Bhore

Abstract After the first introduction of 4D Printing in 2013, this new area has attracted researchers from academics and industries to explore novel possibilities. The foundation of the 4D Printing technology is primarily laid upon the similar process of 3D printing technology with additional requirements of stimuli environment and stimulus-responsive materials. In this article, three fundamental foundation pillars of 4D Printing, i.e., Smart Materials, Smart Designing, and 3D Printing Technologies, are reviewed. The literature concluded that the new dimension of time and exhibiting smart behavior differentiate 4D printing technology from 3D Printing. It was observed that 4D Printing is time-dependent, stimuli-dependent, design-dependent, and material-dependent. In this article, a review of the 4D Printing process is presented and summarized the two key features, i.e., Smart materials and Smart Design which draw the line between 3 and 4D Printing and pointed out the utility areas.

Keywords 4D Printing · Additive manufacturing · Smart manufacturing · Smart designing · Smart materials

1 Introduction

Additive manufacturing (AM), first described in the '80s by Chuck Hull [1] and additionally popularized as three-dimensional (3D) printing, has been distinguished as the pathway of the second industrial revolution of the age [2]. It is widely popular in scientific and public colonies and enables anyone to be a designer. It is also an

P. John (✉) · V. R. Komma · S. P. Bhore
Department of Mechanical Engineering, Motilal Nehru National Institute of Technology
Allahabad, Prayagraj, Uttar Pradesh, India
e-mail: preteshjohn@yahoo.com; pretesh.2020rme08@mnnit.ac.in

V. R. Komma
e-mail: kvrao@mnnit.ac.in

S. P. Bhore
e-mail: skylabpbhore@mnnit.ac.in

area of attention for industries because of the fabrication of involved and Daedalian components with a time and material-saving economical approach [3]. 3D Printing is annotated as a CAD design-based layers adhesive manufacturing method to produce 3D parts [4]. Expeditious proceedings in printing technologies and materials expansion have opened a door for the 3D Printing of smart, composite, and hybrid materials [5].

New efforts are always made to develop futuristic materials with required functionality by adding functionalized, bio, or other foreign particles in conventional 3D printing materials [6, 7]. Researchers have adjoined these smart futuristic materials with 3D Printing to explore an innovative routine for shaping active structures [8–10]. It is termed 4D Printing, where the scope for a function is inherent within the additive manufactured part. Parts manufactured with 3D Printing from CAD models in 3D coordinates are static, but 4D Printing adds another dimension of time and provides a dynamic behavior influenced by surrounding stimuli. 4D printing technology results from interdisciplinary research of Smart materials, Smart designs, and 3D printers [11].

2 4D Printing

In 2013, Skylar Tibbits, at the TED2013 conference, California, first announced 4D Printing [12]. 4D printing technology is like 3D Printing except for time as the fourth dimension in a 3D printed object. Ergo, the 4D Printing can be comprehended as enabling the 3D structure to change its phases concerning time under stimuli conditions such as light, water, heat, load, current, or magnet [5, 13, 14] without using additional equipment [15]. Alternatively, 4D Printing gives life to 3D Printing [11].

Initially, 4D Printing was conceptualized as “3D printing + time”, but this definition has also improved with more research in this field. Present modified widespread elucidation of 4D Printing is that the evolution of 3D printed structure with time by stimulus effect with reference to form, functionalities, or properties [11]. Figure 1 differentiates the concepts of 3D and 4D Printing schematically. In 3D Printing, the object remains unchanged with time and stimuli, but in 4D, we can observe the effect of stimuli with time.



Fig. 1 Schematic of the 3D and 4D concepts

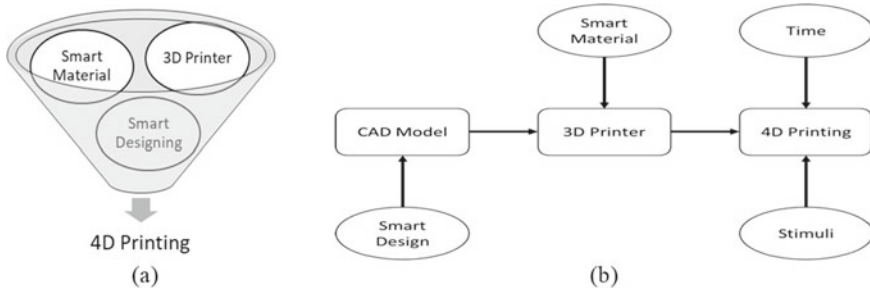


Fig. 2 4D printing **a** basic concept, **b** process layout

2.1 Process

Both the 4D and 3D printing processes are nearly coequal. In both approaches, the first step is to design the computer-aided design (CAD) model of the object, then printed it with a suitable 3D printer. There are two core aspects, which differentiate 4D Printing from 3D Printing:

- (i) Smart Materials and (ii) Smart Designs.

The smart design of 4D printed structures means that they should be detailed, totally pre-programmed, and all time-dependent deformations oriented [16]. Sometimes mathematical modeling becomes advantageous in designing the material distribution [17].

Another core feature of 4D printing technology is Smart Materials, which can transform in other phases in response to applied stimuli. Smart materials have two or more stable states, and the structure can switch configuration under the corresponding trigger. In Fig. 2, the basic concept of the 4D Printing and process layout is described as it is discussed above.

In Table 1, available types of key features of 4D printing technology are given along with the types of shape changes, type of stimuli, and various application areas. All the data are collected from multiple research articles and summarized in tabulated form.

In Fig. 3, schematics of various sorts of shapes changing in 4D printing technology are illustrated. These kinds of transformations lead the 4D printing products in various applications as listed in Table 1 such as soft robots, soft electronics, biopsy tools, product packaging, sensors and actuators, drug delivery, smart valves, electromagnetic applications, aerospace applications, stet, tissue engineering, etc.

2.2 Smart Materials

Conventional materials for 3D Printing cannot be applied in 4D Printing because of their irresponsive behavior to applied stimuli conditions. The list of smart materials

Table 1 Brief description of 4D printing

Smart materials	Shape memory alloys (SMA) [18], liquid crystal elastomers (LCE) [19], shape memory polymers (SMP) [20], Hydrogels [21], etc
Printers	Fused deposition modeling (FDM) [22], Inkjet [23], Stereolithography (SLA) [24], Digit light processing (DLP) [25], etc
Smart design considerations	Deformed/changed shape drawing [26], Pre-programmed design [27], Mathematical modeling [17], etc
Types of shape changes	1D to 1D [28], 1D to 2D [29], 2D to 2D [30], 1D to 3D [29], 2D to 3D [21], 3D to 3D [31]
Stimuli	Electricity, heat, light, moisture, magnetic field [32–36], etc
Applications	Soft robots [37], products packaging [38], sensors [39], drug delivery [40], micro valve [41], electromagnetic applications [23], self-healing [42], etc

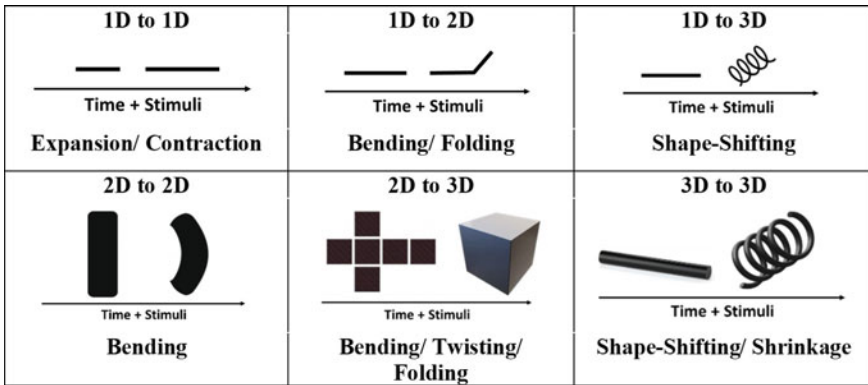


Fig. 3 Types of shape-changing in 4D printing

for 4D printing include SMPs [24], SMAs [18], Hydrogels [43], and LCEs [19], etc. Out of these materials, Low costing, Simple processing, and large and one-way or two-way deformation capability triggered by numerous stimuli conditions like Temperature [44], Moisture [32], Electricity [6], Light [45], Magnetic [36], and pH [46], ranked up the SMPs popularity in research community [36]. Several smart materials are found in the literature for smart 3D Printing, including materials that self-assemble, self-degradation, self-healing [29, 31, 47–49] in response to external stimuli. Choong et al. investigated the durability of SMP with SLA technology [24]. Caputo et al. used magnetic SMA with powder bed binder jetting [18]. Ambulo et al. found that with controlled geometry and thermal conditions LCEs can be used for reversible 3D structures [19]. Tolley et al. modeled and characterized four thermal responsive self-folding SMP structures along with self-healing applications [44]. Hann et al. fabricate, characterize and model the temperature and pH-triggered liquid crystalline polymer films for 90-degree mechanical actuation [46]. Water responsive

shape-changing multi-materials structure was printed at the Massachusetts Institute of Technology (MIT) [29]. SMPs and SMAs inherit the thermal responsive shape-shifting ability [50]. There are Photo or light-responsive materials for 4D printing materials, in which 3D printed object shows color variation initiated by UV irradiation or sunlight [45, 49]. Color shifting occurs when the material's polymeric chains are transformed from the arranged nematic phase to the disarrayed phase [51]. Photo-thermal responsive shape-shifting structures are also mentioned in literature, in which performance is correlated with infrared (IR) light intensity, ambient temperature, and other parameters [43]. Another smart material Hydrogel ink functions as infrared (IR) light-absorbing agent and causes light to thermal energy conversion and creates the deformation [21]. Zhao et al. experimented with shape memory polyurethane via STL and found excellent shape memory performance, high recovery rate, and good accuracy and durability with good strength and toughness [20]. Magnetic programmable shape memory polylactic acid (PLA) composites were studied by Zhang et al. and found a high recovery rate and applicable in healthcare and biomedical applications [36]. Arazoe et al. investigated the ambient humidity-driven carbon nitride polymer (CNP), which can be used as a low power consumption actuator and electronic devices with a rapid response time of 50 ms with more than 10,000 repeat abilities [32].

2.3 *Smart Design*

Designing smart objects is another core technique for 4D Printing, which is directly reflected in the phase change. As discussed before, the smart material acts as a decisive agent in transfiguring the printed object's configuration but designing and printing these intelligent materials in an optimized manner also holds the same importance as the smart materials. It is essential to decoding the degree of convolution of the structure and response mechanism with the stimuli environment and its required conditions, governing principles, and required parameters to achieve desired results in a controlled manner [52, 53]. Smart materials' orientation during Printing and their placement within composite materials affect the response to external stimuli. Also, the size, density, and shape of the compounded geometry play a crucial role in 4D Printing [54]. Self-evolving structures by means of folds, curls, twists, expansion, and contraction, as well as other transformations, can be controlled by a variety of detailed joint designs [28]. In a study [55], it was observed that the physical dimensions of the printed parts affect the sequential bending of the 4D printed structure when applied to even external stimuli. 3D printing control parameters also affect the shape transformation time and rate of shape-changing [21]. Pre-programming of SMP models is possible during Printing with different printers such as DLP [56] or SLA [57] and taking advantage of printing parameters effects. For working with multi-material smart materials, mathematical modeling is a very effective tool in designing 4D structures [17]. Ryu et al. used the simulation-based design to develop a 4D Photo Origami self-folding cube [49]. Proper designing can enable miniature origami robots

to self-fold, swim, walk or degrade [50]. A shape optimization route was given by Kwok et al. to convert 2D surface into shape-changing 2D pattern achieved by adding interior/boundary cuts [52]. Rudykh et al. from MIT designed some hybrid designs to make components flexible, and penetration resisting and provided new design guidelines for improved flexible armor systems [53]. Manen et al. presented a novel method for simultaneously printing and programming SMP for shape-shifting application by a hobbyist printer. They demonstrated that the design strategies could lead SMP to achieve self-folding, sequential shifting, etc. [27]. Gladman et al. designed and printed botanical system-inspired composite hydrogel structures governed by fiber directions. By controlling the printing direction, they pre-programmed the 4D structures [6].

2.4 3D Printer

4D Printing is an application or function targeted technique that effectively works with optimized printing parameters and requires a specific processing method for specific material properties. Suitable solutions for 4D printing include PolyJet [13], DLP [25], direct writing (DW) [31], and FDM [22].

SLA type of printer is widely used to print 4D origami actuators with photo-responsive polymer resin network with shape memory properties [24]. FDM type printer is also employed for developing SMP actuators at low cost [22], especially in pre-programming models [27]. Its parameters were investigated to analyze the effect on the Self-folding mechanism [3]. Inkjet printers are also recorded to fabricate 4D origami actuators and sensors [23]. According to Lewis J. A., direct-write technology enables to design and manufacture of components without expensive tools, dies, or lithographic masks [48]. DLP type technology is also used to fabricate unsupported 4D origami through backward direction motion [25]. Selective Laser Melting (SLM) technology was also used to process Cu-based shape memory alloy to obtain dense martensitic samples with optimized parameters [58]. SMA powders can be processed by Powder bed binder jetting printers followed by Curing and Sintering operation [18]. Kokkinis, Schaffner, and Studart developed a magnetically assisted five-dimensional design space 3D printer with a multi-material dispenser system and component mixing unit to control the particle orientation and local composition in the ink writing process and named it MM-3D printing [31]. Ge et al. used a PolyJet printer to print multi-material components to control the origami folding pattern and developed a theoretical model to select appropriate design parameters [13].

3 Conclusions

4D Printing has gained scientific society's attention because of the introduction of the time axis in the 3D space coordinates and providing dynamic behavior to the 3D structures as a function of time when introduced to triggering stimuli. In the paper, a brief review was given on the various 4D printing methods, smart stimuli-responsive materials, and Smart designing considerations. However, there are still many practical challenges to introducing 4D Printing at the industry level or mass production.

The development of new multiphase materials is opening doors to utilize them with traditional 3D printing technology to print 4D structures. Various SMAs, SMPs, Hydrogels, etc., are there, which shows stimuli response. Still, there is a great possibility to enhance the outputs in terms of response time, load capacity, recovery rate, etc. Most of the materials are in the development phase. Product-oriented research can enable these materials as a substitute for traditional devices and systems. These intelligent materials can be used in lightweight actuators, low energy consumption systems, self-folding, and self-healing systems, etc. Also, there are many scopes in understanding the designing parameters of 4D structures to pre-program them or select printing parameters. Layer directions, fiber orientation, infill pattern, etc., play an essential role in 4D printed structures. A well-defined smart design and proper modeling are needed to enable a CAD model to be used in shape-shifting applications.

From 2013 till now, it has evolved very rapidly and still growing amazingly, but it is still a very young and significant number of works needed for firm establishment in the future. The up-gradation and innovation in new printing methods, novel futuristic smart materials, and new smart structural design will introduce 4D Printing to various functional applications, including soft robotics, soft electronics, aerospace application, tissue engineering, etc.

References

1. Hull C (1986) Apparatus for production of three dimensional objects by Stereolithography
2. Zhai Y, Lados DA, Lagoy JL (2014) Additive manufacturing: making imagination the major limitation. *JOM* 66:808–816
3. Bodaghi M, Damanpack AR, Liao WH (2017) Adaptive metamaterials by functionally graded 4D printing. *Mater Des* 135:26–36
4. ISO/ASTM: Additive manufacturing—general principles terminology (ASTM52900). <https://www.iso.org/obp/ui/#iso:std:iso-astm:52900:dis:ed-2:v1:en>. Accessed 12 Apr 2021
5. Choi J, Kwon OC, Jo W, Lee HJ, Moon MW (2015) 4D printing technology: a review. *3D Print. Addit Manuf* 2:159–167
6. Campbell TA, Tibbitts S, Garrett B (2014) The next wave : 4D printing—programming the material world. *Atl Counc* 1–15
7. Campbell TA, Ivanova OS (2013) 3D printing of multifunctional nanocomposites. *Nano Today* 8:119–120

8. Godec D, Cano S, Holzer C, Gonzalez-Gutierrez J (2020) Optimization of the 3D printing parameters for tensile properties of specimens produced by fused filament fabrication of 17–4PH stainless steel. *Materials* (Basel) 13:774
9. Momeni F, Mehdi Hassani NS, Liu X, Ni J (2017) A review of 4D printing. *Mater Des* 122:42–79
10. Ding Z, Yuan C, Peng X, Wang T, Qi HJ, Dunn ML (2017) Direct 4D printing via active composite materials. *Sci Adv* 3:e1602890
11. Kuang X, Roach DJ, Wu J, Hamel CM, Ding Z, Wang T, Dunn ML, Qi HJ (2019) Advances in 4D printing: materials and applications. *Adv Funct Mater* 29:1–23
12. Tibbits S. The emergence of 4D printing. https://www.ted.com/talks/skylar_tibbits_the_emergence_of_4d_printing. Accessed 12 Apr 2021
13. Ge Q, Dunn CK, Qi HJ, Dunn ML (2014) Active origami by 4D printing. *Smart Mater Struct* 23:094007
14. Khoo ZX, Teoh JEM, Liu Y, Chua CK, Yang S, An J, Leong KF, Yeong WY (2015) 3D printing of smart materials: a review on recent progresses in 4D printing. *Virtual Phys Prototyp* 10:103–122
15. Wang Y, Li X (2020) An accurate finite element approach for programming 4D-printed self-morphing structures produced by fused deposition modeling. *Mech Mater* 151:103628
16. Hawkes E, An B, Benbernou NM, Tanaka H, Kim S, Demaine ED, Rus D, Wood RJ (2010) Programmable matter by folding. *Proc Natl Acad Sci U S A* 107:12441–12445
17. Zhou Y, Huang WM, Kang SF, Wu XL, Lu HB, Fu J, Cui H (2015) From 3D to 4D printing: approaches and typical applications. *J Mech Sci Technol* 29:4281–4288
18. Caputo MP, Berkowitz AE, Armstrong A, Müllner P, Solomon CV (2018) 4D printing of net shape parts made from Ni-Mn-Ga magnetic shape-memory alloys. *Addit Manuf* 21:579–588
19. Ambulo CP, Burroughs JJ, Boothby JM, Kim H, Shankar MR, Ware TH (2017) Four-dimensional printing of liquid crystal elastomers. *ACS Appl Mater Interfaces* 9:37332–37339
20. Zhao T, Yu R, Li X, Cheng B, Zhang Y, Yang X, Zhao X, Zhao Y, Huang W (2018) 4D printing of shape memory polyurethane via stereolithography. *Eur Polym J* 101:120–126
21. Zolfagharian A, Kaynak A, Khoo SY, Kouzani A (2018) Pattern-driven 4D printing. *Sensors Actuators A Phys.* 274:231–243
22. Ly ST, Kim JY (2017) 4D printing—fused deposition modeling printing with thermal-responsive shape memory polymers. *Int J Precis Eng Manuf Green Technol* 4:267–272
23. Kimionis J, Isakov M, Koh BS, Georgiadis A, Tentzeris MM (2015) 3D-printed origami packaging with inkjet-printed antennas for RF harvesting sensors. *IEEE Trans Microw Theory Tech* 63:4521–4532
24. Choong YYC, Maleksaeedi S, Eng H, Wei J, Su PC (2017) 4D printing of high performance shape memory polymer using stereolithography. *Mater Des* 126:219–225
25. Invernizzi M, Turri S, Levi M, Suriano R (2018) 4D printed thermally activated self-healing and shape memory polycaprolactone-based polymers. *Eur Polym J* 101:169–176
26. Sydney Gladman A, Matsumoto EA, Nuzzo RG, Mahadevan L, Lewis JA (2016) Biomimetic 4D printing. *Nat Mater* 15:413–418
27. Van Manen T, Janbaz S, Zadpoor AA (2017) Programming 2D/3D shape-shifting with hobbyist 3D printers. *Mater. Horizons.* 4:1064–1069
28. Raviv D, Zhao W, McKnolly C, Papadopoulou A, Kadambi A, Shi B, Hirsch S, Dikovsky D, Zyracki M, Olguin C, Raskar R, Tibbits S (2014) Active printed materials for complex self-evolving deformations. *Sci Rep* 4:1–8
29. Tibbits S (2014) 4D printing: multi-material shape change. *Archit Des* 84:116–121
30. Villar G, Graham AD, Bayley H (2013) A tissue-like printed material. *Science* (80-) 340:48–52
31. Kokkinis D, Schaffner M, Studart AR (2015) Multimaterial magnetically assisted 3D printing of composite materials. *Nat Commun* 6
32. Arazoe H, Miyajima D, Akaike K, Araoka F, Sato E, Hikima T, Kawamoto M, Aida T (2016) An autonomous actuator driven by fluctuations in ambient humidity. *Nat Mater* 15:1084–1089
33. Davis D, Chen B, Dickey MD, Genzer J (2016) Self-folding of thick polymer sheets using gradients of heat. *J Mech Robot* 8

34. Chen S, Li J, Fang L, Zhu Z, Kang SH (2017) Simple triple-state polymer actuators with controllable folding characteristics. *Appl Phys Lett* 110:133506
35. Liu C, Schauff J, Joung D, Cho J-H (2017) Remotely controlled microscale 3D self-assembly using microwave energy. *Adv Mater Technol* 2:1700035
36. Zhang F, Wang L, Zheng Z, Liu Y, Leng J (2019) Magnetic programming of 4D printed shape memory composite structures. *Compos Part A Appl Sci Manuf* 125:105571
37. Onal CD, Tolley MT, Wood RJ, Rus D (2015) Origami-inspired printed robots. *IEEE/ASME Trans Mechatron* 20:2214–2221
38. Peraza-Hernandez EA, Hartl DJ, Malak RJ, Lagoudas DC (2014) Origami-inspired active structures: a synthesis and review. <https://doi.org/10.1088/0964-1726/23/9/094001>
39. Shin B, Felton SM, Tolley MT, Wood RJ (2014) Self-assembling sensors for printable machines. In: *Proceedings—IEEE International conference on robotics and automation*, pp 4417–4422. Institute of Electrical and Electronics Engineers Inc
40. Li M, Yang Q, Liu H, Qiu M, Lu TJ, Xu F (2016) Capillary origami inspired fabrication of complex 3D hydrogel constructs. *Small* 12:4492–4500
41. Saez J, Etxebarria J, Antoñana-Diez M, Benito-Lopez F (2016) On-demand generation and removal of alginate biocompatible microvalves for flow control in microfluidics. *Sensors Actuators B Chem* 234:1–7
42. Habault D, Zhang H, Zhao Y (2013) Light-triggered self-healing and shape-memory polymers. *Chem Soc Rev* 42:7244–7256
43. Zolfagharian A, Kouzani ZA, Nasri-Nasrabadi B, Adams S, Yang Khoo S, Norton M, Gibson I, Kaynak A (2017) 3D printing of a photo-thermal self-folding actuator. In: *DesTech conference proceedings*, p 22. Knowledge E
44. Tolley MT, Felton SM, Miyashita S, Aukes D, Rus D, Wood RJ (2014) Self-folding origami: shape memory composites activated by uniform heating. *Smart Mater Struct* 23:094006
45. Liu Y, Boyles JK, Genzer J, Dickey MD (2012) Self-folding of polymer sheets using local light absorption. *Soft Matter* 8:1764–1769
46. de Haan LT, Gimenez-Pinto V, Konya A, Nguyen T-S, Verjans JMN, Sánchez-Somolinos C, Selinger JV, Selinger RLB, Broer DJ, Schenning APHJ (2014) Accordion-like actuators of multiple 3D patterned liquid crystal polymer films. *Adv Funct Mater* 24:1251–1258
47. Tibbitts S (2012) Design to self-assembly. *Archit Des* 82:68–73
48. Lewis JA (2006) Direct ink writing of 3D functional materials. *Adv Funct Mater* 16:2193–2204
49. Ryu J, D'Amato M, Cui X, Long KN, Jerry Qi H, Dunn ML (2012) Photo-origami—bending and folding polymers with light. *Appl Phys Lett* 100:161908
50. Miyashita S, Guitron S, Ludersdorfer M, Sung CR, Rus D (2015) An untethered miniature origami robot that self-folds, walks, swims, and degrades. In: *Proceedings—IEEE International conference on robotics and automation*, pp 1490–1496. Institute of Electrical and Electronics Engineers Inc
51. Mu X, Sowan N, Tumbic JA, Bowman CN, Mather PT, Qi HJ (2015) Photo-induced bending in a light-activated polymer laminated composite. *Soft Matter* 11:2673–2682
52. Kwok TH, Wang CCL, Deng D, Zhang Y, Chen Y (2015) Four-dimensional printing for freeform surfaces: design optimization of Origami and Kirigami structures. *J Mech Des Trans ASME* 137:111712
53. Rudykh S, Ortiz C, Boyce MC (2015) Flexibility and protection by design: imbricated hybrid microstructures of bio-inspired armor. *Soft Matter* 11:2547–2554
54. Ge Q, Qi HJ, Dunn ML (2013) Active materials by four-dimension printing. *Appl Phys Lett* 103:131901
55. Nakata K, Sakai M, Ochiai T, Murakami T, Fujishima A (2012) Bending motion of a polyacrylamide/graphite fiber driven by a wide range of light from UV to NIR. *Mater Lett* 74:68–70
56. Huang L, Jiang R, Wu J, Song J, Bai H, Li B, Zhao Q, Xie T (2017) Ultrafast digital printing toward 4D shape changing materials. *Adv Mater* 29:1605390

57. Miao S, Cui H, Nowicki M, Xia L, Zhou X, Lee S-J, Zhu W, Sarkar K, Zhang Z, Zhang LG (2018) Stereolithographic 4D bioprinting of multiresponsive architectures for neural engineering. *Adv. Biosyst.* 2:1800101
58. Gustmann T, Neves A, Kühn U, Gargarella P, Kiminami CS, Bolfarini C, Eckert J, Pauly S (2016) Influence of processing parameters on the fabrication of a Cu-Al-Ni-Mn shape-memory alloy by selective laser melting 11:23–31

Stabilization and Trajectory Control of High-Altitude Balloons for Rockoons—A Review



A. A. Mandal

Abstract High-altitude balloons and sounding rockets are two near-space technologies. Together they can launch satellites to suborbital space. Rockoon's concepts were abandoned due to their inaccuracy. With an increase in nanosatellite development, there is an increase in affordable launches desire. This paper aims to discuss altitude stabilization and trajectory control techniques for an enhanced flight of high-altitude balloons. This paper's Stabilization techniques include Stratosail Balloon Guidance system, Dual Balloon System, Electrohydrodynamic Propulsion, and Cold Gas Propulsion system. Stratosail provides stability using the wing and rudder suspended at 10–15 km below the primary balloon. A dual balloon system provides stability by pumping in or venting out the atmospheric air to change the altitudes. It helps restrict trajectory within 25 km. Electrohydrodynamic thrusters ionize the surrounding air to produce thrust and propel the system in the desired path. The cold gas propulsion system provides a yaw moment for trajectory control. Using these techniques, a better flight of high-altitude balloons is expected, the stability helps in the proper launch of the rocket from the high-altitude platform. This paper provides a detailed literature review of these concepts. There is much future scope in the research field of stabilization and Trajectory Control of High-altitude balloons for Rockoons.

Keywords Rockoons · Altitude stabilization · Trajectory control · High-altitude balloons

1 Introduction

Leading towards enhance progress in space flight technology, it becomes necessary to work and research on space flight's current minute changes could be observed which specifically include launching rockets in lower earth launching methods. From the beginning of the space flight era to modern rocketry only orbit. There is a requirement for an alternative solution with an increase in suborbital nanosatellites and

A. A. Mandal (✉)

Department of Mechanical Engineering, MCT's Rajiv Gandhi Institute of Technology,
Mumbai 400053, India

e-mail: anirudha13mandal@gmail.com

microsatellites. Various innovative designs and theoretical concepts like Rockoon [1], Space Elevator [2], Orbital electromagnetic catapult [3], LEO rotovator [4], Supersonic launcher aircraft [5] were proposed, but many remain untested to date. The concept of lifting a sounding rocket using a high-altitude balloon to the stratosphere and launching was proposed, known as Rockoon. At higher altitudes, the drag on the spacecraft reduces significantly, reducing the rocket's propellant consumption, which reduces the cost of the launch. The concept dates back to 1949 by Lee Lewis and Van Allen, who made Rockoons' first attempts in Naval Research in the US [6]. Various launches were conducted after the first test, but due to less development in high-altitude balloons, the concept did not meet a significant outlook. In recent times, the high-altitude balloon sector's growth is increasing exponentially with its uses in navigation, communication, weather prediction, and for high-altitude launch systems; it is an optimum solution to our problem with its few consequences. The flight path depends on the wind, which is an unpredictable factor; strong winds may cause launch delays; hence, we require stable conditions for the setup's proper inflation [7]. The trajectory of the balloon needs to be in a controlled manner. There is a need for attitude control to provide stability for the rocket launch to control the trajectory. This paper presents various stability techniques and concepts to overcome the problem and make this a viable option for the future of spaceflight.

2 Ballooning

The high-altitude balloon's basic working principle is given by the buoyant lift of a balloon as a function of the density difference between it and the surrounding air, multiplied by the volume displaced by the lifting gas [8]. The attitude control is constantly adjusting the lifting gas volume and the payload mass to get an equilibrium. To get the hold on the rockoon's stability, the ballooning structure and the type of ballooning play a significant role. It determines the trajectory and the attitude of the high-altitude balloon being used to launch the rocket from a certain altitude. It is further classified as a single ballooning structure and multi-ballooning structure.

2.1 *Single Ballooning Structure*

A single balloon can be considered to lift off the rocket and the payload from the ground to the stratosphere level of 25–30 km. Using a single balloon configuration will reduce the balloon drag and help in an easy ascent.

Table 1 in this paper illustrates the survey conducted through a literature review. Suppose we consider the giant He (Helium) balloon available in the market to be of burst diameter 18 m and weight of 5 kg. It reaches 30 km with a payload not exceeding 15 kg, which is not a feasible option as the cumulative weight of a sounding rocket and the payload must exceed 15 kgs [9]. A longer time duration is required to reach

Table 1 Performance of a hypothetical 5 kg balloon, lifting a payload of 15 kg for different possible burst diameters [9]

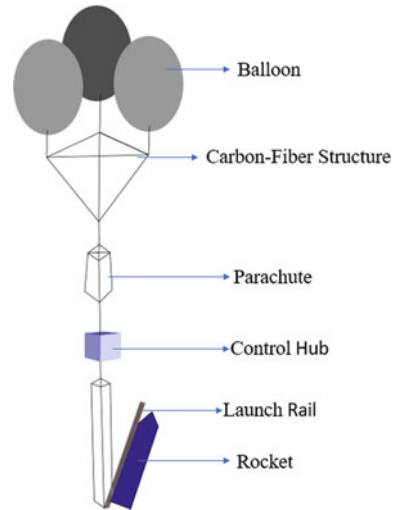
Burst dia (m)	Ascent speed (m/s)	Helium volume at launch (m ³)	Theoretical Burst altitude (km)	Practical Burst altitude (km)
15	1.7	20.0	32.4	26.0–28.2
	4.1	22.5	31.5	25.2–27.3
16	1.7	20.0	33.4	26.7–29.0
	4.1	22.5	33.0	26.4–28.7
18	1.7	20.0	36.4	29.1–31.7
	4.1	22.5	35.5	28.4–30.9

the stratosphere due to low ascent speed. This increases the deviation of trajectory due to prolonged attacks from the winds. To achieve a lift of 15 kg payload without any deviation from the flight path, the balloon must have a higher rate of ascent. We need to use zero pressure balloons or super pressure balloons for larger payloads. Zero pressure balloons are partially inflated, and it expands when rising as the gas expands to maintain a zero pressure difference between atmosphere and balloon [10]. Super Pressure balloons overcome the disadvantages of zero pressure balloons. The concept maintains a highly positive pressure differential between the lifting gas and the atmosphere [11]. These balloons are customized as per our requirements which increases their cost due to lower manufacturing demands. While using a single balloon, it gets difficult to maintain the system’s stability in stratospheric conditions. To overcome this drawback of single ballooning, a multi-Ballooning system is proposed.

2.2 Multi-Ballooning System

Figure 1 depicts the multi-ballooning system; the payload and the rocket attachment are at the center of the frame. The trajectory control mechanism and the attitude control mechanism are situated here. The launch rail for a rocket is at an angle of 15-20° to avoid an intersection with the balloon [12].

Multi-balloon system is used to reach the stratosphere for a rocket launch. A multi-balloon system is an optimized structural design that increases the flight’s stability. It is achieved by triangular placement of balloon, and the payload is attached to the center of the frame. The frame is made of carbon fiber rods to reduce the system’s weight [9]. The structure needs to be designed so that there is no balloon-to-balloon contact as it leads to friction and may rupture the balloon. To prevent the intersection of rockets trajectory and balloon, a factor of safety is considered. The multi-ballooning system increases drag but provide stability and ease in attitude control.

Fig. 1 Multi-balloon system

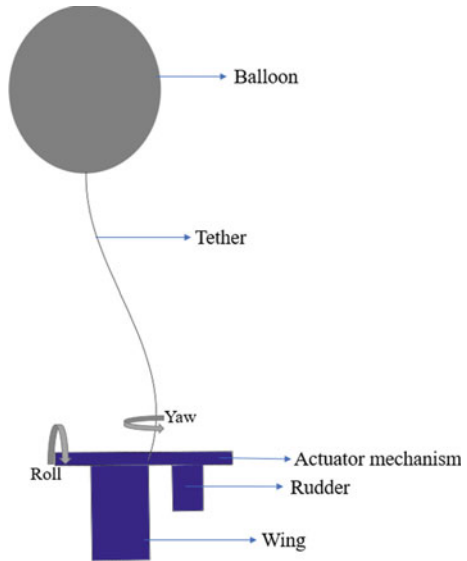
3 Stabilization and Trajectory Control

Altitude stabilization and trajectory control have been major deciding factors for the success of rockoons. The system's high stability is needed for a proper launch of a sounding rocket. Due to high winds at higher altitudes, a free flight balloon without any trajectory control system leads to drifting away from the balloon's intended flight path. This paper's Stabilization and trajectory control include the Stratosail Balloon Guidance system, Dual Balloon System, Electrohydrodynamic Propulsion, and Cold Gas Propulsion system.

3.1 Stratosail Balloon Guidance System

Figure 2 depicts the stratosail mechanism tethered to the primary high-altitude balloon system. The wind speed varies with different altitude levels; as the balloon shifts towards an upwards direction, the wind speed increases. The high-altitude balloon flies at an altitude of 30–35 km, to which the stratosail tethers 10–15 km below [13]. The function of stratosail is to provide directional forces required to steer the system to keep it on the intended flight trajectory and maintain the system's stability [14]. The stratosail consists of a wing and a rudder attached at the end of a pole. The wing produces a lateral lift force which slows down the system due to drag force. Ease in maneuverability is achieved by positioning the wing at a particular angle with mechanical actuators' help. The actuator mechanism generates a roll to achieve the required optimum angle. Rudder angle adjustments are made to maintain reasonable drift speeds and increase the balloon's performance. Due to the ease

Fig. 2 Stratosail mechanism

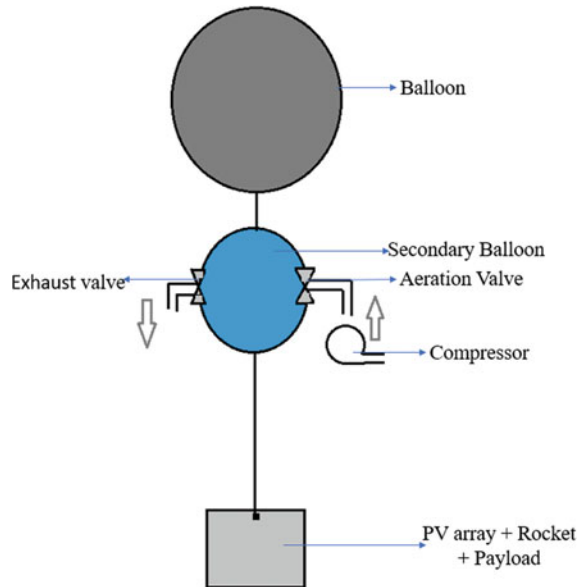


in maneuverability and total control over flight trajectory, the high-altitude balloon system can be brought back to the initial launch site with minimal effort. Stratosail maintains the trajectory and altitude using the natural wind present in the atmosphere. This makes the operations much simpler [15]. The rocket is attached below the high-altitude balloon system, and the stratosail system is attached further below to be influenced by the winds at lower altitudes.

3.2 Dual Balloon System

Atmospheric conditions in the stratosphere consist of wind layers moving in different directions and at different speeds. Changing the different wind layers with different speeds helps provide stability to the high-altitude balloon system. A secondary air balloon is introduced with the primary high-altitude balloon system [16].

Figure 3 illustrates the dual balloon system; it consists of air vents and a compressor to regulate the air around. Stability Altitude and altitude pressure are inter-dependable factors. To raise the system’s altitude to optimum altitude, the secondary balloon vents out the extra air, which reduces the system’s weight and provides a lift to reach the required altitude. If descent is required, the compressor works to pump in the air from the atmosphere; it increases the system’s mass, which results in a decrease in altitude [17]. A source of electricity is required to operate the compressor, which can be fulfilled by using PV arrays. The dual Balloon system provides stability to HAB and restricts the trajectory within 25 Km of the launch site.

Fig. 3 Dual balloon system

3.3 Electrohydrodynamic Propulsion

Electrohydrodynamic Propulsion (EHD) is proposed for the trajectory control and the attitude control of the High-altitude balloon. This type of system is lightweight and has no moving parts involved, reducing the wear and risk of failure of the system. It works on the principle that a semi-ionized fluid gains momentum when placed under an electric field which generates thrust [18].

Figure 4 illustrates EHD thrusters; it is made by placing aluminum plates in a triangular pattern. Lightweight, non-conducting balsa wood makes the supports. The aluminum plates are connected to an energy source producing a 30–40 kV, which is connected relative to the ground collector plate. The higher voltages ionize the surrounding air, which produces a thrust [19]. A single EHD thruster produces a thrust of less than 1 N but weighs only a few grams. An array of thrusters can be used as per the design requirements. An additional wire can help to reverse the direction of the thrust [20]. EHD thrusters help in trajectory control and altitude control using solar energy.

3.4 Cold Gas Propulsion System

The cold gas propulsion system has been used in many satellites and CubeSats to generate thrust. It is a simple, efficient, and low-power-consuming propulsion system that can incorporate a wide range of propellants. The working of cold gas

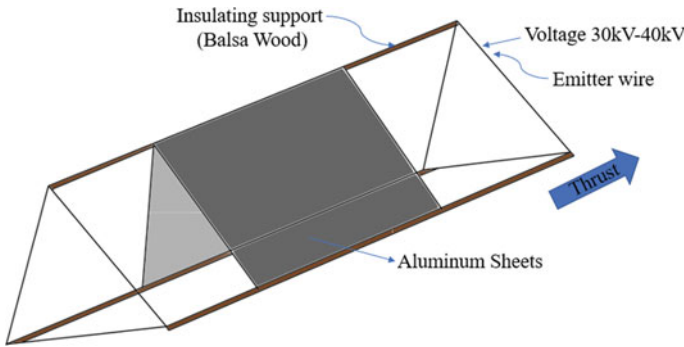


Fig. 4 Electrohydrodynamic propulsion thruster

propulsion illustrates—the propellant in the storage tank is allowed to flow to a converging/ diverging nozzle that produces thrust due to gas expansion [21]. The cold gas propulsion system can generate a thrust of a varying range. Cold gas propulsion allows various propellant types to be used, but the primary factor for selection is; it should be capable of handling changes in pressure, be light in weight yet provide the required thrust, and not react with the material of the tank or other atmospheric gases. The storage tank plays a significant role since it regulates the propellant towards the nozzle. The tank is designed keeping in mind the criteria of atmospheric pressure at higher altitudes, the propellant properties, the Number of nozzles to control the direction of the thrust, and lighter weight. The nozzles design is based on the thrust required and the propellant type [22]. This system provides a Yaw movement to the whole system maintaining it in the intended flight path and maintaining the stability of the system. A nozzle can be placed at the X-direction of the plane to maintain the high-altitude balloon system's altitude stability. The propulsion system is set up above the rocket near the high-altitude balloon system's control hub to maintain the center of gravity of the system.

4 Results and Discussion

High-altitude balloon systems can be seen in remote sensing, communications, navigations, and launching rockets from the stratosphere. Wind speed and wind direction influence the high-altitude balloon system's flight path. Altitude stability and flight path trajectory control are significant drawbacks for high-altitude balloon systems. This paper illustrates some of the stabilization and trajectory control techniques for high-altitude balloon stabilization in Rockoon to overcome this concept's drawbacks.

Ballooning is classified into two types such as single ballooning system and multi-ballooning system. Regular high-altitude balloons can carry a payload of less than 15kgs. Considering Zero pressure and high-pressure balloons, they are used for a single ballooning system with larger payloads. Single balloon systems provide

an unstable system for a rocket launch. To overcome these drawbacks in single ballooning system multi-ballooning system is introduced. A multi-balloon system maintains altitude stability and trajectory control with minimum external efforts. Using a multi-ballooning system increase the drag on the system but provides better stability. External Mechanism and stabilization techniques are utilized to maintain the system's stability. The Stratosail Balloon Guidance system, Dual Balloon System, Electrohydrodynamic Propulsion, and Cold Gas Propulsion system are the techniques discussed in this paper.

Startosail guidance system uses the wind speeds at lower altitudes to steer the system and keep it in an intended path. The wing generates lateral lift force that provides the required trajectory, when given an optimum angle. Rudder angle makes changes in drift speed to increase the performance. Dual balloon system maintains the altitude by venting out the excess air from the secondary balloon. It reduces weight and increases the altitude or pumping in air through a compressor. This system works on a feedback loop principle by detecting the pressure change at different altitudes. Electrohydrodynamic Propulsion system works on the ionization of the surrounding air to generate thrust to propel the system. EHD system produces low thrust, i.e., of less than 1 N. Hence, an array of thrusters is needed. Here the power source for the thrusters is not specified in detail. The cold gas propulsion system is achieved by generating thrust due to the propellant's expansion through the nozzle. It provides yaw movement to the system, which helps control the system's trajectory control. Addition of nozzle in X-direction is preferable to maintain the altitude stability through a closed feedback loop.

5 Conclusion

Rockoons provide affordable access to suborbital flight, which creates a new opportunity for the future of space flight and for testing various technologies. It requires significant development in rockoons for commercial flight in the present day. In this way, a study of stabilization techniques and trajectory control is illustrated in the paper for an efficient flight.

References

1. HAAS Orbital Rocket Launcher (Brochure) ARCASPACE
2. Edwards BC (2000) Design and deployment of a space elevator. *Acta Astronaut* 47(10):735–744
3. Jones RM (1989) Electromagnetically launched micro spacecraft for space science missions. *AIAA J Spacecraft Rockets* 26(5):338–342
4. Williams P, Blanksby C (2004) Prolonged payload rendezvous using a tether actuator mass. *AIAA J Spacecraft Rockets* 41(5):889–893
5. Sarigul-Klijn N, Sarigul-Klijn M, Noel C (2005) Air-launching earth to orbit: effect of launch conditions and vehicle aerodynamics. *AIAA J Spacecraft Rockets* 42(3):569–572

6. Foerstner A, Allen JV (2009) *The first eight billion miles*, University of Iowa Press, Iowa
7. Laby JE, Unthank EL (1966) Day-to-day fluctuations of the winds in the lower strato-sphere over Australia 24:98–100
8. Sushko A, Tedjarati A, Creus-Costa J, Maldonado S, Marshland K, Pavone M (2017) Low cost, high endurance, altitude-controlled latex balloon for near-space research (ValBal). In: 2017 IEEE aerospace conference, Big Sky, MT, USA, pp 1–9. <https://doi.org/10.1109/AERO.2017.7943912>
9. Okninski A, Raurell DS (2016) A feasibility of a low-cost sounding rockoon platform. *Acta Astronaut* 127:335–344. <https://doi.org/10.1016/j.actaastro.2016.06.010>
10. Keese DL (1979) Zero-pressure balloon design. *AIAA J* 17(1):12–16. <https://doi.org/10.2514/3.61056>
11. Smith MS, Rainwater EL (2004) Optimum designs for superpressure balloons. *Adv Space Res* 33(10):1688–1693
12. Okninski A, Marciniak B, Bartkowiak B, Kaniewski D, Matyszewski J, Kindracki J, Wolanski P (2015) Development of the polish small sounding rocket program. *Acta Astronaut* 108:46–56
13. http://www.gaerospace.com/projects/ULBDStratoSail/StratoSail_system.html
14. Ramesh SS, Ma J, Lim KM, Lee HP, Khoo BC (2018) Numerical evaluation of station-keeping strategies for stratospheric balloons. *Aerosp Sci Technol* 80:288–300
15. Aaron KM, Heun MK, Nock KT (2002) A method for balloon trajectory control. *Adv Space Res* 30:1227–1232
16. Sherif S, Weiliang H (2018) New design simulation for a high-altitude dual-balloon system to extend lifetime and improve floating performance. *Chin J Aeronaut* 31(5):1109–1118. <https://doi.org/10.1016/j.cja.2018.03.009>
17. Du H, Lv M, Zhang L, Zhu W, Wu Y, Li J (2019) Energy management strategy design and station-keeping strategy optimization for high altitude balloon with altitude control system. *Aerosp Sci Technol* 93:105342
18. van Wynsberghe E, Turak A (2016) Station-keeping of a high-altitude balloon with electric propulsion and wireless power transmission: a concept study. *Acta Astronaut* 128:616–627
19. Masuyama K, Barrett SR (2013) On the performance of electrohydrodynamic propulsion. *Proc R Soc A Math Phys Eng Sci* 469(2154):20120623
20. Shibata H, Watanabe Y, Yano R, Suzuki K (2014) Numerical study on fundamental characteristics of electro-hydrodynamic thruster for mobility in planetary atmosphere. *Trans Japan Soc Aeronaut Space Sci Aerospace Technol Japan* 12:5–9
21. Bzibziak SR (1992) Miniature cold gas thrusters. In: 28th Joint propulsion conference and exhibit, vol 3256
22. Köhler J, Bejhed J, Kratz H, Bruhn F, Lindberg U, Hjort K, Stenmark L (2002) A hybrid cold gas micro thruster system for spacecraft. *Sensors Actuators A Phys* 97:587–598

A Review on “Designs and Fabrication” for the Next Generation of Organic Solar Cells Technology



Neeraj Kant and Pushendra Singh

Abstract An interest in and advanced research in organic solar cells has grown due to their low-cost and flexible use in power devices, their environmental benefits, and their outstanding promise to be an economical and efficient technology for utilizing solar energy as a sustainable power resource. Much attention has recently been drawn to the use of organic solar cells with a bulk heterojunction active layer of a non-fullerene acceptor material, which has technical advantages for overcoming photon harvesting, charge recombination, and lower manufacturing costs. Efficiency, cost, and stability are the primary factors in these organic-based solar cells. However, to stay competitive with traditional solar cells, organic solar cell technology must be innovative and lead to a breakthrough to fill the gap in renewable energy. This article presents findings focusing on the significance of optimizing the organic solar cell concerning its organic semiconductor morphology and optical properties, power conversion efficiency, device stability, fabrication processability, and the organic solar cell's enhanced performance with parallel tandem configuration about enhanced device development engineering.

Keywords Solar energy · Organic solar cells · Bulk heterojunction donor/acceptor materials · Power conversion efficiency (PCE) · Organic solar cell stability and degradation · Solar cell fabrication and designs

1 Introduction

One of the most pressing issues of the twenty-first century is addressing global warming by reducing net carbon emissions to zero. To achieve the goal of limiting the global warming temperature reach to 1.5 °C, we will need to make a rapid transition from fossil fuels to renewable energy sources [1]. The qualitative methods of renewable energy technologies will necessitate surpassing current capacity, such

N. Kant · P. Singh (✉)

Department of Mechanical Engineering, Delhi Technological University, Delhi, India
e-mail: Dr.psinghs@gmail.com

as wind and solar power. Silicon-based solar cells dominate the current solar module market, accounting for more than 95% of sales of modules [2].

However, the true potential emerges from many new technologies that are poised to reduce costs and speed up this transition. OSCs, the technology most advanced in the commercialization process, use carbon-based polymer materials and work as an active layer in solar cells [3]. The least advanced technology for commercialization is organically modified clay. Particular benefits come with organic semiconductors such as being made to fit a specific purpose, based on non-toxic raw materials, and the technologies used to create them, which mainly involve vacuum coating and solution processing, enable the use of coating large areas for a cheap and low cost [4, 5].

This, together with a relatively low consumption of material (1 g of an organic semiconductor per m^2) processing at low temperatures and the ability to be applied to flexible substrates, enables roll-to-roll production and an extreme range of different products. This advancement has the potential to make OSC the world's cheapest source of electricity. Organic solar cell thin-film light absorption does not produce abundant free charge carriers. But instead, in firmly bound excitons with inadequate diffusion length, polymer-based solar cells are inherently less efficient than traditional-based materials such as silicon solar cells in the commercialization phase. An efficient excitons separation solution was found by Tang in 1986 [6, 7]. Two different organic semiconductors were joined together at the planar interface, one a donor and the other an acceptor, which yielded a type II heterojunction. Hiramoto et al. [8] first presented their findings on the limited exciton diffusion length in 1991.

They developed a bulk heterojunction (BHJ) lively layer of an organic solar cell with a distributed donor–acceptor interface by co-evaporating donor and acceptor molecules. Electrons can be created within the diffusion length of the heterojunction when an exciton is formed. Important to efficient OSC is the use of such BHJs, no matter if they are made in a vacuum or with solution-based processing. Ongoing R & D in organic semiconductors has resulted in improved absorption and donor–acceptor energy counterbalances [9, 10], as well as an optimized BHJ microstructure donor–acceptor interface [11, 12] and stack design [13] helping to push single-junction solar cell efficiency to 18% [14, 15]. More than 20% PCEs give the impression to be feasible, and module efficiencies are rapidly increasing. This review begins with a basic introduction to the fundamentals of OSCs and how these technologies have evolved to achieve better PCE and stability and design configuration to enhance solar cell performance. Following this is a discussion of how various OSC devices and processing technologies have advanced to allow for the development of large-area OSCs for commercialization. Finally, some final thoughts on OSC performance are provided in this section to enhance solar energy.

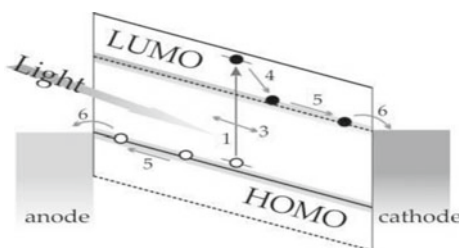
2 The Fundamental Principles of Organic Solar Cells

When Alan G. M. Heeger and Alan G. Shirakawa stumbled upon organic semiconductors in 1977, they discovered the fundamental phenomenon of organic solar cells [16]. Due to their conjugated electron system, organic semiconductors have unique optical and electrical properties. While this conjugation may be small, it's also among the least powerful. These pi electrons are also highly mobile, making them significantly more elusive than sigma electrons. An increase in the light-absorbing and light-emitting capacity of organic molecules is realized when the energy gap between the HOMO–LUMO levels of the molecules is reduced.

The diagram in Fig. 1 illustrates the fundamental principle of a solar cell. The light passed through a transparent electrode is absorbed by the active material, causing excited electron–hole pairs to be created (excitons). Back to ground state exciton relaxation can occur by many pathways. It is one of the many ways in which carriers can be supported. Once the created excitons have diffused through the donor phase, they reach the interface with the acceptor, and they then diffuse into the acceptor phase. In this case, dissociation happens through a charge transfer that is completed within 45 fs. This method separates the charges. The photo-generated holes and electrons are transported to the electrodes by the internal electric field, aided by electrodes of different work functions. As a result, the photovoltaic device produces a flow of electricity.

The sun's light can be transmitted through a transparent electrode. In between the transparent and metal electrodes is an organic layer containing a donor and an acceptor; when photons are absorbed by the polymer chain, an exciton forms, resulting in charge carriers (electron and hole). Conductive particles migrate to the electrode producing a current. The energy levels of the acceptor are depicted in this example by the dotted lines. For the donor's energy levels in the PV cell, the complete lines show whether an orbital within the molecule is occupied or in use [17].

Fig. 1 An illustration of a polymer-based solar cell is shown here



3 A Perspective on Organic Solar Cell Design

The light-absorbing conjugated molecules have a critical band gap when it comes to designing organic solar cells. The silicon case can capture up to 77% of solar energy. Above 2 electron volts (which can only absorb a maximum of 30% of solar photons), organic semiconductor molecules have a higher band gap, resulting in lower overall efficiency. The D–A type conjugated polymers, which are prevalent in high-performance organic optoelectronic devices, are used frequently as donors in donor–acceptor (D–A) type conjugated polymers. To achieve the desired performance in organic solar cells, the band gap of the absorbing molecules is optimized. Tunable solubility and energy levels, as well as the attachment of various molecules or chemicals to the backbone polymer chain, are the two approaches to this problem. Other chemicals have been added to various classes of compounds, resulting in many new compounds [18, 19].

PSCs have been synthesized from a wide range of products [20–22], and Fig. 2 depicts the chemical structure of the most common ones used in BHJ PSCs. They are all linked by alternating carbon–carbon double bonds, which account for their electronic properties, low-energy optical transitions, and high electron affinities. Raw conjugated polymers are typically isolated and then efficient via oxidation (p-doping) or reduction (n-doping). The layer into which the polymers are introduced determines the classification of PSC developments. The substrate design should have a low thickness and be flexible. As a result, polyethylene terephthalate (PET) or polyethylene naphthalate (PEN) are commonly used because they have good mechanical and thermal properties and good stability during solution treatments.

The first step in developing organic solar cells is optimizing the low band gap efficiency of the active layer. Many aspects must be considered when optimally converting electromagnetic radiation or light energy into electrical energy such as the intrinsic and extrinsic properties of many components. To separate the excitons, the heterojunction composed of donor and acceptor materials is used. Thus, the next important thing is the selection and design of acceptor material, which influences the cell's performance. A fullerene derivative is typically used to create the most successful design. At the same time, other polymer acceptors consist of compounds based on Rylene Diimide [23], fluorine, BT-based polymer acceptors [24], and polymer acceptors based on CN [25].

Researchers are now reporting tremendous progress in developing organic solar cells (OSCs) due to the appearance of non-fullerene acceptors (NFAs). A broadband gap NFA, which ranges from 1.3 to 1.6 eV and features excellent absorption, as well as an absorption coefficient that is easily tunable, can collect more solar energy while keeping a slight voltage loss when combined with suitable donors. While the efficiency of OSCs is dependent on compatible donor and acceptor materials, active layer morphology control, and device engineering, efficient OSCs also depend on the management of the overall morphology of the active layer. Typically, in the majority of organic solar cell designs, ITO is utilized as the conducting agent, with a high work function electrode such as Al, Ca, or Mg, serving as the current collector; while

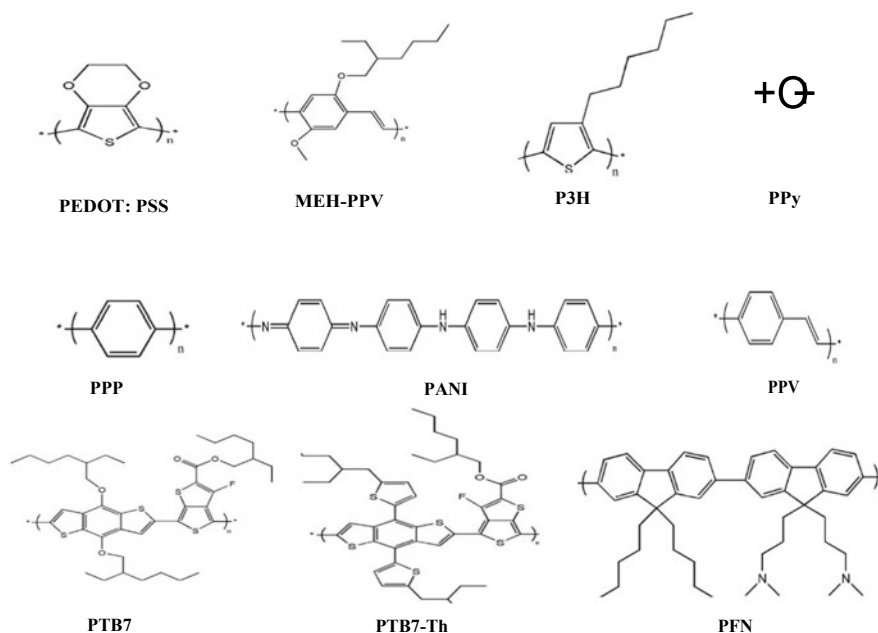


Fig. 2 The chemical structure of conjugated polymers, which are commonly used in polymer solar cells [26]

ITO is good for the anode, it also serves as a decent cathode, since ITO's electrical and optical properties make it an excellent choice as an anode. Al outperforms Mg and Ca, even though Mg and Ca have greater potential to yield better performance. A class of cutting edge electrodes is made from graphene [27] and carbon nanotube electrodes [28].

4 Integration of Device Engineering and New Architectures for Improving OSC Performance

The next section discusses various approaches for improving the efficiency of organic solar cells in terms of structure.

4.1 Single-Layer Organic Solar Cells

In single-layer organic solar cell, the active layer Donor/Acceptor (D/A) of organic semiconductor photoactive material, sandwiched between anode and cathode of different work functions, constitutes a single-layer semiconductor solar cell [29].

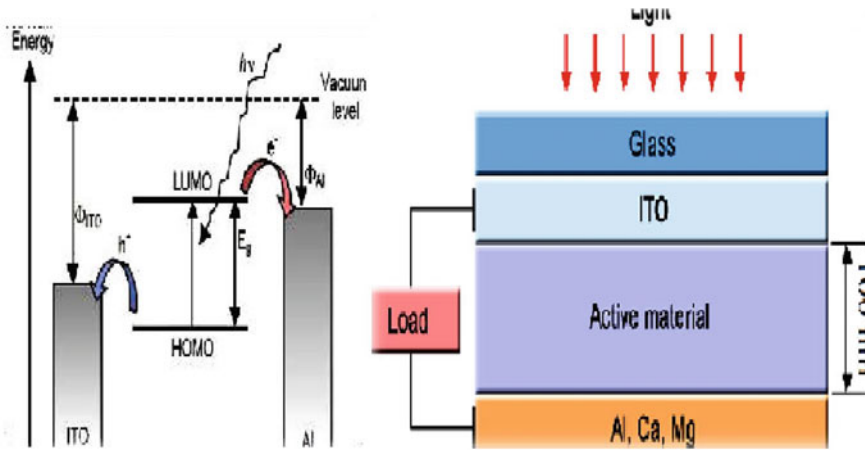


Fig. 3 The energy level diagram and structure of a single-layer organic solar cell

Although cell efficiency is low, two significant issues are currently impeding its improvement: insufficient electric field strength to dissociate the excitons and restricted electrical junctions, where separated charges must pass through the same medium. However, an organic semiconductor's insulating nature, as well as its short exciton diffusion length, results in the recombination of the excited charge carriers (Fig. 3).

4.2 Organic-Polymer Bilayer Heterojunction Solar Cells

The first heterojunction is a pair of layers with an intimate link to electrons and holes. The interface between the acceptor and donor molecules allows the hole pair to be separated into free carriers. This device structure promotes better exciton separation due to the presence of a well-designed disassociation space. A two-layer structure can improve the exciton diffusion length and shunt resistance. To achieve directional photo-induced charge transfer across the interface, the bilayer structure is used. However, the active layer remains constrained because only excitons near the depletion layer can reach the interface and become dissociated [30] (Fig. 4).

4.3 Bulk Heterojunction Organic Solar Cell

The donor and acceptor materials are blended to form a uniform length scale, where the effective diffusion length of the exciton is equal to the blend's length. This way, we can more efficiently extract charges, which lead to much higher performance

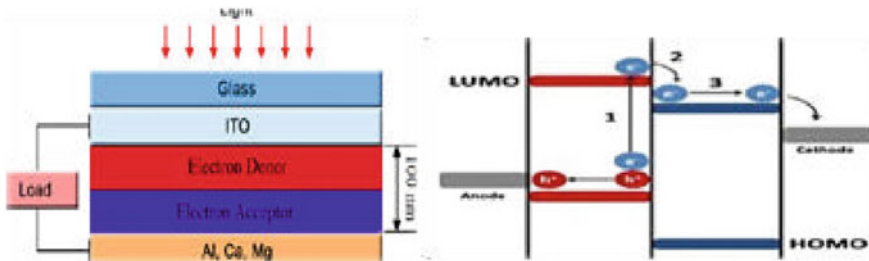
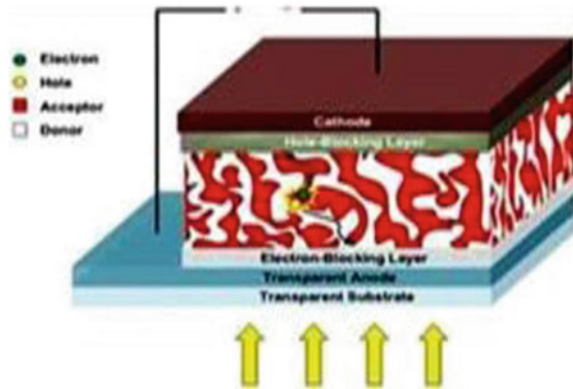


Fig. 4 The structure and level diagram of a bilayer heterojunction organic solar cell with a bifacial heterojunction organic solar cell

Fig. 5 Architecture utilizing bulk heterojunction solar cells



to reduce leakage energy loss; electrolysis introduces further layers, like electron transfer layer or hole transfer layers [31, 32] (Fig. 5).

4.4 Organic Tandem Solar Cell’s Structure

A tandem organic photovoltaic (TPVO) is the system in which multiple junction OPV cells are stacked atop each other to extract more energy. One can use either parallel or serial connections to stack sub-cells. A two-terminal series is the common multijunction solar cell design in which two active layers are stacked one atop the other.

To play a critical role in separating different cells, acting as a recombination layer, the layer should be thin, semiconducting, or metallic and have very little or no absorption; please refer to Fig. 6b. Intermediate electrodes are required for parallel connection so that each cell has enough charge to do its job. Minimizing photon losses and maximizing charge carrier collection are important here. Indium tin oxide (ITO) would be an obvious electrode material.

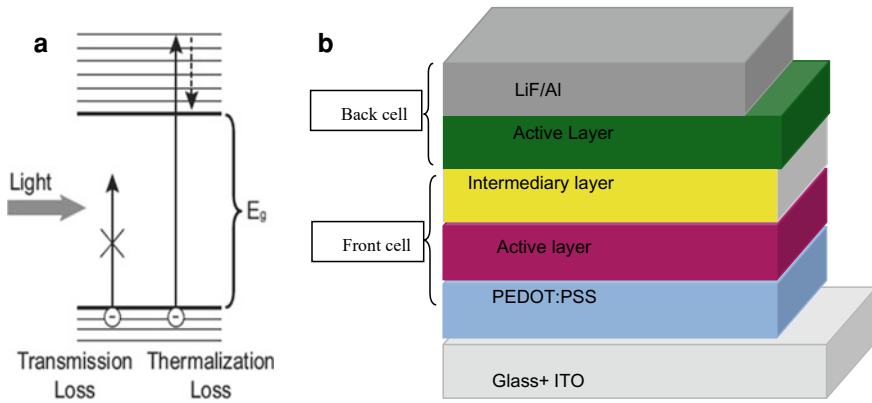


Fig. 6 **a** Thermalization and transmission loss. **b** A polymer tandem solar cell device structure

Here you can see Fig. 6a, b, which illustrates this statement. Organic photovoltaic devices are more efficient when multiple junction (tandem) solar cells are used—using single heterojunction cells to form multilayer structures clump off each other so that single heterojunction cells are combined in this example. Higher energy photons should collect to form one form of the material, while lower-energy photons should collect in the other to create a different form of the material. By incorporating a large and small band gap polymer into a tandem solar cell, it is possible to harness more significant amounts of energy from photons, which improves the device’s usefulness for a wider range of applications [33].

While reactive sputtering is often used to deposit ITO, this might significantly damage the conjugated polymer. This makes the difficult-to-fabricate organic semiconductor solar cells for that material used. Electrons in the LUMO of the front cell can recombine with holes in the HOMO of the back cell because the connecting layer has an intermediate recombination site when cells are series connected. The electrolyte of the front cell and the electrolyte of the back cell are separate in an electrochemical cell because the two cells are in contact with an electron transporting layer (ETL) and a hole transporting layer (HTL), respectively. A polymer tandem solar cell’s energy band diagram is shown in Fig. 7. The LUMO and HOMO of the front cell align with the ETL and HTL, respectively.

Additionally, to prevent voltage losses, the Fermi levels align at the ETL/HTL interface. The absorption of light creates excited states of electrons in both photovoltaic cells. The donor–acceptor interface in every cell then disintegrates. Electrons at the ETL/HTL interface recombine with holes from the front cell, which are then collected on electrodes that are situated between the two cells. The total current required to power the device is the same whether the cells are connected in series or in parallel (current matching).

The upper current of the two sub-cells is the lower current for organic semiconductors, which for the most part is the upper cell. If the cell’s lowest power limit is employed, then the overall generated power must be kept under the upper limit of the

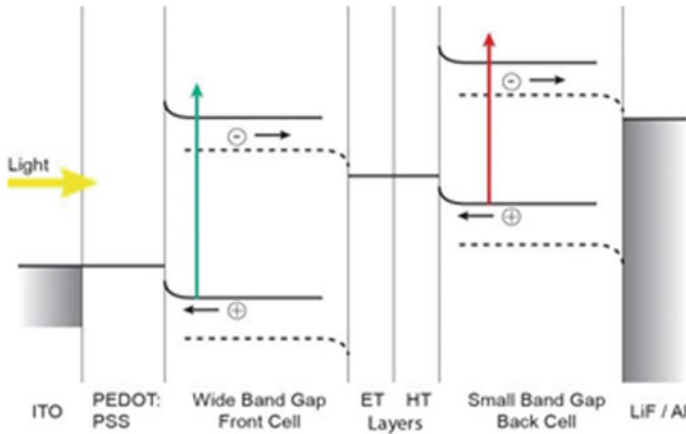


Fig. 7 Energy band diagram of a polymer tandem solar cell under V_{oc} conditions [34]

configuration. Thus, charge accumulation will be prevented in the intermediate layer, and the photocurrent will increase. Because of the built-in potential, these charges create an electric field and compensate for it. The lower compensation also means that the tandem cell has a lower fill factor. The optimization of each cell thickness is necessary to avoid these types of situations. When connected in series, two tandem cell voltage sums to the sub-cell voltages. The sum of the cell voltages results in the maximum short circuit current. It can improve the performance of a parallel solar cell tandem over a series-connected solar cell tandem. The parallel tandem (configuration) cell is indeed close to the front and back cells, with the current equal to the sum of the photocurrents generated by both sub-cells [35].

5 Innovative Thoughts and Recent Advancements in Organic Solar Cell Architectures

The different parameter settings in the devices being researched, such as the morphology of the active layer, the interface state, and the size of the electrodes, which are all being targeted to optimize them. Several techniques are currently being investigated to see if better results can be achieved. Optical spacers such as zinc oxide or Titanium oxide were used to customize the device's light intensity distribution to suit individual preferences in such a way that everyone sees the same light intensity. There is a local optical maximum just at the donor–acceptor interface [35]. Additional advances include photovoltaic (PV) panels, microelectrode structures, and nanostructural technologies incorporating diffraction gratings, embossed and patterned gratings, and buried nanoelectrodes. Different approaches to enhance the external quantum efficiency include light confinement and light trapping. See Fig. 8

Fig. 8 A schematic showing the architecture of a light pinning device

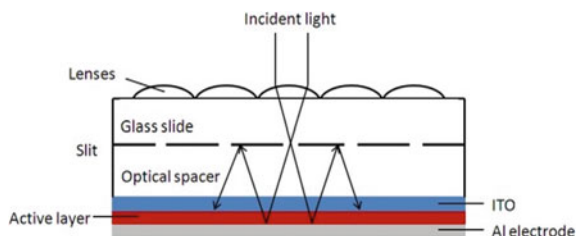
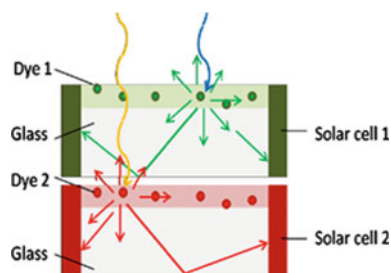


Fig. 9 Shows a light behavior diagram for a radiant solar energy concentrator device of two dye-coated substrates



for an example of a device. According to various reports, these kinds of equipment could be as efficient as 25% [36, 37].

Another innovative approach is Luminescent concentrators, which use light to produce other, desirable wavelengths. While white light travels through the fiber, low-wavelength dyes are deposited and emitted at higher wavelengths. Also, it supports efficient multi-colored organic solar cells, which are generated by unique designs. It is shown in Fig. 9 [38].

Indium tin oxide (ITO) is used as a light absorber in OSC analysis to help facilitate charge collection. Nevertheless, indium is rare, and indium tin oxide (ITO) is brittle, thus making large-scale OSC production of any sort difficult. This has allowed for a large amount of research on different materials and module concepts utilizing ITO-free alternatives. One of the most promising approaches to replacing ITO is to increase the conductivity of organic semiconductors, particularly PEDOT: PSS, metallic nanowires, carbon nanotubes, and thin metal layers.

6 Stability

Encapsulation, morphological control in the BHJ layer, interfacial engineering involving buffered layers, inverted geometry, and alternative electrode material are all necessary to ensure the long-term stability of OSCs.

6.1 Chemical Degradation

Oxidation is said to be the leading cause of degradation in the device. The photooxidation of organic layers and interfaces occurs due to an extrinsic factor. This is due to the water and oxygen sensitivity of organic materials, causing photooxidation. Layout design [39, 40], Oxidation of the organic layer causes a change in the conductivity and interface energetics of the material, as well as optical characteristics.

Helping to avoid oxygen and water-induced degradation is provided by embedding the device. Many sources of degradation such as UV light, are typically intrinsic rather than extrinsic. It has been proposed that long-lived excitons in organic materials contribute to molecular fragmentation. Burn-in losses in the OSC efficiency occur due to intrinsic chemical degradation of fullerenes (especially C60 and PC61BM). First described in 1993, it was demonstrated to result in substantial losses in many BHJ and small molecule/C60 planar heterojunction.

6.2 Physical Degradation

The device's embedding aids in the prevention of oxygen and water-induced degradation [41]. UV light is frequently cited as an example of a naturally occurring source of degradation. Organic materials with long-lived excitons have been linked to molecular fragmentation. Another source of intrinsic chemical degradation is the photoligomerization of fullerenes, especially C60 and PC61BM, which can result in significant burn-in losses in the efficiency of the OSC.

7 Conclusion

This article discusses recent advances in the architecture and design of organic photovoltaic devices. “For a sustainable future, we will still require innovations that focus on critical issues such as device stability and degradation, power conversion efficiency (PCE), and mass production process capability for the long life of cells.” Optical advanced designs, such as light trapping concentrators and geometries and developing parallel tandem configurations with innovative materials, will boost PCE further. A multidisciplinary approach that encompasses various disciplines is required to achieve the generation of organics, execute the next generation of solar cells with enhanced performance and fill the energy gap. It should be noted that, regardless of how well organic solar cells perform in terms of market integration, a variety of materials will be used in the solar power generation process, necessitating an exceptionally high degree of cell efficiency at times, resulting in the creation of a massive market for photovoltaic power and saving Earth's life on the planet.

References

1. <https://www.ipcc.ch/sr15/>. Accessed June 2021
2. <https://www.ise.fraunhofer.de/content/dam/ise/de/documents/publications/studies/Photovoltaics-Report.pdf>. Accessed June 2021
3. Deibel C, Dyakonov V (2010) Polymer–fullerene bulk heterojunction solar cells. *Rep Prog Phys* 73(9):096401
4. Qu B, Forrest SR (2018) Continuous roll-to-roll fabrication of organic photovoltaic cells via interconnected high-vacuum and low-pressure organic vapor phase deposition systems. *Appl Phys Lett* 113(5):053302
5. Abbel R, Galagan Y, Groen P (2018) Roll-to-roll fabrication of solution-processed electronics. *Adv Eng Mater* 20:1701190
6. Chamberlain GA (1983) *Sol Cells* 8:47; Tang CW (1986) *Appl Phys Lett* 48:183
7. Tang CW (1986) Two-layer organic photovoltaic cell. *Appl Phys Lett* 48(2):183–185
8. Hiramoto M, Fujiwara H, Yokoyama M (1991) Three-layered organic solar cell with a photoactive interlayer of co deposited pigments. *Appl Phys Lett* 58(10):1062–1064
9. Zhang G et al (2018) No fullerene acceptor molecules for bulk heterojunction organic solar cells. *Chem Rev* 118(7):3447–3507
10. Tong Y (2020) Progress of the key materials for organic solar cells. *Sci China Chem* 63(6):758–765
11. Shaheen SE, Radspinner R, Peyghambarian N, Jabbour GE (2001) Fabrication of bulk heterojunction plastic solar cells by screen printing. *Appl Phys Lett* 79(18):2996–2998
12. Ye L, Hu H, Ghasemi M, Wang T, Collins BA, Kim JH, Ade H et al (2018) Quantitative relations between interaction parameter, miscibility and function in organic solar cells. *Nat Mater* 17(3):253–260
13. Maennig B (2004) Organic p-i-n solar cells. *Appl Phys A* 79(1):1–14
14. Di Carlo Rasi D, Janssen RAJ (2019) Advances in solution-processed multijunction organic solar cells. *Adv Mater* 31(10):1806499
15. Xiong J, Xu J, Jiang Y, Xiao Z, Bao Q, Hao F, Ding L (2020) Fused-ring bislactone building blocks for polymer donors. *Sci Bull* 65:1792
16. Shirakawa H (1977) Synthesis of electrically conducting organic polymers: halogen derivatives of polyacetylene, (CH)_x. *J Chem Soc, Chem Commun* 16:578–580
17. Blom PWM (2007) Device physics of polymer: fullerene bulk heterojunction solar cells. *Adv Mater* 19(12):1551–1566
18. Nunzi J-M (2002) Organic photovoltaic materials and devices. *C R Phys* 3(4):523–542
19. Carsten B (2011) Stille polycondensation for the synthesis of functional materials. *Chem Rev* 111(3):1493–1528
20. Jørgensen M, Carle JE, Søndergaard RR, Lauritzen M, Dagnres-Hansen A, Byskov SL, Andersen TR, Larsen-Olsen TT, Bottiger APL, Andreasen B et al (2013) The state of organic solar cells—a meta analysis. *Sol Energy Mater Sol Cells* 119:84–93
21. Etxebarria I, Ajuria J, Pacios R (2015) Solution-process able polymeric solar cells: a review on materials strategies and cell architectures to overcome 10. *Org Electron* 19:34–60
22. Hemavathi B, Ahipai TN, Pai RK (2015) Polymer design for solar cell—current trend and future scenario. *Eur Polym J* 72:309–340
23. Kim Y, Lim E (2014) Development of polymer acceptors for organic photovoltaic cells. *Polymers (Basel)* 6(2):382–407
24. Taretto K, Rau U (2004) Modeling extremely thin absorber solar cells for optimized design. *Prog Photovolt Res Appl* 12:573–591
25. Ray B, Nair PR, Alam MA Unraveling the role of morphology on organic solar cell performance. 47906:1–10
26. Luceño-Sánchez JA, Díez-Pascual AM, Peña Capilla R (2019) Materials for photovoltaics: state of art and recent developments. *Int J Mol Sci* 20(4):976
27. Iwan A, Chuchmała A (2012) Perspectives of applied graphene: polymer solar cells. *Prog Polym Sci* 37(12):1805–1828

28. Rowell MW, Topinka MA, McGehee MD, Prall HJ, Dennler G, Sariciftci NS, Hu L, Gruner G (2006) Organic solar cells with carbon nanotube network electrodes. *Appl Phys Lett* 88
29. Tessema Mola G, Mbuyise XG, Oseni SO, Dlamini WM, Tonui P, Arbab EA, Maaza M et al (2018) Nanocomposite for solar energy application. In: *Nano hybrids and composites*, vol 20. Trans Tech Publications Ltd., pp 90–107
30. Spanggaard H, Krebs FC (2004) A brief history of the development of organic and polymeric photovoltaic. *Sol Energy Mater Sol Cells* 83(2–3):125–146
31. Scharber MC, Sariciftci NS (2013) Efficiency of bulk-heterojunction organic solar cells. *Prog Polym Sci* 38(12):1929–1940
32. You J, Dou L, Hong Z, Li G, Yang Y (2013) Recent trends in polymer tandem solar cells research. *Prog Polym Sci* 38(12):1909–1928
33. Prall H-J (2005) Tandem solar cells. PhD thesis, Johannes Kepler Universität Linz
34. Kim JY (2007) Efficient tandem polymer solar cells fabricated by all-solution processing. *Science* 317(5835):222–225
35. Niggemann M, Riede M, Gombert A, Leo K (2008) Light trapping in organic solar cells. *Phys Status Solidi* 205:2862–2874
36. Duché D, Simon JJ, Escoubas L, Torchio P, Le Rouzo J, Vervisch W, Flory F, Cézanne UP (2009) Photonic crystals for light trapping within organic solar cells. pp 4–7
37. van Sark WGJHM (2013) Luminescent solar concentrators—a low-cost photovoltaic alternative. *Renew Energy* 49:207–210
38. Norrman K (2010) Degradation patterns in water and oxygen of an inverted polymer solar cell. *J Am Chem Soc* 132(47):16883–16892
39. Rivaton A, Tournebize A, Gaume J, Bussièrè PO, Gardette JL, Therias S (2014) Photostability of organic materials used in polymer solar cells. *Polym Int* 63(8):1335–1345
40. Klumbies (2014) Influence of calcium corrosion on the performance of an adjacent permeation barrier. *Rev Sci Instrum* 85(1):016104
41. Bruner C, Dauskardt R (2014) Role of molecular weight on the mechanical device properties of organic polymer solar cells. *Macromolecules* 47(3):1117–1121

Parametric Study of Stiffened Composite Structures Using Design of Experiments



Nagaraj Kishor Kelageri, Deepak C. Patil, and Santosh Nandurkar

Abstract The study of polymer composite structures under uniform external pressure is vital in the design of pressure vessels of submarines or submersibles in which hydrostatic pressure-induced buckling tends to dominate structural performance. Advanced grid stiffened structures show superior buckling resistance to that of the unstiffened. The present work mainly aimed at examining the effects of grid thickness, grid height, inner shell thickness, outer shell thickness, and the number of segments on the structural performance of ortho-grid stiffened vinyl ester/glass composite shells. Design of Experiments (DOE) was used to identify significant parameters and their effects on critical buckling pressure and the total volume of the structure. Parametric study of ortho-grid stiffened polymer composite structures was performed using ANSYS buckling analysis, for their survival at 1000 m depth of the sea. Approximations of critical buckling pressure and total volume of the structure in the design space were developed using Response Surface Methodology. These approximations with design constraints were used to develop the optimization problem which was then solved using Penalty Function Approach. The DESIGN-EXPERT tool was used to perform an Analysis of Variance, develop approximations using response surface methodology, and finally find optimal design points. The results of the ANOVA of the parametric study indicated that inner and outer shell thicknesses of the stiffened composite shells had a significant effect on both critical buckling pressure and the total volume of the shells. The optimization results were compared with that of unstiffened shells of identical dimensions to estimate the weight saving due to the stiffeners. Volume saving of 30% compared with unstiffened structures achieved.

Keywords Grid stiffened shell · Finite element method · Design of experiments · Response surface method

N. K. Kelageri (✉) · D. C. Patil · S. Nandurkar
KLE Dr. M. S. Sheshgiri College of Engineering and Technology, Belagavi 590008, Karnataka, India
e-mail: nagarajkelager@gmail.com

1 Introduction

Grid stiffeners significantly increase the buckling resistance of cylindrical structures without much increase in weight. Kidane et al. [1, 2] presented the parametric study on iso-grid stiffened structures subjected to axial compression, for aerospace application, by numerical approach. The parameters considered were skin thickness, shell winding angle, stiffener orientation, and modulus of elasticity. The parametric study shows that, buckling resistance increases with skin thickness; for a stiffened cylinder failing in global buckling failure mode, an optimum shell winding angle of 54° is observed. Both stiffener orientation angle and longitudinal modulus increase are observed to continuously increase the buckling resistance of the stiffened cylinder structure. Mostafa [3] reported a parametric study of ortho-grid stiffened structures subjected to axial compression for aerospace application. The optimum shell winding angle for a stiffened cylinder having a skin thickness of 2.4 mm is found to be about 45° . Hao et al. [4] presented the effect of stiffener height and stiffener thickness on the structural response of iso-grid stiffened shell subjected to axial compression based on the Kriging model of the structural response. Parametric analysis shows that the increasing value of stiffener height promotes structural efficiency, whereas stiffener thickness harms structural efficiency. It was also shown that the number of stiffeners in grid stiffened shell has very less effect on structural efficiency.

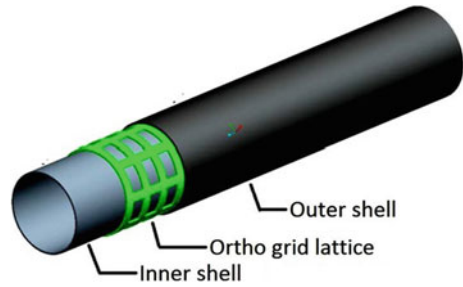
Bushnell [5] presented an optimal design of internally T-Iso-grid and T-ring stiffened isotropic cylindrical shells. Stiffener spacing, stiffener height, panel skin, grid web thickness, grid flange thickness, and the width of grid flange web were considered as design variables and the design objective is the minimization of weight. Hao et al. [4] developed an adaptive approximation-based optimization (AABO) procedure for the optimum design of a composite advanced grid stiffened cylinder subjected to axial compression. The design variables considered are stiffener height, stiffener thickness, and the number of stiffeners. An important observation in the AABO procedure is its dependency on the Design of Experiments (DOE) procedure. This approximation with given constraints is optimized using a genetic algorithm.

Literature indicates that the research on grid stiffened structures is mainly focused on aerospace applications and such structures are made out of metallic materials. Grid stiffeners for marine applications are new and such structures using polymer composites are in the beginning stage. Polymeric grid stiffeners are highly promising for underwater applications and hence parametric studies using numerical approaches help designers concentrate on selected parameters.

2 Problem Statement

The shell geometry considered for the parametric study was made of the following three layers: Inner shell, Outer shell, and Middle layer made of ortho-grid (Fig. 1). The model of composite shells of length ranging between 810 and 860 mm and inner

Fig. 1 Three layers of ortho-grid stiffened shell



diameter of 175 mm was considered. The factors considered for the parametric study of grid stiffened composite shells were: inner shell thickness, outer shell thickness, grid height, grid thickness, and number of segments made circumferentially.

The selected responses for DOE are:

- As the grid stiffened cylinder design is carried out considering buckling as failure criteria, *Critical Buckling Pressure* is considered as one of the response values.
- The other response considered here is the *total volume of the cylinder*, as the objective of design optimization is volume minimization.

The *Vinyl ester/Glass* composite is the material considered for grid stiffened shells. The work presented is aimed at performing a parametric study of ortho-grid stiffened polymer composite structures considering grid height, grid thickness, grid spacing, inner and outer skin thicknesses for critical buckling resistance and total volume of the structure, using Design of Experiments and ANOVA, and performing design optimization for ortho-grid stiffened composite structures of overall length around 825 mm and inner diameter of 175 mm, which can sustain the external hydrostatic pressure at 1000 m depth from sea level without buckling.

3 Design Factors and Their Levels

In Ortho-grid stiffened structures, the stiffeners are arranged perpendicular to each other such that the spacing between vertical and horizontal stiffeners remains the same and each segment of the stiffener forms the side of a square. The parameters or factors considered were: inner shell thickness, outer shell thickness, grid stiffener height, grid thickness, number of segments made circumferentially. The spacing between horizontal and vertical stiffeners remains the same this parameter is incorporated in parametric analysis in terms of the number of segments made circumferentially. This factor is also a deciding factor of the overall length of the cylinder as the length will be the multiple of the unit square segment formed. The parameters considered are shown in Fig. 2 with the diagram of the ortho-grid stiffened shell model considered. Table 1 represents the levels assigned for each of the factors being considered to perform DOE and ANOVA.

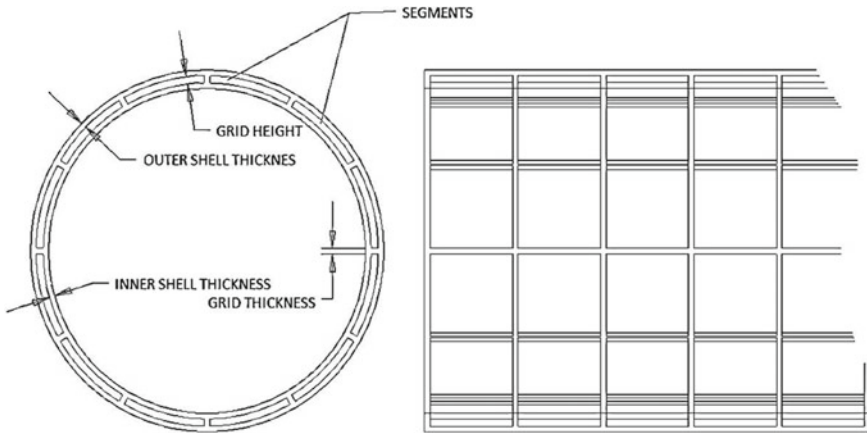


Fig. 2 Ortho-grid stiffened composite shell parameters

Table 1 Factors and their levels for ortho-grid stiffened composite shell

Factors	Notations	Levels		
		-1	0	1
Grid height (mm)	GH	4	6	8
Grid thickness (mm)	GT	3	6	9
Inner shell thickness (mm)	IST	3	6	9
Outer shell thickness (mm)	OST	3	6	9
Number of segments made circumferentially	NS	6	8	12

4 Taguchi's Standard Design Array

Five main factors are having 3 levels each, and in this research work, only two factors' interactions are considered. Hence, there is a total of 10 two-factor interactions that are considered. Therefore, the total degrees of freedom is

$$\text{DOF} = 5 \times 2 + 10 \times (2 \times 2) = 50 \quad (1)$$

Hence, Taguchi's standard L81 design array is chosen to perform DOE.

5 Finite Element Modeling

The Finite Element Analyses were performed using ANSYS buckling analysis to find critical buckling pressure. The outer shell and inner shell were meshed using the LAYERED SHELL element. The grid stiffeners were meshed using LAYERED

SOLID elements. Each layer thickness given is 0.23 mm. The fiber orientation of 55° and -55° are considered for alternative layers. The nodes at the interface of skin and stiffeners were merged to establish the connectivity between the two types of elements used. The boundary conditions and load applied are as follows:

1. The displacements were fixed to zero at both ends of the cylinder in all directions.
2. A uniform unit pressure is applied to the external shell area.

Linear buckling analysis in ANSYS finite elements software is performed in two steps. In the first step, a static solution to the structure is obtained. In this analysis, the pre-buckling stress of the structure is calculated. The second step involves performing an eigen buckling analysis using the Block-Lanugos method to extract the eigenvalues.

6 Results and Discussions

6.1 Analysis of Variance [ANOVA]

The result of ANOVA performed for responses, critical buckling pressure, and total volume of the ortho-grid stiffened shell, in the DESIGNEXPERT tool, is presented in Table 2. Following observations were made from ANOVA performed on both responses: for the buckling pressure, the F-values of outer shell thickness, inner shell thickness, number of segments, and grid height are higher than the F-distribution critical value at 1% significance level and 50 degrees of freedom, which is 7.5. Among these parameters, the outer shell thickness and inner thickness show very high values. Hence, these factors have a significant effect on buckling pressure. The higher values of these factors will increase the critical buckling pressure. For the total volume of the shell, all main factors have very high F-values than F-distribution critical value, which is 7.5. Hence, these factors are having a significant effect on the volume of the cylinder. These factors should be kept at the lower level as it is possible to minimize total volume.

The interaction plots for the total volume of the composite structure were shown in Fig. 3. It is clear from these interaction plots that interactions of grid height and grid thickness, grid height and the number of segments, and finally grid thickness and number of segments are having a positive interaction effect on the total volume of the composite structure.

The interaction plots for buckling pressure were shown in Fig. 3. It is clear from these interaction plots that the interactions of grid height and grid thickness, grid height and outer shell thickness, grid height and number of segments, inner shell thickness and outer shell thickness, and finally, inner shell thickness and the number of segments are having positive interaction effect on critical buckling pressure.

Increasing the specific buckling strength of the composite shell means simultaneous maximization of buckling pressure and minimization of the total volume

Table 2 ANOVA for buckling pressure and volume of ortho-grid stiffened shell

Buckling pressure				Total volume of shell			
SOURCE	Sum of squares	DOF	F-RATIO	SOURCE	Sum of squares	DOF	F-RATIO
A—GH	1187.98	2	72.44	A—GH	3.68e+12	2	1208.01
B—GT	63.50	2	3.87	B—GT	4.59e+12	2	1505.56
C—IST	5413.41	2	330.10	C—IST	1.28e+14	2	41992.61
D—OST	6538.93	2	398.73	D—OST	1.40 + 14	2	46094.72
E—NS	2981.06	2	181.78	E—NS	2.15e+12	2	706.55
AB	55.30	4	1.69	AB	339646709528	4	55.69
AC	36.99	4	1.13	AC	1235522500	4	0.203
BC	4.59	4	0.14	BC	2778853653	4	0.456
AD	115.09	4	3.51	AD	32553661760	4	5.338
BD	8.28	4	0.25	BD	11418767.361	4	0.002
CD	607.21	4	18.51	CD	53827480056	4	8.827
AE	181.58	4	5.54	AE	168876647521	4	27.69
BE	4.54	4	0.14	BE	358928105314	4	58.85
CE	260.73	4	7.95	CE	1381722373	4	0.227
DE	28.54	4	0.87	DE	13591088.922	4	0.002

of the composite shell. For the factors of internal shell thickness and external shell thickness, the direction in which the critical buckling pressure increases significantly will also increase the total volume of the shell. Thus, a trade-off between buckling pressure and the total volume of the cylinder must be made in choosing optimum levels of these values.

6.2 Design Optimization

The estimated coefficients of each parameter and interactions by response surface methodology using the DESIGN EXPERT tool are given in Table 3. With these approximation equations in design space considered, the optimization problem statement as interpreted by DESIGN EXPERT is as follows:

$$\text{Minimize Volume, } V = f(\text{GH, GT, IST, OST, NS}) \tag{2}$$

Subjected to $BP = 10 \text{ MPa}$; $4 \text{ mm} \leq \text{GH} \leq 8 \text{ mm}$; $3 \text{ mm} \leq \text{GT} \leq 9 \text{ mm}$; $3 \text{ mm} \leq \text{IST} \leq 9 \text{ mm}$; $3 \text{ mm} \leq \text{OST} \leq 9 \text{ mm}$; and $6 \leq \text{NS} \leq 12$.

The optimal values of factors found by the DESIGN EXPERT tool using the penalty function approach are: Grid Height (GH) = 5.7 mm, Grid Thickness (GT) = 3.00 mm, Inner Shell Thickness (IST) = 3.00 mm, Outer Shell Thickness (OST) = 3.00 mm, and Number of Segments made circumferentially (NS) = 12. The overall

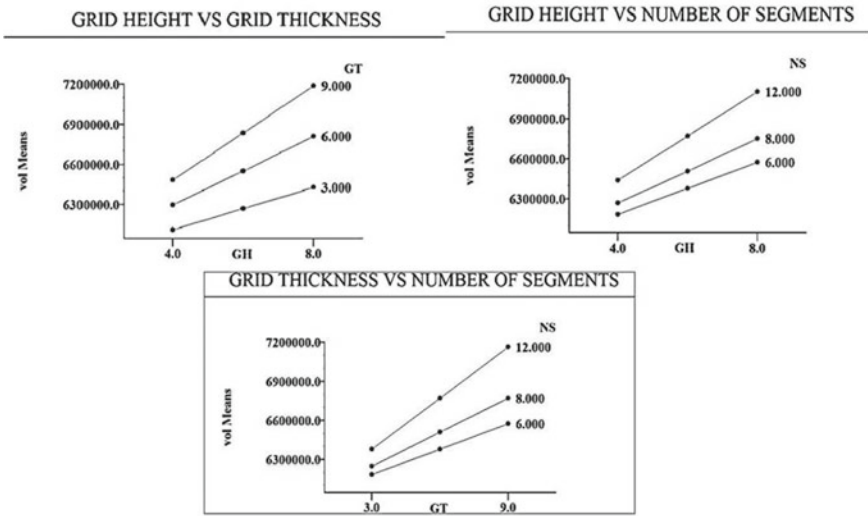
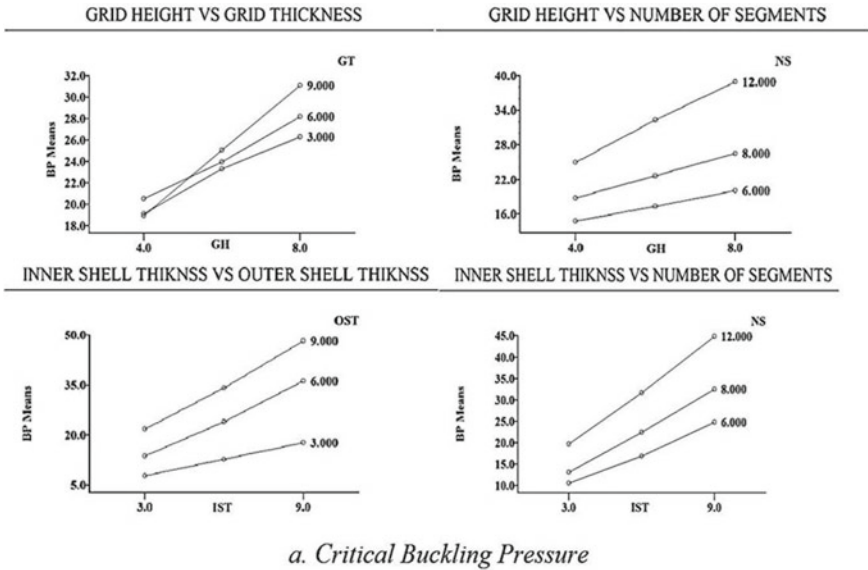


Fig. 3 Interaction plots for ortho-grid stiffened structure

length of the composite shell for 12 segments made circumferentially is 828 mm. ANSYS buckling analysis deformed shape for the above parameter optimal values are shown in Fig. 4. A comparison of ortho-grid stiffened structure is made with the simple unstiffened composite shell of the same length and buckling capacity in terms of percentage volume saving in Table 4.

Table 3 Coefficients of factors and interactions for critical buckling pressure and total volume

Factor	Ortho-grid structure		Iso-grid structure	
	Coefficient for buckling pressure	Coefficient for total volume of the shell	Coefficient for buckling pressure	Coefficient for total volume of the shell
Intercept	+31.24	+4.58132E+005	+43.33	+7.622E+005
A-gh	-4.98	-1.02202E+005	-4.06	-1.512E+005
B-gt	-1.78	-1.02614E+005	-1.19	-1.505E+005
C-ist	-3.26	+4.74259E+005	-5.18	+4.527E+005
D-ost	-2.019	+4.87670E+005	-3.38	+4.711E+005
E-ns	-2.350	-70898.98	-3.91	-1.067E+005
AB	+0.20	+16188.67	+0.12	+23420.00
AC	+0.17	+976.39	+0.13	+1416.81
AD	+0.29	+5011.84	+0.32	+4952.06
AE	+0.36	+11209.47	+0.33	+16640.53
BC	+0.04	+976.20	+0.09	+1395.09
BD	+0.05	-62.57	+0.07	-93.35
BE	+0.04	+10894.63	-0.01	+16045.01
CD	+0.46	+4296.43	+0.31	+3861.73
CE	+0.29	+675.95	+0.55	+3211.31
DE	+0.09	-67.04	+0.25	+2250.80

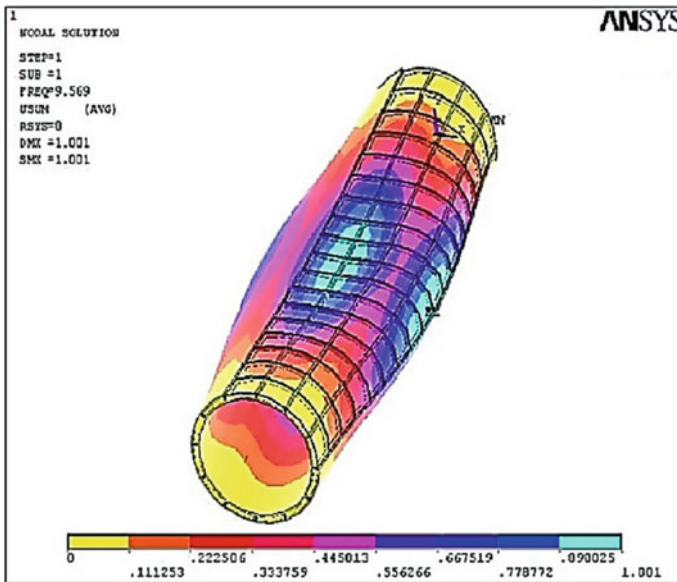


Fig. 4 Deformed shape of optimal design of ortho-grid stiffened shell

Table 4 Comparison of ortho-grid stiffened shell with the unstiffened cylinder in terms of percentage volume saving

	Plain composite shell	Ortho-grid stiffened shell	% volume saving
Volume of shell, mm ³	4,629,421	3,222,762	30.4

7 Conclusions

Following conclusions were drawn from the research work carried out. The results of ANOVA showed that the inner and outer shell thickness of the stiffened composite shell is having a significant effect on buckling pressure and total volume of the shell. Optimization results indicated a 30% of volume saving compared to plain composite shells.

Acknowledgements The authors are grateful to CAMA lab, the Department of Mechanical Engineering, KLE Dr. M. S. Sheshgiri College of Engineering for letting us use the ANSYS APDL. Also, the authors humbly acknowledge Stat-Ease, Inc. for making the DESIGNEXPERT trial version available.

References

1. Wodesenbet E, Kidane S, Pang SS (2003) Optimization for buckling loads of grid stiffened composite panels. *Compos Struct* 60:159–169. [https://doi.org/10.1016/S0263-8223\(02\)00315-X](https://doi.org/10.1016/S0263-8223(02)00315-X)
2. Kidane S (2002) Buckling analysis of grid stiffened composite structures. Addis Ababa University
3. Mostafa NH (2016) Buckling analysis of ring-stringer stiffened composite cylinder
4. Hao W, Ying Y, Wei Y, Baohua L (2010) Adaptive approximation-based optimization of composite advanced grid-stiffened cylinder. *Chin J Aeronaut* 23(4):423–429
5. Bushnell D (2002) Global optimum design of externally pressurized isogrid stiffened cylindrical shells with added T-rings. *Int J Non-Linear Mech* 37:801–831. [https://doi.org/10.1016/S0020-7462\(01\)00100-7](https://doi.org/10.1016/S0020-7462(01)00100-7)

Design and Optimization of Trestle Jack



M. Sadiq A. Pachapuri, R. G. Lingannavar, Nagaraj K. Kelageri,
and Sudarshan Kasar

Abstract With the increasing levels of technology, the automobile sector is coming up with several changes to their existing designs of auxiliary parts. The main auxiliary part of any vehicle is a jack, which comes in various types, shapes, and sizes, where the effort required to use them varies. Some of these types include scissor jacks, floor jacks, bottle jacks, pneumatic/hydraulic jacks, high lift jacks, and stand trolley jacks. Among this for lifting the vehicles, mechanical or hydraulic jacks are used. In this paper, an attempt is made to minimize the effort applied using the jack to lift the vehicle in a very short time. We bring in the concept of the Trestle Jack, which uses driving motion from the vehicle to lift and lower trailer axles. For the model, the finite element analysis was carried out and the fatigue life estimation and optimization for material and size were executed as a case study. The trestle jack was optimized in terms of weight so that it eliminates the requirement of skilled labor and saves time for the operation.

Keywords Trestle jacks · Material properties · Design and optimization

1 Introduction

The increasing levels of technology in the automobile sector such as anti-braking system, self-driving, Internet of Things (IoT), occupant safety, levels of mechatronics, and so on, has enhanced the driving and passenger experience. At the same time, there is not much development in the auxiliary equipment such as security, comfort, safety, lighting, and information systems. Here we are investigating the safety and ease of usage of the jack.

A jack is an auxiliary of equipment, employed for maintenance and tire replacement by raising the car off the ground. Generally, available jacks are either screw thread or hydraulic powered for lifting the load. Based on maximum capacity, the

M. S. A. Pachapuri (✉) · R. G. Lingannavar · N. K. Kelageri · S. Kasar
Department of Mechanical Engineering, KLE Dr. M. S. Sheshgiri College of Engineering and
Technology, Belgaum 590008, Karnataka, India
e-mail: pachapuri@gmail.com; sapachapuri@klescet.ac.in



Fig. 1 Adjustable and fixed height trestle jack

ratings are given to jacks. The following figure shows the currently available variety of Jacks used in the automobile industry as auxiliary equipment [1–3].

Female drivers faced difficulty using mechanical jacks which came to light after having an survey with them [4]. The trestle jack has been developed and optimized so that it's used with minimal effort and does not require any special skills. Currently, most vehicles are lifted by using screw jack as shown in Fig. 1, which requires more human effort. Jacks like scissor, bottle, and floor jacks have the similar disadvantage of human effort, wherein we bring the concept of the trestle jack, which overcomes this disadvantage.

1.1 Trestle Jack

The trestle jack is currently used in major garages for small to large commercial vehicles, with wheel sizes ranging from 13 to 16 inches. As human effort is not required for lifting and lowering down the jack, this results in safer environment. When Trestle jack is in upright position or engaged, its changes into a pivot support with protected working load of 30 Tons. The jack has five height adjustable positions, suiting a wide variety of trailer sizes, supporting both square and circular axles (Table 1) [5, 6].

1.2 Types of Trestle Jacks

There are mainly three types of trestle jack available, based on their size, lifting abilities, structure, and cost (Table 2).

Table 1 Advantages and uses of trestle jack

Advantages	Uses
It increases the width of the base by adding extra metal plates which increases stability as well as improves its strength	New, quick, safe, and airless solution
Design can be modified, in order to increase the load-bearing capacity	Fast axle lifting
Uses good quality rubber, thus eliminating the slipping condition	Usage in different fields
It is adjustable, so it is useful for the axle of the vehicle at any height	Easy to operate and manufacture
	Minimizes the disadvantages of a car jack
	There is always a provision for a new approach to modification

Table 2 Specifications of trestle jack models

Content	Trestle Jack TJ220	Trestle Jack TJ230	Trestle Jack TJ470
Lifting load	6 tons	15 tons	32 tons
Min height of the jack	13 inches	16 inches	24 inches
Max height of the jack	16 inches	22 inches	24 inches
Adjustable positions	5	5	Fixed

2 Objectives and Methodology

The main objectives of the study are:

1. Analyzing the trestle jack for stress, strains, and the fatigue loads
2. Weight and Cost Optimization

The methodology involves referring to the existing models of the trestle jack and considering the Mahindra XUV 500 vehicle; the geometric design is developed using CATIA software. The trestle jack geometry is analyzed using the solver ANSYS. Validation of the same is done through analytical calculation. Optimization is carried out on various materials and the thickness.

3 Literature Survey

Arun Kumar [7] discusses the overall features of the Jack Scissor Jacks must be strong and without difficulty controllable through a switch in order that jacking may be carried out from a safety point of view. It must be effortlessly movable in place under the axle of the vehicle. Author (s) has found satisfactory results though finite element analysis.

It is posited from Patil Manoj [4] et al.'s work that the analysis results show that it is safe to use the car Jack under specified conditions. The torque generated by the system can lift a car of weight 1200 kg easily. In addition, it is observed that certain weak areas can be optimized in the design and balancing of the Jack system.

Author Sonu Yadav briefly discusses about the solar powered screw jack, which operates on an external power source, i.e., solar-powered battery. It was analyzed for various loading conditions to determine the performance found to be satisfactory. For the same loading conditions, a mathematical model was developed and worked effectively.

Emergency always exists during a tire puncture; an automatic car jack is powered from a 12 V internal cigarette lighter. Authors suggested that by changing the gear ratios the lifting power of the jack can be increased. It was tested practically and used commercially. Analysis carried out for checking the factor of safety and design was discussed by M. M. Noor [8].

4 Material Selection

The material selected here is ASTM A36, which is the most commonly used mild and hot-rolled steel. It has excellent welding properties and is suitable for grinding, punching, tapping, drilling, and machining processes. The yield strength of ASTM A36 is less than that of cold roll C1018, thus enabling ASTM A36 to bend more readily than C1018.

Normally, larger diameters in ASTM A36 are not produced since C1018 hot roll rounds are used. Some of the Mechanical Properties of ASTM A36 are Tensile Strength—400–550 MPa, Elongation at Break—23%, Modulus of Elasticity—210 GPa, Bulk Modulus—140 GPa, Poisson's Ratio—0.260, and Shear Modulus—79.3 GPa [9].

4.1 Design and Calculations

Trestle jack uses the motion of the vehicle to lift and lower vehicle as appeared in Fig. 2 Since no one is required underneath for the lifting and bringing down systems, the outcome is a far more secure workplace. Trestle jack in upright or engaged

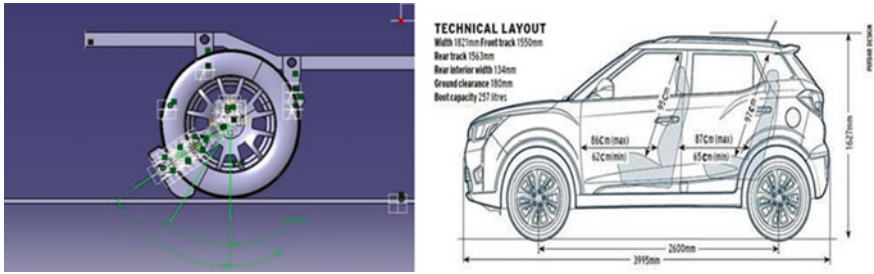


Fig. 2 Angle on which trestle jack is laying and side view of the vehicle

position, it changes into a pivot bolster remain with a protected working heap of 30 tons. Where a total hub or void trailer should be lifted, you should utilize two Trestle Jacks for each pivot.

4.2 Design of Trestle Jack

The dimensions are taken by measuring the actual dimension of the vehicle

- The total weight = 1455 kg
- The gross weight of the vehicle is = 2038.73 kg
- The payload = 583.73 kg

4.3 Calculations

Theoretical calculations.

Specification of the vehicle:

- Model = Mahindra XUV 300
- The ground clearance is = 310 mm till the axel of the chassis

Calculation of load carrying capacity of the vehicle:

- The total weight (Kerb weight) of Mahindra XUV 300 is = 1455 kg
- The gross weight that Mahindra XUV 300 can carry = 2038.73 kg
- Single wheel can carry upto = 509.71 kg.

In the 1st case, the load is acting in the horizontal direction $F_x = 4193.56 \text{ N} \cdot \text{mm}$ and in the 2nd case, the load is acting in the vertical direction $F_y = 2723.33 \text{ N} \cdot \text{mm}$. The summation of the above forces = 5000 N · mm.

Figure 3 shows the 2D diagram of the trestle jack sidebars which are used to support the cup on it; the sidebars are the main part of the trestle jack.

Specification of a hollow tube of trestle jack:

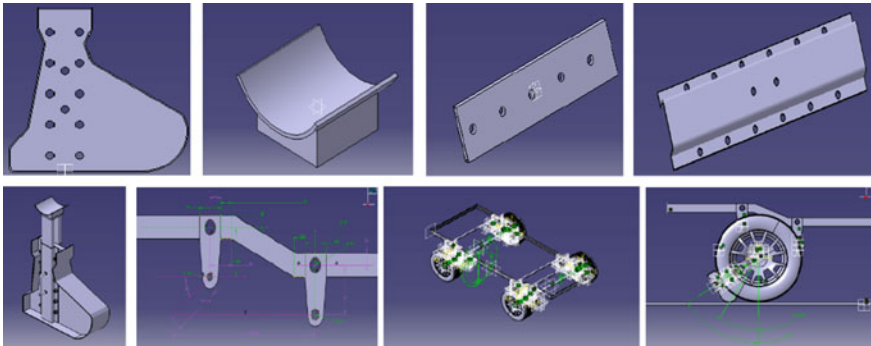
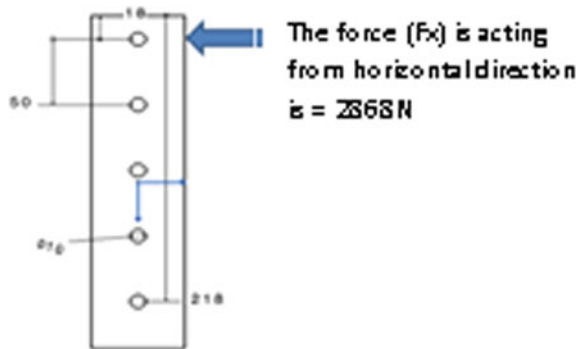


Fig. 3 Design details

Fig. 4 2D diagram of trestle jack side bars



- a. Length of the tube = 254 mm
- b. Cross section area of the hollow tube = (60 × 20 mm)
- c. Thickness of the hollow tube at both sides = 3 mm
- d. In the horizontal direction, the Force acting is $F_x = 4193.56 \text{ N}$ (Fig. 4)

From the bending equation, we get the bending stress formula $F_b = \frac{M \times Y}{I}$

Where we get moment $M = 733,873 \text{ N} \cdot \text{mm}$

We can calculate the distance from the neutral axis $Y = \frac{60}{2} = 30 \text{ mm}$

Moment of inertia denoted by (I) can be calculate as.

We can calculate the bending stress.

The load is shared by two hollow tubes and the bending stress for the two hollow tubes is Bending stress (F_b) = 112 MPa I = 97,643 mm⁴ F_b 225.20 MPa.

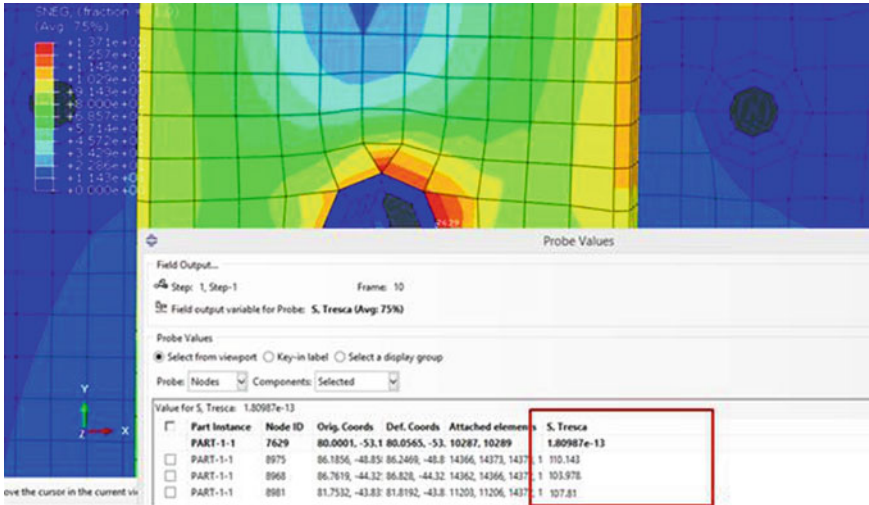


Fig. 5 Maximum principle stress

4.4 Analytical Calculation

The analysis results are given in Fig. 5, which shows the maximum principal stress acting on the jack.

The finite element analysis results $\sigma_c = 107.30$ MPa and while the Analytical calculation is 112 MPa and the percentage of error comes around 5% which is within acceptable limits.

4.5 Meshed Model

4.6 Static Structural Analysis

The static analysis is carried out for three load cases and the three load cases are at different inclinations of the trestle jack. The angles in which the load conditions are calculated, Load condition 1 (LC_1) at an angle of 33.0690, load condition 2 (LC_2) at the angle of 21.3160, and load condition 3 (LC_3) is at the angle of 900. The force component is calculated by using the above angles. The result in each case is discussed below. The static structure analysis is of two types: Von Mises criteria and [10] Tresca criteria (Figs. 6 and 7) (Table 3).

Fig. 6 Meshed model of trestle jack



4.7 Modal Analysis

4.8 Buckling Analysis

Structural failures can occur due to buckling. Mathematical models can obtain simple failure modes, and numerical tools are used for complex structures. Here linear buckling analysis has been obtained (Fig. 8).

Figure 9 shows the buckling load criteria of the trestle jack and Table 4 shows the Buckling load criteria with its mode and shape. Buckling analysis is used to determine the buckling loads causing buckling modes and failure. Buckling load factors can be calculated by using any of the FEA software where the minimum magnitude was zero and maximum magnitude was 17.77 for mode 1.

4.9 Optimization

Design variables can be optimized for better performance; saving material cost using available optimization techniques. While optimizing, one needs to consider all the constraints.

Figure 10 shows the load diagram for the 3 mm model, which has a weight of 0.897kg and maximum stress of 34MPa (Fig. 10), with the maximum displacement of 0.12mm for 3 mm model. The analysis made is for weight reduction.

Figure 10 shows the Load Diagram for the 2 mm model of optimization, which has a weight of 0.731kg and maximum stress of 48 MPa. Figure 10 shows the maximum displacement of 0.15mm for the 2 mm model. The analysis is for the Trestle jack which is optimized from 3to2mm.

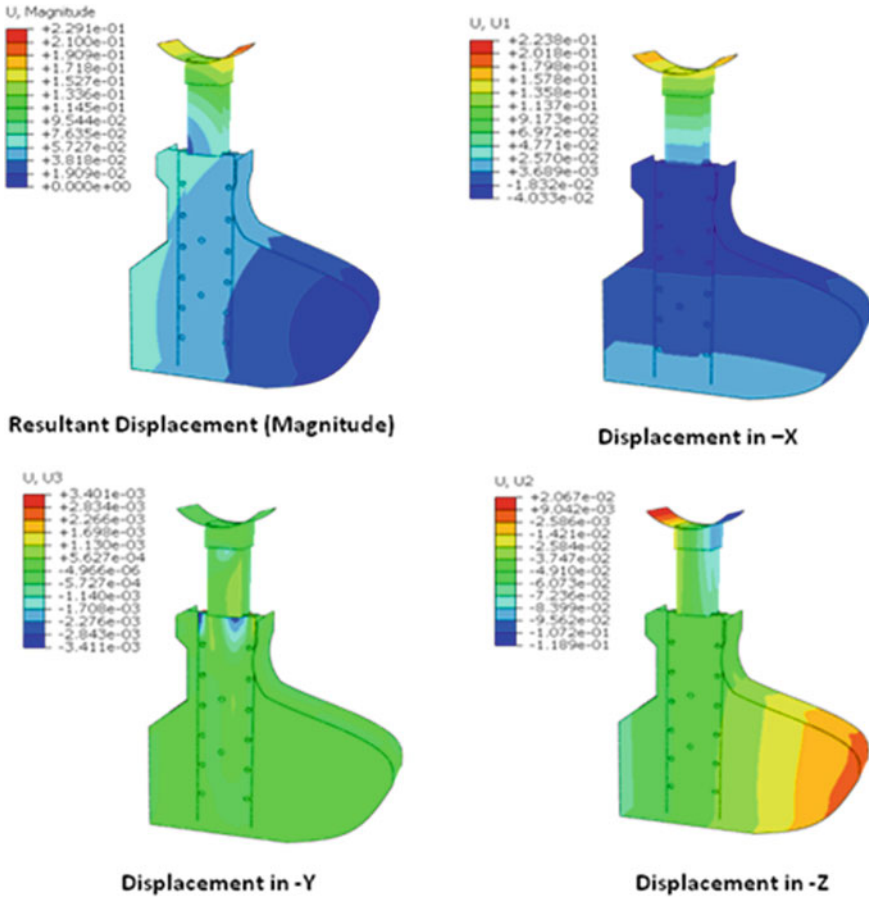


Fig. 7 Displacement in all directions

Table 3 Maximum displacement and stress

Maximum	Loading condition		
	(LC1)	(LC2)	(LC3)
Displacement in—X	0.2238 mm	0	0
Displacement in—Y	0.1189 mm	0.2736 mm	0.02736 mm
Displacement in—Z	0.003401 mm	0	0
Magnitude	0.229 mm	0.0833 mm	0.03844 mm
von Mises stress	48 MPa	119.0 MPa	17.77 MPa
Tresca stress	55 MPa	137.1 MPa	18.02 MPa

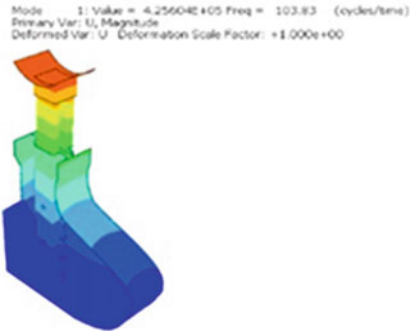


Fig. 8 Mode shape 1 and 2

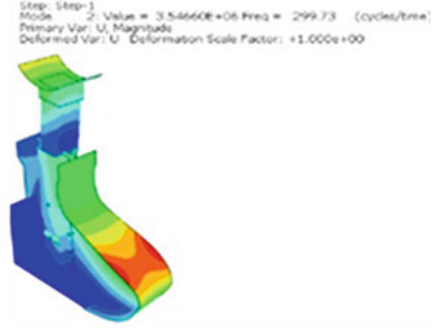


Fig. 9 Buckling load criteria

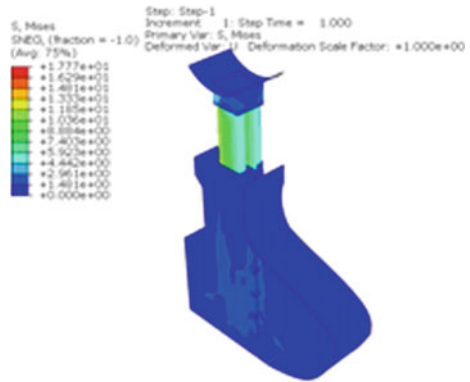


Table 4 Mode shapes of the trestle jack

Modes	Values	Frequency	Mode shapes
Mode 1	$4.2560 \times e^{+5}$	103.83	Bending
Mode 2	$3.5446 \times e^{+6}$	299.73	Bending and twisting
Mode 3	$4.09821 \times e^{+6}$	322.19	Bending
Mode 4	$5.74485 \times e^{+7}$	381.47	Twisting
Mode 5	$1.27166 \times e^{+7}$	567.55	Twisting
Mode 6	$2.51184 \times e^{+7}$	797.66	Transverse bending
Mode 7	$2.6766 \times e^{+7}$	823.41	Twisting
Mode 8	$2.7766 \times e^{+7}$	838.65	Transverse bending
Mode 9	$2.90223 \times e^{+7}$	857.41	Bending and twisting
Mode 10	$3.10835 \times e^{+7}$	887.33	Bending and twisting

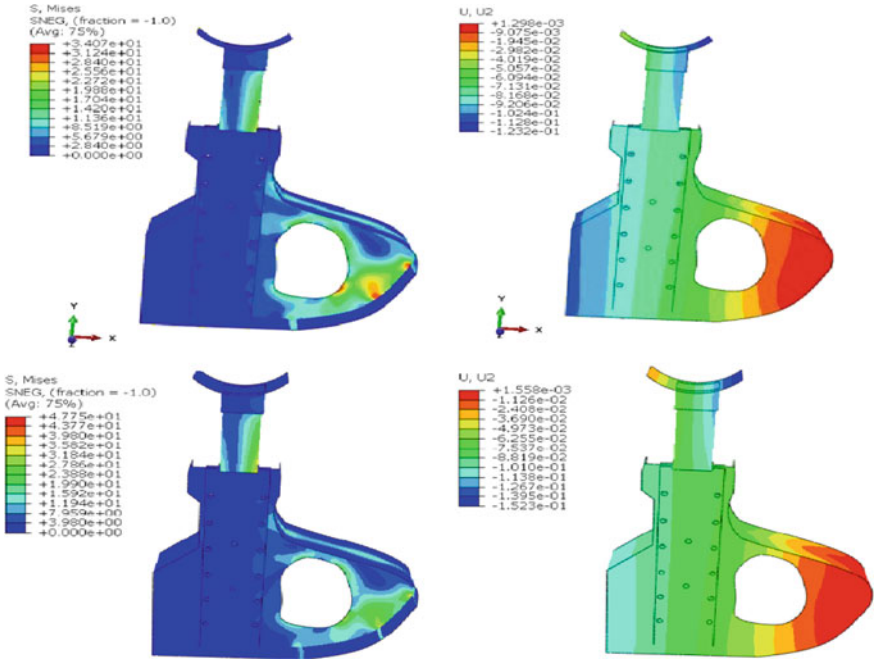


Fig. 10 Load and displacements for 3 mm and 2 mm, respectively

Optimization is the field of ideal control hypothesis. The regular issue is to discover the shape, which is ideal in that it limits specific cost utilization while fulfilling given limitations. As a practical rule, the arrangement of given fractional.

Table 5 shows the maximum load carrying capacity of the trestle jack that is for 2 mm it is 3000 N and for 3 mm it is 5000 N.

Table 5 Comparison of optimized model

Sl. No.	Content	Thickness	
		2 mm	3 mm
1.	Weight	1.47 kg	1.78 kg
2.	Minimum stress	0.00 kg	0.00 kg
3.	Maximum stress	48 MPa	34 MPa
4.	Minimum displacement	-0.1523 mm	-0.1232 mm
5.	Maximum displacement	0.15 mm	0.12 mm
6.	Maximum load carrying capacity	3000 N	5000 N

Table 6 Result summary

Content	Displacement (mm)			von Mises criteria, MPa	Tresca criteria
	X	Y	Z		
LC1	0.2238	0.1189	0.003401	48	55
LC2	0	0.2730	0	119.0	137.1
LC3	0	0.256	0	17.77	18.02

5 Result Summary

Table 6 shows the result summary for three load cases, LC1, LC2, and LC3, where all the maximum load conditions and maximum displacement are taken, and the factor of safety is calculated.

The above table shows the quotations of the trestle jack which are based on their weight, cost, and thickness (2 mm).

6 Conclusions

- Existing problem with jacks are they are time consuming in operation, heavy in weight and they require of skilled labor for lifting and lowering the jack. For eliminating such problems [11], the Trestle jack is designed in such a way that consumes less time for fixing with no skilled labor and has less weight. Below is the comparison of Trestle jack with other jacks (Table 7)
- Modal analysis obtained from Table 4, shows ten mode shapes each with its different natural frequency as well as the mode shapes by the modal analysis we

Table 7 Comparison of all the jacks

Sl. No.	Names	Material	Weight (kg)	Lifting weight (tons)	Dimensions (mm)	Min height lift (mm)	Max height lift (mm)	Cost
1.	Scissor jack	Steel	2	1.5	420 × 76 × 100	100	250	1100
2.	Hydraulic jack	Steel	1.7	2	100 × 12	120	300	1170
3.	Screw jack	Steel	3	2	150 × 102	100	300	1000
4.	Trestle jack	Steel	4	6	330 × 127 × 330	330	400	13,000
5.	Customize trestle jack	ASTM-A36	2.2	2.5	425 × 250	250	450	1517

can see that trestle jack can bend, twist, and it can even transversely bend in the direction of applied load.

3. The design optimization of trestle jack, from 3 to 2 mm, is carried out in the hyper-mesh software to analyze the load carrying capacity of the jacks. Table 5 gives the comparison of the two trestle jacks. After optimization comparing the results, the 2 mm thickness jack is more feasible than 3 mm thickness one.
4. Trestle jack parts were analyzed in the hyper works software using the ABAQUS solver, by comparing the analysis, it can be concluded that the theoretical results are nearby the vicinity of the analytical results.
5. Optimizing for weight and analyzing the value of deformation is below than the yield point of the material and hence the plastic deformation will not occur.

References

1. Rajendar N, Vangala R, Kumar N (2018) Design and fabrication of static load testing machine by screw jack mechanism. *Int J Sci Res Rev* 7(2)
2. Ranjeet D, Bhawe M (2017) Analysis and modification of screw jack body using FEM. *Int J Sci Technol Eng* 3
3. Pawar PR, Shinde MS (2015) Recent technology in automobile and need of motorized jack. *Int J Recent Dev Eng Technol* 4
4. Patil M (2014) Requirements and that comfort of women in the automobile. *J Sci Res* 20:868–870. ISSN 1990-9233
5. Suresh P, Kumar MS (2018) Design and analysis of hydraulic trestle jack. *Int J Sci Res Rev* 7
6. Noor MM, Patel NR (2010) Design of toggle jack considering material selection of screw—nut combination. *Int J Innov Res Sci, Eng Technol* 2(5)
7. Haribaskar G, Dhenesh Kumar N, Arun Kumar C (2015) Remote controlled scissor jack to lift the vehicle. *Int J Adv Res* 3:1279–1282
8. Dayanand D (2017) Structural analysis of screw jack. *Int J Res Appl Sci Eng Technol (IJRASET)* 5(IX). ISSN 2321-9653
9. Chandra N, Yadav S (2014) Failure of screw is happening due to tensile stresses in material. *Int J Sci Res Dev* 2. ISSN 2321-0613
10. Udgirkar GS (2015) Design and analysis traditional car jacks use mechanical advantage to allow a man to raise up vehicle by manual effort. *Int J Mech Eng Res India* 4(1). ISSN 2278-0149
11. Yadav S et al (2014) Design and implementation of car jack. *Sci Q J* 1(1)
12. Chandra S, Patil D (2011) Design and analysis of scissor jack using Catia. *Int J Sci Technol Eng* 5

Simulation of a Vision-Based Model of a Robotic Work Cell (6-Axis)



Mitul Milind Gajbhiye, Amol Chaudhary, and Sangharatna Ramteke

Abstract In this paper, a technique is demonstrated to notice the end-effector's Denavit Hartenberg (DH) parameters as per the necessity of the labor envelope. For this purpose, here we have used Roboanalyzer software. The manipulator's gripper is designed in such a way to move and perform a particular task in a specific way. In recent research papers, simulation for the ARISTO robot functioning for welding a curved surface has been discussed. We aim to design and simulate the MTAB ARISTO robot integrated with a vision module that perfectly suits pick and place operation on the conveyor, upon which kinematics and simulation are done for the respective joints and links for the end effector. Motion analysis of the manipulator is shown on graphs as a time sequence of links and joints. Each of which is performed and done using RoboAnalyzer software.

Keywords Denavit Hartenberg (DH) parameters · Forward kinematics · Inverse kinematics · Manipulator · RoboAnalyzer

1 Introduction

An articulated mechanism may be a robot with rotary joints; articulated robots can vary from straightforward two-jointed structures to systems with ten or a lot of interacting joints and materials. They are high-powered by a range of means, as well as electrical motors. Some sorts of robots, resembling robotic arms, maybe articulated or non-articulated. ARISTO has a simulation software package that allows the users to learn the robot's functions, applications, and programming. MTAB ARISTO robots are widely accepted in completely different work applications like pick and place, palletizing, machine loading and unloading, and fastening incurved methods. This mechanism is often equipped with grippers of two types, i.e., pneumatic and electrical grippers with varieties of the path, potential of square measures say defined destined point to point, Linear and circular interpolation methods. The required power for the

M. M. Gajbhiye (✉) · A. Chaudhary · S. Ramteke
Department of Mechanical Engineering, G. H. Raisoni College of Engineering, Affiliated to
R.T.M.N.U., Nagpur, Maharashtra, India
e-mail: gajbhiyemitul@gmail.com

automation is 230 V AC, 50/60 Hz, 5 A, and the payload capability is 2.5 kg. The robot can be used directly by calling from the software library and modified as per the preferences for various practical and simulation purposes. Individual link lengths and joint parameters can be introduced in the robot. Performing various position-based analyses and carrying out the individual center of gravity link graphic properties over the task's whole process.

Rajeevlochana and Saha gave a brief overview of the tools and software available in the market and research domain, either free or paid for robot visualization [1]. Saha et al. proposed other advanced robot visualization tools such as RVS4W [2], and similarly, Botero et al. proposed ROBOMOSP [3], which can specifically perform the forward and inverse kinematics and trajectory planning. Sadanand et al. proposed the software named RoboAnalyzer, which allows a user to analyze multiple inverse kinematic solutions and observe the motion among any of the two possible solutions [4].

This article presents the simulation and graphical properties of the MTAB ARISTO for the vision-based robotic work cell over the number of steps involved in the simulation to generate a smooth path for trajectory generated by the movement of the manipulator and gripper. It also plots graphs for various variables like acceleration v/s time and force/torque v/s time (Fig. 1).

2 Background

Vision system

While carrying out the experiment, the following accessories were used: ITEX 15040—a monochrome camera with a mono-focal lens, an image monitor, IMA-150/40 advanced image manager with 4 MB reconfigurable memory, an AM-VS variable scan acquisition module, a DM-PC pseudo color display module, a CM-PA programmable accelerator, and a BIT 3 model 466 Sbus-VME adaptor.

As shown in Fig. 2, on the final axis of the robot, a camera is linked, and for its complete movement, the robot can freely make the necessary adjustments by moving its wrist.

Force/torque sensing module

During the final stages of automation, i.e., offline simulation to rectify the positional errors, the Force/Torque-sensing module takes charge, observes, and modifies the errors based on position. The sensing module carries the neural network and mathematical equations and obtains the accurate and precise response of the acting programs; this sensing module has already been transformed into C programs to monitor sensor inputs and cause a correct response for the following program.

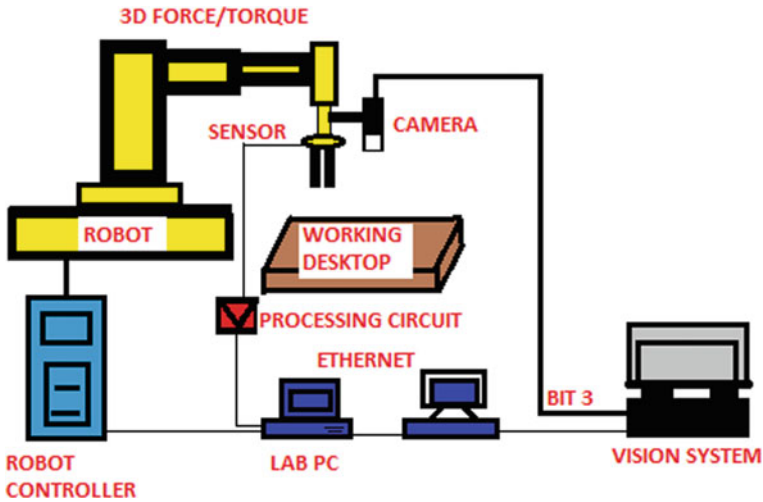
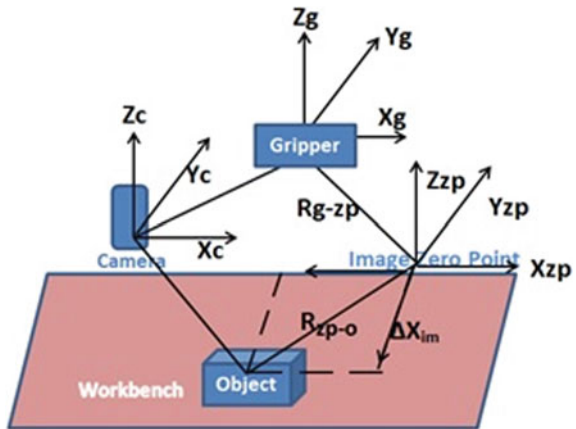


Fig. 1 System hardware configuration

Fig. 2 The coordinate system for robot and vision system



Acting programs

The following three functions: The image module, The F/T sensing module, and the automation management, are managed by the acting program module, which handles the time and sequence. Following the other functions like system information passing, knowledge extracting and change, and system-level deciding. Similarly, simulating robot path knowledge, transferring the knowledge among different coordinate systems, and transferring the information to the automation controller to regulate automation are also the functions handled by the acting module. Where the output of subsystems is used to automate each job request and work cell condition. Such as which machine is suitable to be serviced, which workpiece is found to be

proper and loaded, which machine is not in working condition, and where the new machinery is extra.

Denavit and Hartenberg (DH) parameters

Denavit–Hartenberg (DH) parameters are a convention used by robotics experts to mathematically describe the size and range of a robot’s arms.

a. **Joint offset (b):**

Offset to the standard normal for z.

b. **Joint angle (θ):**

Angle from old x to new x.

c. **Link length (a):**

Length of the normal, keeping a revolute joint in mind, this is the radius along z.

d. **Twist angle (α):**

Angle from old z-axis to new z-axis.

Hence, for revolute/prismatic joint, the two terms used for a variable and the other three constant parameters are joint variable and link parameters, respectively [5].

Forward and Inverse Kinematics

Both forward and inverse kinematics are vital to Artificial Intelligence. Forward kinematics refers to the process of computing the position of the end effector from a given value for the joint parameters by using the kinematic equations of a robot.

These kinematic equations are used in animation, robotics, and computer games. Moreover, the reverse process of achieving a desired position of the end effector by computing the joint parameters is known as inverse kinematics.

- Joint Variables \rightarrow End effector’s pose of a Robotic Arm = Forward Kinematics.
- End effector’s pose of a Robotic Arm \rightarrow Joint Variables = Inverse Kinematics.

Forward Kinematics

Determination of the end effector’s parameters, the link length, and joint variables (angles) are provided. We used known joint variables (i.e., servo motor angles, displacement of a linear actuator) to calculate a robotic arm’s end-effector orientation and end-effector position in 3D space.

Inverse Kinematics

In robotics, inverse kinematics uses the kinematics equations to find the joint settings that allow each of the robot’s end effectors to achieve the required configuration. Motion planning is the process of determining a robot’s movement in order for its end effectors to go from one configuration to another. The motion is transformed using inverse kinematics. The transformation of the position and orientation of a manipulator end effector from Cartesian area to joint area is named as Inverse mechanics downside.

Joint No	Joint Type	Joint Offset (b) m	Joint Angle (theta) deg	Link Length (a) m	Twist Angle (alpha) deg	Initial Value (JV) deg or m	Final Value (JV) deg or m
1	Revolute	0.322	Variable	0	90	0	60
2	Revolute	0	Variable	0.3	0	90	60
3	Revolute	0	Variable	0	90	180	150
4	Revolute	-0.375	Variable	0	90	-180	-200
5	Revolute	0	Variable	0	90	-90	60
6	Revolute	0.063	Variable	0	0	0	60

Fig. 3 Model of MTAB ARISTO robot

3 Experimental Details

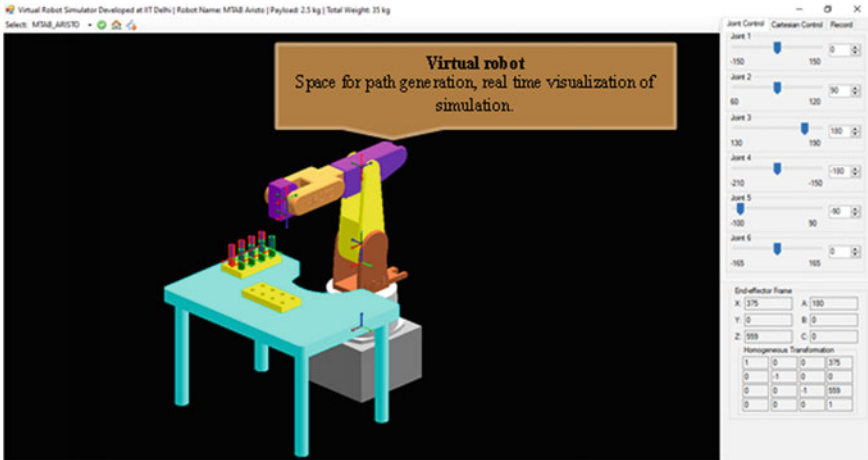
3.1 Selection of Robot

The ARISTO robot in RoboAnalyzer software gives an advantage over creating a CAD model and then working over it. Importing the robot type from the library, at the preliminary step, we must give the degree of freedom (DOF) as shown in Fig. 3. Available robots of every type will appear in the list below. Choosing the working condition of the robot and then incorporating the necessary configurations.

Pupils find the mathematics involved in robotics, such as forward and inverse kinematics, challenging to comprehend at first, and teachers find it challenging to explain the essentials of robotics mathematics to students. This is because, forward and inverse kinematics, for example, need 3D transformations. The industrial robots are also depicted using Denavit and Hartenberg (DH) characteristics, which are difficult to comprehend and visualize in 3D. RoboAnalyzer is designed to help students and instructors overcome the challenges listed above. In other words, study/teach the physics of robotics using the fun of RoboAnalyzer animations before attempting to understand the mathematics of robotics, which is addressed in the book “Introduction to robotics” by Saha [6].

3.2 Parametric Setup for Analysis

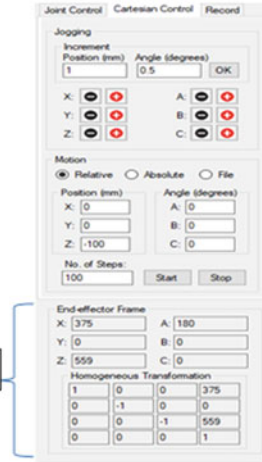
The setting up of the parameters for inverse kinematics through the two available options, i.e., joint control and cartesian control is shown in Fig. 4. The path generated by both methods allows us to compare and analyze the curve. These methods allow us to get complete control of the robot and move as per the specific position or angle as described below. The output of these methods will be the end-effector coordinates and the total homogeneous transformation of the robot.



Method 1: Joint control



Method 2: Cartesian control



End-effector Frame

Fig. 4 The photographic view shows the motion of the robot

Method 1

Joint control of each joint, i.e., joint 1 to joint 6, will let us drive the joints according to the angle of the links on which it is mounted. Respective joints and links let us drive the gripper to the object's exact position over the workbench. Angle related to each joint is given below (degree): joint 1: -150 to 150; joint 2: 60 to 120; joint 3: 130 to 190; joint 4: -210 to -150; joint 5: -100 to 90; joint 6: -165 to 165.

Method 2

Cartesian control—this technique mainly uses the jogging method with increments in X, Y, and Z direction and motion, i.e., relative motion and absolute motion, which

takes X, Y, and Z axis into account for the motion in millimeter (mm) and angle (degree).

4 Results and Discussions

4.1 Inverse Kinematics

Figure 5 represents eight different solutions for the position where the end effector has to reach. However, the robot prefers only a single path to approach and reach the target point and keeps all the other seven options in the reading history. This table helps us detect the variations in all the joint angles, which enables us to find the difference between the highest and the lowest values for each joint from all the solutions. It also provides the joint offset (m), link length (m), twist angle (deg), and end effector’s position (m) for each joint separately.

Figure 6 shows the line graph, consisting of three lines for X, Y, and Z directions representing the end-effector distance of each link per unit time (s), respectively. Each link has three lines representing the end effectors’ X, Y, and Z directional movement.

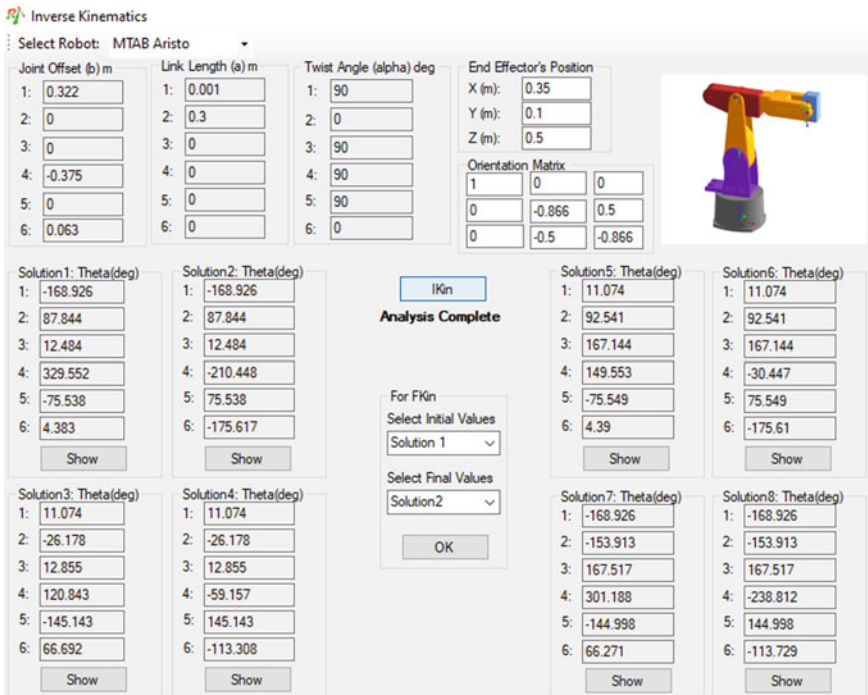


Fig. 5 Inverse kinematics of the ARISTO

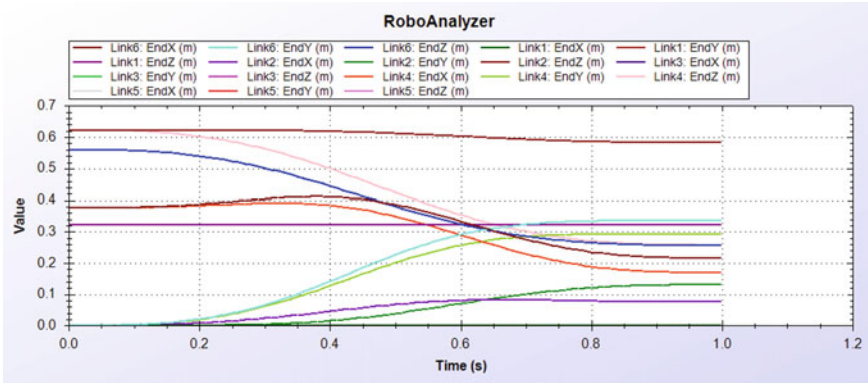


Fig. 6 End effector distance in X, Y, and Z direction for links 1–6

This graphical representation of the data about all the six links of the ARISTO robot gives easy access to compare data with individual link movements, for example, link one and link 6; we can compare and see the difference in the distances moved by their links in X, Y, and Z directions in a time interval of 0.2 s.

Figure 7 shows the joint values, joint velocities, joint acceleration, and force/torque information. The almost straight line shows very low deflection or change from initial values. The sinusoidal wave curves show the acceleration curves for joints 1, 2, and 3, respectively, where joint one is highly accelerated compared to joint two and joint 3. Joint 3 shows the slightest acceleration and is closest to the origin axis.

Figure 8 indicates the difference in the joints' values that increase compared to the difference in values for joints 1, 2, and 3, which is almost doubled the values. Joint 5 shows the maximum change in the value of its acceleration as compared to every other joint. Low deflection in lines proves the downward movement of the

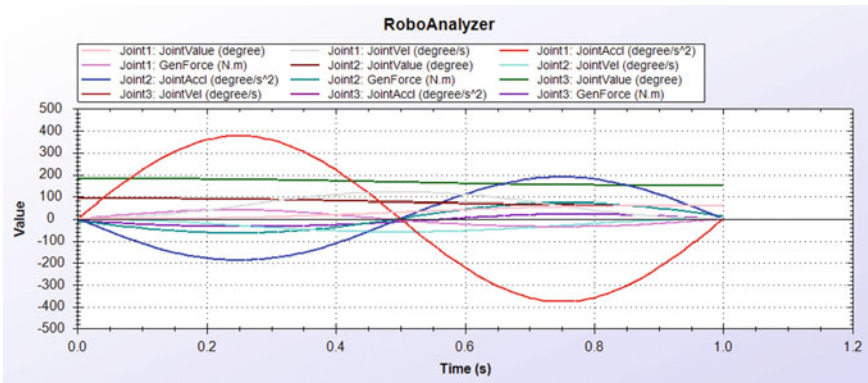


Fig. 7 Velocity, acceleration for joints 1, 2, and 3

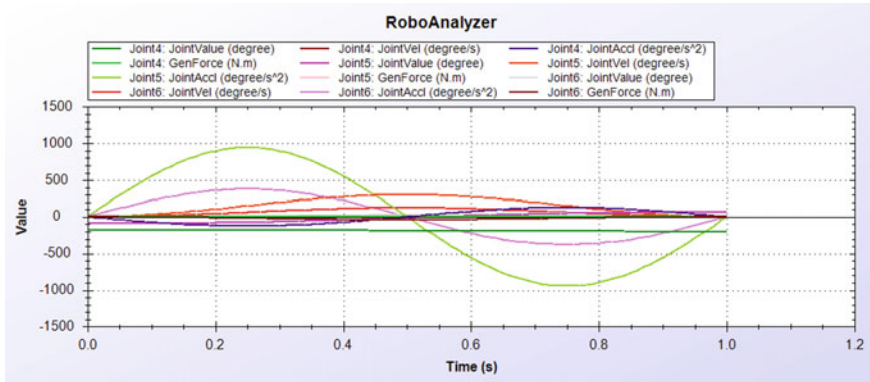


Fig. 8 Velocity, acceleration for joints 4, 5, and 6

joints as that of joint 4. The graphs combined gave us link by link and joint by joint detailed information regarding the velocity, acceleration, and forces with torque. All these results show faster and more reliable solution to any problem concerning any other method, especially when done with real-time simulation and modification of the robot.

5 Conclusions

In this work, the RoboAnalyzer software is used to determine the kinematics of the MTAB ARISTO robot, i.e., forward kinematics and inverse kinematics. However, the theoretical approach consumes much time and can lead to more errors in obtaining the data of each link and joint for individual parameters like force, acceleration, velocity, and torque. Existing experiments lead us to only the kinematics solution of the robot; by using the RoboAnalyzer software, we can obtain the values of velocity, acceleration, and other corresponding values for links and joints, in addition to the robot end-effector simulation. This robot (MTAB ARISTO) is particularly most suited for operations like pick and place, palletizing, writing, assembly, and curvy welding paths. The significant finding from this study is, except for link 6, the end-effector distance for all the link ranges under 0.35 m. Acceleration for joint 5 is almost double the values of joint 1, i.e., the range for joint 1: -400 to 400 and for joint 5: -850 to 850 .

References

1. Rajeevlochana CG, Saha SK (2011) RoboAnalyzer: a 3D model-based robotic learning software. In: International conference on multi-body dynamics, pp 3–13

2. Gupta V, Chittawadigi RG, Saha SK (2017) RoboAnalyzer: robot visualization software for robot technicians. In: Proceedings of the advances in robotics, pp 1–5
3. Botero AJ, Gomez AM, Correa-Caicedo JF, Perea-Castro W (2006) ROBOMOSP. *IEEE Robot Autom Mag* 13(4):62–73
4. Sadanand OR, Sairaman S, Sah PB, Udhayakumar G, Chittawadigi RG, Saha SK (2015) Kinematic analysis of MTAB robots and its integration with RoboAnalyzer software. In: Proceedings of the 2015 conference on advances in robotics, pp 1–6
5. Srikanth A, Ravithej Y, Sivaraviteja V, Sreechand V (2013) Kinematic analysis and simulation of 6 DOF of robot for industrial applications. *Int J Eng Sci* 3(8):01–04
6. Saha SK (2014) Introduction to robotics. Tata McGraw-Hill Education
7. Zhang H, Zhao J (2017) Bio-inspired vision-based robot control using featureless estimations of time-to-contact. *Bioinspir Biomim* 12(2):025001
8. Sampei M, Furuta K (1988) Robot control in the neighborhood of singular points. *IEEE J Robot Autom* 4(3):303–309
9. Gupta V, Saha SK, Chaudhary H (2019) Optimum design of serial robots. *J Mech Des* 141(8)
10. Wei HZ, Xue D, Jiao LQ, Bai WF (2012) Error analysis and simulation based on KUKA six-degree robust. *J Chang Univ Technol (Nat Sci Ed)* 3

Numerical Simulations of an Interaction of a Blast Wave Produced from a Shock Tube with an Object Placed at Various Positions



Datti Ganapathi and Abhishek Kundu

Abstract The pressure blast wave generated by a shock tube was simulated using a computational fluid dynamics technique to investigate blast load due to pressure distribution on the wall which is located at the downstream of shock tube at a specified distance. In the present world, blast wave mitigation is very important to be produced as a defence system for military vehicles and commercial structures. An object is placed between the exit of the shock and wall for the calculation of blast load on a wall. Blast wave interacting with a circular object is placed at four different locations for the pressure ratio of 40 and 50, respectively, across the diaphragm. Numerical simulations are performed for blast wave which is produced inside a driver section by solving the unsteady, axi-symmetric Navier–Stokes equations using Advection Upstream Splitting Method with Third-Order Monotone Upstream Centred method for Conservation Law approach. It has been observed that the blast load on a wall decreases if the object is placed nearer to the shock tube exit and the blast load on a wall increases if the object is displaced towards the wall from the shock tube exit. The computed result demonstrates that when the pressure ratio in a shock tube rises, the maximum pressure on the wall also increases.

Keywords Shock tube · Blast wave · Computational fluid dynamics · AUSM scheme

1 Introduction

The objective of the current work is to reduce blast loading on a wall with the help of computational fluid dynamics. Over the last couple of decades, there has been increased interest in blast wave mitigation studies to protect buildings and structures. Satish et al. (2011) examine the pressure distribution at the various locations away

D. Ganapathi (✉) · A. Kundu
MNNIT Allahabad, Prayagraj, UP 211004, India
e-mail: ganapathidatti495@gmail.com

A. Kundu
e-mail: abhishekkunduumd@mnnit.ac.in

from the axis of the cannon. Shock waves, blast waves and vortices are captured by using computed results that are produced when a projectile is launched at supersonic speeds. Satish et al. (2011) compute pressure variations by patching a high pressure and high temperature in the driver portion and ambient temperature and pressure in the driven portion. He used the Spalart–Allmaras turbulence one equation model [1]. Kundu et al. [2] examine the interaction of a shock tube-generated vortex with an adjacent wall. The vortex ring interacts with a wall that is located at 0.3 m from the exit of a shock tube. A Kundu et al. [2] use the pressure in a 0.165 m long driver section which is 10 times more than that of a 1.2 m long driven portion of a shock tube [2]. The interaction of shock wave-generated vortices with flat and perforated plates is studied by Kontis et al. (2008). According to him, the flow interaction of reflected waves generates an area of high flow growth along the wall surface. Multiple pressure variations are generated on the wall as a result of this flow behaviour [3]. With a pressure ratio of 56:1 in a shock tube, Murugan et al. (2018) investigated that the three objects were affected by the blast wave (sphere, cone and circular disc). Murugan et al. (2018) generate the blast wave in a driver section having short in length of a shock tube using ANSYS Fluent software to solve the Euler equations. For the same frontal area, it was found that disc accelerates the blast wave more efficiently than the sphere and cone [4]. Kundu et al. (2017) examined high-pressure blast which is numerically generated from a driver portion having short in length of the shock tube and its influence on solid obstacles (sphere, cuboid and wedge) by solving the axi-symmetric Navier–Stokes equations. The governing equations are solved by assuming helium gas as driver section gas for two shock tube diaphragm pressure ratios of 13 and 56, respectively. Kundu et al. (2017) have observed that the blast wave was formed at $x = 3.741$ m from the diaphragm inside the driver portion of the shock tube for the pressure ratio of 13 and it occurs at the exit of a shock tube (6005 mm) for a pressure ratio of 56 in the diaphragm. Kundu et al. (2017) concluded that the unsteady blast loads acting on the cuboid are much stronger than compared to other objects. Yuta Sugiyama et al. (2017) examined the explosions in a straight tube having a square cross section for understanding the mitigation effect of water on blast waves. Yuta Sugiyama et al. (2017) utilized numerical simulations to understand the action of water which is filled within a square tube and modelled the experiments to know the impact of water on reducing the explosion due to blast [5]. Yuta Sugiyama et al. (2016) capture the blasts in an underground magazine model and it is built underground to minimize the impacts of blast waves. In this numerical method, the most important factor is to reduce the blast on the earth by transfer of the internal energy at the air–water interface. Yuta Sugiyama et al. (2016) have concluded that in the condition of water inside the magazine model, the exit impulse and pressure are predicted and well decreased, since high-pressure gas propels the blast wave at the exit [6]. Inderpal Singh Sandhu et al. (2016) reported in the literature that to reduce the shock, they studied various granular and porous materials using shock tubes. Inderpal Singh Sandhu et al. (2016) investigate the creation of blast wave in the lab, which is a shock tube with a high-pressure-driver portion and a low-pressure-driven section separated by a metal diaphragm. The length of the driver section is adjusted to produce the blast within a shock tube [7]. In this current study, we need to examine

the pressure distribution on the wall which is placed at 1 m downstream from the shock tube exit. The blast load is produced in the shock tube by using two diaphragm pressure ratios of 40 and 50, respectively. An object is kept at four different positions between the shock tube exit and wall to see the pressure variation on the wall.

2 Numerical Methodology

Figure 1 depicts the computational domain of a shock tube with a wall separated by the atmosphere [2]. Figure 2 depicts the computational domain of the shock tube driver and driven portions, as well as the location of the circular object from the exit of the shock tube [4]. This circular object having a diameter of 64 mm is placed in four different locations at a distance of $5D$, $6D$, $7D$ and $8D$ from the downstream exit of the shock tube, respectively, where D indicates the shock tube diameter. The shock tube diameter (D) is 0.164 m. The shock tube is 1.365 m long such that 0.165 m long driver portion and 1.2 m long driven portion. The wall is placed at 1 m downstream of the shock tube exit. The domain is widened to 0.3 m long in the perpendicular direction to the axis of the shock tube. At the starting, the driven portion and the remaining domain other than the shock tube are held at pressure and temperature of 1 bar and 300 K, respectively. The working fluid throughout the entire domain is air, which is considered as an ideal gas. The pressure and temperature of the driver portion patches are extremely high for two separate conditions. It has been simulated for two diaphragm pressure ratios of 40 and 50 in the shock tube. The temperature and density of the driver section were calculated from the Rankine-Hugoniot conditions. In the present study, the pressure variations on the wall due to blast from the shock tube have been simulated by utilizing the commercial Fluent. The Advection Upstream Splitting Method (AUSM) for flux calculation and the Third-Order Monotone Upstream Centred Scheme for Conservation Law method for flow discretizations are used to solve the transient, axi-symmetric, Navier–Stokes equations numerically. Because of high compressibility effects, a density-based solution was chosen for this simulation, and standard K-omega two equation turbulence models were chosen which are suitable for boundary layer separation-related problems. The numerical simulations are carried out for half of the shock tube, with the flow field considered to be axi-symmetric. The initial conditions for the two cases used in the simulations are shown in Table 1.

The meshing was done for the computational domain. The grid has been generally fine and is of high quality in which the accuracy and stability of simulated solutions majorly depend on grid generation. Various tools are useful for developing a good grid which was provided by the ANSYS mesh file inbuilt. In this study, quadrilateral mesh was used which was patch confirming and the number of elements was to be 341,652. And also the quality of the mesh, aspect ratio, orthogonal quality and skewness are to be checked whether they are in the acceptable range.

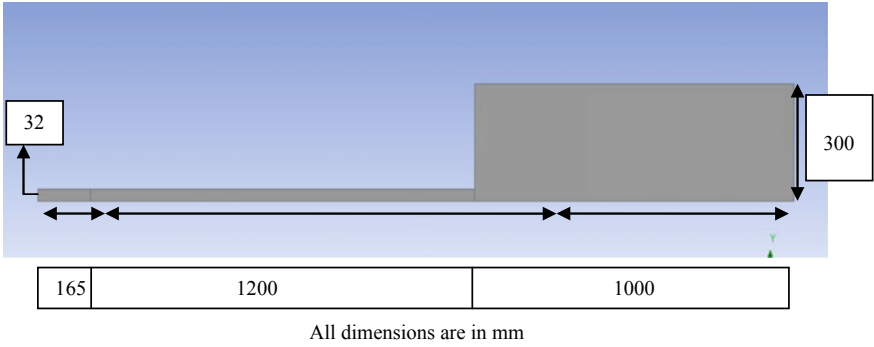


Fig. 1 Computational domain

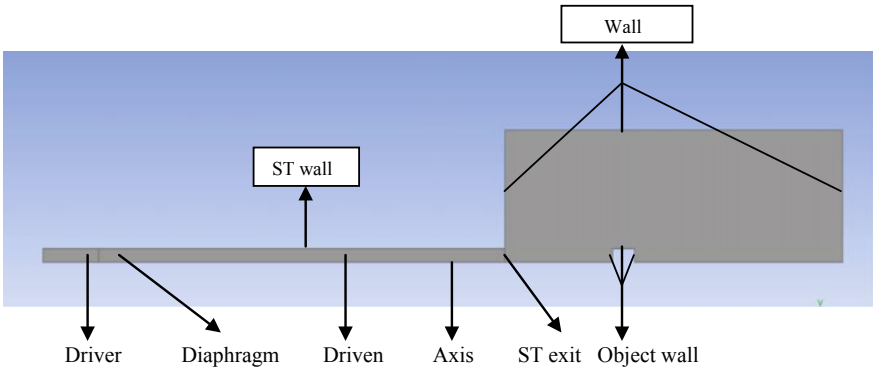


Fig. 2 Boundary conditions and nomenclature of the computational domain

Table 1 The initial conditions for the current simulation

Cases	P_1 (atm)	T_1 (K)	ρ_1 (Kg/m ³)	P_2 (atm)	T_2 (K)	ρ_2 (Kg/m ³)
Case 1	1	300	1.17	40	2280	6.17
Case 2	1	300	1.17	50	2800	6.29

3 Results and Discussion

The purpose of this research is to investigate the pressure variation along the axis of the shock tube and on a wall. Despite the fact that the blast wave spreads spherically outward and gains intensity along the axis due to its planar nature and it decreases away from the shock tube axis. The wall pressure maintains ambient before the blast from the shock tube hits the wall. When a blast reaches the wall, the wall pressure rises to a maximum and then falls to ambient pressure when the blast is reflected by the wall. The pressure was measured at $X = 2.365$ m and $Y = 0$ m for the comparison

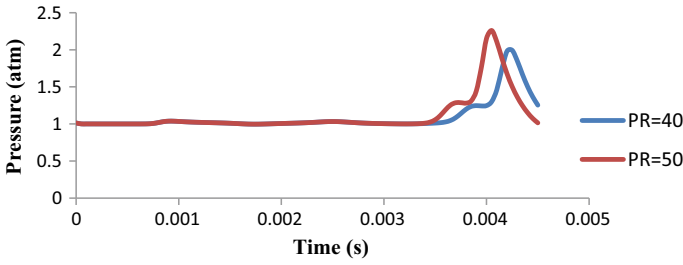


Fig. 3 Pressure variations on the wall

as origin was taken at the inlet of the shock tube. It has been observed that raising the pressure ratio causes an increase in the peak pressure on the wall as demonstrated in Fig. 3. It also demonstrates that when the pressure ratio increases, the time taken for the pressure to attain peak value decreases.

The pressure on the wall peaks at $t = 4.25$ ms for a pressure ratio of 40 and $t = 4.05$ ms for a pressure ratio of 50. Figure 4 depicts the pressure histories generated at five distinct positions for a pressure ratio of 40, where $x = 0$ indicates the inlet of the shock tube. It has been observed that similar to blast explosions, a rapid pressure surge is followed by an exponential decline. The interaction of blast waves reflected from the shock tube back end with incident shock waves leads to a continual drop in pressure along the shock tube downstream.

Figure 5 depicts the distribution of pressure along the vertical wall when the blast wave interacts with it. Evaluation of pressure was done on a vertical line at $(X = 2365$ mm, $Y = 0$ mm) to $(X = 2365$ mm, $Y = 300$ mm) at the time of $t = 4.05$ ms for the diaphragm pressure ratio of 50 without and with an object placed at different locations. The pressure value is decreasing along the wall due to the absence of lifting of primary vortices and reflection of shock at that specific time. From the result, it is also clear that the blast load on the wall decreases when the object is placed nearer to the exit of the shock tube and it increases when the object is placed towards the wall. It will help to design a blast wave mitigating structure.

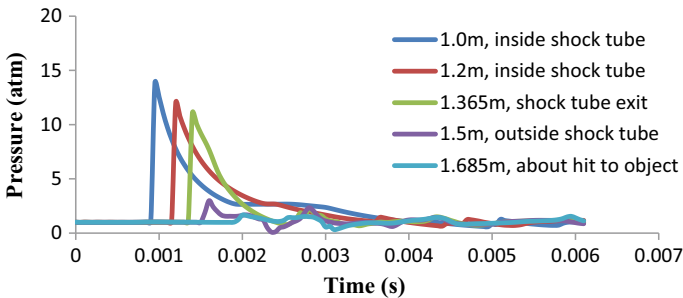


Fig. 4 Unsteady variations of the pressure due to blast it before hitting the object for the pressure ratio of 40 in the shock tube

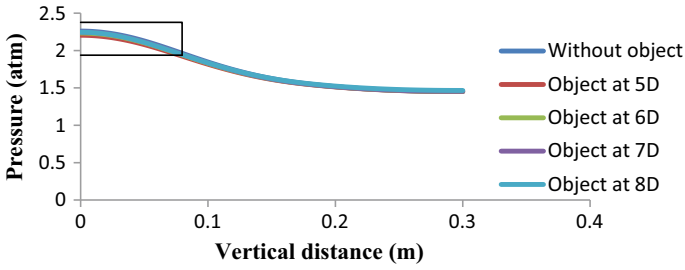


Fig. 5 Pressure variations along the vertical wall

Blast load has been calculated on the wall after interaction with the object by using average pressure for a diaphragm pressure ratio of 40 and 50, respectively (Fig. 6). Figure 7 shows how the peak load fluctuates on the wall as the pressure ratio rises. From the figure, it is clear that initially blast load is zero before it strikes the wall and then it reaches a peak value when it strikes the wall and then reduces due to its reflection of it from the wall.

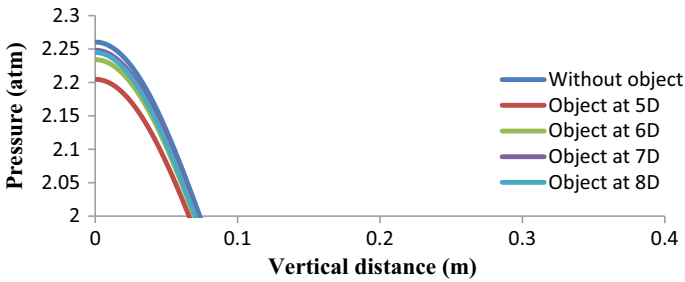


Fig. 6 Zoom view of box shown in Fig. 5

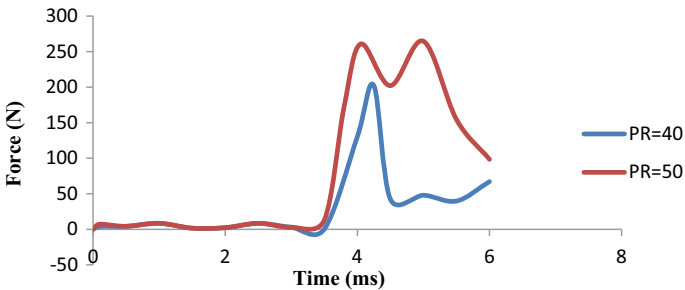


Fig. 7 Instantaneous load on the wall when blast directly interacts with the wall

4 Conclusions

By using the commercial CFD software ANSYS Fluent, the blast wave interacting with the wall owing to pressure explosion from the shock tube was simulated.

- The unsteady, axi-symmetric, compressible Navier–Stokes equations were solved along the energy equation and equation of state, and the unsteady flow is solved with second-order implicit method.
- The Advection Upstream Splitting Method (AUSM) is used for flux splitting with the Third-Order Monotone Upstream Centred Scheme for Conservation Laws (MUSCL) method is used to solve the convective terms.
- The problem has been simulated for five different cases for pressure ratios of 40 and 50, respectively, in the shock tube to investigate the blast load acting on the wall due to pressure distribution.
- The results show that the blast load decreases if the object is placed nearer to the downstream of the shock tube exit and it increases when the object is located towards the wall from the shock tube exit.
- This study will be helpful to design a blast wave mitigating structure. The future scope lies to study a different shape of the object placed at various locations from the shock tube exit.

References

1. Xavier S (2011) Numerical analysis of gun barrel pressure blast using dynamic mesh adaption
2. Kundu A, De S, Thangadurai M, Dora CL, Das D (2016) Numerical visualization of shock tube-generated vortex–wall interaction using a fifth-order upwind scheme. *J Visualization* 19(4):667–678
3. Kontis K, An R, Zare-Behtash H, Kounadis D (2008) Head-on collision of shock wave induced vortices with solid and perforated walls. *Phys Fluids* 20(1):016104
4. Dey S, Murugan T, Chatterjee D (2018) Numerical visualization of blast wave interacting with objects. *J Appl Fluid Mech* 11(5):1201–1206
5. Sugiyama Y, Homae T, Wakabayashi K, Matsumura T, Nakayama Y (2017) Numerical study on the mitigation effect of water in the immediate vicinity of a high explosive on the blast wave. *Int J Multiph Flow* 99:467–473
6. Sugiyama Y, Tanaka T, Matsuo A, Homae T, Wakabayashi K, Matsumura T, Nakayama Y (2016) Numerical simulation of blast wave mitigation achieved by water inside a subsurface magazine model. *J Loss Prev Process Ind* 43:521–528
7. Sandhu I, Sharma A, Prince Singh M, Kumari R, Alegaonkar P, Saroha D (2017) Study of blast wave pressure modification through rubber foam. *Procedia Eng* 173:570–576
8. Murugan T, De S, Sreevatsa A, Dutta S (2016) Numerical simulation of a compressible vortex–wall interaction. *Shock Waves* 26(3):311–326
9. Kontis K, An R, Edwards JA (2006) Compressible vortex-ring interaction studies with a number of generic body configurations. *AIAA J* 44(12):2962–2978
10. Le J (1999) Numerical simulation of shock (blast) wave interaction with bodies. *Commun Nonlinear Sci Numer Simul* 4(1):1–7

11. Chandra N, Ganpule S, Kleinschmit NN, Feng R, Holmberg AD, Sundaramurthy A, Selvan V, Alai A (2012) Evolution of blast wave profiles in simulated air blasts: experiment and computational modeling. *Shock Waves* 22(5):403–415
12. Rupal H, Sharma J, Arora R, Sandhu I (2018) Validation of CFD modeling and simulation of a shock tube
13. Ansys Fluent, Inc.: Fluent 16.0 user's guide

The Influence of Notch-Width Ratio on Mechanical and Electromagnetic Radiation Parameters During Tensile Deformation in FCC Metals



Anu Anand and Rajeev Kumar

Abstract This paper deals with experimental investigations on the influence of notch-width ratio on the mechanical and electromagnetic radiation (EMR) parameters during tensile deformation in commercial aluminum and cold-rolled high yield strength copper. Mechanical parameters such as maximum stress at crack instability, plastic zone radius, stress intensity factor and elastic strain energy release rate, and EMR parameters such as maximum EMR amplitude, average EMR energy release rate and maximum dominant EMR frequency were chosen for analysis. Correlations between the mechanical and EMR parameters were established. The EMR energy release rate displays an excellent relationship with the elastic strain energy release rate, which may be a tool for determining the fracture toughness of the metals. The EMR parameters also exhibited an excellent correlation with the plastic zone radius. The EMR energy release rate has also displayed a smooth fit with the ratio of the product of lattice period and stress at crack tip instability to the stacking fault energy. The implications of our results for evaluating fracture toughness, crack growth monitoring, and dislocation dynamics during plastic deformation are discussed.

Keywords Semi-circular notches · Dislocation · EMR

1 Introduction

Plastic deformation and crack propagation are predominantly dependent on the material's properties and parameters. Moreover, the plastic deformation phenomena are interlinked with the dynamics of dislocations. Therefore, the mechanism of plastic deformation, initiation of cracks, and its atomic level study are crucial aspects of

A. Anand (✉) · R. Kumar

Department of Mechanical Engineering, Birla Institute of Technology, Mesra, Ranchi 835215, India

e-mail: anuanandynr@gmail.com

R. Kumar

e-mail: rajeevkumar@bitmesra.ac.in

materials research. In this context, EMR emission has emerged as a frontier research area [1, 2]. Misra [3] was the first to discover the EMR emission phenomenon when the metallic materials undergo plastic deformation and fracture. As a result, investigations of EMR emissions have gained impetus, and his research group and other researchers have explored this for various metals and alloys [4–16].

Misra [17] proposed a physical model based on the dislocation–electron interaction mechanism. Another model suggested by Misra and co-workers [18–20] is based on edge dislocations in the area of the plastic zone adjacent to the tip of the crack, generating electric line dipoles. The vibration of electric line dipoles is responsible for EMR emission. They propose how EMR emission is affected by Peierls stress at the yielding of metals. Kothari and co-workers [21, 22] have modified the model proposed by Misra and co-workers. Peierls stress and parameters of strain hardening were introduced in their model. The theoretical results were compared with experimental results and were found to be in good agreement. Thus, the model becomes valid for the entire plastic region. Sharma and co-workers [23] have presented extensive literature research for a variety of materials.

From the preceding, it can be seen that no work has been reported in aluminium and copper on the effect of notch-width ratio with double semi-circular notches on mechanical and EMR parameters. Aluminium and copper are versatile materials, widely employed in domestic as well as in industrial applications. Correlations were established among the mechanical and EMR parameters. The average EMR energy release rate was also related to the ratio of lattice period product and stress at crack tip instability to the stacking fault energy (a cross-slip energy function).

2 Experimental

2.1 Materials and Methods

The chemical constituents of the commercial aluminium and commercial copper specimens are displayed in Tables 1a and 1b. The aluminium specimens of dimension 110 mm · 14 mm · 1.0 mm, and copper samples with dimension 100 mm · 18 mm · 1.5 mm were cut out from a more extended sheet with a mini grinder/cutter machine. The samples were provided with two equal semi-circular notches at the middle of the two sides to confirm open mode fracture during tensile testing. For the study of EMR emission parameters during tensile deformation, dual semi-circular notches ($2a$), each length ' a ' was imparted at the midpoint of the specimen with the help of a circular file. The value of ' a ' was selected as 1, 2, 3, 4 and 5 mm, respectively. The width of the sample (w) was kept as 14 mm in aluminium and 18 mm in copper samples. The samples have been cut out through the longitudinal axis of the rolled sheets. Figures 1a and 1b demonstrate the aluminium and copper specimen's configuration.

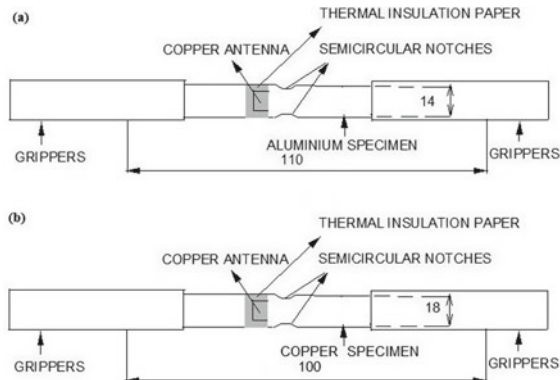
Table 1a The constituents of the commercial aluminium specimen (wt.%)

Fe	Si	Mn	Cu	Ti	V	Zn	Mg	Al
0.35	0.13	0.02	0.01	0.01	0.01	0.002	0.001	99.47

Table 1b The constituents of the commercial copper specimen (wt.%)

Fe	Pb	Ni	Zn	Co	Sn	Mn	P	Al	Cu
0.07	0.06	0.05	0.05	0.04	0.03	0.003	0.002	0.002	99.7

Fig. 1 Specimen configuration and setup for experimentation for (a) Al and (b) Cu



2.2 Instrumentation

Tensile testing was carried out on an H100 KT Tinius Olsen testing machine. Tensile samples deformed at an initial strain rate of 0.025 s^{-1} . Copper chips paired with $10 \cdot 10 \cdot 0.2 \text{ mm}$ dimensions were glued on a thermal insulation sheet and set on both the specimen faces with a suitable binder to function as an antenna for capturing EMR signals. Both copper chips were soldered with an electrical cable. The oscilloscope's voltage measuring probe was connected to electrical wires emanating from both the copper chips. One end was linked to the antenna in the oscilloscope measuring probe, while the other was grounded. The oscilloscope operated in single-shot mode. A Tektronix (200 MHz, 1GS/s) digital phosphor oscilloscope DPO2022B was employed. The 400 ns/division time scale and 20 mV/division voltage scale were set on the oscilloscope to capture the EMR signals in the MHz range. The Fast Fourier Transform capability of the software was employed to change the signals of the time-domain of the EMR to a frequency domain. A USB drive was used for data storage from the oscilloscope, further analyzed using MATLAB (r2016a) software. An electromagnetic shield (three layers of 0.5 mm silicon and 0.3 mm copper sheets) was constructed to eliminate/minimize electromagnetic and external noise influence. The shield was applied to encircle the sample entirely apart from the two axial ends.

2.3 Parameters for Evolution

The mechanical parameters, maximum stress at the crack tip instability, S_{uc} , plastic zone radius r_p , stress intensity factor, K_I , elastic strain energy release rate, G_I and $(b \cdot S_{uc})/U_f$, were calculated. 'b' is the lattice period, and U_f is the stacking fault energy. The EMR parameters, maximum EMR amplitude, V_{pmax} , average electromagnetic energy release rate, A , and maximum dominant energy frequency f were measured. The stress intensity factor K_I , for a double semi-circular notched specimen was calculated using the following equation [24].

$$K_I/\sigma\sqrt{\pi a} = 1.122 \left[0.933 + 0.180 \left(\frac{2a}{w} \right) - 1.060 \left(\frac{2a}{w} \right)^2 + 1.710 \left(\frac{2a}{w} \right)^3 \right] \quad (1)$$

Here σ is the maximum value of applied tensile stress at the crack tip instability, and S_{uc} . 'a' represents the notch radius. The plastic zone radius is estimated as [25].

$$r_p = \frac{1}{2\pi} \left(\frac{K_I}{\sigma_{ys}} \right)^2 \quad (2)$$

where σ_{ys} is the yield stress of the specimen G_I . The elastic strain energy release rate for the condition of plane stress is calculated as [26].

$$G_I = K_I^2/E \quad (3)$$

E (Young's Modulus of elasticity) value for aluminium and copper is considered 69 and 129.6 GPa, respectively.

2.4 Measurement of EMR Parameters

Power is deployed for time-domain signals, which are periodic in nature. For signals of the time-domain, which are non-periodic, energy is applied. The magnitude spectrum's square value determines the signal's energy spectrum [27]. Therefore, to measure the average EMR energy release rate, A , the plot of EMR signal V_p vs time (t) was transformed into V_p^2 vs t graph with the help of MATLAB (r2016a) software. The maximum dominant EMR frequency, f , was recorded from the graphs V_p vs t . 'A' the average EMR energy release rate is estimated [9].

$$A = \int \frac{V_p^2 dt}{\Delta t} \quad (4)$$

$$\frac{\text{Area below the } V_p^2 - \text{time, curve portion}}{\Delta t} \tag{5}$$

3 Results and Discussions

Table 2a shows the effect of notch-width ratios on calculated mechanical parameters and measured EMR parameters in aluminium and Table 2b in copper. Throughout the plastic deformation, the signals were oscillatory in nature for both aluminium and copper specimens. Figures 2a and 2b are an imprint of EMR signals of the aluminium sample at notch-width ratio = 0.43 and the copper sample at notch-width ratio = 0.71, shown as representatives.

3.1 Correlation Between Notch-Width Ratio and Mechanical and EMR Parameters

The material’s plane stress fracture toughness depends on both metallurgical factors and specimen geometry [26]. The influences of mechanical parameters, such as the plastic zone radius and elastic strain energy release rate on notch-width ratios, are shown in graphical forms in aluminium and copper in Figs. 3a, b, 5a, b, respectively. With an increasing notch-width ratio, there is an increase in the stress level (Tables 2a and 2b). Thus, the notch-width ratio is an essential factor to study the fracture behavior

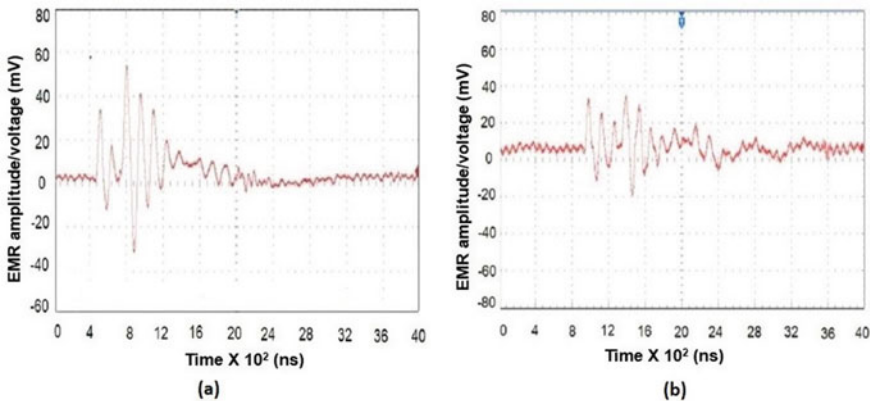


Fig. 2 An imprint of EMR signals of **a** aluminium specimen at notch-width ratio = 0.43 and **b** of copper specimen at notch-width ratio = 0.71

of metals. Therefore, the specimen with varying notch-length ‘2a’ to specimen width ratio ‘w’ was selected for investigations.

The plastic zone is formed in front of the crack’s tip with load increment [18]. The plastic zone extension at the crack’s tip essentially depends on factors, such as the material’s yield stress, loading condition, and the size of the crack [29], which increases with increasing notch-width ratio leading to an increase in the value of

Table 2a Notch-width ratio effect on mechanical and EMR parameters in aluminium

2a/w	S _{uc}	r _P (mm)	K _I (MPa·m ^{1/2})	G _I · 10 ⁻³ (MPa·m)	(b · S _{uc})/ U _f	V _{pmax} (mV)	A · 10 ⁻⁶ (V ² s · s ⁻¹)	f (Mhz)
0.14	29.2	1.68	1.84	0.05	0.059	24	6.8	7.6
0.29	35.8	3.36	3.17	0.15	0.072	32	9.2	7.4
0.43	48.3	7.46	5.31	0.41	0.098	52	16.4	6.6
0.57	57.0	11.29	7.66	0.85	0.115	56	24.7	5.0
0.71	71.7	12.34	12.14	2.14	0.145	68	32.4	4.6

Table 2b Notch-width ratio effect on mechanical and EMR parameters in copper

2a/w	S _{uc}	r _P (mm)	K _I (MPa·m ^{1/2})	G _I · 10 ⁻³ (MPa·m)	(b · S _{uc})/ U _f	V _{pmax} (mV)	A · 10 ⁻⁶ (V ² s · s ⁻¹)	f (Mhz)
0.11	330	0.78	20.79	3.34	1.48	22	6.8	7.7
0.22	338	1.62	30.05	6.97	1.52	28	11.5	7.6
0.33	359	2.35	39.04	11.76	1.61	30	14.2	6.6
0.44	429	3.22	54.69	23.07	1.93	32	19.68	5.5
0.55	461	4.16	68.64	36.35	2.07	34	20.72	4.8

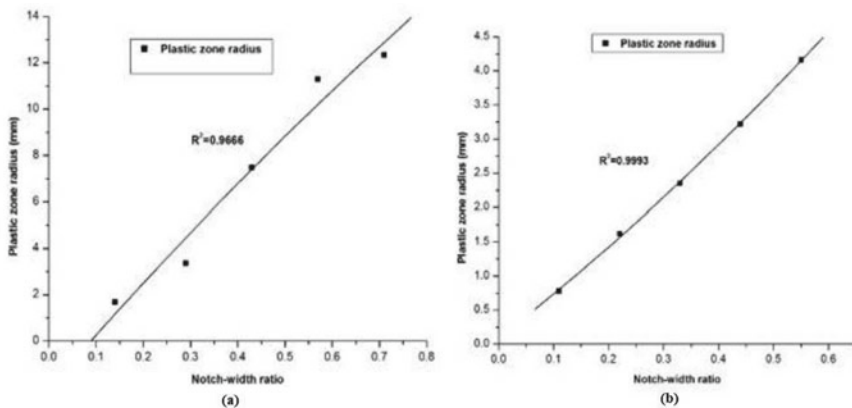


Fig. 3 Influence of plastic zone radius with notch-width ratios **a** Al and **b** Cu

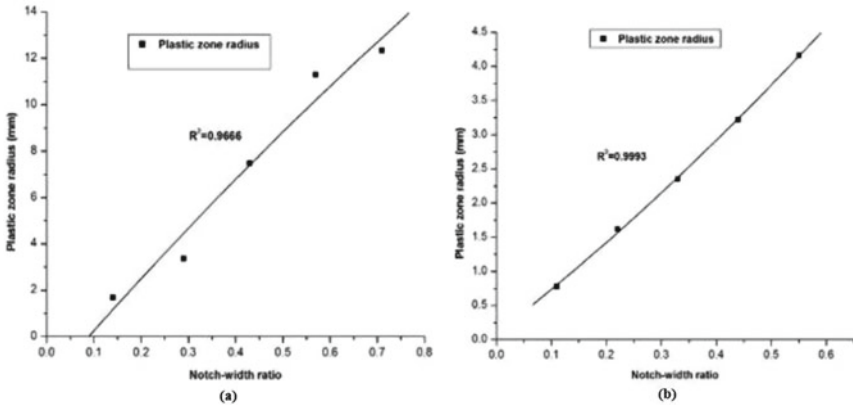


Fig. 4 Influence of elastic strain energy release rate with notch-width ratios for **a** Al and **b** Cu

plastic zone size (Fig. 3a, b). The stress intensity factor is a valuable concept for characterizing the stress field near the crack tip. It is an integral property of the material defined for cracks or flaws. A material can resist the fracture up to a specific critical value, after which failure will occur. The elastic strain energy release rate, G_I , depends on the stress intensity factor K_I (Eq. 3). Hence, the fracture toughness measurement is possible from the critical stress intensity or the elastic strain energy release rate. Therefore, with an increasing notch-width ratio, the elastic strain energy release rate also shows an increasing trend (Fig. 5a, b).

The influences of the maximum amplitude, average EMR energy release rate and Elastic strain energy release rate on the notch-width ratio in aluminium and copper have been indicated in graphical forms (Figs. 6a, b, 7a, b, 5a, b). Both fracture toughness and EMR emissions are energy phenomena; it becomes relevant that EMR emissions are also influenced by specimen geometry ($2a/w$).

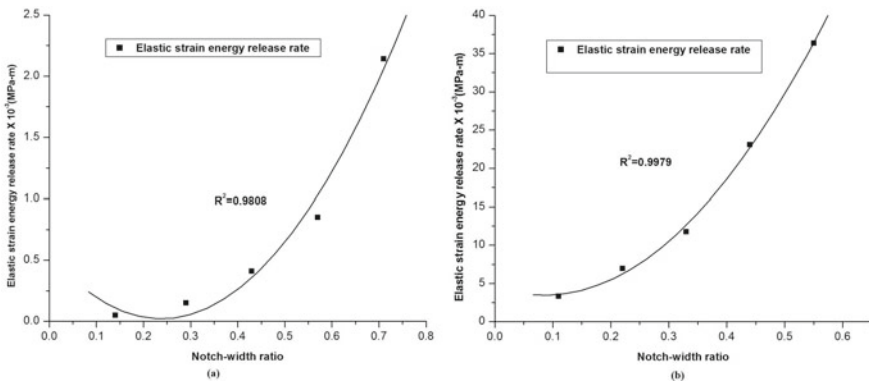


Fig. 5 Influence of Elastic strain energy release rate with notch-width ratios for **a** Al and **b** Cu

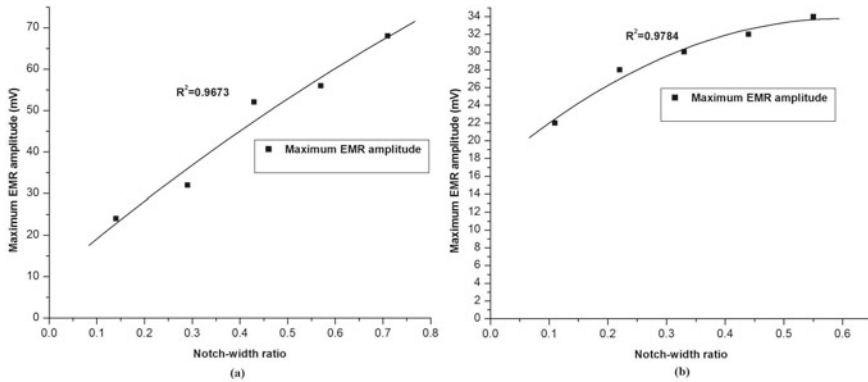


Fig. 6 Influence of Maximum EMR amplitude with notch-width ratios **a** Al and **b** Cu

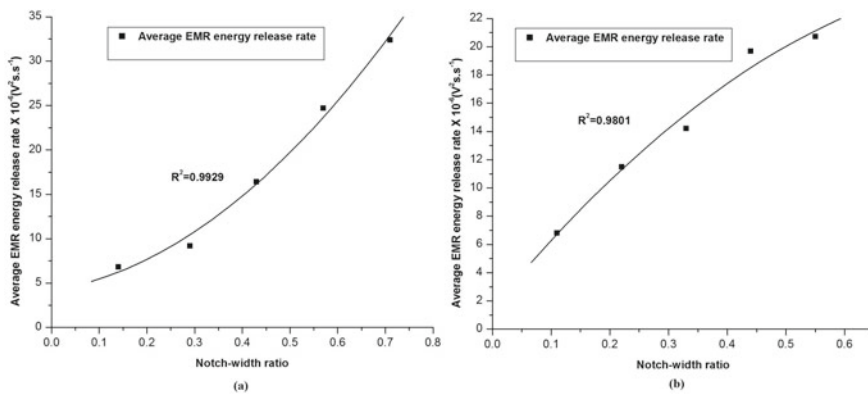


Fig. 7 Influence of Average EMR energy release rate with notch-width ratios **a** Al and **b** Cu

3.2 Correlations Between EMR Parameters and the Plastic Zone Radius in Aluminium and Copper

The influences of EMR parameters, maximum amplitude, average EMR energy release rate and maximum dominant EMR frequency with the plastic zone radius in aluminium and copper have been indicated in graphical forms in Figs. 8a, b, 9a, b, 10a, b, respectively. The smooth relationship between EMR parameters, EMR amplitude and EMR energy release with the plastic zone radius (Figs. 8a, b and 9a, b) proposes a novel method to ascertain the crack growth behavior of metallic materials. With an increment in loading conditions, the increase in plastic zone size created in advance of the crack’s tip affects EMR emissions. Thus, the EMR amplitude and EMR energy release rate are directly affected, unlike EMR frequency. The theoretical model developed [21] suggests that when the metallic materials deform plastically

under progressive loading, edge dislocations inside the plastic zone, time-varying bending leads to the formation of accelerated electric line dipoles. This mechanism is responsible for inducing the observed EMR emissions.

Furthermore, it is a fact that the EMR amplitude displays an inverse relationship with the frequency. This fact is well supported where the maximum dominant EMR frequency decreases with the notch-width ratio (Table 2a, b) and the plastic zone radius (Fig. 10a, b). Moreover, it confirms the findings of Singh and co-workers [16].

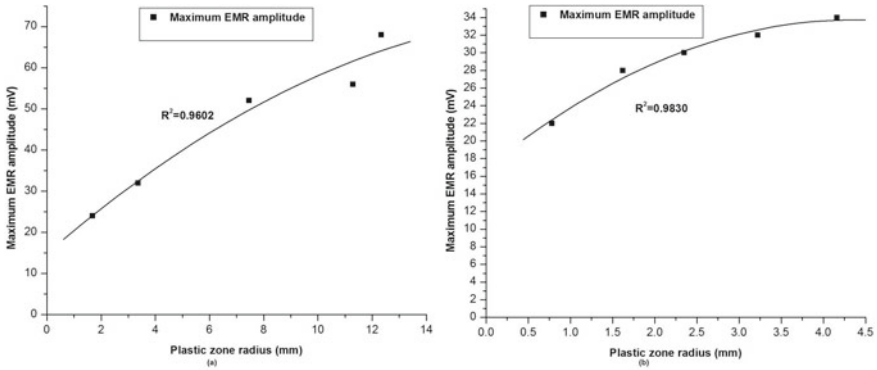


Fig. 8 Influence of maximum EMR amplitude with plastic zone radius for a Al and b Cu

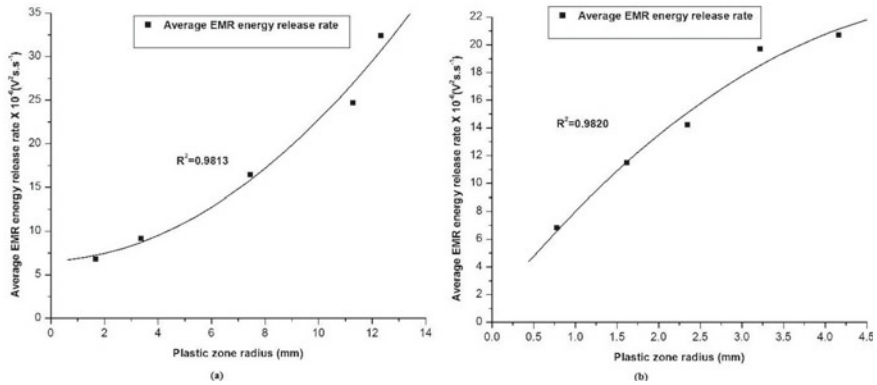


Fig. 9 Influence of average EMR energy release rate with plastic zone radius a Al and b Cu

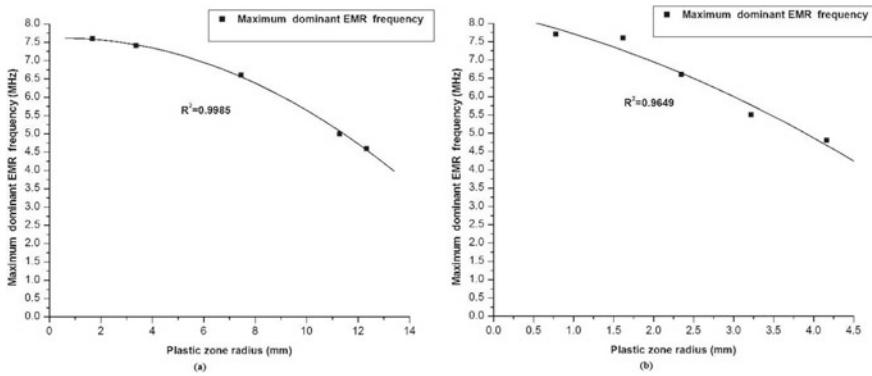


Fig. 10 Influence of the maximum dominant frequency with plastic zone radius for **a** Al and **b** Cu

3.3 Correlation Between Average EMR Energy Release Rate and Elastic Strain Energy Release Rate

The average EMR energy release rate relationship with the elastic strain energy release rate in aluminium and copper is indicated in Fig. 11a, b, respectively. Furthermore, there is an excellent correlation between the average EMR energy release rate, A , and the elastic strain energy release rate, G_I , confirmed by Singh and co-workers [14]. It is already known [17–20] that the new dislocation generation and their multiplications occur with progressive deformation. In this process, the edge dislocations are gradually infused with energy. A part of this gained energy attained by the edge dislocations disperses as EMR emission energy. For the movement of edge dislocations, energy is provided in the form of strain energy. Thus, the EMR energy release rate measurement may prove a boon for estimating fracture toughness, a fundamental property of metallic materials.

3.4 Correlation of Average Electromagnetic Release Rate with $(b \cdot S_{uc}) / U_f$ in Aluminium and Copper

The plot of electromagnetic release rate, A with $(b \cdot S_{uc}) / U_f$ exhibited a smooth parabolic behavior in aluminium and copper (Fig. 12a, b). The aluminium and copper stacking fault energy (SFE) values were taken as 0.2 J/m^2 and 0.08 J/m^2 , respectively [14]. As mentioned by Escaig [28], the cross-slip energy varies with σ / U_f . This function can be computed numerically. Asymptotic forms give analytical formulas acceptable for the conditions, $(b \cdot \sigma) / U_f$ greater than 1 or $(b \cdot \sigma) / U_f$ less than 1. Here $\sigma = S_{uc}$, b is the lattice parameter, and U_f is the stacking fault energy in our investigation. High SFE materials (like aluminium of SFE 0.2 J/m^2 in our present investigations) deform by the glide of complete dislocations [30]. The Frank-Read

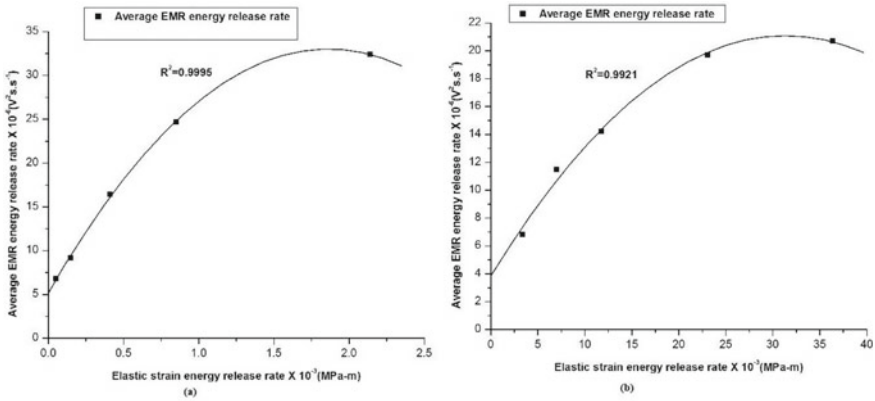


Fig. 11 Influence of average EMR energy release rate with elastic strain energy release rate for **a** Al and **b** Cu

sources and the stress concentrations lead to slip loop formation due to external stress. Gliding may cause these loops to widen and maybe even more substantial in crystals of pure metals (Cu and Al in our present study). Thus, it can be likely that the dipoles will be formed mainly through edge dislocations (widespread at the beginning of plastic deformation). Edge dislocations contribute to EMR emissions [5]. As previously stated, the vibration of electric line dipoles is responsible for EMR emission. Therefore, the energy generated in this process may be responsible for the EMR emissions observed. That is why the EMR parameter average EMR energy release rate and $(b \cdot S_{uc}) / U_f$ show an excellent correlation (Fig. 12a, b). The direct correlation between the above parameters may help assess the dislocation dynamics during the deformation of metals.

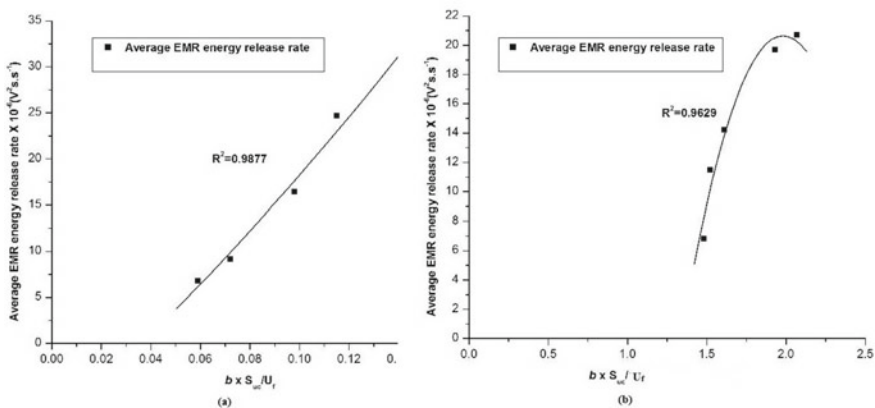


Fig. 12 Influence of $(b \cdot S_{uc}) / U_f$ with avg EMR energy release rate for **a** Al and **b** Cu

4 Conclusions

Excellent correlations of notch-width ratio with mechanical and EMR parameters have been observed. The EMR emissions emitted during tensile testing always exhibited oscillatory nature irrespective of the notch-width ratios and strain values obtained. The value of the maximum EMR amplitude increases with the plastic zone radius. The behavior proposes that the pinning barriers increase with the plastic zone radius with new Frank Reed sources. The excellent correlation of EMR emissions parameters with the plastic zone radius will help develop a new tool for monitoring crack growth. The direct parabolic correlation of the EMR energy release rate with the elastic strain energy release rate may turn out a boon for estimating fracture toughness, an essential characteristic of metallic materials. The EMR energy release rate exhibits an excellent fit with the ratio of the product of lattice parameter and maximum stress at crack instability to the stacking fault energy of the material. These findings may help to assess the dislocation dynamics during the plastic deformation of metals.

References

1. Courtney TH (2005) Mechanical behavior of materials, 2nd edn. Waveland Press, USA
2. Sause MGR (2016) In situ monitoring of fiber-reinforced composites. Springer series in material science
3. Misra A (1975) Electromagnetic effects at metallic fracture. *Nature* 254(5496):133–134
4. Jagasivamani V, Iyer K (1988) Electromagnetic emission during the fracture of heat-treated spring steel. *Mater Lett* 6(11–12):418–422
5. Misra A, Kumar A (2004) Some basic aspects of electromagnetic radiation during crack propagation in metals. *Int J Fract* 127(4):387–401
6. Srilakshmi B, Misra A (2005) Electromagnetic radiation during opening and shearing modes of fracture in commercially pure aluminium at elevated temperature. *Mater Sci Eng A* 404(1–2):99–107
7. Srilakshmi B, Misra A (2005) Secondary electromagnetic radiation during plastic deformation and crack propagation in uncoated and tin-coated plain-carbon steel. *J Mater Sci* 40(23):6079–6086
8. Srilakshmi B, Misra A (2005) Effects of some fracture mechanics parameters on the emission of electromagnetic radiation from commercially pure aluminium. *Manuf Technol Res-Int J* 1(2):97–104
9. Kumar R, Misra A (2006) Effect of processing parameters on the electromagnetic radiation emission during plastic deformation and crack propagation in copper-zinc alloys. *J Zhejiang Univ-Sci A* 7(11):1800–1809
10. Kumar R, Misra A (2007) Some basic aspects of electromagnetic radiation emission during plastic deformation and crack propagation in Cu–Zn alloys. *Mater Sci Eng A* 45:203–210
11. Chauhan VS, Misra A (2008) Effects of strain rate and elevated temperature on electromagnetic radiation emission during plastic deformation and crack propagation in ASTM B 265 grade 2 titanium sheets. *J Mater Sci* 43(16):5634–5643
12. Chauhan VS, Misra A (2010) Electromagnetic radiation during plastic deformation under unrestricted quasi- static compression in metals and alloys. *Int J Mater Res* 101(7):857–864
13. Chauhan VS, Misra A (2011) Assessment of grain size and lattice parameters of titanium alloy through electromagnetic emission technique. *Int J Microstruct Mater Prop* 6(6):486–506

14. Singh R, Lal SP, Misra A (2014) Variation in electromagnetic radiation during plastic deformation under tension and compression of metals. *Appl Phys A* 117(3):1203–1215
15. Singh R, Lal SP, Misra A (2015) Correlation of plastic deformation induced intermittent electromagnetic radiation characteristics with mechanical properties of Cu-Ni Alloys. *Int J Mater Res* 106:137–150
16. Singh R, Lal SP, Misra A (2019) Effect of notch-depth ratio on intermittent electromagnetic radiation from Cu–Ni alloy under tension. *Mater Test* 61(9):885–893
17. Misra A (1978) A physical model for the stress-induced electromagnetic effect in metals. *Appl Phys* 16(2):195–199
18. Misra A, Prasad RC, Chauhan VS, Srilakshmi B (2007) A theoretical model for the electromagnetic radiation emission during plastic deformation and crack propagation in metallic materials. *Int J Fract* 145(2):99–121
19. Misra A, Prasad R, Chauhan VS, Kumar R (2010) Effect of Peierls' stress on the electromagnetic radiation during yielding of metals. *Mech Mater* 42(5):505–521
20. Misra A, Singh R, Lal SP (2015) A physical model for the intermittent electromagnetic radiation during plastic deformation of metals. *Appl Phys A* 121(2):597–605
21. Kothari A, Chauhan VS, Misra A, Abbas S, Kumar R (2016) Effect of strain hardening on the electromagnetic radiation during plastic deformation of metals and alloys beyond yield point. *Nonlinear Dyn* 85(4):2687–2704
22. Kothari A, Chauhan VS, Kumar A, Kumar R, Vaish R, Abbas S (2016) Effect of Peierls stress and strain-hardening parameters on EMR emission in metals and alloys during progressive plastic deformation. *Int J Mater Res* 107(6):503–517
23. Sharma SK, Chauhan VS, Sinapius M (2021) A review on deformation-induced electromagnetic radiation detection: history and current status of the technique. *J Mater Sci* 56:4500–4551
24. Rooke DP, Baratta FI, Cartwright DJ (1981) Simple methods of determining stress intensity factors. *Eng Fract Mech* 397–426
25. Broek D (1982) *Elementary engineering fracture mechanics*, 3rd edn. Martinus Nijhoff Publishers, Springer, Netherlands
26. Hertzberg RW (1996) *Deformation and fracture mechanics of engineering materials*, 4th edn. Wiley, New York, pp 321–336
27. Haykin S, Van Veen B (2002) *Signals and systems*. Wiley, Singapore
28. Escaig B (1968) In: Rosenfield AR, Hahn GT, Bement Jr AL, Jaffee RI (eds) *Dislocation Dynamics*, Mc-Graw Hill, New York, pp 655–677
29. Caputo F, Lamanna G, Soprano A (2013) On the evaluation of the plastic zone size at the crack tip. *Eng Fract Mech* 103:162–173
30. Kroupa F (1966) Dislocation dipoles and dislocation loops. *J Phys Colloq* 27(C3):C3-154–C3-167

Comparison of In-Vitro Corrosion Behavior for Polished and WEDM Machined ZM21 Magnesium Alloy Used as Biodegradable Orthopedic Implants



Sarbjee Singh

Abstract Magnesium represents a very attractive material for biodegradable orthopedic implants because of its capability to resolve the problem of stress shielding, osteocompatibility in addition to its biodegradability. Yet, pure Mg does not have adequate strength when exposed to body fluids as it starts degrading at a higher rate. The aim of this research is to study the effect of wire electric discharge machining on Mg-based alloy ZM21 to increase its effectiveness by surface grain refinement as a tool to limit the initial corrosion rate in body fluids (modulus of elasticity remains unchanged). Comparison of microstructural, mechanical, and in-vitro corrosion changes along with biocompatibility of the polished and wire EDM machined samples of ZM21 Magnesium alloy were performed in this study. The alloy experiences a change in grain size in the recast layer formed on the machined surface which retards the initial degradation rate due to the occurrence of less number of high energy grain boundaries. Also ensures the production of corrosion resistive Mn_2O_3 and Mn_3O_4 compounds on the newly formed surface with MgO_2 as the base.

Keywords ZM21 Mg alloy · Biodegradability · Orthopedic implant · WEDM · Corrosion rate · SBF

1 Introduction

Biodegradable implants, a new world-shattering concept, are shaping the future design for orthopedic implants [1]. A perfect implant must have adequate mechanical strength, biocompatibility and degradation rate, which must be in comparison with the curative time of bone tissues [2]. Among all the metals, magnesium is preferred to be the most promising biodegradable metal because of its low density in comparison to human bone (for Mg: $1.78\text{--}2.0\text{ g/cm}^3$) [3], (for Human bone: $1.8\text{--}2.1\text{ g/cm}^3$) [4]. The value of Young's Modulus for Magnesium (35–45GPa) is also in close proximity to that of human bone (3–20 GPa) in comparison to other metallic orthopaedic

S. Singh (✉)
Punjab Engineering College Chandigarh, Chandigarh, India
e-mail: singh.sarbjee639@gmail.com

implant materials such as CoCrMo alloys (240 GPa), Ti alloys (105–125 GPa) and 316L stainless steel (200GPa) [5]. Although these bio-inert metallic implants are having satisfactory biocompatibility, mechanical strength and wear resistance but creating problems when used in fracture fixation. Firstly, it may occupy the drilled holes when used for long-term implantation and thus require secondary surgery for its removal [6]. Secondly, due to their high modulus of elasticity the stress shielding effects may cause peri-implant bone loss which eventually leads to fixation weakening and often requires secondary surgery. Third, in some cases if there are astonishing clinical hitches like impaired functioning, intense pain or swelling leads to revision surgery for implant removal [7]. Apart from this, bio-inert metal implants cause problems in computed tomography and X-ray images due to hardened beam and streaking artefacts [8].

As a result, a paradigm shift in research is focused on biodegradable metal implants which will eventually dissolve after several months of service, hence depleting residual implant mitigates the inflammation and cost associated with secondary surgery to remove metallic implants [9, 10]. Among all known metals, magnesium matrix orthopedic implants help in the formation of the new blood vessel and bone tissues [11, 12]. Mg or its alloys can lessen the stress shielding on the surrounding bone when used as an implant and would allow the progressive transfer of the mechanical load to the adjacent tissues. Mg being an important mineral for the human body is involved in various metabolic reactions and helps in new bone and tissue formation [13]. An adult normally requires 24–30 g of Mg for daily metabolic functions and 310–420 mg of daily magnesium reserve to maintain health. Therefore Mg-based orthopedic implants can be termed novel resorbable metallic implants. The Mg ions formed with dissociation of Mg matrix implants in the vicinity of implant bone matrix can be dispersed into the circulation system without affecting Mg ion level in blood serum [14].

The problem associated with magnesium is its faster degradation in the presence of body fluids [15] which affects the mechanical integrity during tissue recovery [16, 17]. Also the speedy degradation may lead to excessive hydrogen gas formation and release of OH^- ions in body fluids, which affects the homeostatic mechanisms and slow down the healing process [18, 19]. The controlled hydrogen gas evolution during degradation reactions of Mg implants with body fluids will act as a novel antioxidant to reduce senescence process induced oxidative stress during mesenchymal stem cell (MSC) expansion [20] and prevents bone loss in the osteoporosis group [21]. Therefore, an effective approach to control H_2 accumulation in the body is to retard the degradation of Mg implants in the human body [22, 23]. Also, hydroxide ions associated with rapid degradation of Mg alloy increase the local pH value above 7.8 which may lead to alkaline poisoning in the body. Although at a controlled degradation rate the in vivo pH value gets neutralized with time in the region adjacent to the Mg-based implants [24].

Researchers have suggested that calcium (Ca), zinc (Zn) and manganese (Mn) can be added to the Mg matrix as an alloying element to improve its properties to make it suitable for biomedical claims. As zinc is a vital element for the human body and is needed for many enzymatic activities [25]. Alloying of magnesium

matrix with zinc will not cause any serious issue as the excess amount of both gets excreted out through the urination route [26, 27]. Moreover, zinc also helps in new bone formation and allows bone resorption [28, 29]. Due to biocompatibility and osteo-conductivity calcium can also be used as an alloying element but produces chalk-like insoluble corrosion products that piled up rapidly and also make magnesium brittle by lowering failure strain [30]. Therefore, in this study specific interest is focused on Zn and Mn as an alloying element in Mg matrix implants as both improve their mechanical strength and grain structure along with their biocompatibility [31]. Zn concentration up to 3 wt% increases strength and act as a corrosion inhibitor, above this it will precipitate out and inhibits crack formation with reduced ductility[32]. Whereas Mn is effective for corrosion resistance in the case of pure magnesium[33]. In this study, ZM21 Mg alloy contains 2.0 wt% Zn and 1.0 wt% Mn in the Mg matrix. ZM21 alloy exhibits good formability which makes it a favorable material for biodegradable bone implants. Further, to achieve the geometrical accuracy required for medical devices and surface integrity to enhance the cell adherence for finest fitting, mechanical solidity and biocompatibility to lessen inflammatory disorders Wire Electrical Discharge Machining (WEDM) is highly recommendable [34–36]. However conventional machining operations such as CNC turning, milling and hole drilling may produce chatter, built up edges and cracks during implant fabrication causes inflammatory response [37]. With sudden heating and cooling of workpiece during wire EDM, surface modifications with newly formed recast layer favor the cell stickiness and tissue development for orthopedic implants [38, 39]. In this study, changes in corrosion behavior after WEDM machining in comparison to polished samples of ZM21 Mg alloy are investigated in the biological environment. Its biocompatibility and biodegradability in SBF (simulated body fluid) solution was estimated by the extent of material loss, linear polarization and Electrochemical Impedance Spectroscopy (EIS) study. Linear polarization and impedance studies are also used to estimate the degradation rate and corrosion shielding capability of Mg with its alloys. In view of this, the present work evaluates the degradation behavior of ZM21 Mg alloy before and after the machining in SBF for 7 days.

2 Materials and Methods

2.1 Alloy Preparation and Sample Processing

In the current study, Magnesium (99.9% purity) containing the alloying composition of 2wt% Zinc, and 1wt% Manganese was casted with a homogeneous structure. The obtained alloy, called as ZM21 Magnesium alloy, was sliced into a square cross-section with dimensions (10 mm × 10 mm) of 2 mm thickness. This square cross-section of ZM21 Magnesium alloy was abraded with SiC abrasive paper (800, 2000) and followed by manual polishing using alumina and diamond paste on velvet cloth to a mirror finish (with average roughness value Ra: 0.145 μm). Another ZM21

Magnesium alloy sample was machined with Wire—Electric Discharge Machining (CONCORD Wire EDM, Versa Cut 01) to cross-section of (10 mm × 10mm) of 2 mm thickness (With optimized Parameters, Ton: 128mu, TOff: 50mu, Peak Current: 220Amp., Peak Voltage:2 V, Water Pressure:1 kg/cm², Wire Feed:3 m/min, Wire Tension:10mu, Servo Voltage:20 V, Servo Feed: 2100mu, Brass Wire diameter:0.25 mm). Now both polished and Wire EDM machined samples were washed with Distilled water followed by incubator drying.

2.2 Simulated Body Fluid (SBF) Preparation

- All the bottles and wares should be rinsed using 1 N HCl solution and distilled water followed by drying in an incubator.
- Take one-liter capacity polyethylene bottle and add 500 ml deionized and distilled water to it.
- Start the magnetic Stirrer to stir the water contained in the bottle and add the chemicals one by one in order as mentioned in the given Table 1 (before the addition of another reagent make sure the former is completely dissolved).
- The solution temperature should be maintained at 36.5 °C and pH at 7.40 with continuous stirring and titrating 1 N- HCl solution.
- After the addition of all the reagents, add ion-exchanged and distilled water to make the total solution volume to one liter with shaking the bottle at 20 °C.
- Store the solution in the refrigerator at 5–10 °C and during storage if precipitation starts do not use this solution as an SBF solution.

Table 1 Chemicals for preparing SBF (pH 7.40, 1L) [40]

Sr. no	Chemical name	Chemical formula	Quantity
1	Sodium Chloride	(NaCl)	7.996 g
2	Sodium Bicarbonate	(NaHCO ₃)	0.350 g
3	Potassium Chloride	(KCl)	0.224 g
4	Dipotassium hydrogen phosphate trihydrate	(K ₂ HPO ₄ .3H ₂ O)	0.228 g
5	Magnesium Chloride hexahydrate	(MgCl ₂ .6H ₂ O)	0.305 g
6	Hydrochloric Acid	1 M-(HCl)	40 mL
(About 90% of total amount of HCl to be added)			
7	Calcium Chloride	(CaCl ₂)	0.278 g
8	Sodium Sulphate	(Na ₂ SO ₄)	0.071 g
9	Tris-hydroxymethyl aminomethane	((CH ₂ OH) ₃ CNH ₂)	6.057 g

2.3 Microstructure and Surface Analysis

Both polished and machined samples were etched using (HF-5 ml, Nitric Acid-20 ml, HCl—20 ml, water—60 ml) etchant for milliseconds and washed with methanol. Then microstructure of samples was analyzed using SEM (Scanning Electron Microscope (JEOL, JSM-IT 100). For measuring the grain size from SEM images Image J software (Abramoff et al., 2004) was utilized. X-ray Diffractometry (Panalytical X'Pert Pro) was administered to examine the phases present on both polished and Wire EDM machined samples using copper α lines generated at 40 kV and 20 mA. The chemical composition of polished and machined samples was examined using Energy dispersive X-ray Spectroscopy (OXFORD X-act) equipped with SEM (JEOL, JSM-IT 100).

2.4 Mechanical Characterization

Microhardness values of both Polished and machined surfaces were measured using Vickers Micro Hardness Tester (MVH- V LVD). For average hardness values minimum of 10 indents per sample were made. The weight loss study was performed using initial weights of the specimen and final weights of the specimen after corrosion in the electrochemical test cell for both the specimen. The surface roughness values were measured before and after corrosion of the specimen using (Mitutoyo SJ 310) roughness tester.

2.5 Characterization of Corrosion Behavior

Both specimen (polished and wire EDM machined) of 1 cm² surface area were used one by one for the Electrochemical study. The electrochemical test was conducted in a glass compartment containing 400 ml SBF solution [41] at pH 7.40 and 37 °C temperature by using AUTOLAB Electrochemical Workstation (AUT 302 N) potentiostat/galvanostat. This electrochemical workstation uses three probe cells for potentiodynamic polarization test, where the Ag/AgCl was used as reference probe, the graphite rod was made as counter probe and the specimen was act as a working probe. Both experiments were performed at a constant scan rate of 0.01 V/s initiated at – 0.900 V to +3.5 V. For EIS study, the excitation frequency from 10 kHz to 0.01 Hz and rms value of 32 mV was fixed for excitation in case of both specimens.

2.6 Evaluation of Biocompatibility

The dissimilarity in pH values of the SBF was recorded using MICROPROCESSOR (pH-mV-Temp Meter, G-2020) during the electrochemical study after a regular interval of 24 h. After electrochemical test, the surface topography of the corroded specimen was observed using Scanning Electron microscope (JEOL, JSM-IT 100) and energy dispersive X-ray technique (OXFORD X-act). Phases present or formed after electrochemical test were examined by X-ray Diffractometry (Panalytical X'Pert Pro).

3 Results and Discussions

3.1 Microstructural Analysis for Polished and WEDM Machined ZM21 Magnesium Alloy

SEM micrographs of polished ZM21 Magnesium sample are shown in Fig. 1a. It shows the homogenous distribution of β -phase particles consisting of Zn and Mn on the polished surface. X-Ray Diffraction analysis of polished ZM21 Magnesium sample Fig. 1b also depicts the presence of α -Mg matrix containing β phase Mn particles and confirms the presence of $MgZn_2$ compound on the surface of polished substrate. Energy Dispersive X-ray analysis (EDX) data Fig. 1c confirms the presence of Mg and Zn compound with some amount of Mn in it, also some impurities contained in the Mg alloy introduced during casting of an alloy. It confirms the presence of Mg matrix as 97% in the given alloy sample. As the magnesium degrades at higher pace in body fluids therefore alloying of magnesium with biocompatible alloying element such as Zn and Mn is the best method to limit its degradation [42]. Alloying in very low quantity is not harmful for human body whereas Zn is responsible for the enhancement of mechanical properties such as ductility. Whereas Mn is responsible for retarding the corrosion behavior of pure magnesium.

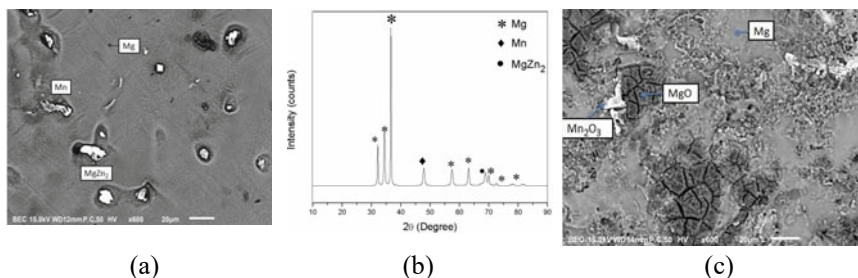


Fig. 1 a Microstructure b X-Ray diffraction analysis and c energy dispersive spectroscopy analysis of polished ZM21 Mg alloy

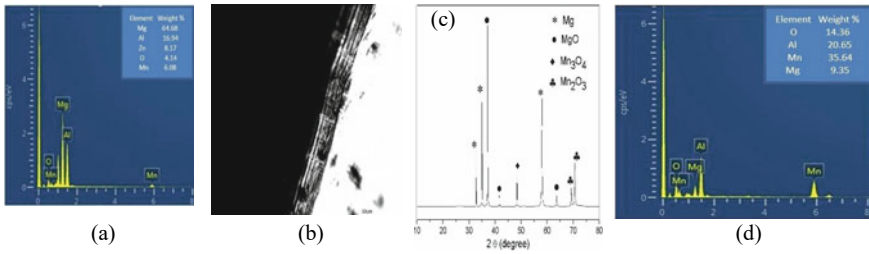


Fig. 2 a Microstructure **b** recast layer **c** X-Ray Diffraction analysis and **d** energy dispersive spectroscopy analysis of WEDM ZM21 Mg alloy

Moreover, the degradation behavior of Mg and its alloys depends on the grain structure. The heat generated due to the spark produced between the brass wire and ZM21 Mg sample during Wire Electric Discharge machining results in the surface modification. The SEM images of machined sample Fig. 2a, b depicts the formation of 60 μm thick recast layer with increased grain size. A larger grain size lead to a decrease in corrosion current density (icorr). This can be due to the presence of lower energy grain boundaries with controlled electron movement and its diffusion to retard the reactivity of the surface [43]. X-Ray Diffraction analysis of machined ZM21 Magnesium sample Fig. 2c depicts the presence of MgO₂ as the Mg gets oxidized and the Zn from the surface gets evaporated due to its low melting point temperature (i.e. 419.5 degree C). XRD data ensure the presence of Mn₂O₃ and Mn₃O₄ compounds on the machined surface. The EDS analysis Fig. 2d described that Zn is completely eliminated from the surface, low melting point of the Zn was responsible for such elimination. And the Mg gets oxidized as MgO and this will form a recast layer on the machined surface.

3.2 Mechanical Properties

Table 2 represents the mechanical properties such as surface roughness, microhardness and tensile strength for polished and machined surfaces. It shows that the surface after machining (ZM21-M) has higher surface roughness values than the polished surface (ZM21-P), which means the recast layer formed with a larger grain size. These larger grain-size machined surfaces have lower hardness and tensile strength values as compared to polished samples. The mechanical properties which improve with grain refinement include yield strength, ultimate tensile strength and hardness [44]. During Wire electric discharge machining, the continuous heating and cooling of material results in the melting of material and the formation of a recast layer with a larger grain size. These larger grain-sized surfaces with less number of corrosion-active grain boundaries help in corrosion control of magnesium implants in contact with body fluids.

Table 2 Mechanical characteristics of polished and WEDM machined ZM21 Magnesium Samples

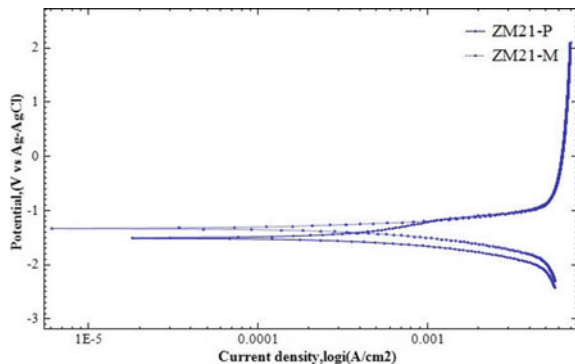
Sample	Average roughness value(Ra) (μm)	Ten point mean roughness (Rz) (μm)	Vickers micro hardness value (HV)	Tensile strength (MPa)
ZM21-P	0.1483	1.1495	25.4	249.0978
ZM21-M	3.2396	17.8995	16.775	164.51

3.3 Degradation Study of ZM21 (Polished and WEDM Machined) Sample

Linear Polarization study: To confirm the corrosion behavior, tafel plots for potentiodynamic polarization curves at 0 hr are obtained for both the substrates as shown in Fig. 3. PDP curves for WEDM machined substrate (thin line) shifted to a more noble direction as compared to the polished substrate (thick line). The shift of Ecorrosion (-1.45V to -1.35V) and decrease in $I_{\text{Corrosion}}$ (0.00339 A/cm^2 to 0.00281 A/cm^2) demonstrates the improved corrosion resistance of the WEDM machined substrates in comparison to polished one. For WEDM machined substrate, due to the presence of a large quantity of Mn on the surface recast layer $\text{Mn}(\text{OH})_2$ is formed. Manganese hydroxide surface layer has more passivation tendency in the Cl⁻ environment as compared to $\text{Mg}(\text{OH})_2$

EIS (Electrochemical Impedance Spectroscopy) study Detailed EIS analysis of both the samples including Nyquist, bode phase and bode modulus plots are carried out. Nyquist plots recorded for continue 7 days are depicted in Fig. 4a and b. Analysis for seven days is preferred to predict the corrosion behavior and corrosion product formation in SBF. The EIS spectra of both the samples for 0 h reading are categorized with three well-defined loops. First, a high-frequency capacitive loop, another medium frequency capacitive loop and low-frequency inductive loop. The charge transfer reaction of electric double layer formed between metal surface and corrosive medium is depicted from high-frequency capacitive loop [45]. The medium frequency capacitive loop attributes the mass transfer phenomena due to the

Fig. 3 Linear polarization curve for ZM21 (Polished and WEDM machined) Sample



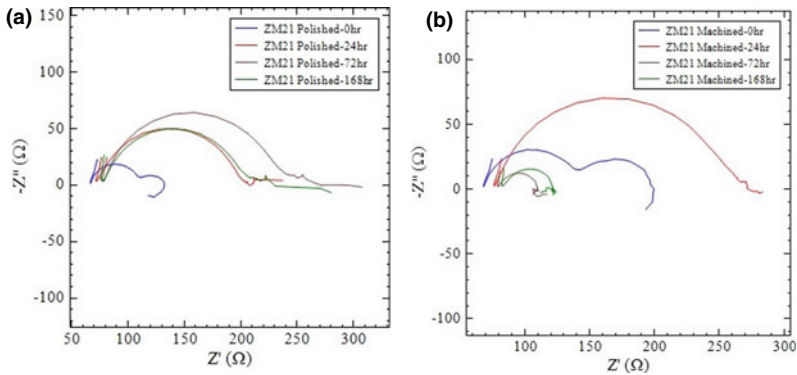


Fig. 4 a Nyquist plots for polished and b machined ZM21 Mg samples

dispersion of the ions through the corroded product layer [46]. The inductive loop occurred at a low-frequency region signifying the pitting of alloy [47].

For 0 h observation, the indication of bigger diameter capacitive loops indicated the more corrosion retardation of the machined substrate in comparison to the polished substrate. Moreover, a higher pitting tendency is observed for the WEDM machined substrate. For 24 h, the same pattern for corrosion behavior has been observed. After 72 h, the Nyquist plot shows the drastic decrease in corrosion resistance for machined substrate along with frosted pitting tendency. On the other hand, the corrosion resistance of the polished sample is better as compared to its 24-h. For 168-h observation the corrosion resistance of the machined sample is slightly increased, but still far lesser than the polished substrate. The pitting behavior after 168 h is more pronounced in WEDM machined substrate. Nyquist plots for polished & WEDM machined ZM21 substrates at 0 h indicates the presence of $Mg(OH)_2$, a stable oxide layer on the surface of polished samples. For WEDM machined substrate, due to the presence of the large amount of Mn on the surface recast layer $Mn(OH)_2$ is formed. Manganese hydroxide surface layer has a more passivation tendency in the Cl^- environment as compared to $Mg(OH)_2$ [47]. The presence of such a recast layer also provides necessary corrosion resistance to the WEDM machined substrate [39]. The occurrence of the recast layer increased the surface activity of the WEDM machined substrate. So the whole covering of the exposed area with the oxide layer formation is quicker in WEDM machined substrate as compared to the polished one. The larger diameter of semicircles for 0 h reading indicates the same behavior.

The low-frequency induction loop observed at 72 h for WEDM machined substrate also depicts the pitting tendency. Whereas for polished substrates relatively high corrosion resistance is observed due to the presence of stable corrosion products $Mg_3(PO_4)_2$, $MgCO_3$, $Ca_3(PO_4)_2$, $CaCO_3$ on its surface [48]. No pitting behavior has been observed for polished substrate at 72 h. It is interesting that at 72 h the polished samples exhibit maximum corrosion resistance whereas WEDM machined substrate possesses least corrosion resistance. This can also be validated by the pH

versus time graph (Fig. 7). It is clearly indicated that the steep rise in pH for the machined substrate is halted. Again, a decrease in R_{ct} for 84–96 h has been observed for the machined substrate. As the Cl^- ions rich corroded media (SBF) came into contact with newly formed $Mg(OH)_2$, the formation of insoluble $MgCl_2$ takes place which in turn decreases the corrosion resistance and increases the amount of free OH^- ions in the solution. Formation of $MgCl_2$ is justified by the consecutive rise in pH value of the solution after 4 days as shown in Fig. 10. Afterwards, from 96–108 h the increase in corrosion resistance is due to the formation of stable corrosion products (i.e. $Mg_3(PO_4)_2$, $MgCO_3$, $Ca_3(PO_4)_2$, $CaCO_3$). After 108 h onwards, due to the occurrence of high pitting corrosion, the R_{ct} value again drop for machined samples corrosion. Nyquist plot reading for 168 h also indicates the formation of low-frequency induction loop for machined substrate, justifying the pitting phenomena.

Bode phase diagrams are shown in Fig. 5a, b for polished and WEDM machined substrates respectively. At high-frequency region, the slope of 72 and 168-h graphical lines for polished substrate shows phase value of 18° and 19° , whereas for WEDM machined substrates the values are 10° and 11° respectively. The higher phase value depicts the more capacitive behavior results in the formation of an oxide layer which tends to retard the corrosion tendency [49]. It clearly indicates that the corrosion tendency of WEDM machined substrates at 72 & 168 hours is higher than the polished samples. This makes a good combination with the Nyquist plot details & R_{ct} versus time graph as shown in Fig. 7. For the medium frequency region, the max phase value is occurred after 24 h of immersion of machined substrate and 72 h for polished substrate. Nyquist plot & R_{ct} versus time graph also verify the same behavior.

The low-frequency bode phase plots indicate the poor corrosion resistance for both the alloys and it can be better understood by the Bode Modulus plot as shown in Fig. 6a, b respectively for polished and machined substrate. It indicates that up to 24 h of immersion, the corrosion resistance of machined substrate is better than polished substrate. Dramatic decrease in impedance is observed after 72 h for the machined substrate. The least impedance value observed after 168 h for machined substrate signifies its higher pitting tendency than the polished substrate.

The bode phase angle and modulus plots shown in above figures depicts higher impedance values and phase angle over whole frequency range at 0 & 24 h immersion of machined substrates. Thereby it is found that up to 24 h of immersion machined substrate is more corrosion resistant as compared to the polished surface. Once

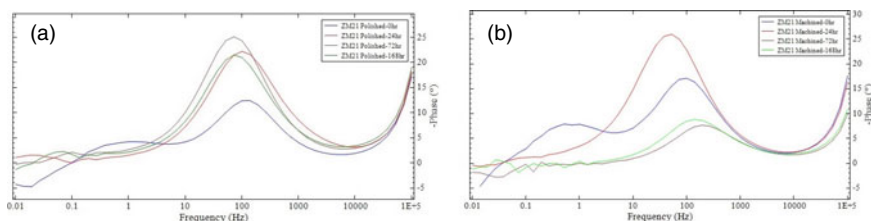


Fig. 5 Bode phase plot **a** polished ZM21 Mg Substrate and **b** machined ZM21 Mg substrate

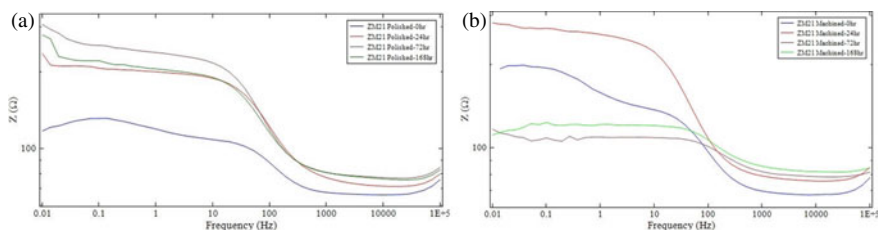


Fig. 6 Bode Modulus plot **a** Polished ZM21 Mg substrate and **b** WEDM machined ZM21 Mg substrate

Table 3 Observation table for Nyquist, Bode modulus and Bode Phase

Sample	Rct (ohms)	Z	Phase angle(degree)
ZM21-P	131.79	117.73	12.44
ZM21-P7	279.76	279.83	21.54
ZM21-M	199.25	194.45	17.16
ZM21-M7	123.8	111.58	8.88

the recast layer is diminished corrosion occurs at a very high rate. For long-term immersions severe pitting is observed on the machined surfaces as compared to the polished surface.

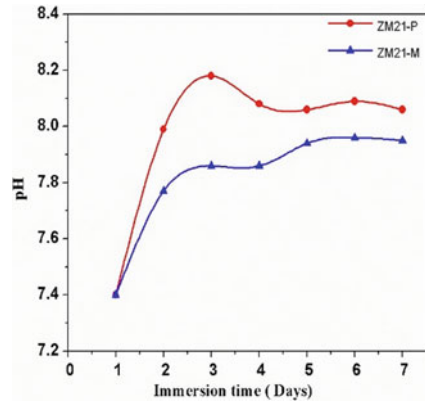
3.4 pH Variation Study of SBF Solution in Contact with ZM21 Samples

pH variation of the SBF solution is continuously measured for 7 days at a regular interval of 24 h to check its biocompatibility. Figure 7 data reveals that the increase in pH is relatively higher for polished substrate as compared to the machined substrate. A steep increase in pH for polished and machined substrates is observed for 2 and 3 days respectively. Furthermore, after 3 days the rapid increase in pH is retarded for machined substrate & for polished sample it is highest at that point. It suggests that free OH⁻ ions are bound up by a machined surface. For 3 to 5 days, polished samples exhibits a decrease in pH value whereas machined sample possesses a rise in pH value. Afterwards nearly constant behavior is observed for both the substrates.

3.5 Surface Morphology of Corroded ZM21 Mg Alloy

Figure 8a, b represents the SEM-EDS details for polished and WEDM machined ZM21 corroded substrate after submerged in SBF for 7 days. The corrosion product deposition is inhomogeneous in nature on both substrates. For polished samples it

Fig. 7 pH variation graph of SBF solution for polished and machined ZM21 Mg alloy



is clearly indicated that a large amount of Zn is existing in the bottom regions of pores. However, the machined sample illustrates a larger number of pitting corrosion sites. Lunder et al. 1987 [50] explain that the combination of oxidized manganese in the layered structure, due to the exchange of magnesium cations, the interaction of chloride anions in the $Mg(OH)_2$ Surface is limited. Thereby the presence of Mn increases the stability of the recast layer and improves corrosion resistance. But the presence of micro-structured pores and cracks on this layer critically hampers the corrosion resistance [51]. The presence of higher crystal defects and local stress concentrators on machined surfaces (Fig. 8) deteriorates the passivity of the recast layer by the pitting corrosion phenomena.

On polished samples, the deposition and deepening of $Mg(OH)_2$ layer is delayed due to the lack of surface activity possessed by the polished surface. After immersion for seven days in SBF, corrosion product on the machined surface depicts higher mud crack patterns than the polished surface. The existence of cracks facilitates the

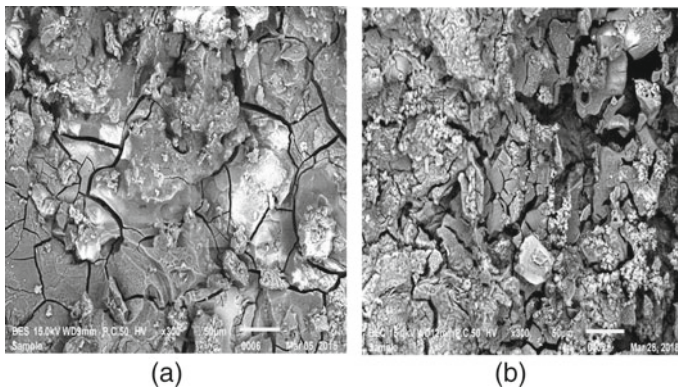


Fig. 8 SEM images of **a** corroded polished ZM21 **b** corroded WEDM machined ZM21 samples

increased surface contact between corroded media and Mg substrate, thus accelerating the corrosion of the WEDM machined substrate. So it is observed that for a long immersion period (i.e. 168 h) machined substrates are more prone to corrosion as compared to the polished substrate. XRD pattern shown in Fig. 9a, b confirmed the fostered formation of $Mg_3(PO_4)_2$, $MgCO_3$, $Ca_3(PO_4)_2$, $CaCO_3$ & $MgCl_2$ compounds on the corroded WEDM machined surface as compared to the polished substrate. The EDS data in Fig. 10a, b mentioned that the deposition wt% of apatite forming elements (i.e. Ca, P) on machined surfaces are relatively higher than the polished surface.

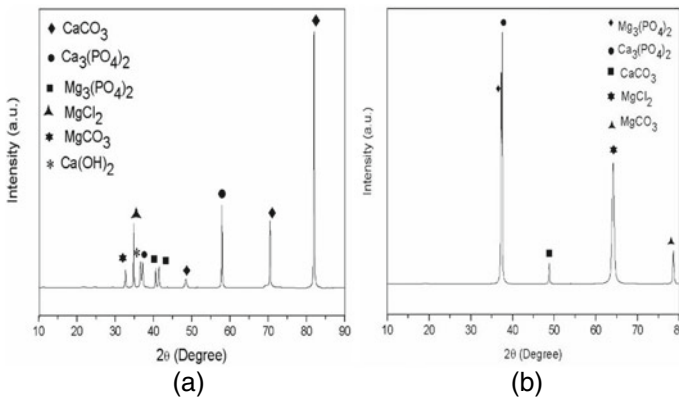


Fig. 9 XRD analysis of a corroded ZM21 polished b corroded WEDM machined sample

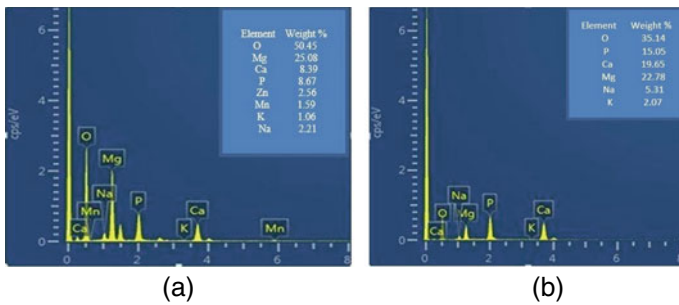


Fig. 10 Energy Dispersive Spectroscopy analysis a corroded ZM21 polished b corroded WEDM machined sample

4 Conclusion and Future Scope

In the present study, the consequence of wire electric discharge machining on ZM21 Mg alloy was compared with polished ZM21 Mg alloy used as biodegradable orthopedic implants. The motive behind this research is to study the change in the degradation rate of Mg alloy after immersion in simulated body fluid. It was observed that using optimal wire EDM parameters the corrosion rate of Mg implants can be controlled for the initial period of immersion to increase its lifespan up to the healing time of bone fracture. As seen from the above results, the degradation rate intensifies if this recast layer gets eroded by the corrosive environment. In order to protect this recast layer for a longer timespan various biodegradable material coatings or films can be applied to the substrate. It was also concluded that the WEDM machining is best-suited machining process for implant fabrication in terms of its biocompatibility and complex geometry formation of implants.

Acknowledgements This work is sponsored under research funding by SERB, DST, India.

References

1. Lu Y, Bradshaw AR, Chiu Y-L, Jones IP (2014) The role of β ' precipitates in the biocorrosion performance of Mg–3Zn in simulated body fluid. *J Alloys Compd* 614:345–352
2. Avedesian MM, Baker H et al (1999) ASM speciality handbook: magnesium and magnesium alloys. ASM Int
3. Guan R, Cipriano AF, Zhao Z, Lock J, Tie D, Zhao T, Cui T, Liu H (2013) Development and evaluation of a magnesium–zinc–strontium alloy for biomedical applications—Alloy processing, microstructure, mechanical properties, and biodegradation. *Mater Sci Eng C* 33:3661–3669
4. Gu X-N, Zheng Y-F (2010) A review on magnesium alloys as biodegradable materials. *Front Mater Sci China* 4:111–115
5. Long M, Rack HJ (1998) Titanium alloys in total joint replacement—a materials science perspective. *BioMater* 19:1621–1639
6. Haseeb M, Butt MF, Altaf T, Muzaffar K, Gupta A, Jallu A (2017) Indications of implant removal: a study of 83 cases. *Int J Health Sci (Qassim)*. 11(1)
7. Reith G, Schmitz-Greven V, Hensel KO, Schneider MM, Tinschmann T, Bouillon B, Probst C (2015) Metal implant removal: benefits and drawbacks—a patient survey. *BMC Surg* 15:1–8
8. Zhang Y, Pu Y-F, Hu J-R, Liu Y, Chen Q-L, Zhou J-L (2011) Efficient CT metal artifact reduction based on fractional-order curvature diffusion. *Comput Math Methods Med*
9. Hermawan H (2012) Biodegradable metals: state of the art. *Biodegrad Met* 13–22
10. Moravej M, Mantovani D (2011) Biodegradable metals for cardiovascular stent application: interests and new opportunities. *Int J Mol Sci* 12:4250–4270
11. Zheng L-Z, Wang J-L, Xu J-K, Zhang X-T, Liu B-Y, Huang L, Zhang R, Zu H-Y, He X, Mi J (2020) others: Magnesium and vitamin C supplementation attenuates steroid-associated osteonecrosis in a rat model. *Biomaterials* 238:119828
12. Zhao D, Huang S, Lu F, Wang B, Yang L, Qin L, Yang K, Li Y, Li W, Wang W (2016) others: Vascularized bone grafting fixed by biodegradable magnesium screw for treating osteonecrosis of the femoral head. *Biomaterials* 81:84–92
13. Saris NE, Mervaala E, Karppanen H, Khawaja JA, Lewenstam A (2000) 891 Magnesium. An update on physiological, clinical and analytical aspects. *Clin Chim Acta* 294:893

14. Grünewald TA, Rennhofer H, Hesse B, Burghammer M, Stanzl-Tschegg SE, Cotte M, Löffler JF, Weinberg A-M, Lichtenegger HC (2016) Magnesium from bioresorbable implants: distribution and impact on the nano- and mineral structure of bone. *Biomaterials* 76:250–260
15. Staiger MP, Pietak AM, Huadmai J, Dias G (2006) Magnesium and its alloys as orthopedic biomaterials: a review. *Biomaterials* 27:1728–1734
16. Zeng R, Dietzel W, Witte F, Hort N, Blawert C (2008) Progress and challenge for magnesium alloys as biomaterials. *Adv Eng Mater* 10:B3–B14
17. Krause A, der Höh N, Bormann D, Krause C, Bach F-W, Windhagen H, Meyer-Lindenberg A (2010) Degradation behaviour and mechanical properties of magnesium implants in rabbit tibiae. *J Mater Sci* 45:624–632
18. Witte F, Hort N, Vogt C, Cohen S, Kainer KU, Willumeit R, Feyerabend F (2008) Degradable biomaterials based on magnesium corrosion. *Curr Opin Solid State Mater Sci* 12:63–72
19. Erinc M, Sillekens WH, Mannens R, Werkhoven RJ (2009) Applicability of existing magnesium alloys as biomedical implant materials
20. Kawasaki H, Guan J, Tamama K (2010) Hydrogen gas treatment prolongs replicative lifespan of bone marrow multipotential stromal cells in vitro while preserving differentiation and paracrine potentials. *Biochem Biophys Res Commun* 397:608–613
21. Guo J-D, Li L, Shi Y-M, Wang H-D, Hou S-X (2013) Hydrogen water consumption prevents osteopenia in ovariectomized rats. *Br J Pharmacol* 168:1412–1420
22. Kraus T, Fischerauer SF, Hanzi AC, Uggowitzer PJ, Löffler JF, Weinberg AM (2012) *Acta Biomater* 8:1230
23. Zberg B, Uggowitzer PJ, Löffler JF (2009) MgZnCa glasses without clinically observable hydrogen evolution for biodegradable implants. *Nat Mater* 8:887–891
24. Wang J, Witte F, Xi T, Zheng Y, Yang K, Yang Y, Zhao D, Meng J, Li Y, Li W (2015) others: Recommendation for modifying current cytotoxicity testing standards for biodegradable magnesium-based materials. *Acta Biomater* 21:237–249
25. Tapiero H, Tew KD (2003) Trace elements in human physiology and pathology: zinc and metallothioneins. *Biomed Pharmacother* 57:399–411
26. Barker ES, Elkinton JR, Clark JK (1959) others: Studies of the renal excretion of magnesium in man. *J Clin Invest* 38:1733–1745
27. McCance RA, Widdowson EM (1942) The absorption and excretion of zinc. *Biochem J* 36:692–696
28. Yamaguchi M, Oishi H, Suketa Y (1987) Stimulatory effect of zinc on bone formation in tissue culture. *Biochem Pharmacol* 36:4007–4012
29. Yamaguchi M (1998) Role of zinc in bone formation and bone resorption. *J Trace Elem Exp Med Off Publ Int Soc Trace Elem Res Humans* 11:119–135
30. Chen Q, Thouas GA (2015) Metallic implant biomaterials. *Mater Sci Eng R Rep* 87:1–57. <https://doi.org/10.1016/j.mser.2014.10.001>
31. Brar HS, Wong J, Manuel M (2012) V: Investigation of the mechanical and degradation properties of Mg–Sr and Mg–Zn–Sr alloys for use as potential biodegradable implant materials. *J Mech Behav Biomed Mater* 7:87–95
32. Gao J-C, Sha W, Qiao L-Y, Yong W (2008) Corrosion behavior of Mg and Mg–Zn alloys in simulated body fluid. *Trans Nonferrous Met Soc China* 18:588–592
33. Ralston KD, Birbilis N (2010) Effect of grain size on corrosion: a review. *Corrosion* 66:75005
34. Klocke F, Schwade M, Klink A, Kopp A (2011) EDM machining capabilities of magnesium (Mg) alloy WE43 for medical applications. *Procedia Eng* 19:190–195
35. Demir AG, Previtali B, Ge Q, Vedani M, Wu W, Migliavacca F, Petrini L, Biffi CA, Bestetti M (2014) Biodegradable magnesium coronary stents: material, design and fabrication. *Int J Comput Integr Manuf* 27:936–945
36. Sealy MP, Guo YB, Liu JF, Li C (2016) Pulsed laser cutting of magnesium-calcium for biodegradable stents. *Procedia Cirp* 42:67–72
37. Razak MA, Abdul-Rani AM, Rao T, Pedapati SR, Kamal S (2016) Electrical discharge machining on biodegradable AZ31 magnesium alloy using Taguchi method. *Procedia Eng* 148:916–922

38. Daud MAM, Omar MZ, Syarif J, Sajuri Z (2010) Effect of wire-EDM cutting on fatigue strength of AZ61 magnesium alloy. *J Mek* 30
39. Xu J, Xia K, Zhang L, Yu Z, Yu H (2015) The surface element deposition and corrosion behavior study of multi-cutting in the machining of magnesium alloys. In: 2015 2nd international workshop on materials engineering and computer sciences
40. Kokubo T, Ito S, Huang ZT, Hayashi T, Sakka S, Kitsugi T, Yamamuro T (1990) Ca, P-rich layer formed on high-strength bioactive glass-ceramic A-W. *J Biomed Mater Res* 24:331–343
41. Xu L, Yu G, Zhang E, Pan F, Yang K (2007) In vivo corrosion behavior of Mg-Mn-Zn alloy for bone implant application. *J Biomed Mater Res Part Off J Soc Biomater Jpn Soc Biomater Aust Soc Biomater Korean Soc Biomater* 83:703–711
42. Alvarez-Lopez M, Pereda MD, Del Valle JA, Fernandez-Lorenzo M, Garcia-Alonso MC, Ruano OA, Escudero ML (2010) Corrosion behaviour of AZ31 magnesium alloy with different grain sizes in simulated biological fluids. *Acta Biomater* 6:1763–1771
43. Soleimani M, Mirzadeh H, Dehghanian C (2020) Effect of grain size on the corrosion resistance of low carbon steel. *Mater Res Express* 7:16522
44. Wang J-L, Xu J-K, Hopkins C, Chow DH-K, Qin L (2020) Biodegradable magnesium-based implants in orthopedics—a general review and perspectives. *Adv Sci* 7:1902443
45. Liu Q, Chen D, Kang Z (2015) One-step electrodeposition process to fabricate corrosion-resistant superhydrophobic surface on magnesium alloy. *ACS Appl Mater Interfaces* 7:1859–1867
46. Baril G, Blanc C, Pébère N (2001) AC impedance spectroscopy in characterizing time-dependent corrosion of AZ91 and AM50 magnesium alloys characterization with respect to their microstructures. *J Electrochem Soc* 148:B489
47. Zhang Y, Yan C, Wang F, Li W (2005) Electrochemical behavior of anodized Mg alloy AZ91D in chloride containing aqueous solution. *Corros Sci* 47:2816–2831
48. James M, Kumar S, Narayanan TSNS (2011) Corrosion behavior of commercially pure Mg and ZM21 Mg alloy in Ringer's solution—Long term evaluation by EIS. *Corros Sci* 53:645–654
49. Jin W, Wang G, Lin Z, Feng H, Li W, Peng X, Qasim AM, Chu PK (2017) Corrosion resistance and cytocompatibility of tantalum-surface-functionalized biomedical ZK60 Mg alloy. Elsevier
50. Lunder O, Aune TK, Nisancioglu K (1987) Effect of Mn additions on the corrosion behavior of mould-cast magnesium ASTM AZ91. *Corrosion* 43:291–295
51. Walter R, Kannan MB (2011) Influence of surface roughness on the corrosion behaviour of magnesium alloy. *Mater Des* 32:2350–2354

Investigation of Angular Distortion Using Mathematical Modelling in TIG Welded Dissimilar Stainless Steel 304 and 316 Grades



Deeksha Narwariya , Aditya Kumar Rathi, and Pradeep Khanna

Abstract Gas tungsten arc welding is a type of arc welding in which a non-consumable electrode of tungsten is used to weld. The electrode and weld area are protected by an inert shielding gas to avoid atmospheric contamination. This welding process is considered as a high heat input process which occasionally leads to the generation of non-uniform thermal stresses in the material that causes weld abnormalities like angular distortion. Where distortion is crosswise to the welding track and caused by shrinkage adjacent to the fusion zone ensuing change in the angle of the parts. Thus, it is important to predict the extent of these distortions to a certain level of accuracy so that remedial steps can be taken while selecting the input parameters to curtail the final angular distortion. In this research work, angular distortion is investigated during the GTA welding of two dissimilar grades of stainless steel i.e. 304 and 316. The effect of input constraints like current, welding torch angle and speed on the angular distortion of the plate was investigated by developing the mathematical model between the input parameters and its response by using the factorial approach. The results were analyzed using graphical representations.

Keywords GTAW · Angular distortion · Stainless steel · Input parameters · Mathematical model · Factorial approach

D. Narwariya (✉)
Netaji Subhas University of Technology, Dwarka, New Delhi, India
e-mail: deeksha.pe19@nsut.ac.in

A. K. Rathi · P. Khanna
Netaji Subhas University of Technology, Dwarka, New Delhi, India
e-mail: aditya.kumar@nsut.ac.in

P. Khanna
e-mail: khanna@gmail.com

1 Introduction

Gas–tungsten arc welding is also recognized as tungsten inert gas welding. It is a process that joins similar or dissimilar metals by heating them to melt with an arc produced between a non-consumable tungsten electrode and the specimen under an inert shielding gas medium. GTAW is used in the fabrication industry, especially for stainless steel, titanium alloys and other materials in thin sections for high-quality welds. GTAW and SMAW comparison for dissimilar welded joint shows that TIG joint has better strength and uniform hardness [1]. Transverse distortion was studied on TIG by taking into consideration of various welding parameters and concluded that a mathematical model was helpful to optimize the GTAW method to make it cost-effective by eradicating the weld flaws due to distortion [2]. The heating and cooling cycles in a non-uniform manner are part of the welding process that causes thermal stress in the welded specimen hence distortion. During the welding process, different type of distortion was observed with angular distortion being the most prominent one [3]. Wire feed rate and voltage has encouraging result on angular distortion whereas welding speed has an undesirable consequence on angular distortion for SS304 steel [4]. GTAW has various applications like welding of sheets, plates and tubes for use in aerospace, food processing and other light fabrication application [5]. Austenitic steel such as 316 is widely used in steam generating plants and nuclear reactors its study for the TTP diagram shows that phase instability due to carbon content and constituents can provide thermodynamic stability and other precipitation reaction [6]. Tensile strength was influenced by the welding speed for AISI 316 welded joint for TIG welding, and the highest bend strength can be obtained by optimized welding speed [7, 14]. Two different types of ribbed bars of steel were welded, and the effect on mechanical properties was investigated to see that hot-operated duplex stainless steel can be welded in creation for the alteration of its properties [8]. Mechanical properties of 316L stainless steel welded joint were compared with micro-sample and standard sample with no significant difference, with corrosion resistance in other cases [9, 16]. Dissimilar metal joining was performed on 8 mm thickness plates with four types of fluxes on TIG welding for the microstructure study with the best result for TiO₂ flux [10, 12, 15]. Mild steel and stainless steel were welded together to study the consequence of different types of fluxes on TIG welding the result was best with SiO₂ flux [11]. 310SS was welded with different filler material rods on TIG welding and the result shows the best tensile and bending strength with 309 L [13, 18]. Dissimilar aluminum alloys can be joined by pulse TIG welding the result shows the microhardness of the fusion zone vary from 72 to 98 HV with an impact toughness of 22 J [17]. It is clear from the literature review that a lot of work was carried out for dissimilar metal joining with the TIG welding process. To the best information of authors, unlike steel joining of 304 and 316 steel with 2 mm thickness is still missing. So, an effort is made to carry out the work on above said two metals joining (Fig. 1).



Fig. 1 GTAW setup

2 Experimental Setup

In the current research work, TIG welding machine of duty cycle 60%, and flat V-I characteristics constant voltage power source was used with 250 Amp as rated current output and voltage range of 18–20 V, capable to weld a sheet up to 4 mm thickness. Non-consumable tungsten conductor of 2.5 mm span used with argon as the shielding gas during the welding process. Specimens are prepared by welding two different grades of stainless steel i.e. 304 and 316 of 150 mm × 150 mm and 2 mm thickness. The GTAW machine is shown in Fig. .1, and the welding process in operation is shown in Fig. 2.



Fig. 2 TIG welding

3 Methodology of Investigation

Welding of thin plates has been considered in the present study owing to its wide use in the automotive and food processing industry for the production of lightweight structures with high strengths in tension, compression, shear resistance to creep, fatigue failure, etc. Many researchers have published work on the prediction of welding distortions and stresses during TIG welding of thin plates [1]. However, the majority of all these have been conducted for low-carbon steels. Considering the rapid transition of the industry to high-strength alloys, relatively limited literature on welding exists for the same, thus the current work has been agreed with the objective of acquiring a quantitative insight into some of the welding aspects of stainless steel. Stainless steel 304, austenitic grade steel owing to its excellent form-ability, deep draw-ability, weld-ability and superior mechanical and physical properties. 316 is an 18/8 steel improved with an additional Molybdenum by 2.5%, providing excellent corrosion resistance property to 304 stainless steel. 316 has enhanced pitting corrosion resistance and also has excellent resistance to phosphates, sulphates and salts, in comparison to standard 18/8 types, 316 has better resistance to reducing acids, seawater and solution of bromides, iodides and chlorides. Its exceptional resistance towards corrosion, even in extreme environmental condition makes it an excellent choice for the manufacturing of various industrial products like catalytic converters, turbochargers and automotive fuel tanks, architectural panelling, railings, chassis for vehicles, and other components. The composition of 304 and 316 stainless steel is given in Tables 1 and 2 respectively. The angular distortion in plates of a butt joint is shown in Fig. 3.

This work was specifically focused on the investigation of angular distortion and its prediction under different combinations of input variables as angular distortion is more pronounced in the case of butt-welded thin sheets and causes more rejections

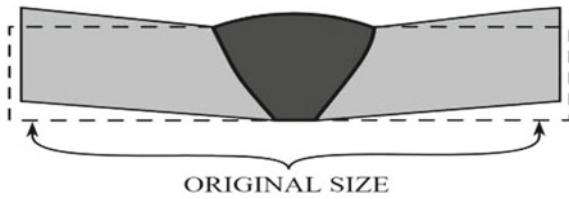
Table 1 Composition of SS 304

Elements	Carbon	Manganese	Silicon	Chromium	Nickel	Phosphorus	Sulphur
Weight (%)	0.060	0.86	0.031	18.350	8.200	0.0310	0.010

Table 2 Composition of SS 316

Elements	Carbon	Manganese	Silicon	Chromium	Molybdenum	Nickel	Phosphorus	Sulphur
Weight (%)	0.04	1.6	0.05	19	2.5	12.5	0.03	0.03

Fig. 3 Angular distortion



than any other type of distortion. In the current study, a mathematical model has been developed using MINITAB software. Assigning process parameters to the orthogonal array of L-9, experiments were conducted and optimization condition was obtained along with the identification of the most influencing parameters using ANOVA.

3.1 Identification of Input Parameters and Their Operating Range

At the origin of the literature survey experimental runs were shown, and it was found that angular distortion is affected by current, welding speed and torch angle. Although, there is no substantial effect shown because of the gas flow rate. The gas flow rate was kept constant at 15 lpm throughout the experiment. All the input limits along with their choice are represented in Table 3

Table 3 Input parameters with their range

S. No	Parameter	Units	Level	
			Lower Limit	Upper Limit
1	Current	Amp	120	140
2	Speed	Cm/min	25	35
3	Torch Angle	Degree	0	45

3.2 *Measuring of Angular Distortion*

Experiments were carried out as per the design matrix as revealed in Table 4. Angular distortion of each plate was measured with the aid of height gauge fitted with the dial test indicator as shown in Fig. 4a. The base of the height gauge is placed on the surface plate; specimen placed on surface plate with slight weight on other side so that other plate gets elevated by some height. Taking three reading of each specimen, then take the average distortion for each run. The weld beads put on different samples as the groupings given in Table 4 by bead on plate, technique are shown in Fig. 4b.



(a)



(b)

Fig. 4 a Measurement of angular distortion using height gauge. b Welded specimen

Table 4 Design matrix with angular distortion reading

S. No	Current (Amp)	Speed(cm/min)	Torch angle (Degree)	Distortion(mm)			
				Reading 1	Reading 2	Reading 3	Average reading
1	120	35	0	4.12	3.08	3.04	3.413
2	140	25	45	7.10	6.56	7.0	11.887
3	120	25	45	9.44	11.0	12.92	11.130
4	120	25	0	12.12	10.72	8.72	10.520
5	140	35	45	8.04	11.14	13.00	10.727
6	140	25	0	6.06	7.08	7.12	10.753
7	120	35	45	3.28	5.00	7.16	5.147
8	140	35	0	6.18	8.08	9.20	7.820

3.3 Development of Mathematical Model

The experiments were conducted in a random order with all the groupings as recommended by the design matrix. These experiments were showed to ensure the abolition of systematic error, if any. The value of the angular distortion was noted and articulated in Table 4.

4 Result and Discussion

ANOVA investigation was performed to inspect the feasibility of the developed model as revealed in Table 5. The developed regression model has a P-value of 0.050 shows that the model is significant. The most significant factor is speed followed by the interaction of speed and current. Secondly, the higher value of R square and adjusted R-square also suggest the suitability of the established model shown in Table 6.

The mathematical relation generated by software MINITAB is shown below which comprises the effect of separate terms and the dealing terms as shown below in Eq. (1). Distortion can be measured from this equation.

$$\begin{aligned} \text{Distortion} = & 95.83 - 0.5588 \text{ current} - 3.426 \text{ speed} - 0.1837 \text{ Torch angle} \\ & + 0.02249 \text{ current} * \text{ speed} + 0.000943 \text{ current} * \text{ Torch angle} \\ & + 0.003219 \text{ speed} * \text{ Torch angle.} \end{aligned} \quad (1)$$

Table 5 Analysis of variance

S. NO	Source	DF	Adjusted SS	Adjusted MS	F-value	P-value	
1	Regression	6	68.5921	11.4320	225.13	0.050	Significant
2	Current	1	6.5733	6.5733	124.85	0.057	
3	Speed	1	13.7282	13.7282	260.74	0.039	Significant
4	Torch Angle	1	0.6631	0.6631	12.59	0.175	
5	Current*Speed	1	10.1183	10.1183	192.18	0.046	Significant
6	Current*Torch Angle	1	0.3600	0.3600	6.84	0.233	
7	Speed*Torch Angle	1	1.0491	1.0491	19.93	0.140	
8	Error	1	0.0527	0.0527			
9	Total	7	68.6447				

Table 6 Model Summary

Model Summary			
S	R-Square	R-Square (Adjusted)	R-Square (Predicted)
0.229456	99.92%	99.46%	95.09%

4.1 Main Effect of Input Parameters on the Angular Distortion

Figure 5 demonstrates the probability plot drawn using software; in this plot, it can be seen that all the points are nearby the centre line in random order which validates this mathematical model. Main effect plot of current, welding speed and torch angle are shown in Fig. 6; it can be understood that as the current rises the heat input increases hence more thermal stresses generated in the specimen producing more angular distortion. The angular distortion is originated to decreases as speed increase is due to decrease in the heat per unit length which generates lesser thermal distortion. As torch angle increases angular distortion also increases, the probable reason is, with the increase in angle, the spreading of heat increases or in other words more area comes in the contact of heat results more angular distortion.

4.2 Interaction Plots of Distortion, Speed and Torch Angle

Increase in torch angle, the angular distortion is found to increase because of spreading of the arc ahead of the torch thereby spreading the heat in a wider area. The current i.e. 130 Amp is kept constant in this condition. The angular distortion varies in the range of 10 to 12 mm approximately. The effect of welding speed on the contrary

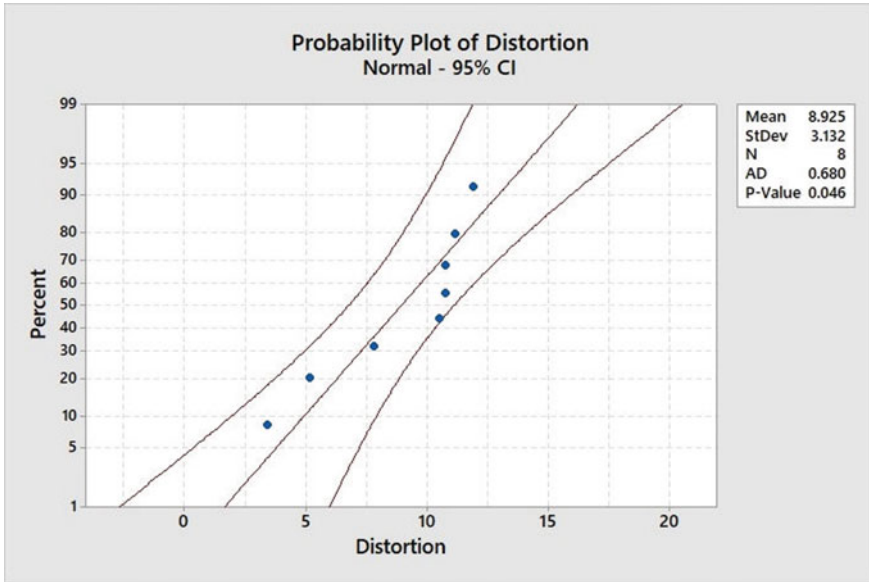


Fig. 5 Probability plot of distortion

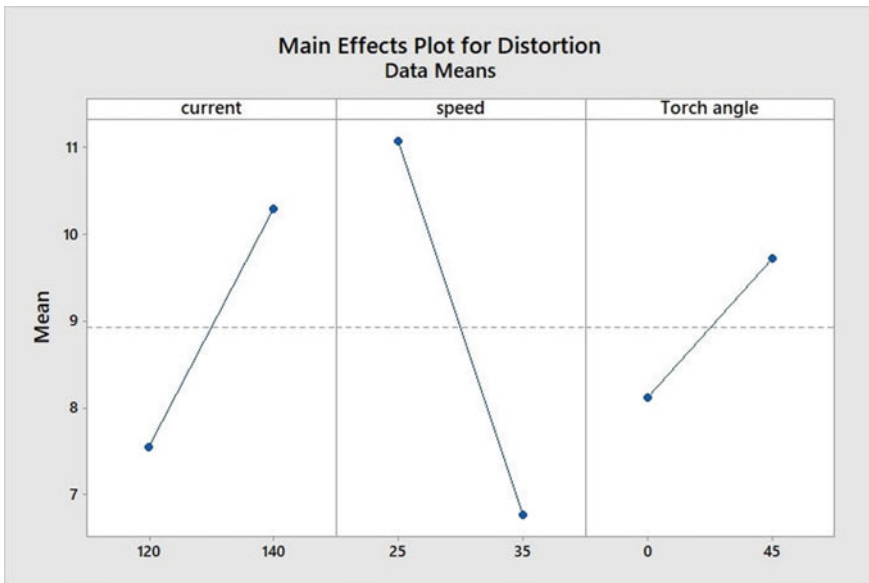


Fig. 6 Main effect of input parameter on distortion

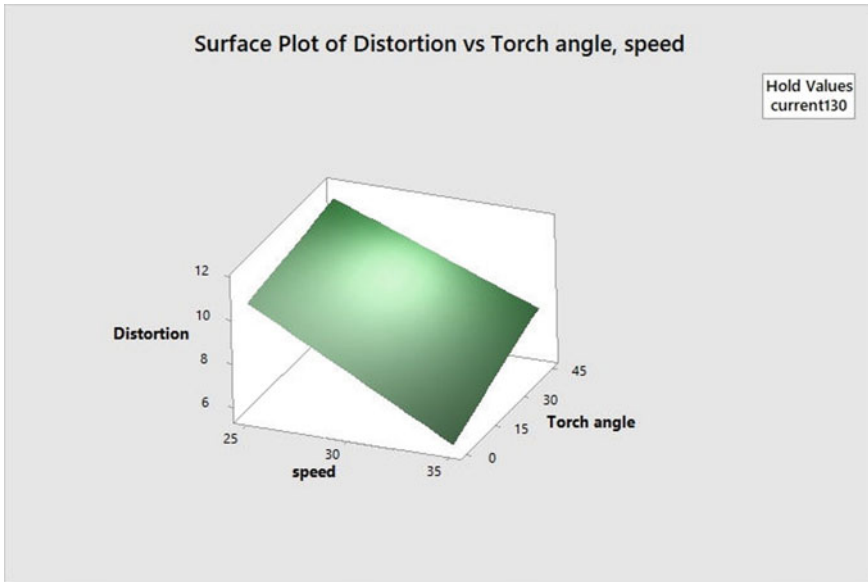


Fig. 7 Collective effect of torch angle and speed on distortion

was negative on the angular distortion probably because with the rise in welding speed, the heat input per unit length of the weld gets reduced thereby reducing the angular distortion. The angular distortion ranges from 6 to 10 mm (Fig. 7).

4.3 Interaction Plot of Distortion, Current and Torch Angle

Increase in torch angle, the angular distortion is found to increase because of spreading of the arc ahead of the torch thereby spreading the heat in a wider area. The increase in current increases, heat input which generates the internal thermal stress due to this distortion also increases. It is clear from Fig. 8 that an increase in current and torch angle both increases the angular distortion whereas the speed is kept constant at 30 cm/min. Angular distortion in this case ranges from 7 to 11.5 mm.

4.4 Interaction Plot of Distortion, Speed and Current

If we keep the torch angle at 22.5° as constant the surface plot as shown in Fig. 9 clearly indicates the distortion rises with the rise in current whereas it declines with the rise in the speed, probably because with the rise in welding speed, the heat input

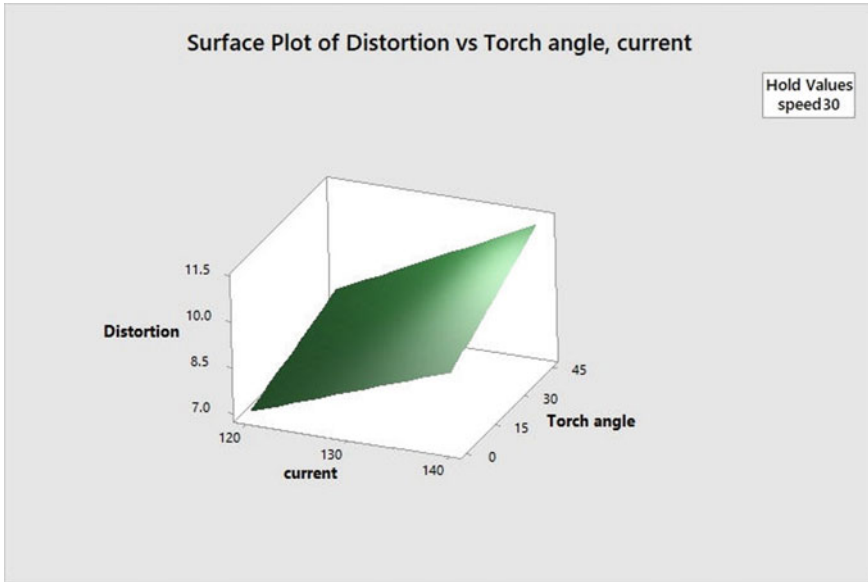


Fig. 8 Collective effect of torch and current on distortion

per unit length of the weld gets reduced. The range of distortion varies from 4 to 10 mm.

5 Conclusion

The following conclusion can be drawn from the presented research work that was carried out on the two dissimilar metals such as SS 304 and SS 316 joined by the GTAW process with 2 mm thickness plates.

- The design of the experiment is found to be useful for carrying out this investigation work to study the result of speed, current and torch angle on the angular distortion of TIG welded joints.
- Speed is the most significant factor that can optimize the angular distortion for this type of dissimilar TIG welded joint.
- An increase in the current increases the angular distortion because more heat is generated in that particular area so the angular distortion is higher.
- An increase in speed decreases the angular distortion because heat input per unit length of weld shortens.
- A surge in torch angle also rises the angular distortion because of the spreading of the arc ahead of the torch thereby spreading the heat in a wider area

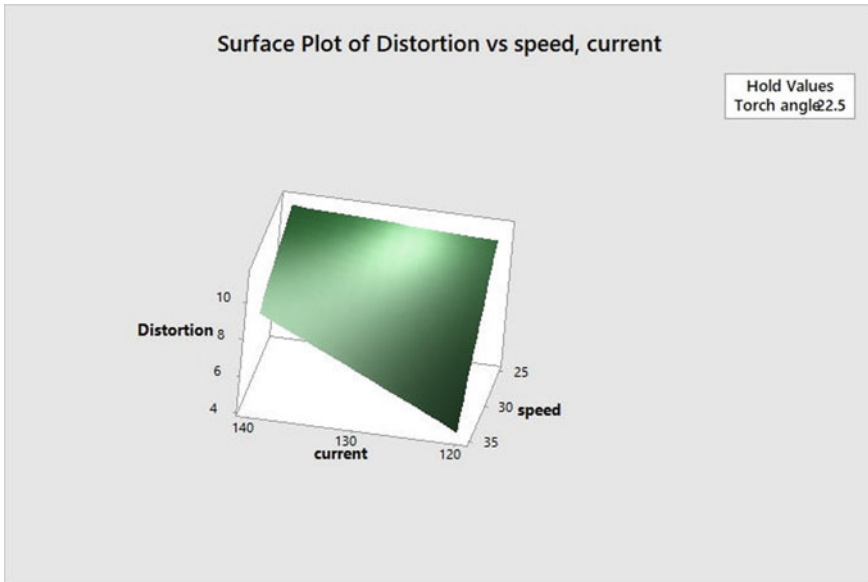


Fig. 9 Collective effect of current and speed on distortion

References

1. Basu S, Gupta V, Khanna P (2019) Mathematical modelling to predict angular distortion in butt welded stainless steel 304 thin plates. *JPE* 22(2)
2. Kant R, Mittal R, Kumar C (2018) Bharat Singh Rana, Manish Kumar, Rajnish Kumar, Fabrication and Characterization of Weldments AISI 304 and AISI 316 used in industrial applications. *Mater Today: Proc* 5:18475–18481
3. Duhan S, Mor A, Malik D (2015) Study of angular distortion of SS 302 and MS plate with GTAW. *Int J Recent Res Asp* 2(2):159–163
4. Kumar Bhaskar A, Pal K, Khanna P (2020) Mathematical analysis of angular distortion on GTA welded hot rolled E250 grade low carbon steel plates. *Int Res J Eng Technol* 7(3)
5. Gourd LM (1995) Principles of welding technology, 3rd edn. Edward Arnold publication
6. Weiss B, Stickler R (1972) Phase instabilities during high temperature exposure of 316stainless steel. *Metall Trans* 3:851–866
7. Bharath P, Sridhar VG, Senthil Kumar M (2014) Optimization of 316 stainless steel weld joint characteristics using Taguchi technique. *Procedia Eng* 97:881–891
8. Velasco F, Blanco G, Bautista A, Martez MA (2009) Effect of welding on local mechanical properties of stainless steels for concrete structures using universal hardness tests. *Constr Build Mater* 23:1883–1891
9. Molak RM, Paradowski K et al (2009) Measurement of mechanical properties in a 316L stainless steel welded joint. *Int J Pressure Vessels Piping* 86:43–47
10. Sharma P, Dwivedi D (2019) TIG welding of dissimilar P92 steel and 304H austenitic stainless steel, mechanisms, microstructure and mechanical properties. *J Manuf Process* 44:166–178
11. Sathe SS, Harné MS (2015) Optimization of process parameters in tig welding of dissimilar metals by using activated flux powder. *Int J Sci Res (IJSR)* ISSN 4(6):2319–7064
12. Kulkarni A, Dwivedi DK, Vasudevan M (2019) Dissimilar metal welding of P91 steel-AISI 316L SS with Inconel 800 and Inconel 600 interlayers by using activated TIG welding process and its effect on the microstructure and mechanical properties. *J Mater Process Tech* 274

13. Rao VA, Deivanathan R (2014) Experimental investigation for welding aspects of stainless steel 310 for the process of TIG welding. *Procedia Eng* 97:902–908
14. Pasupathy J, Ravisankar V (2013) Parametric optimization of TIG welding parameters using Taguchi method for dissimilar joint. *Int J Sci Eng Res* 4(1). ISSN 2229-5518
15. Badheka VJ, Basu R et al (2016) Microstructural aspects of TIG and A-TIG welding process of dissimilar steel grades and correlation to mechanical behaviour. *Trans Indian Inst Met* 69(9):1765–1773. <https://doi.org/10.1007/s12666-016-0836-5>
16. Dadfar M, Fathi MH et al (2007) *Mater Lett* 61:2343–2346
17. Baghel PK, Nagesh DS (2018) Mechanical properties and microstructural characterization of automated pulse TIG welding of dissimilar aluminium alloy. *Indian J Eng Mater Sci* 25:147–154
18. Khalifeh AR, Dehghan A, Hajjari E (2013) Dissimilar joining of AISI 304L/St37 steels by TIG welding process. *Acta Metall Sin (Engl Lett)* 26:721–727

Development of Probe for Arsenic and Fluoride Detection in Drinking Water



Shivani Pandey, Satanand Mishra, H. N. Bhargaw, and Archana Singh

Abstract Water plays a unique and crucial function on the globe but due to population growth, industrialization, the effects of climate change, the populace lacks access to adequate drinking water. Water 4.0, often known as “Digital Water,” is poised to change the water sector and address this threat to human survival. Given the highly localised nature of the contamination, it is also advisable to create local prediction models and assess at least multiple robust and applicable algorithms. Heavy Metals before settling on a final model and hybrid ML–DL models are very effective. For simple and sensitive application in the construction of Arsenic specific chromogenic and fluorescent probes, such as hydrogen bonding interactions, a definite sensing method and aggregation-induced emission (AIE); chemodosimetric approach; metal coordination. The detection of Arsenic and Fluoride ions was made possible by the development of two sensitive and ratio-metric fluorescent probes (probe I and probe II). Both Probes have a certain detection limit with a stable detection range. The developed smart sensor works on the fluorogenic principle and its design is divided into four modules such as sensing, measurement, control and display unit. Artificial intelligence prediction models can be utilised as a decision-making tool and to develop proactive environmental policy. International Centre for Clean Water (ICCW) is speeding the dawn of Water 4.0, which will lead to clean and sustainable water for all, through its implementation strategies in water treatment plants, industry and the community.

Keywords Artificial intelligence · Fluorescence probe · Probe design · Sustainable water

S. Pandey · S. Mishra (✉) · H. N. Bhargaw · A. Singh
Academy of Scientific and Innovative Research (AcSIR) and CSIR-Advanced Materials and Processes Research Institute, Bhopal, Madhya Pradesh 462026, India
e-mail: snmishra07@gmail.com

© The Author(s), under exclusive license to Springer Nature Singapore Pte Ltd. 2023
S. Hegde et al. (eds.), *Recent Developments in Mechanics and Design*, Lecture Notes in Mechanical Engineering, https://doi.org/10.1007/978-981-19-4140-5_13

145

1 Introduction

It is desirable to develop selective, sensitive, feasible, and high-throughput analytical techniques for heavy metal detection. Fluorescence coupled plasma, atomic emission spectrometry quantum yield, and fluorescence lifetime are examples of specific atomic effects on Fluorophore performance for absorption spectrometry, for example, inductively heavy metals detection (QY). Traditional elemental-based approaches are used. The width spectrometry has a high level of sensitivity and the shape of its absorption, as well as the mass width and form of Stokes shift. Accuracy and transmission [1]. Bulky instrumentation, broad emission band maxima, emission bands, sample pre-treatment techniques, and expert molar absorption coefficients, to name a few. Operators are required, all of whom are expensive. Their use, particularly in-situ analysis, should be restricted.

A slew of new sensing systems based on low-cost sensors have been released. Electrochemical detection of surface plasmon resonance Fluorescence techniques has many advantages, including high sensitivity, precision, and relative simplicity. The sensitivity, reliability, dynamic range, and repeatability of a sensor are all determined by the type of sensor used [2]. Chemi-luminescence (CL), quartz crystal microbalance, fluorescence technologies, and other low-cost and simple operational approaches are some of the alternatives [3–5]. Fluorescence techniques have many advantages, including high sensitivity, precision, and relative simplicity. The type of sensor employed determines the fluorescent lighting, sensitivity, reliability, dynamic range, and repeatability of the sensor. The most important elements that will have an impact on the Fluorophore performance for heavy metals detection includes Fluorescence quantum yield, fluorescence lifetime (QY). The width and form of Stokes shift, as well as the thickness and nature of the absorption [1]. Accuracy and spread Bulky instrumentation, a large number of emission band maxima, emission bands, sample pre-treatment methods, and expert molar absorption coefficients, among other things. A fluorophore that works must have an elevated mole dependent absorption coefficient and be brilliant with an elevated fluorescence QY under ideal conditions [6].

Fluorescence techniques have many advantages, including high sensitivity, precision, and relative simplicity. The responsiveness, consistency, dynamic scope, and repeatability of a sensor are all determined by the type of sensor used [2]. An effective fluorophore under the optimal excitation wavelength necessarily be bright, have an elevated mole based coefficient, and have a high fluorescence QY. It should also be steady, with adequate functional groups to cooperate with the objective heavy metals successfully. Several fluorophores, such as tiny organic colour dyes, metal based ligand complexes, metal containing organic frameworks (MOFs), semi-conductors (NCs) and metal nano-aggregate, silica nano-particles (NPs), and zero-dimensions based Carbon Quantum dots, possibly will be developed separately either in combination of heavy metals sensing stage [7–11]. The most common and commonly used small molecule organic dyes in classic fluorophore are rhodamine, fluorescein, cyanine, and coumarin. However, tiny Stokes shift (usually fewer than 25 nm),

easily changed excitation or emission wavelengths, and hence the self-quenching effect limit their applications. Carbon dots are an alternative and superior to heavy metal fluorescence sensors when compared to other fluorophores [12]. Carbon dots, primarily revealed in arc based-discharge filth in 2004 [13], are nano-sized carbon through unique diameters of less than 10 nm and intrinsic fluorescence [14]. Based on their basic architecture, they can be divided into three classes.

Carbon dots with graphene layers on the sides are appropriate for use as luminous probes for heavy metal imaging in cell, bacteria, plants, and animals, as opposed to spherical carbon NPs with amorphous or animals. Carbon heavy metals ions and species have made significant progress in recent decades, with novel respectively, and carbon dots with polymer cross applications in environmental and food safety linking or grafting are known as polymer dots testing, cell and animal imaging, chemical logic (PDs) [15].

Carbon dots are excellent electron acceptors and donors, and they are frequently utilized in sensing function that utilize fluorescence or CL recognition. There is no need for photoexcitation in the CL system, and the luminescence is attributed to the electromagnetic energy produced during the response procedure [16]. Carbon dots can be employed as oxidants, emitting species, chemical process energy acceptors, and even catalysis [17–19]. Photo-excitation is necessary for photoluminescence (PL) emissions in fluorescence detection, and Carbon Dots are thus excellent signal reporters [20].

Carbon dots-based fluorescence sensors offer significant advantages over luminous dyes and decent metal/metal oxide nano-based materials for sensing and imaging heavy metals of interest. Many carbon dots-based fluorescence sensors have been claimed to detect heavy metals with exceptional precision, especially when “turn-on” and ratio-metric measurements are used. More effort is being put into multi-heavy metals detection to improve detection throughput, heavy metal speciation for highly contaminated variety, production of gel as well as solid sensor platforms for example paper-dependent procedure, sensor arrays, polymer or else hydrogel films, in addition to IIPs for lucrative recognition, smart based visual recognition, and on-site based analysis [21].

The overall merits of Carbon Dots as a heavy metals sensor can be summarised as follows. Carbon Dots, for example, have fluorescent ocular property with outstanding photostability as well as minimal photobleaching, making them right like fluorophores for heavy metal fluorescence detection. Second, mainly Carbon Dots are hydrophilic and have strong water solubilities, allowing them to be used as heavy metals sensors in the environmental, biological, and medicinal areas [22]. Most Carbon Dots have low toxicity due to their carbon core and effortlessly customised microporous functional set on the surface, they are suitable for heavy metal imaging within cell, microorganisms, flora and fauna because they are fluorescent probes. Carbon Dots as fluorescence based sensors for heavy metals ions and group have made significant progress in recent decades, with fresh application in ecological and fare protection testing, Chemical logic (PDs) [15], cell and animal imaging anticounterfeiting ink in ger print security, as well as document counterspy [23–29].

Table 1 Toxicity information of arsenic

Heavy metal	Toxicity information
Arsenic (As)	<p>1. Mainly environmentally dangerous Arsenic group are arsenite (As(III)) along with arsenate (As(V)), with As(III) being ten instances greater poisonous than As(V) and 70 instances greater toxic than natural species such mono-methyl arsonic acid (MMA) and dimethylarsinic acid (DMA) [32]</p> <p>2. As(III) and As(V) have pKa,1 values of 9.22 and 2.20, correspondingly, suggesting that As(III) be present in an impartial medium as uncharged As(OH)three at the same time as As(V) is negatively charged [33]</p> <p>3. According to the World Health Organization, a healthful degree of overall As is 10 g/L [34]</p>

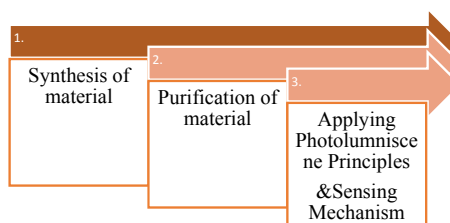
The methods for synthesising and purifying carbon dots, related PL basics, heavy metal sense methods, and hence the binding methods involving carbon dots in addition to heavy metals are all briefly discussed [30].

The reception method and progress on single heavy metal ions and multi-heavy metals detection are crucial. The improvement of solid-based shape sensor technologies, as well as applications for heavy metal detection in water using Carbon Dots, are discussed [31]. The toxicity of heavy metal is shown in Table 1. Concerns about the environment and human health As(III) are more poisonous than As(V).

2 Methodology

The majority of fluorescent carbon dots-based heavy metals sensors are used in real-time sample analysis using matrix based water. Mainly ecological and biological sample have more complex matrix, containing a variety of charges and organic substances. Chemicals with the aim of damage or spoil performance Fluorescent sensors are deteriorating. Layout of carbon dots-based sensors that are robust and reliable for detecting heavy metals in the environment is divided into three steps (Fig. 1) explains process flow of fluorescence based sensor development includes synthesis of material, purification of material and applying photoluminescence principles and sensing mechanism.

Fig. 1 Process flow diagram for sensor development



2.1 Synthesis of Material

The production of Carbon Dots through efficient and adequate functional groups be critical towards establishing binding or else response spot through heavy metals in carbon dots-based heavy metals fluorescence sensors. Surface modification and heteroatom doping are viable methods [26]. Because the carbon resource or precursor and N- and S-doping of Carbon Dots are mainly widely used techniques, carbon materials have hetero based atoms, such as nitrogen (N), sulphur (S), boron (B), silicon (Si), and phosphorus (P), are excellent possibilities for heteroatom doping. [33, 34]. The production of the Carbon Dot S-BHHCT-Eu(III) dual-fluorophore system is shown in Fig. 2.

The fraction of hetero-based atoms to primary concern detail of carbon, and consequently the surface chemical science, may be altered with the aid of using the usage of distinctive artificial strategies and synthesis circumstances. In raw and purified carbon dots, the fraction of hetero based atoms in doped carbon dots can change greatly, indicating a significant increase in the optical characteristics of carbon dots [35]. Carbon Dots' excitation band may change from usual 260–320 nm to more long wavelengths, causing the emission band to shift to green, yellow, and red regions when compared to non-doped carbon dots [36]. As a result, the anti-matrix interference adaptability of Carbon Dots as heavy metals sensors has been strengthened, as ordinary fluorescence of trial medium by low down wavelengths can be avoided [37].



Fig. 2 Carbon Dots (CARBON DOTS)-BHHCT-Eu(III) dual-fluorophore system preparation [38]

2.2 Purification of Material

Filtration, chromatographic, centrifugal method, chemical precipitation, measurement based on pH manage cloud factor extraction [39], solid-segment extraction [40], in addition to dialysis are only a few of the new purification technologies that have been documented. So far, the most common method for separating Carbon Dots from colloidal solutions that uses a membrane has been dialysis. The small-dimension target Carbon Dots permeate the film pore, whilst the bigger-sized no target compound is held within dialysis membrane, thanks to the appropriate molecular weight cut-off of dialysis bags. Strength of dialyzed Carbon Dots resolution, as well as the prolonged dialysis procedure, are the two most significant disadvantages of this approach. Another method for purifying carbon dots has been suggested: centrifugation. Varied fractions of NPs of various weights can be obtained by varying centrifugation speeds [41]. To detach the portion in slight mass variety, organic based solvent like acetone might be used Separating manufactured Carbon Dots products into multiple fractions has also been done using size-exclusion chromatography, however the process is time-consuming, thus the elution conditions must be carefully tuned. After organic solvent extraction, Koutsoukis et al. [40] described an excellent purification approach using SPE.

2.3 Photoluminescence (PL) Principles and Sensing Mechanism

When photons excite carbon dots, the electrons shift to energized condition further come again toward the stability condition/ground status, discharge excess of energy throughout the radiation procedure, produce PL. Quantum based confinement cause, surface or edge position, particle position, in addition to cross-link improved discharge (CEE) effect are four PL principles that may be clarified for carbon dots [33]. Additional functional grouping like C=N/C=O along with C-N groups are produced on the exterior of coloured Carbon Dots than on surface of Carbon Dots with single emissions, according to fluorescent probe dependent Carbon Dots. The molecular state is related to an organic fluorophore on the carbon core's surface that may emit PL directly. Small fluorophore molecules develop alongside the carbonogenic core when Carbon Dots are synthesised at low reaction temperatures [35]. The presence of molecular fluorophores is advantageous to QY development. The CEE impact entailed the aggregation or cross-linking of a newly new PL centre. Yang's group [36] discovered that the CEE effect fluorescence of (PEI) polyethyleneimine base Polymer dots, which they recognized to reduce quivering and revolution in cross-linking PEI-based polymer dots configuration. Fluorescence of carbon quantum dots is generally known by one or more a permutation of required principle [37].

While absorption spectrum of heavy metals perfectly overlies through the emission and excitation spectrum of target materials, IFE phenomena occurs (carbon dots)

[42]. Consequently the reduction of excitation ray or absorption of emitted waves ends up in the apparent dependent fluorescence quenching of carbon dots [43]. In the IFE, no latest material is created, and average fluorescence duration of Carbon Dots tested in the presence of Heavy Metals show no significant changes. Because Cr(VI) includes a broad optical phenomenon that could successfully overlies with the excitation as well as emission spectrum of blue colour-emitting Carbon Dots, IFE technique used to sense Chromium (VI) [44].

Temperature, solvent, and additions such as heavy metals are all linked to the aggregation of Carbon Dots [45]. When molecules clump together, intramolecular mobility is inhibited, obstructing the nonradiative route and triggering radiative decay [46]. To directly prove ACQ or AIEE processes, characterization methods such as transmission microscope (TEM), DLS and small-angle based X-ray spreading are applied. Variations in Zeta based-potential and UV–VIS spectrum can be there used in direction of indirectly understand development depends on heavy metals–carbon dots compounds [47].

2.4 Sensor Modules

Sensing Node—In this node sensor (transducers) and signal conditioning is done.

Measurement Node—In this node measurement is done by microcontroller.

Wireless Node—Wireless transmission is done via Bluetooth and other sources.

Notification node—Alarming and visual system to display readings and notify alert with alarm.

2.5 Artificial Intelligence in Sensor Development

Local intelligence and disbursed information disclosure cycles update centralized manage and information processing in IoT and IoT-like applications, and AI-primarily based totally sensors extensively empower new architectures in IoT and IoT-like applications. The subtleties of embedding AI approaches, in addition to the layout and improvement of AI-primarily based totally sensing structures, can be high-quality finished thru a higher expertise of the function of embedded clever sensing structures in Industry 4.0, IoT architectures and technologies.

3 Results and Discussions

The chemical configuration and anticipated sense system of sensor for Arsenic and Flouride detection is obtained with different source of materials having different chemical structure.

3.1 The Chemical Configuration and Planned Sense Method of Sensor for as Detection

Figure 3 suggests the chemical systems of 95a and 95b together with the proposed sensing mechanism of 95a [48]. A norbornene-derived monomer 95a and its homo-polymer 95b have been evolved for detecting As(III), in which rhodamine B became used as the signalling unit [48]. Both the monomer and polymer answer in methanol–water answer remained colourless moreover as non-emissive due to the spirolactam ring-closed shape of the rhodamine unit.

Within the presence of KIO_3 and HCl , the solution of 95a turned pink in colour and reddish in emission because of the opening of the spirolactam ring. After the addition of As(III) solution, the pH changed from 1.34 to 4.23, and therefore the colour of the answer changed to brown, and the emission changed to greenish within the presence of KIO_3 and HCl , As(III) oxidized to As(V) and generated I_2 within the

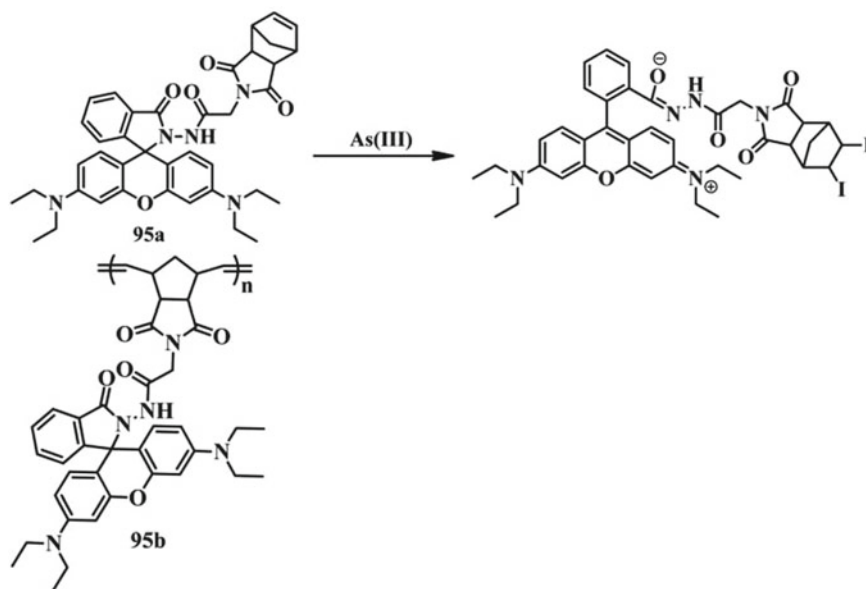


Fig. 3 Chemical configuration of 95a and 95b along with proposed sensing mechanism of 95a [48]

solution. This I_2 further reacted with the covalent bond of the norbornene unit, and as a result, the colour and fluorescence were changed (Fig. 3). The same mechanism was followed by polymer 95b.

Within the presence of KIO_3 and HCl, the answer of 95a grew to become purple in shadeation and reddish in emission due to the hole of the spirolactam ring. After the addition of As(III) solution, the pH modified from 1.34 to 4.23, and consequently the shadeation of the solution modified to brown, and the emission modified to greenish. Inside the presence of KIO_3 and HCl, As(III) oxidized to As(V) and generated I_2 inside the solution. This I_2 further reacted with the covalent bond of the norbornene unit, and as a result, the shadeation and fluorescence have been modified (Fig. 3) the equal mechanism turned into observed through polymer 95b.

The oxidation procedure turned into in addition supported through cyclic voltammetry which recommended that two-electron oxidation passed off at some stage in the sensing procedure. Paper strips lined with polymer 95b have been effectively used for the “in-field” detection of As(III) in water sources. So it is clean that 95a and 95b are precise for his or her selective detection of As(III) in each colorimetric and fluorometric strategies in a very novel mechanistic pathway. Sensor 95a functions a detection restrict of 2 hundred nM for As(III) ions.

3.2 The Chemical Configuration and Planned Sense Method of Sensor for Fluoride (F^-) detection

Fig. 4 shows Diindolyl quinoxalines (DIQs) 4-a and subsequent indolocarbazole quinoxalines 4-b [49].

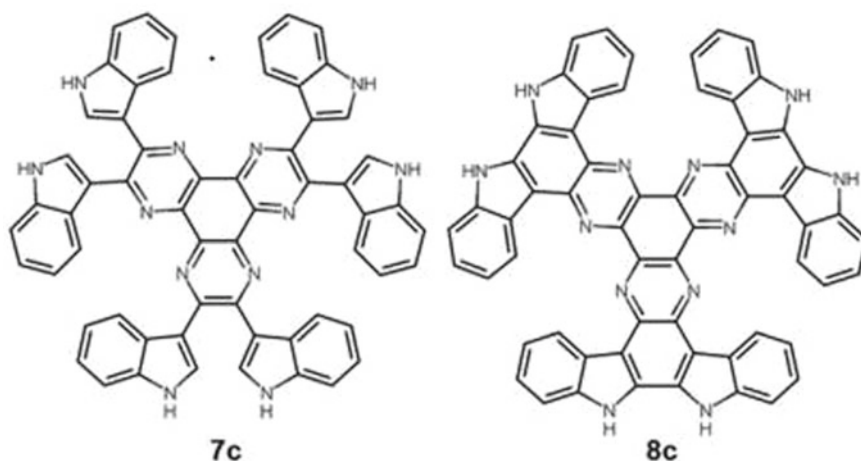


Fig. 4 Diindolyl quinoxalines (DIQs) 4-a and corresponding indolocarbazole quinoxalines 4-b [49]

Yan and friends have oxidized compounds 4-a and 4-b with DDQ in TFA to afford the corresponding indolocarbazole quinoxalines. Both the receptors confirmed excessive binding affinity for fluoride, acetate, and dihydrogen phosphate, as decided through UV/Vis–fluorescence titration in DMSO. An analogous approach become used by Liu et al. to offer polydentate conjugate molecules supported an inflexible quinoxaline aircraft surrounded through six indole @NH groups, that is, 4-a and 4-b [49]. Figure 5 indicates Fluorescence titration of (A) receptor 4-a with F@ (as a TBAF salt from zero to 30 equiv) in DMSO ($\lambda_{\text{ex}} = 420 \text{ nm}$) and (B) receptor 4-b with F@ (as a TBAF salt from zero to a hundred equiv) in DMSO ($\lambda_{\text{ex}} = 440 \text{ nm}$); the insets in (A) and (B) display fluorescence emission colour adjustments of the receptor 4-a and 4-b answer upon addition of Fluoride [49]. Both 4-a and 4-b (Fig. 4) confirmed selectivity for fluoride ions. The interplay of receptor 4-a and 4-b with F@ become investigated through suing UV/Vis and fluorescence spectroscopic titration. Compared to 4-a, receptor 4-b, with the equal legating web sites and chemical surroundings however with shape it truly is greater inflexible and no conformational flexibility, ended in numerous sensing behaviour. The flexibility of 4-b to stumble on F@ become proven through ratio-metric fluorescence measurements, as proven in Figs. 5a and b [49].

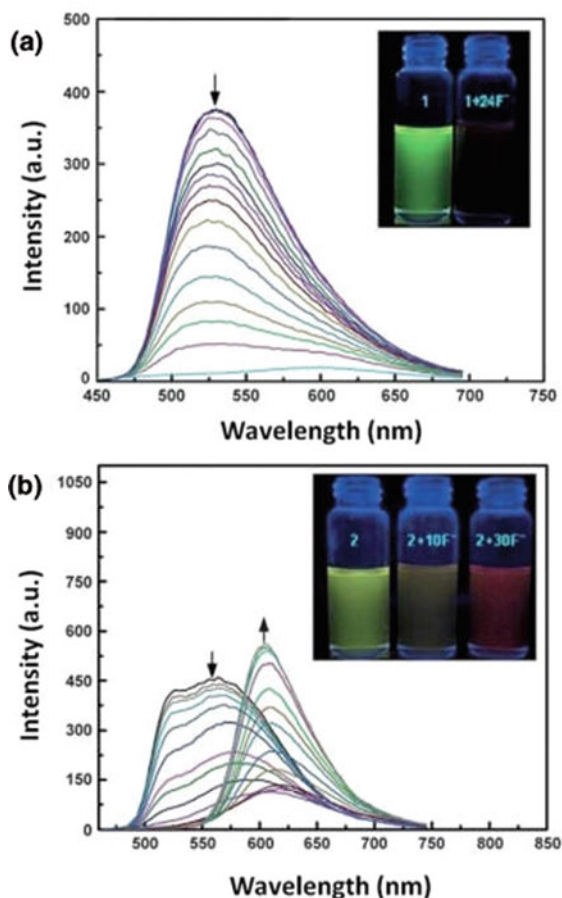
4 Material-Receptor Binding Techniques

A signal producer and probe essentials for selective fastening are generally used in fluorescent carbon dots-based heavy metals sensors. As a result, functionalized plane of Carbon dots containing dissimilar moieties be important. Moieties as well as target heavy metals are required to be selective and effective. Coordination in addition to chelation, electrostatic things, oxidation–reduction response, and exchanges through (DNA) based aptamers are just a few of the binding techniques that might be used.

4.1 Coordination and Chelation

The interaction constant can be influenced by several types of coordination structures, for example linear otherwise tetrahedral coordination, size based controlled macro based molecule ligands, and additional factors [45]. Furthermore, the hardness of multiple species of the same heavy might differ significantly, requiring adaptation [50]. Coordination ligands of various types As(III), for example, As(V), is a soft metal and a PO₄³⁻ [51] homologue. There were several interference ions and matrices in the original sample, while the vast majority of synthesized Carbon dots had oxygen-doped functional group hindrance. Damage created by non-marked ions must examine and handled in a systematic manner [52].

Fig. 5 Fluorescence titration of **a** receptor 4-a with F⁻ (as a TBAF salt from 0 to 30 equiv) in DMSO (λ_{ex} = 420 nm) and **b** receptor 4-b with F⁻ (as a TBAF salt from 0 to 100 equiv) in DMSO (λ_{ex} = 440 nm); the insets in **a** and **b** show fluorescence emission colour changes of the receptor 4-a and 4-b solution upon addition of Fluoride [49]



4.2 Electro-Static Effect

Binding locations on plane of Carbon dots contain ionized functional sites, electrostatic effects can arise at specific pH ranges. It's possible that CDs and HMs are different. When the pH value is less than 7, the hydroxyl as well as carboxyl, along with thiol, sulfonate, in addition to phosphonate groups are deprotonated and negatively charged [39]. Medium exceeds their pK_a values; the media exceeds the pK_a values of amine, imine, and urea. The amide and imidazole groups will have a favourable impact on them. They become ionized at a pH lower than their pK_a when protonated [53].

4.3 Oxidation–Reduction Reaction

It has been demonstrated that photoexcited CDs are excellent electron donor and are capable of reducing metal ions [54]. As a result, an RO reaction might exist used on the way to build a CD-based Heavy metals based sensor. An RO reaction can be able to happen between heavy metals and Carbon dots, resulting in electron relocation and non-radiation based electron/hole repairing and changing the photo-luminescence property [55].

4.4 Affinity of DNA Aptamer

Aptamer based on oligonucleotide based binder sequence can be able to preferentially engage through heavy metals to shape stable metal-containing mediated base pairs with groove binding, as well as electrostatic contact also intercalation property [56, 57]. The fluorescence of Liang et al./Ce-doped's CDs was initiated on the way to be covered up with As(III) particular aptamer using development of a bulky CD-based aptamer combined because of—electron stack, hydrogen based bond, (water repellent) hydrophobic force, and inter-molecular strength [58]. While As(III) is introduced to this As(III) sensing system, it can act in response through aptamers create a constant As(III) complex containing aptamer, restoring fluorescence intensity [59].

5 Conclusion

Most of detection techniques for As(III) are mediated by hydrogen-bond connections, result in alteration in colour or change in fluorescence. Selectivity aside, the majority sensors have a detection edge well under World health organization guidelines. In the area of As(III) sensing, there are enormous opportunities for expansion with regard on the way to sensor planning as well as growth. For a greater useful kits for As(III) detection, fantastically choosy and touchy sensors be within excessive call for at this time. Growingly expansion of polymer based techniques for sensors because the recognition of As(III) be necessary in favour of the manufacture of the device to provide a lasting solution to companies strongly affected by arsenic poisoning. Because of its main advantages over fluorescent dyes or metal nano-materials/noble metals, carbon based fluorescence techniques are effective measures for detecting heavy metals of interest [60, 61]. Many carbon point-based fluorescence sensors have been shown to have exceptional performance in detecting heavy metals, with turn-on and ratio-metric measurements particularly useful [62, 63]. Multi-heavy metal detection to improve detection capability, speciation of heavy metals for highly contaminated class, production of gel or solid sensor techniques for example paper based

devices, arrays, polymer or hydro-gel based films and IIP for effective commercial recognition, intelligent illustration recognition and on-site based analytics are all areas where more work is being done [64].

6 Future Scope

We will develop an Artificial Intelligence-based cellular phone functional platform which may take into custody the sensor icon by an integral smart-phone based camera, recognize the existence of sensing factor and categorize the level of sensing factor supported colour intensity dependent known within the teaching set on the captured figure by deep Convolutional neural network(CNN) algorithms. This technology of sensor will create an early warning system that may help people in getting Arsenic and Fluoride-free water.

Acknowledgements The Authors acknowledge Director CSIR AMPRI Bhopal for his continuous support, guidance, motivation and providing facilities for this work.

References

1. Suvarapu LN, Baek SO (2015) Recent developments in the speciation and determination of mercury using various analytical techniques. *J Anal Methods Chem* 2015:1–19
2. Herawati N, Suzuki S, Hayashi K, Rivai IF, Koyoma H (2000) Cadmium, copper and zinc levels in rice and soil of Japan, Indonesia and China by soil type. *Bull Environ Contam Toxicol* 64:33–39
3. Shen Y, Hu JW, Liu TT, Gao HW, Hu ZJ (2019) Colorimetric and fluorogenic chemosensors for mercury ion based on nanomaterials. *Prog Chem* 31:536–549
4. Fen YW, Yunus WMM (2013) Surface plasmon resonance spectroscopy as an alternative for sensing heavy metal ions: a review. *Sens Rev* 33:305–314
5. Khanmohammadi A, Ghazizadeh AJ, Hashemi P, Afkhani A, Arduini F, Bagheri H (2020) An overview to electrochemical biosensors and sensors for the detection of environmental contaminants. *J Iran Chem Soc* 1–19. <https://doi.org/10.1007/s13738-020-01940-z>
6. Banfalvi G (2011) Cellular effects of heavy metals. Springer, Netherlands, London, New York
7. Samanta P, Let S, Mandal W, Dutta S, Ghosh SK (2020) Luminescent metal-organic frameworks (LMOFs) as potential probes for the recognition of cationic water pollutants. *Inorg Chem Front* 7:1801–1821
8. Rasheed T, Bilal M, Nabeel F, Iqbal HMN, Li CL, Zhou YF (2018) Fluorescent sensor based models for the detection of environmentally-related toxic Heavy Metals. *Sci Total Environ* 615:476–485
9. Oliveira E, Nunez C, Santos HM et al (2015) Revisiting the use of gold and silver functionalised nanoparticles as colorimetric and fluorometric chemosensors for metal ions. *Sensor Actuator B Chem* 212:297–328
10. Kumar P, Kim KH, Bansal V, Lazarides T, Kumar N (2017) Progress in the sensing techniques for heavy metal ions using nanomaterials. *J Ind Eng Chem* 54:30–43
11. Heavy Metal sad RA, Tripathy N, Khosla A et al. (2019) Review-recent advances in nano-structured graphitic carbon nitride as a sensing material for heavy metal ions. *J Electrochem Soc* 167:1–19

12. Shunmugam R, Gabriel GJ, Smith CE, Aamer KA, Tew GN (2008) A highly selective colorimetric aqueous sensor for mercury. *Chem Eur J* 14:3904–3907
13. Xu XY, Ray R, Gu YL et al (2004) Electrophoretic analysis and purification of fluorescent single-walled carbon nanotube fragments. *J Am Chem Soc* 126:12736–12737
14. Duran N, Simoes MB, de Moraes ACM, Favaro WJ, Seabra AB (2016) Nanobiotechnology of carbon dots: a review. *J Biomed Nanotechnol* 12:1323–1347
15. Zhang DD, Jiang WZ, Zhao YP, Dong Y, Feng X, Chen L (2019) Carbon Dots rooted PVDF membrane for fluorescence detection of heavy metal ions. *Appl Surf Sci* 494:635–643
16. Wei JY, Lou Q, Zang JH et al (2020) Scalable synthesis of green fluorescent carbon dot powders with unprecedented efficiency. *Adv Opt Mater* 8:1901938
17. Cui L, Ren X, Sun M, Liu H, Xia L (2021) Carbon dots: synthesis, properties, and applications. *Nanomaterials* 11(12):3419. <https://doi.org/10.3390/nano11123419>
18. Shen CL, Zheng GS, Wu MY et al (2020) Chemiluminescent carbon nanodots as sensors for hydrogen peroxide and glucose. *Nanophotonics* 9:3597–3604
19. Shen CL, Lou Q, Zang JH et al (2020) Near-infrared chemiluminescent carbon nanodots and their application in reactive oxygen species bioimaging. *Adv Sci* 7:1903525
20. Shen CL, Lou Q, Lv CF et al (2019) Bright and multicolor chemiluminescent carbon nanodots for advanced information encryption. *Adv Sci* 6:1802331
21. Tian M, Liu YM, Wang YT, Zhang Y (2019) Facile synthesis of yellow fluorescent Carbon Dots for highly sensitive sensing of cobalt ions and biological imaging. *Anal Methods* 11:4077–4083
22. Boakye-Yiadom KO, Kesse S, Opoku-Damoah Y et al (2019) Carbon Dots: applications in bioimaging and theranostics. *Int J Pharm* 564:308–317
23. Qin JJ, Dong BH, Gao RJ et al (2017) Water-soluble silica-coated ZnS: Mn nanoparticles as fluorescent sensors for the detection of ultratrace copper(II) ions in seawater. *Anal Methods* 9:322–328
24. Cheng CG, Xing M, Wu QL (2019) A universal facile synthesis of nitrogen and sulfur co-doped Carbon Dots from cellulose-based biowaste for fluorescent detection of Fe³⁺ ions and intracellular bioimaging. *Mater Sci Eng C* 99:611–619
25. Xu Q, Zhang MR, Liu Y et al (2018) Synthesis of multi-functional green fluorescence Carbon Dots and their applications as a fluorescent probe for Hg²⁺ detection and zebrafish imaging. *New J Chem* 42:10400–10405
26. Bogireddy NKR, Barba V, Agarwal V (2019) Nitrogen-doped graphene oxide dots-based “Turn-OFF” H₂O₂, Au(III), and “TurnOFF-ON” Hg(II) sensors as logic gates and molecular keypad locks. *ACS Omega* 4:10702–10713
27. Guo YM, Chen YZ, Cao FP, Wang LJ, Wang Z, Leng YM (2017) Hydrothermal synthesis of nitrogen and boron doped carbon quantum dots with yellow-green emission for sensing Cr(VI), anti-counterfeiting and cell imaging. *RSC Adv* 7:48386–48393
28. Fan CH, Ao KL, Lv PF et al (2018) Fluorescent nitrogen-doped Carbon Dots via single-step synthesis applied as fluorescent probe for the detection of Fe³⁺ ions and anti-counterfeiting inks. *NANO* 13:1–14
29. Li RS, Liu JH, Yang T et al (2019) Carbon quantum dots-europium(III) energy transfer architecture embedded in electrospun nanofibrous membranes for fingerprint security and document counterspy. *Anal Chem* 91:11185–11191
30. Xie HZ, Dong J, Duan JL, Waterhouse GIN, Hou JY, Ai SY (2018) Visual and ratiometric fluorescence detection of Hg²⁺ based on a dual-emission Carbon Dots-gold nanoclusters nanohybrid. *Sensor. Actuator. B Chem.* 259:1082–1089
31. Niu WJ, Shan D, Zhu RH, Deng SY, Cosnier S, Zhang XJ (2016) Dumbbell-shaped carbon quantum dots/AuNCs nanohybrid as an efficient ratiometric fluorescent probe for sensing cadmium (II) ions and L-ascorbic acid. *Carbon* 96:1034–1042
32. Yang T, Wang XY, Wang LY, Chen ML, Wang JH (2016) Biological cells in the speciation analysis of Heavy Metals. *Anal Methods* 8:8251–8261
33. Bhati A, Anand SR, Saini D, Khare P, Dubey P, Sonkar SK (2018) Self-doped nontoxic red-emitting MgN-embedded Carbon Dots for imaging, Cu(II) sensing and fluorescent ink. *New J Chem* 42:19548–19556

34. Das NK, Sengupta SR (2008) Arsenicosis: diagnosis and treatment. *Indian J Dermatol Venereol Leprol* 74(6):571–581
35. Li F, Yang DY, Xu HP (2019) Non-metal-heteroatom-doped Carbon Dots: synthesis and properties. *Chem Eur J* 25:1165–1176
36. Liu FJ, Jiang Y, Fan C et al (2018) Fluorimetric and colorimetric analysis of total iron ions in blood or tap water using nitrogen doped Carbon Dots with tunable fluorescence. *New J Chem* 42:9676–9683
37. He X, Han Y, Luo XL et al (2020) Terbium (III)-referenced N-doped Carbon Dots for ratiometric fluorescent sensing of mercury (II) in seafood. *Food Chem* 320:1–8
38. Ye ZQ, Tang R, Wu H, Wang BB, Tan MQ, Yuan JL (2014) Preparation of europium complex-conjugated Carbon Dots for ratiometric fluorescence detection of copper(II) ions. *New J Chem* 38:5721–5726
39. Beiraghi A, Najibi-Gehraz SA (2020) Purification and fractionation of Carbon Dots using pH-controlled cloud point extraction technique. *J Nanostruct* 10:107–118
40. Koutsoukis A, Akouros A, Zboril R, Georgakilas V (2018) Solid phase extraction for the purification of violet, blue, green and yellow emitting Carbon Dots. *Nanoscale* 10:11293–11296
41. Sahu S, Behera B, Maiti TK, Mohapatra S (2012) Simple onestep synthesis of highly luminescent Carbon Dots from orange juice: application as excellent bio-imaging agents. *Chem Commun* 48:8835–8837
42. Kokorina AA, Sapelkin AV, Sukhorukov GB, Goryachev IY (2019) Luminescent carbon nanoparticles separation and purification. *Adv Colloid Interface Sci* 274:1–14
43. Zheng M, Xie ZG, Qu D et al (2013) On off on fluorescent carbon dot nanosensor for recognition of chromium(VI) and ascorbic acid based on the inner filter effect. *ACS Appl Mater Interfaces* 5:13242–13247
44. Wang HT, Liu S, Xie YS et al (2018) Facile one-step synthesis of highly luminescent N-doped Carbon Dots as an efficient fluorescent probe for chromium(vi) detection based on the inner filter effect. *New J Chem* 42:3729–3735
45. Xu Y, Li HY, Wang B et al (2018) Microwave-assisted synthesis of Carbon Dots for “turn-on” fluorometric determination of Hg(II) via aggregation-induced emission. *Microchim Acta* 185:1–7
46. Wang CX, Jiang KL, Xu ZZ, Lin HH, Zhang C (2016) Glutathione modified carbon-dots: from aggregation-induced emission enhancement properties to a “turn-on” sensing of temperature/Fe³⁺ ions in cells. *Inorg Chem Front* 3:514–522
47. Tian YC, Kelarakis A, Li L et al (2018) Facile fluorescence “Turn on” sensing of lead ions in water via carbon nanodots immobilized in spherical polyelectrolyte brushes. *Front Chem* 6:1–13
48. Bhattacharya S, Sarkar S, Shunmugam R (2013) Unique norbornene polymer based “in-field” sensor for As (III). *J Mater Chem A* 1:8398–8405
49. Holak W (1980) Determination of arsenic by cathodic stripping voltammetry with a hanging mercury drop electrode. *Anal Chem* 52:2189–2192
50. Bjorklund G, Crisponi G, Nurchi VM, Cappai R, Djordjevic AB, Aaseth J (2019) A review on coordination properties of thiol-containing chelating agents towards mercury, cadmium, and lead. *Molecules* 24:1–32
51. Roshni V, Gujar V, Pathan H et al (2019) Bioimaging applications of carbon dots (C. dots) and its cystamine functionalization for the sensitive detection of Cr(VI) in aqueous samples. *J Fluoresc* 29:1381–1392
52. Kaur H, Raj P, Sharma H, Verma M, Singh N, Kaur N (2018) Highly selective and sensitive fluorescence sensing of nanomolar Zn²⁺ ions in aqueous medium using Calix 4 arene passivated Carbon Quantum Dots based on fluorescence enhancement: real-time monitoring and intracellular investigation. *Anal Chim Acta* 1009:1–11
53. He X, Han Y, Luo XL et al (2020) Terbium (III)-referenced N-doped carbon dots for ratiometric fluorescent sensing of mercury (II) in seafood. *Food Chem* 320:1–8
54. Molaei MJ (2020) The optical properties and solar energy conversion applications of carbon quantum dots: A review. *Sol Energy* 196:549–566

55. Fernando KAS, Sahu S, Liu YM et al (2015) Carbon quantum dots and applications in photocatalytic energy conversion. *ACS Appl Mater Interfaces* 7:8363–8376
56. Jash B, Muller J (2018) A stable zinc(II)-mediated base pair in a parallel-stranded DNA duplex. *J Inorg Biochem* 186:301–306
57. Miyake Y, Togashi H, Tashiro M et al (2006) Mercury(II)-mediated formation of thymine-Hg-II-thymine base pairs in DNA duplexes. *J Am Chem Soc* 128:2172–2173
58. Sinha I, Guerra CF, Muller J (2015) A highly stabilizing silver(I)-mediated base pair in parallel-stranded DNA. *Angew Chem Int Ed* 54:3603–3606
59. Zhang ZH, Li J, Wang XY, Liang AH, Jiang ZL (2019) Aptamer-mediated N/Ce-doped carbon dots as a fluorescent and resonance Rayleigh scattering dual mode probe for arsenic(III). *Microchim Acta* 186:1–9
60. Liu Y, Gong XJ, Gao YF et al (2016) Carbon-based dots co-doped with nitrogen and sulfur for Cr(VI) sensing and bioimaging. *RSC Adv* 6:28477–28483
61. Huang S, Yang EL, Yao JD, Chu X, Liu Y, Xiao Q (2019) Nitrogen, phosphorus and sulfur tri-doped Carbon Dots are specific and sensitive fluorescent probes for determination of chromium(VI) in water samples and in living cells. *Microchim Acta* 186:1–10
62. Huang S, Yang EL, Yao JD, Liu Y, Xiao Q (2018) Red emission nitrogen, boron, sulfur co-doped Carbon Dots for “on-off-on” fluorescent mode detection of Ag⁺ ions and L-cysteine in complex biological fluids and living cells. *Anal Chim Acta* 1035:192–202
63. Chen YQ, Sun XB, Wang XY, Pan W, Yu GF, Wang JP (2020) Carbon Dots with red emission for bioimaging of fungal cells and detecting Hg²⁺ and ziram in aqueous solution. *Spectrochim Acta Mol Biomol Spectrosc* 233:1–9
64. Tian M, Liu YM, Wang YT, Zhang Y (2019) Facile synthesis of yellow fluorescent Carbon Dots for highly sensitive sensing of cobalt ions and biological imaging. *Anal Methods* 11:4077–4083

Study of Smart Sensor Designing Parameters for Water Resources Management



Tanmay Sardar, Satanand Mishra, and Shivani Pandey

Abstract Geo-specific data of water contaminants are important and rare for water resources management. Smart sensors are a basic and powerful tool for managing water resources. Many technologies like Digital Twinning, Automation, Smart Industries, and smart cities are designed with the help of real-time intelligent sensors. Lab-based sensing technology misses the location accuracy and the time. The location-based portable smart sensor is a key changer for the scenario. A smart sensor module is divided into 5 nodes such as Sensing Node, Controlling Node, Wireless Network Node, Alarming Node, and Power Node. For designing any module, it is very important to compare and select different parts and the components. This study consists of a detailed description of different nodes, controlling parameters, and selective parameters. Comparative parameters for the selection and designing of components are discussed in this paper. The primary objective of the study is to highlight the essential parameters and selection criteria, which are required for sensor designing inset of water resources management and to know about smart technology and different components, and select parameters for a specific application. Suitable nodes and components are selected and simulated for an optimized interface. The study shows the noble design of the sensor which is required for the detection of water contaminant (Arsenic) at the point of care.

Keywords Arsenic · Smart sensor · Water quality monitoring · Geo-specific

T. Sardar

Mechanical Engineering Department, Motilal Nehru National Institute of Technology, Allahabad 211004, India

S. Mishra (✉) · S. Pandey

Academy of Scientific and Innovative Research (AcSIR), CSIR-Advanced Materials and Processes Research Institute (AMPRI), Bhopal 462026, India

e-mail: snmishra07@gmail.com

1 Introduction

Earth’s 71% of the surface is covered with water even though only 2.5% of freshwater exists for use, that’s the reason monitoring water is very vital [1]. The sensor is a key in Water Quality Monitoring (WQM). WQM was performed in the lab-based sensing system, this system takes time to get a result as the sampling process is way away from labs. Lab-based systems are costly, they need technical experts, and they miss geo-specific data. Geo-specific data is the contamination data referring to a specific location (latitude and longitude) and the information of source like underground, surface, etc. [2, 3]. The actual concentration parameters are to be determined in time, stored securely, easily accessed, and serve with a user-friendly interface for a user. The smart sensor is an easy solution for the need [4].

Smart sensor or intelligent sensor is an upcoming technology and assembly for a new era. Smart sensor is also the simple, basic, and important starting node of the IoT cycle or cyber world [5–7]. Figure 1 shows a detailed view of the smart sensors and their applications.

Smart sensors consisting different nodes like sensing, controlling, display and alarming, networking, and power node. Blue marked blocks in Fig. 1 show the main nodes of the smart sensing module. Smart sensor has a wide application area. Smart industry, Digital Twining, and Smart cities emerge with a basic and initial point as a Smart sensor. Not only the industries but Water Quality Monitoring, Environmental Study, Agricultural and Forest Monitoring, and many more fields are monitored with the use of smart sensors [8–10].

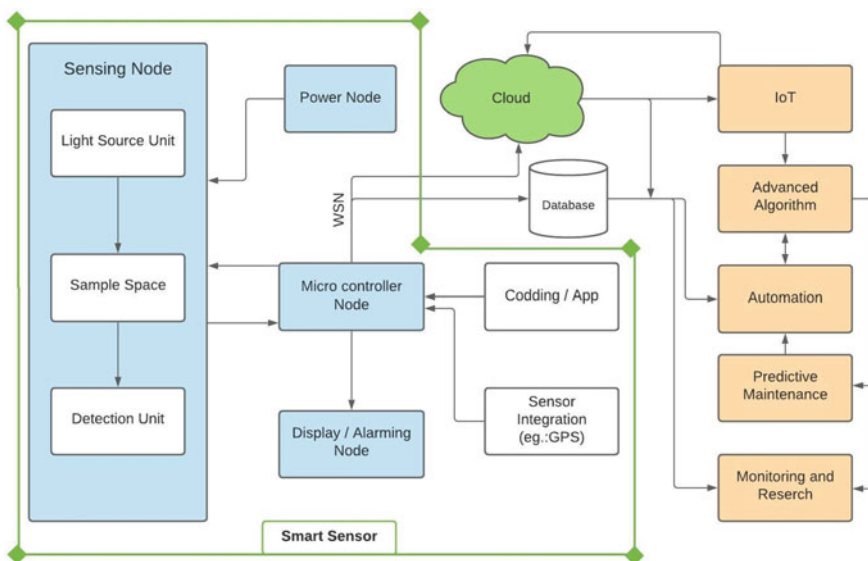


Fig. 1 Conceptual figure of smart sensing world

2 Methodology

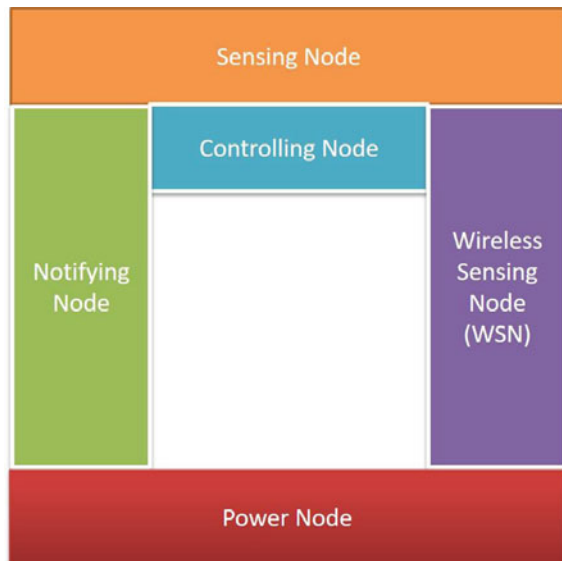
The compact design of a specific real-time application-based sensor is needed for the fieldwork. The smart sensor is divided into different nodes. Different nodes are studied deeply and have been chosen for the study. Figure 1 shows different nodes and sub-nodes of the smart sensing module. Figure 2 shows the block diagram for the proposed design. In this section, a detailed description of the sensor design is given.

2.1 Sensing Node

The most varying and important part of the sensor module is the sensing node. It consists of the sensor as a transducer and the process of signal conditioning [11–13]. The transducer is part that is converted to the optical energy of the receptor material into the known value of current energy in this study. The importance of a node is to sense the target molecules, which are to be detected. In this study, Arsenic (III) is a target molecule. The prime objective is to find out the best suitable sensing material and phenomenon for the detection of the target molecule.

Different sensing materials and phenomena like Colorimetry, Fluorescence, FRET and Surface Plasmon Resonance (SPR) are used in this node. Carbon Quantum Dot (CQD) is chosen as a sensing material for Arsenic showing a fluorescence quenching

Fig. 2 Block diagram of a proposed design



mechanism. The Sensing Node covers material, phenomenon, and signal conditioning. Material that helps to attract the target molecule and reflect the concentration as a change in the emitting light.

Along with optical other phenomena are also can be used in a sensor. For the nobility of the design, different sensing modules like PH, GPS and Temp sensors are included for advancement. Different GPS modules for geo-specificity are also given in this study. For the designing purpose, the sensing node is divided into 3 major parts which are the source unit, cuvette unit, and detection unit which is detailed in the subsequent section.

2.1.1 Energy Source Unit

Sensing material for detection of Arsenic, gives optical phenomena like colorimetric, fluorescence, surface plasmon resonance (SPR), etc. these phenomena are based on rules for Electromagnetic waves [14, 15]. Light is an electromagnetic wave that gets absorbed, reflects and emits by the receptor or target molecules when kept under an external monochromatic source. Light energy is absorbed to show colorimetric, scattering, or fluorescence phenomena by different materials [15]. Different intensity of light at different wavelength gets absorbed to excite the material from a normal state to a higher-level energy state as shown in Fig. 3.

The monochromator is one major part of the sensor/spectrometer. The sole objective of the monochromator is to provide monochromatic (single wavelength) light for detection purposes [17]. Figure 4 shows the components and working diagram of the monochromator. Prism/Gratings separates the white light into different wavelengths. The white light contains a range of wavelengths so that need to separate those to get specific wavelength light for detection accuracy. The major difference between these two elements is that the dispersion of prisms is non-linear while gratings offer linear

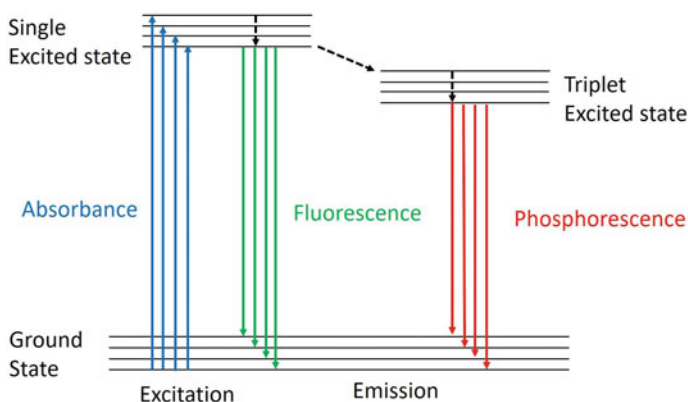


Fig. 3 Energy transmission of materials from the ground to excited state for a different phenomenon [16]

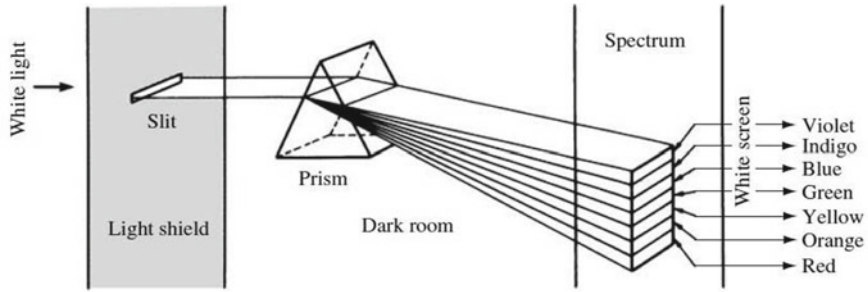


Fig. 4 The architectural flow diagram in the Monochromator [19]

dispersion [18]. These complex assemblies are easily upgraded with Light Emitting Diode (LED). LED with different colors means different wavelengths are easily used over the monochromator.

2.1.2 Cuvette Unit

A cuvette unit or sampling unit is a place where different samples are collected and placed for detection. The different cuvettes are available and one is selected according to purpose. Figure 5 shows different types of cuvettes according to sample size and path length. Generally, Cuvettes are found in plastic, glass, and Quartz material [20]. The path length is important in the calculation of absorbance and concentration.

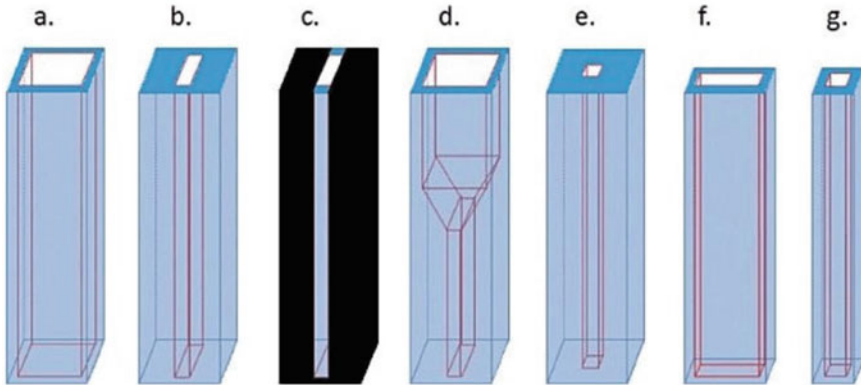


Fig. 5 Cuvette classification is based on different shapes and sizes [21]

2.1.3 Detection Unit

The material gets excited by absorbing the photons (energy) and it releases the energy with a higher wavelength [22]. That energy is to be calculated with the help of a detector. Different spectrometers have different light detectors. A fluorometer is a device that measures several aspects of fluorescence, such as the intensity and wavelength distribution of the emission following excitation. Some of the more popular types of light intensity sensors are CMOS-based, photodetectors, phototransistors, photoresistors, and photodiodes [23–26]. A detector regulates how much current will travel through the circuit based on the amount of light it senses. In a dark environment, the sensor only allows a little quantity of electricity to pass and If it senses a strong light, it allows more electricity to flow [17, 22].

2.2 Microcontroller

Microcontroller Unit (MCU) is used to control the various steps and flow of the process [27]. A controller is a device that is used to control a process. Previously, controllers were built entirely of logical components and were quite big and heavy boxes [28]. Miniaturization continued later. All of the components required for a microcontroller were assembled on a single chip. A microprocessor is a digital computer with a CPU built onto a single VLSI chip. A microprocessor is a CPU that is built onto a single VLSI at a low cost. A microcomputer is a digital computer that includes a microprocessor as a CPU, as well as input/output devices and memory. Table 1 shows comparative chart for microcontroller [29–33].

In Table 1, some specifications will be important while selecting a microcontroller such as RAM, ROM, numbers of Input/Output Pins (GPIO), Processor, Cost and inbuilt wireless networking modules like Bluetooth and WiFi, similarly coding part is also important while selecting the microcontroller.

2.3 Wireless Networking Node

Communication Network is one of the important parts of the data transfer process. Wireless Sensor Network (WSN) is one important part and factor in managing huge systems like smart cities, industries and Water Quality management. If some sensor senses some important factor, then that data has to be stored and communicated with the cyber world. Old techniques of communication were cabling and wired networking which are costly, restricted, and complex in structure.

Portability is a key feature of our sensor than to be in lab-based research/detection process. For that reason, being wireless is much important. The proposed design is portable i.e. it will be a real-time field-based sensor so, it will be very complex to carry those wires and connect them through wired networking by Fiber optics,

Table 1 Comparative chart for selection of microcontroller

Specifications	Arduino Uno	Raspberry Pi-3	Intel Galileo gen 2	ESP32	Arduino Nano
Processor	ATmega328P	ARM Cortex-A7	Intel Pentium	Xtensa	ATmega328P
Input Voltage	/7-12 V	5 V/7 V	3.3–5 V	3.3 V	7–12 V
Operating volt	5 V	–	–	2.3–3.6 V	5 V
Speed of CPU	16 MHz	900 MHz	400 MHz	160 MHz	16 MHz
Analog I/O	6/0	0	0	–	8/0
Digital IO/PWM	14/6	17/2	14/6	32	14/6
EEPROM/SRAM	½ (kB)	1 GB Ram	8 KB/512 KB	520 KB	½ (kB)
Flash	32 KB	SD card	8 MB	248 KB	32 KB
USB	Regular	4	2	–	Mini
Dimensions (mm)	68.6 × 53.3	85.60 × 56	123.8 × 72.0	–	18 × 45
BT Module (inbuild)	No	Yes	–	Yes	No
WiFi Module (inbuild)	No	Yes	Yes	Yes	No
Codding	Arduino, C++	Python	Python	C, C++	Arduino, C++
Cost (Rs)	200.00	3000.00	5300.00	400	350.00

Table 2 Comparative chart for wireless networking tool

Specifications	BT	Wi-Fi	Zig Bee	UWB
Range (m)	10	100	10–70	10
Speed	1Mbps	50Mbps	250Kbps	100Mbps
Connectivity/Topology	One to one	One to many	Mesh Topology	–
No. of Cell node (Max)	7	32	Upto 65,000	8
Battery life	1–8 days	1–5 days	100–1000 days	Low
Accuracy	1–5 m	5–15 m	0.5 m	100 cm

telephone cables, Ethernet cables, and many more. Researchers found modern alternative technology like Bluetooth(BT), WiFi, ZigBee, Wide Area Networking (WAN), UWB, and many more upcoming tools which are compared in Table 2 [34–37]. BT is selected for design after considering the battery life and cost of different modules.

2.4 Alarming Node

This is the final part of the flow. The calculated data is informed to the user. It mainly contains a display unit and an alarming unit. The display unit will show the data or

the concentration parts on the screen and alarming nodes will alarm the people of dangerous levels. The display unit is connected with the controller which will control the display interface and data. Computer monitors, mobiles, different screens, colored LEDs, and many more can be included in the display unit. The alarming unit includes different lights and sounds to alarm the user.

3 Geo-Specificity

Contamination parameters mapped with the location, is a precise way to WQM or to decide preventing measures for quality. In the Era of automation, manual data entry is no reliable way for real-time management. Global Positioning System Module (GPS) is a well-grounded tool that helps with geo-specificity. Figure 6 shows a simulated circuit for specific GPS modules.

Some well-known firms rely on geolocation-based apps for best results. Geo-specific applications are widely used in Uber, Ola, Zomato, and many more service providers. Time and positional characteristics are very precise in GPS Modules that can be used for geo-specific sensing devices, data, and study. Mobile GPS or external GPS has been included in the design. Internal GPS from mobile device is used in sensor with the help of Smartphone-Based App (SBA) [38–43]. An independent portable sensor uses external GPS for geo-specificity [44].

Figure 6 shows a simulation of various GPS modules. One portable sensor is enough to map parameters geo-sensitively, and also sensing networks are used with appropriate topology [45]. Table 3 shows comparative study of external GPS module [46–50].

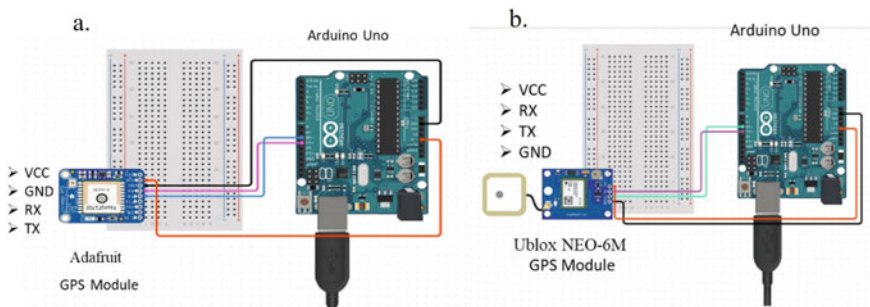


Fig. 6 GPS Module simulation with microcontroller **a** Adafruit Ultimate GPS. **b** Ublox NEO-6M GPS Module

Table 3 Comparative chart for external GPS module

Specifications	Adafruit ultimate GPS Breakout	NZ mini GPS (NAZE32)	Ublox NEO-6 M GPS Module
No of Pins	9 Pins	4 (VCC, RX, TX, GND)	4 (VCC, RX, TX, GND)
Volt	5 V	–	2.7 V–3.6 V
Current	20 mA	–	10–100 mA
Size	25.5 × 35 × 6.5 mm	26 × 25 × 8 mm	16 × 12.2 × 2.4 mm
Weight	8.5 g	10gm	–
Position Accuracy	< 3 m	–	2.5 m
Update rate	1–10 Hz	–	1–5 Hz
Cost(Rs)	2500–4500	900	750.00

4 Result

In this study, we have proposed a specific design of the sensor for Arsenic detection which is given in Fig. 7.

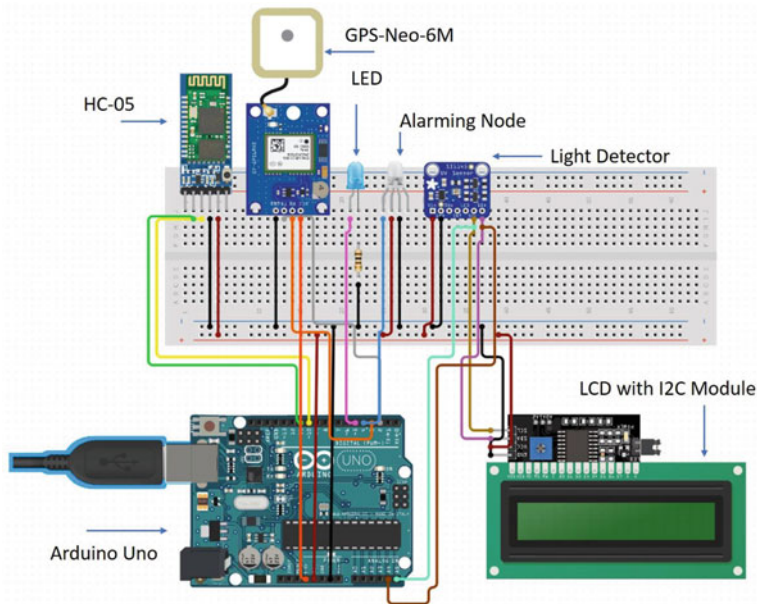


Fig. 7 Simulation for circuit

Figure 7 shows the simulation of the designed circuit. The designed circuit consists of an external GPS Module, Bluetooth, display 16X2 with I2C Module, RGB LED for alarming purposes, and Arduino Uno to control all commands. For a better result, it is recommended that the given circuit is to be simulated before the establishment of the connections. In Fig. 7, the chosen components are compatible, and well interfaced for the specific purpose. These components are connected with the help of jumping cables and breadboards as shown in Fig. 7. This will be widely used for arsenic detection in potable water resources and management.

5 Conclusion

Many parameters are covered in the study of designing the sensing module. The proposed design is economical, reliable, compatible, and re-usable. It has the importance of different nodes and components. The design of the Smart sensor made industries, corporate and cities smarter as they are directly connected through the cyber world. The designed combination of nodes and components has easily marked its importance and requirement. A single smart portable sensor is enough to cover huge areas at the point of care. The selected components have fulfilled the objective and it is simulated and optimized. The proposed design gives compact smart portable wireless geo-Opto-sensor at the point of care rewarding the objective of water quality monitoring.

6 Future Scope

We plan to manufacture the proposed design and test that sensor for water quality monitoring in the field.

Acknowledgements I would like to thank Director, CSIR-Advanced Materials and Processes Research Institute, Bhopal for giving me the opportunity.

References

1. Adu-Manu KS, Tapparello C, Heinzelman W, Katsriku FA, Abdulai JD (2017) Water quality monitoring using wireless sensor networks: current trends and future research directions. *ACM Trans Sens Netw (TOSN)* 13(1):1–41
2. Liao J, Chang F, Han X, Ge C, Lin S (2020) Wireless water quality monitoring and spatial mapping with disposable whole-copper electrochemical sensors and a smartphone. *Sens Actuators B Chem* 306:127557

3. Mamun KA, Islam FR, Haque R, Khan MG, Prasad AN, Haqva H, Mudliar RR, Mani FS (2019) Smart water quality monitoring system design and KPIs analysis: case sites of Fiji surface water. *Sustainability* 11(24):7110
4. Sicard C, Glen C, Aubie B, Wallace D, Jahanshahi-Anbuhi S, Pennings K, Daigger GT, Pelton R, Brennan JD, Filipe CD (2015) Tools for water quality monitoring and mapping using paper-based sensors and cell phones. *Water Res* 70:360–369
5. Schütze A, Helwig N, Schneider T (2018) Sensors 4.0—smart sensors and measurement technology enable Industry 4.0. *J SensS Sens Syst* 7(1):359–371
6. Chen B, Wan J, Shu L, Li P, Mukherjee M, Yin B (2017) Smart factory of industry 4.0: Key technologies, application case, and challenges. *IEEE Access* 6, 6505–6519 (2017)
7. Bačić Ž, Jogun T, Majić I (2018) Integrated sensor systems for smart cities. *Tehnički vjesnik* 25(1):277–284
8. Sartori D, Brunelli D (2016) A smart sensor for precision agriculture powered by microbial fuel cells. *IEEE SensS Appl Symp* 1–6
9. Shafi U, Mumtaz R, Garcia-Nieto J, Hassan SA, Zaidi SAR, Iqbal N (2019) Precision agriculture techniques and practices: from considerations to applications. *Sensors* 19(17):3796
10. Cui F (2020) Deployment and integration of smart sensors with IoT devices detecting fire disasters in huge forest environment. *Comput Commun* 150:818–827
11. Adu-Manu KS, Katsriku FA, Abdulai JD, Engmann F (2020) Smart river monitoring using wireless sensor networks. *Wirel Commun Mob Comput* (2020)
12. Espírito-Santo A, Serra P, Albuquerque S, Ribeiro B, Santos F, Páscoa J (2017) September. Low-power smart sensing in energy and water systems integration. *IEEE Int Work Meas Netw (M&N)* 1–6
13. Adamo F, Attivissimo F, Carducci CGC, Lanzolla AML (2014) A smart sensor network for sea water quality monitoring. *IEEE Sens J* 15(5):2514–2522
14. Frau I, Korostynska O, Mason A, Byrne P (2018) Comparison of electromagnetic wave sensors with optical and low-frequency spectroscopy methods for real-time monitoring of lead concentrations in mine water. *Mine Water Environ* 37(3):617–624
15. Kryuchkyan GY, Shahnazaryan V, Kibis OV, Shelykh IA (2017) Resonance fluorescence from an asymmetric quantum dot dressed by a bichromatic electromagnetic field. *Phys Rev A* 95(1):013834
16. Jasco, “jasco,”. <https://jascoinc.com/learning-center/theory/spectroscopy/fluorescence-spectroscopy/>. Accessed 23 June 2021
17. Chen H, Zhou K, Zhao G (2018) Gold nanoparticles: from synthesis, properties to their potential application as colorimetric sensors in food safety screening. *Trends Food Sci Technol* 78:83–94
18. Martinez OE (1986) Grating and prism compressors in the case of finite beam size. *JOSA B* 3(7):929–934
19. Ohta N, Robertson A (2006) *Colorimetry: fundamentals and applications*. John Wiley & Sons
20. Anzivino G, Arnaudon H, Baillon P, Benetti P, Boskma L, Burger P, Contin A, DeSalvo R, Gorodetzky P, Grassi D, Hao W (1995) Review of the hybrid photo diode tube (HPD) an advanced light detector for physics. *Nucl Instrum Methods Phys Res, Sect A* 365(1):76–82
21. Predotova M, Kretschmann R, Gebauer J, Buerkert A (2011) Effects of cuvette surface material on ammonia-, nitrous oxide-, carbon dioxide-, and methane-concentration measurements. *J Plant Nutr Soil Sci* 174(3):347–349
22. Herman B (2020) *Fluorescence microscopy*. Garland Science
23. Bai YW, Ku YT (2008) Automatic room light intensity detection and control using a microprocessor and light sensors. *IEEE Trans Consum Electron* 54(3):1173–1176
24. Wang Y, Rajib SSM, Collins C, Grieve B (2018) Low-cost turbidity sensor for low-power wireless monitoring of fresh-water courses. *IEEE Sens J* 18(11):4689–4696
25. Seo D, Oh S, Shin S, Lee M, Hwang Y, Seo S (2019) Smartphone compatible on-site fluorescence analyzer for spilled crude oil based on CMOS image sensor. *Sens Actuators B Chem* 289:93–99
26. Demchenko AP (2009) Fluorescence detection techniques. *Introduction to Fluorescence Sensing*, pp 65–118

27. Yadav DS (2004) Microcontroller: features and applications. New Age International
28. Petruzella FD (2005) Programmable logic controllers. Tata McGraw-Hill Education
29. Warren JD, Adams J, Molle H (2011) Arduino for robotics. In: *Arduino robotics*. Apress, Berkeley, CA, pp 51–82
30. <https://www.intel.com/content/dam/www/public/us/en/documents/datasheets/galileo-g2-datasheet.pdf>
31. <https://datasheet.octopart.com/A000066-Arduino-datasheet-38879526.pdf>. Accessed 20 Feb 2021
32. Rai P, Rehman M (2019) ESP32 based smart surveillance system. In: 2019 2nd International Conference on Computing, Mathematics and Engineering Technologies (iCoMET), pp 1–3
33. <https://www.arduino.cc/en/uploads/Main/ArduinoNanoManual23.pdf>
34. Gutierrez Pascual MD (2012) Indoor Location Systems Based on Zigbee Networks
35. Xiao J, Li JT (2020) Design and implementation of intelligent temperature and humidity monitoring system based on ZigBee and WiFi. *Procedia Comput Sci* 166:419–422
36. Leccese F, Cagnetti M, Trinca D (2014) A smart city application: a fully controlled street lighting isle based on Raspberry-Pi card, a ZigBee sensor network and WiMAX. *Sensors* 14(12):24408–24424
37. Uradzinski M, Guo H, Liu X, Yu M (2017) Advanced indoor positioning using zigbee wireless technology. *Wireless Pers Commun* 97(4):6509–6518
38. Xu D, Huang X, Guo J, Ma X (2018) Automatic smartphone-based microfluidic biosensor system at the point of care. *Biosens Bioelectron* 110:78–88
39. Xing Y, Zhu Q, Zhou X, Qi P (2020) A dual-functional smartphone-based sensor for colorimetric and chemiluminescent detection: A case study for fluoride concentration mapping. *Sens Actuators B Chem* 319:128254
40. Xiao M, Liu Z, Xu N, Jiang L, Yang M, Yi C (2020) A Smartphone-based sensing system for on-site quantitation of multiple heavy metal ions using fluorescent carbon nanodots-based microarrays. *ACS sensors* 5(3):870–878
41. Bonyar A, Nagy P, Mayer V, Vitéz A, Gerecs A, Sántha H, Harsányi G (2017) A colorimetry based, semi-automated portable sensor device for the detection of arsenic in drinking water. *Sens Actuators B Chem* 251:1042–1049
42. Covaciu D, Preda I, Ciolan G (2011) GPS based data acquisition system for mobile applications. *Acta Technica Jaurinensis* 4(4):453–464
43. <https://www.seeedstudio.com/Grove-GPS-Module.html>
44. Shen L, Stopher PR (2014) Review of GPS travel survey and GPS data-processing methods. *Transp Rev* 34(3):316–334
45. Available: <https://www.adafruit.com/product/746>
46. [https://www.u-blox.com/sites/default/files/products/documents/NEO-6_DataSheet_\(GPS.G6-HW-09005\).pdf](https://www.u-blox.com/sites/default/files/products/documents/NEO-6_DataSheet_(GPS.G6-HW-09005).pdf)
47. <https://robu.in/product/nz-mini-gps-naze32/>
48. <https://www.indiamart.com/nwitsys/networking-service.html>
49. “Robu.in”; NZ, [Online]. Available: <https://robu.in/product/nz-mini-gps-naze32/>
50. “;robu”; [Online]. Available: <https://robu.in/product/nz-mini-gps-naze32/>

Redesign of Assembly Line for Productivity Enhance in an Automotive Industry Using Line Balancing Technique



S. Karthik, S. Palani, and Ganapathy Srinivasan

Abstract In order to remain competitive in the market, industries have to manufacture more quality products and at the same time have to reduce costs. The main aim of any industry is to increase productivity to meet customer requirements. One of the techniques that industries use is the Line Balancing technique to enhance productivity and to reduce waste. Line balancing can be implemented to reduce the overburdening faced by the operator to distribute the work content equally among operators and at the point where bottle neck occurs. In this paper line, the balancing technique is applied in the crankshaft cell 3 assembly line in an automotive industry. The current study in the crankshaft cell 3 assembly line is carried out to remove wastes and to come up with ideas to solve them. After implementing the Line balancing technique, it resulted in a reduction of manpower from 4 to 3.

Keywords Line balancing · Crankshaft cell 3 Assembly line · Manpower

1 Introduction

Lean is defined as the systematic elimination of waste in order to add value to the product. Many automotive assembly lines implement Lean to meet customer requirements based on demand. The change from traditional Assembly line to Lean line balancing is carried out not only to improve the effectiveness and efficiency but also to increase profitability [1]. Assembly line gets unbalanced due to the fact that a bottle neck often occurs. Therefore, many wastes occur such as Inventory, Work in Progress and Over Processing.

Implementing Lean tools such as Line balancing will ensure smoothening flow of Work in progress between the steps of assembly process. Nallusamy reduced the lead

S. Karthik (✉)

Department of Mechanical Engineering, Veltech Rangarajan Dr.Sagunthala R&D Institute of Science and Technology, Avadi, Chennai, Tamil Nadu, India
e-mail: subburaman.karthik@gmail.com

S. Palani · G. Srinivasan

Department of Mechanical Engineering, Vel Tech Multitech, Avadi, Chennai, Tamilnadu, India

time of the product and improved productivity through the use of Line Balancing Technique [1]. Kulkarni et al., implemented assembly line balancing to improve the throughput of the Hose Assembly line [2]. Rajan et al., utilized a component-oriented line balancing approach and removed bottle neck in the assembly line to increase productivity [3]. Fansuri et al., applied Line Balancing in Electronics Manufacturing Service Company Production Assembly and increased the production output [4]. Rekha et al., enhanced manufacturing through the reduction of cycle time using Line balancing [5]. Nallusamy applied line balancing technique to increase productivity in gas stove burner manufacturing unit by reduction of Lead time [6].

The number of workstations has to be minimized therefore Line balancing must be implemented [7]. The end result of Line balancing would be an equal amount of work being assigned to each workstation. Reduction in idle time and manpower and also working on more than one machine were the results of Line balancing implementation [8]. Therefore, the outcomes were not only a reduction in the number of workstations but also cycle time. Concurrently, through line balancing the operator can work on more than one machine [9].

The above literature review studied that crankshaft cell 3 Assembly lines, which were considered as ineffective due to the occurrence of Work in progress.

In our research work, the line balancing technique is applied in crankshaft cell 3 assembly lines in an automotive industry for removing waste and to come up with ideas to reduce manpower.

2 Methodology

A company named xxxx was considered for the study which is carried out in this paper. Crankshaft cell 3 assembly line has been chosen. The cycle time for each workstation can be found out using multiple activity charts or man machine charts [10]. The steps in line balancing include takt time determination in crankshaft cell 3-line, identification of bottle neck in line, leveling to takt time, work content reallocating and rebalancing [11]. Takt time is defined as the ratio of available time per day in seconds for production to the daily customer demand. The Man machine chart for crankshaft cell 3 Line is shown below. Currently, the workstation count in crankshaft cell 3 lines is 14 and the manpower count is 4. The steps involved in line balancing are Referred below. [11].

2.1 Takt Time Calculation

The first step in Line balancing is the takt time calculation. The main objective is to see that the production rate matches with takt time [11]. The formula used to calculate Takt time can be calculated with the formula.

Takt time = Available production time per shift/Customer demand.

2.2 Establishing Time Studies

Time studies have to be conducted to identify the amount of time duration spent by personnel and equipments for each part of the process [11].

2.3 Identify Bottle Necks and Excess Capacity

After conducting time studies, one has to monitor which parts of the process are taking longer than takt time and also which parts are taking less than takt time [12].

2.4 Reallocate Resources

This involves arranging the task in sequence. Then tasks have to be rearranged to reduce excess capacity and bottle neck [12]. The operator's idle time has to be reduced by grouping all the elementary tasks. This has to be done in order to maximize the utilization of equipments and machines.

2.5 Make Other Improvements

Simultaneously other improvement efforts have to be carried out such as reducing setup time. Training can be given to operators who take a longer time to complete tasks to minimize setups. Machines can be upgraded and operators have to be ensuring that they follow machine setup and standard operating procedures.

3 Lay Out of CrankShaft Cell 3 Assembly Line

The layout of crankshaft cell 3 is shown in Fig. 1.

The Man Machine chart for each work station of crankshaft cell 3 is presented in Tables 1, 2, 3 and 4.

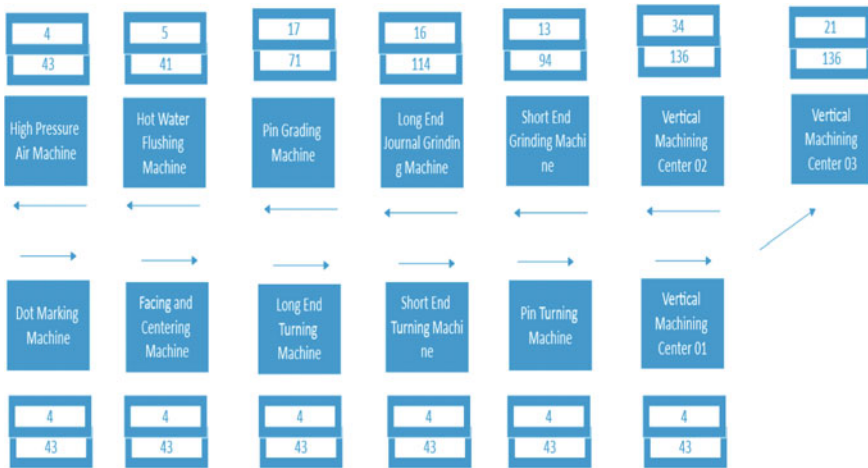


Fig. 1 Assembly line layout of crankshaft cell 3

4 Graph of Manual Time vs Takt Time

For each work station, the cycle time distribution before and after balancing are shown in Figs. 2 and 3.

As it can be seen from the figure above, the cycle time for each workstation is less than takt time. It can be concluded that capacity can meet customer demand but lean wastes would still occur. The comparison of Machine Autocycle time and manual time in seconds are tabulated in Table 5.

4.1 Takt Time Calculation

$$\text{Takt time} = \text{Available time}/\text{customer demand}$$

$$\begin{aligned} \text{Available time} &= 7.25\text{h} \times 3 \text{ shifts} \\ &= 7.25 \times 3 \times 60 \times 60 \times 0.80(\text{Taking operator efficiency as } 80\%) \\ &= 62,640\text{s} \end{aligned}$$

$$\text{Demand} = 460 \text{ units per day}$$

$$\begin{aligned} \text{Takt time} &= 62,640/460 \\ &= 136\text{s} \end{aligned}$$

Table 1 Man machine chart of dot marking machine, facing and centering machine, long end turning machine in Crankshaft cell 3 assembly line

Activity	Machine auto cycle time	Manual time (s)	operator number
<i>DOT MARKING MACHINE</i>			
Walking to the Dot Marking Machine	–	3	1
Picking the work piece	–	1	1
Loading the work piece in the Dot Marking Machine	–	1	1
Starting the cycle	–	1	1
Machine Auto Cycle Time	7	–	1
Unloading the work piece from the Dot Marking Machine	–	1	–
<i>FACING AND CENTERING MACHINE</i>			
Walking to the Facing and Cantering Machine	–	2	1
Loading the work piece in the Facing and Cantering Machine	–	2	1
Starting the cycle	–	1	1
Machine Auto Cycle Time	–	–	1
Unloading the work piece from the Facing and Cantering Machine	54	3	–
<i>LONG END TURNING MACHINE</i>			
Walking to the Long End Turning Machine	–	4	1
Loading the work piece in the Long End Turning Machine	–	2	1
Starting the cycle	–	2	1
Machine Auto Cycle Time	59	–	1
Unloading the work piece from the Long End Turning Machine	–	2	1

4.2 Bottle Neck Time Identification

Machine bottle neck time = 136 s, which occurs in a workstation at Vertical Machining Center-02.

Man bottle neck time = 84 s, which occurs with the 3rd operator manual time.

Table 2 Man, machine chart for short end turning machine, pin turning machine, VMC 01, VMC 02, VMC 03 in Crankshaft cell 3 assembly line

Activity	Machine auto cycle time	Manual time (s)	operator number
<i>SHORT END TURNING MACHINE</i>			
Walking to the Short End Turning Machine	–	1	2
Loading the work piece in the Short End Turning Machine	–	2	2
Starting the cycle	–	2	2
Machine Auto Cycle Time	52	–	2
Unloading the work piece from the Long End Turning Machine	–	2	2
Moving the work piece to Inspection area	–	1	2
Snap gauge inspection for long end turning	–	2	2
Snap gauge inspection for short end turning	–	3	2
Height of Journal End	–	2	2
Moving the work piece from inspection area	–	1	2
<i>PIN TURNING MACHINE</i>			
Loading the work piece to Pin Turning Machine	–	2	2
Starting the cycle	–	1	2
Machine Auto Cycle Time	84	–	2
Unloading the work piece from the Pin Turning Machine	–	2	2
Moving the work piece to Inspection area	–	1	2
Pin position Level Inspection	–	1	2
Notch in pin	–	2	2
Pin gauge	–	1	2
Moving the work piece from inspection area	–	1	2
<i>Vertical Machining Centre—01</i>			
Walking to the Vertical Machining Center—01	–	2	2

(continued)

Table 2 (continued)

Activity	Machine auto cycle time	Manual time (s)	operator number
Loading the work piece to Vertical Machining Center—01	–	2	2
Starting the cycle	–	1	2
Machine Auto Cycle Time	89	2	2
Unloading the work piece from Vertical Machining Center—01	–	2	2
<i>Vertical Machining Center—02</i>			
Loading the work piece to Vertical Machining Center—02	–	2	3
Starting the cycle	–	2	3
Machine Auto Cycle Time	–	1	3
Removing the bur in the machine	–	1	3
Unloading the work piece from Vertical Machining Center—02	–	3	3
Moving the work piece to inspection area	–	4	3
Deburring the work piece	–	5	3
Trimming	–	5	3
Torch Light Viewing	–	3	3
Inspection for oil hole	–	2	3
Inspection for thread	–	–	3
Long drill hole height checking	–	1	3
Picking the work piece inspection area	–	2	3
<i>Vertical Machining Center—03</i>			
Loading the work piece to Vertical Machining Center—03	–	–	3
Starting the cycle	–	1	3
Machine Auto Cycle Time	–	–	3
Removing the bur in the machine	–	2	3

(continued)

Table 2 (continued)

Activity	Machine auto cycle time	Manual time (s)	operator number
Unloading the work piece from Vertical Machining Center—02	–	1	3
Moving the work piece to inspection area	–	3	3
Deburring the work piece	–	3	3
Trimming	–	3	3
Torch Light Viewing	–	3	3
Inspection for oil hole	–	1	3
Inspection for thread	–	2	3
Long drill hole height checking	–	1	3
Picking the work piece inspection area	–	1	3

Bottle neck time = maximum of (Man bottle neck time & Machine bottle neck time)
= 136s

Prior to line balancing with 4 operators.

The output/shift = available time per shift/bottle neck time
= 436minper shift
= $436 \times 60 \times 0.8$ (taking operator efficiency as 80%)
= 20,928/136
= 153 units per shift.

After line balancing with 3 operators.

The work has to be reallocated among the operator bottle neck time is 80 s.

Machine bottle neck time is = 136 s.

Bottle neck time is = 136 s.

The output/shift = $436 \times 60 \times 0.8$ (taking operator efficiency as 80%)

= 20,928/136.

= 153units/shift.

5 Conclusion

The main contribution of the paper is the application of Line balancing in Crankshaft cell 3 Assembly line. A stop watch time study was conducted and man machine chart

Table 3 Man, machine chart for long end grinding machine, short end grinding machine and pin grinding machine in Crankshaft cell 3 assembly line

Activity	Machine auto cycle time	Manual time (s)	Operator number
<i>LONG END GRINDING MACHINE</i>			
Loading the work piece to the Long End Grinding Machine	–	1	3
Starting the cycle	–	1	3
Machine auto cycle time	114	–	–
Unloading the work piece from Long End Grinding Machine	–	2	3
Moving the work piece to inspection area	–	1	3
Air gauge Inspection for Long End	–	4	3
Checking the diameter for Long End	–	3	3
Picking the work piece inspection area	–	1	3
<i>SHORT END GRINDING MACHINE</i>			
Loading the work piece to the Short End Grinding Machine	–	2	4
Starting the cycle	–	1	4
Machine Auto Cycle Time	94	–	4
Unloading the work piece from Short End Grinding Machine	–	2	4
Moving the work piece to inspection area	–	1	4
Air gauge Inspection for Short End	–	3	4
Checking the diameter for Short End	–	2	4
Picking the work piece inspection area	–	1	4
<i>PIN GRINDING MACHINE</i>			
Loading the work piece to the Pin Grinding Machine	–	3	4
Starting the cycle	–	2	4
Machine Auto Cycle Time	71	–	4

(continued)

Table 3 (continued)

Activity	Machine auto cycle time	Manual time (s)	Operator number
Unloading the work piece from Pin Grinding Machine	–	3	4
Moving the work piece to inspection area	–	1	4
Checking the diameter for Pin	–	2	4
Picking the work piece inspection area	–	1	4

Table 4 Man, machine chart for hot water flushing machine, high pressure air machine and final visual inspection in Crankshaft cell 3 Assembly Line

Activity	Machine Auto cycle time	Manual time in Sec	Operator number
<i>HOT WATER FLUSHING MACHINE</i>			
Loading the work piece to the Hot Water Flushing Machine	–	2	4
Starting the cycle	–	1	4
Machine Auto Cycle Time	41	–	4
Unloading the work piece from Hot Water Flushing Machine	–	1	4
<i>HIGH PRESSURE AIR MACHINE</i>			
Loading the work piece to the High Pressure Air Machine	–	2	4
Starting the cycle	–	1	4
Machine Auto Cycle Time	43	–	4
Unloading the work piece from High Pressure Air machine	–	1	4
<i>FINAL VISUAL INSPECTION</i>			
Moving to the inspection area	–	1	4
Checking of cuts in thread	–	–	4
Checking of damages	–	–	4
Dropping the output	–	1	4

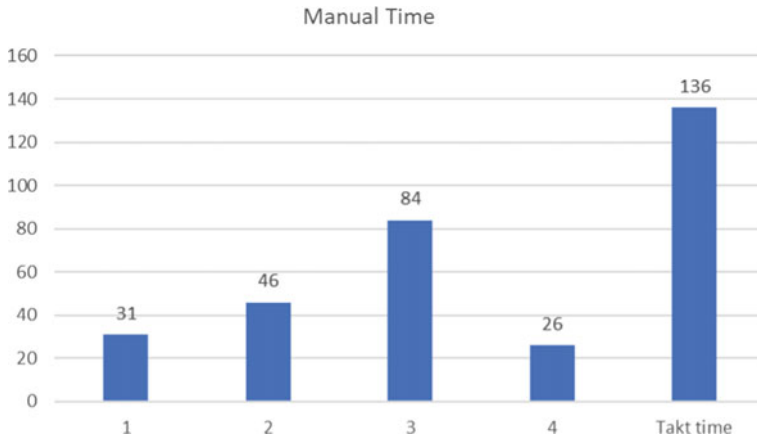


Fig. 2 Manual time prior to line balancing

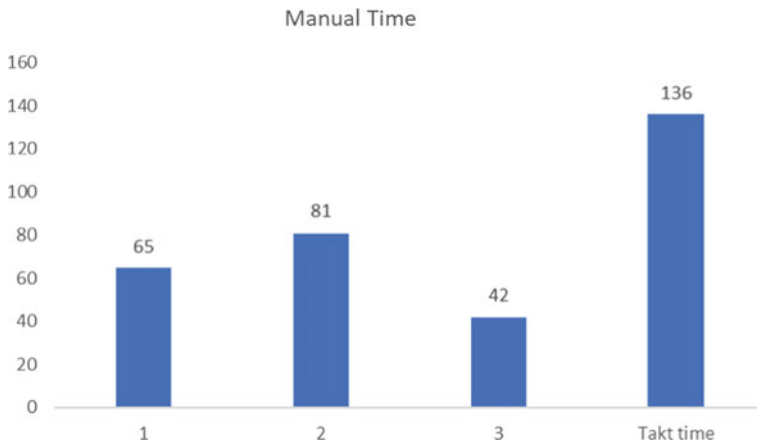


Fig. 3 Manual time after line balancing

for various work stations of the crankshaft cell 3 Assembly line was studied. The Machine Auto cycle time for the operations in crankshaft cell 3 Assembly line was calculated and also takt time was identified. It was found that cycle time for each station was less than takt time. The result of Line balancing implementation is a reduction of one operator and at the same time the same capacity of 153 units/shift was achieved. Prior to line balancing, the manpower count was 4 and bottle neck time was 136 s. The production output per shift was 153 units per shift. After implementing Line balancing in the crankshaft cell 3 Assembly line, the manpower count is reduced to 3 and the output was 153 units per shift. After reallocating work load to operators, the bottle neck time is 136 s.

Table 5 Comparison of machine autocycle time and manual time in seconds

S.No	Operation	Machine auto cycle (s)	Manual time (s)
1	Dot Marking Machine	7	8
2	Facing and Centering Machine	54	11
3	Long End Turning Machine	59	12
4	Short End Turning Machine	52	20
5	Pin Turing Machine	84	14
6	Vertical Machining Center 01	89	12
7	Vertical Machining Center 02	136	34
8	Vertical Machining Center 03	136	31
9	Short Journal Grinding Machine	94	13
10	Long End Journal Grinding Machine	114	16
11	Pin Grinding Machine	71	17
12	Hot Water Flushing Machine	41	5
13	High Pressure Air Machine	43	4

References

1. Nallusamy S (2020) Execution of lean and industrial techniques for productivity enhancement in a manufacturing industry. *Mater Today Proc* 37(2):568–575
2. Kulkarni SD, Mamatha V, Pavan KG, Badigera RR, Gubachi SH (2020) Productivity improvement of a hose assembly plant by the application of an effective line balancing technique. *AIP Conf Proc* 2247:050013
3. John RA, Ramanamurthy EVV, Nath R, Kumar P (2018), Productivity enhancement by component-oriented line balancing method, *Int J Indus Syst Eng* 29(1):31
4. Fansuri AFH, Rose ANM, Rashid MA, Mohamed MFF, Nik NMZ, Ahmad H (2018) Productivity improvement through line balancing at electronic company—case study. *IOP Conf Series: Mater Sci Eng* 409:012015
5. Suganthini RR, Periyasamy P, Nallusamy S (2017) Manufacturing enhancement through the reduction of cycle time using different lean techniques. *IOP Conf Series: Mater Sci Eng* 225:012282
6. Nallusamy S (2016) Productivity Enhancement in a small-scale manufacturing unit through proposed line balancing and Cellular layout. *Int J Performability Eng* 12(6):523–534
7. Morshed MN, Palash KS (2014) Assembly line balancing to improve productivity using work sharing method in Apparel Industry. *Glob J Res Eng G Indus Eng* 14:39–47
8. Pereira J, Vila M.,(2013), An enumeration procedure for the assembly line balancing problem based on branching by non-decreasing idle time. *Europ J Oper Res* 229:106–113
9. Battara O, Dolgui A (2013) A taxonomy of line balancing problems and their solution approaches. *Int J Prod Econ* 142(2):259–277
10. Amardeep, Rangaswamy TM, Gautham J (2013) Line balancing of single model assembly line. *Int J Innov Res Sci Eng Technol* 2:1678–1680
11. James CC, Chen C, Su L, Wu H, Sun C (2012) Assembly line balancing in garment industry. *Expert Syst Appl* 39:10073–10081
12. Shumon Md, Kazi AUZ, Rahman A (2010) Productivity improvement through line balancing in apparel industries, *Proceedings of the 2010 International Conference on Industrial Engineering and Operations Management*

Experimental Characterization and FEA Comparison Between Wave and Helical Springs



S. Balodi and P. Pratim

Abstract Vibration is an unwanted mechanical phenomenon which causes performance deterioration of dedicated equipment and critical electronic hardware. In order to reduce this vibration during the transportation of the dedicated payloads i.e. optical payload or microwave payload and critical electronic hardware such as atomic clocks, detectors etc., containers with vibration isolation systems are used. Traditional vibration or shock absorbing systems are big in size which makes the whole container huge and bulky. In our present paper, we try to characterize different types of springs (helical and wave) and develop a FEM methodology to calculate the stress and displacement of the springs under load. Generally, helical springs are used with shock absorber systems having large displacement areas. In this study, we have selected helical and wave springs [1] for our experiments and compared them for the fulfilment of our objective. The future aim of this study is to select a suitable spring which can be used with a small size damper in order to make a compact vibration isolation system which will provide the same load carrying capacity in a constrained space as that of a traditional system [2]. The CAD files of both the springs are modelled using Autodesk Inventor Professional 2019 and Creo Parametric 5.0, while the FEM methodology is performed using HyperWorks 2019 for both the springs. The theoretical calculations of the models are compared with the FEA results and then validated experimentally.

Keywords Vibration · Vibration isolation · Deflection · Helical spring · Wave springs · Dampers · FEA comparison

S. Balodi (✉)

Payload Integration Quality Assurance Division, Space Applications Centre, Indian Space Research Organisation, Ahmedabad, India
e-mail: balodisudhanshu@sac.isro.gov.in

P. Pratim

School of Automobile, Mechanical and Mechatronics Engineering Department of Mechanical Engineering, Manipal University Jaipur, Jaipur, India

1 Introduction

Vibration isolators are used to reduce the unwanted vibrational and shock inputs received during the transportation of sensitive payloads such as electronic hardware, optical hardware, or fully assembled satellites, from one centre to another. They are placed below the payload interface plate and above the container base plate. Commonly used vibration isolators are passive types i.e. wire rope isolators which are designed for a fixed frequency. They provide isolation for a limited frequency range. In order to make a more advanced and reliable isolation system, semi-active and active types of vibration isolators are used. Active isolation has active actuators which are working in a close loop to provide isolation at all frequency ranges. Active system power requirement is high also if system power fails the active isolation system will act as a rigid system and transmit all the vibration from the ground. Semi-active isolation system has the advantage of both passive isolation system and active isolation system. They have an active damper filled with MR or ER fluid and they can change their damping based on the input received from the ground. Semi-active system is fail safe because if an active damper fails the system will act as a passive isolation system. Semi-active isolation systems have a spring system along with a damper arranged in parallel. In the present study to develop a compact vibration isolation system with spring and damper in parallel a spring needs to be selected which can provide high stiffness but with less free length. So, the objective of the paper is to identify and verify the spring analytically with the FEA results and experimentally that can be used in the above-mentioned conditions.

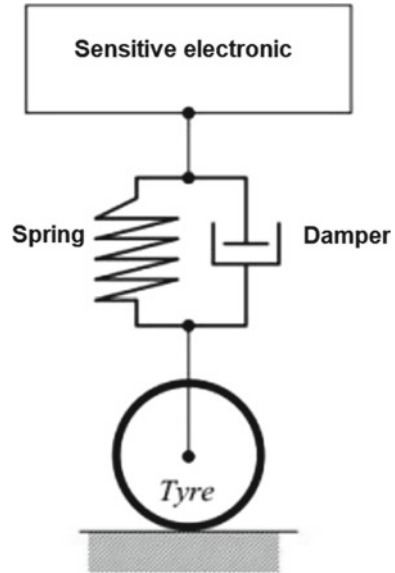
1.1 *Vibration Isolation System*

Vibration isolators are used for reduction in the magnitude of system response for a high value of ground input. This is because of the ability of the isolator to store energy at a relatively higher rate associated with the excitation received via the ground and subsequently releasing it at a relatively lower rate. Release of the strain energy stored in the isolator causes the isolated body to vibrate at a natural frequency of the isolation system until the energy is dissipated by the isolator damping mechanism. Vibration isolation systems are categorised into passive, active and semi-active types of systems, depending on the requirement of external power by the isolator to perform its function [3] (Fig. 1).

A. Helical springs

The Helical spring have Circular cross section area which is bent in the form of helix. The external force acts along the axis of the spring and induces torsional shear stress in the spring wire [4].

Fig. 1 Vibration isolation system between road input and sensitive input [1]



B. Wave Springs

Wave springs are precise flat wire compression springs that fit into assemblies that other springs cannot. The compression force on the wave spring generates bending stress at the cross section of the spring [5].

While designing a vibration isolator for a transport container we keep the natural frequency of the isolator as minimum as possible in order to have isolation for all input vibration. The fundamental frequency of the transport vehicle leaf spring is 3–4 Hz [6] so in order to avoid resonance, we have decided to design an isolation system for a natural frequency of 7 Hz. This is decided keeping in mind that lower the natural frequency, higher the isolating performance.

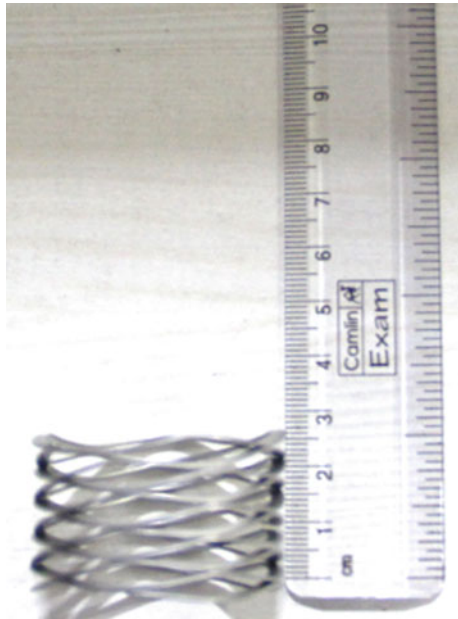
For the part of spring selection process, the above-mentioned natural frequency of the isolation system is used to calculate the stiffness of the spring required by assuming a fixed amount of mass. This is done by the equation for finding out natural frequency: $\omega_n = \frac{1}{2\pi} \sqrt{\frac{k}{m}}$. Now as we have calculated the stiffness of the spring that is required, the dimensions of the spring are to be decided according to what is given in the company catalogue for wave springs keeping the outer diameter fixed.

Now in accordance with the dimensions of the wave spring, a helical spring of same outer diameter and stiffness is selected (Figs. 2 and 3).

Fig. 2 Helical spring



Fig. 3 Wave spring



2 Theoretical Calculations

A. For Helical Spring

Formula for deflection undergone by a helical spring [4]:

$$\delta = \frac{8FD_m^3N}{Gd^4} \quad (1)$$

Stiffness (k) is given as:

$$k = \frac{Gd^4}{8D_m^3N} \quad (2)$$

where δ : Total Deformation, F : Load applied, D_m : Mean diameter, G : Modulus of Rigidity, d : Coil Diameter, N : Number of turns [7].

Load and Boundary Condition: Bottom side of the spring is constrained and compressive load is applied from the top side of the spring.

Spring specifications: ID : 30.5 mm, OD : 40 mm, d : 5 mm, H : 80.5 mm, N : 5, F = 100 N.

Using Eqs. (1) & (2) the value of deflection and stiffness is:

$$\delta = \frac{8FD_m^3N}{Gd^4} = \frac{8 * 100 * (35.25)^3 * 5}{79300 * 5^4} = \frac{175201312.5}{49562500} = 3.53 \text{ mm}$$

$$k = \frac{Gd^4}{8D_m^3N} = \frac{79300 * 5^4}{8 * (35.25)^3 * 5} = \frac{49562500}{1752013.125} = 28.28 \text{ N/mm}$$

Wahl factor for the given spring is:

$$K = \frac{4C - 1}{4C - 4} + \frac{0.615}{C}, \text{ where } C = \frac{35.25}{5} = 7.05$$

$$\text{Or, } K = \frac{4(7.05) - 1}{4(7.05) - 4} + \frac{0.615}{7.05} = 1.122 + 0.087 = 1.209$$

The resultant stress, which includes torsional shear stress, direct shear stress and stress concentration due to curvature is given as:

$$\tau = K \left(\frac{8PD_m}{\pi d^3} \right) \quad (3)$$

Using Eq. (3) Shear stress is;

$$\tau = K \left(\frac{8PD_m}{\pi d^3} \right) = 1.209 * \left(\frac{8 * 100 * 35.25}{\pi * 5^3} \right) = 86.81 \text{ N/mm}^2$$

B. For Wave Spring

Formula for deflection and stiffness of wave spring [8]:

$$f = \frac{PKD_m^3N}{Ebt^3Z^4} * \frac{ID}{OD} \quad (4)$$

$$k = \frac{Ebt^3Z^4}{KND_m^3} * \frac{OD}{ID} \quad (5)$$

where f : Total Deformation, b : Radial Width, P : Load Applied Z : Waves per turn, D_m : Mean Diameter, ID : Inner Diameter, N : No. of Turns, OD : Outer Diameter, E : Young's Modulus, K : Wave Constant, t : Strip Thickness [9].

Spring specifications: ID : 38 mm, OD : 43 mm, H : 25 mm, N : 10, Z : 4.5, t : 0.64 mm, P : 100 N, b : 0.64.

Using Eq. (4) deflection value is calculated as:

$$\begin{aligned} f &= \frac{PKD_m^3N}{Ebt^3Z^4} * \frac{ID}{OD} = \frac{100 * 2.90 * (40.5)^3 * 10 * 38}{200000 * 2.5 * (0.64)^3 * (4.5)^4 * 43} \\ &= \frac{7320599775}{2311151616} = 3.167mm \end{aligned}$$

Stiffness k from Eq. (5) came out to be:

$$\begin{aligned} k &= \frac{Ebt^3Z^4}{KND_m^3} * \frac{OD}{ID} = \frac{200000 * 2.5 * (0.64)^3 * (4.5)^4 * 43}{2.90 * (40.5)^3 * 10 * 38} \\ &= \frac{2311151616}{73205997.75} = 31.57N/mm \end{aligned}$$

Stress S generated in the wave spring while undergoing compression is given as:

$$S = \frac{3\pi PD_m}{4bt^2Z^2} \quad (6)$$

Using Eq. (6) stress value for the wave spring is:

$$S = \frac{3\pi PD_m}{4bt^2Z^2} = \frac{3 * \pi * 100 * 40.5}{4 * 2.5 * (0.64)^2 * (4.5)^2} = \frac{38170.35}{82.94} = 460.21N/mm^2$$

3 Cad Modelling of Springs

CAD modelling of the helical spring was done in AutoDesk Inventor 2019, while the wave spring was modelled in Creo Parametric 5.0 (Figs. 4 and 5).

Fig. 4 CAD Model for helical spring

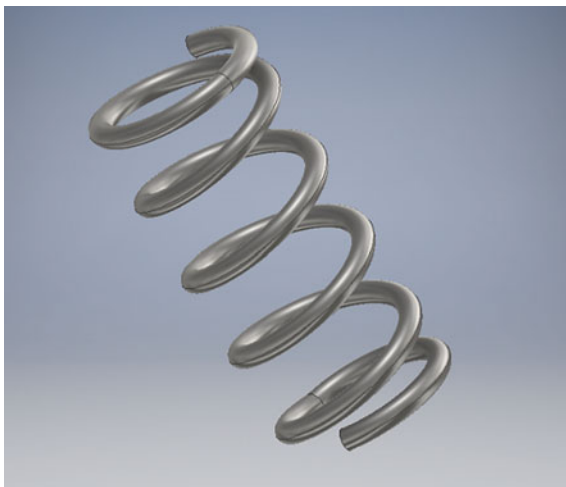


Fig. 5 CAD Model for wave spring

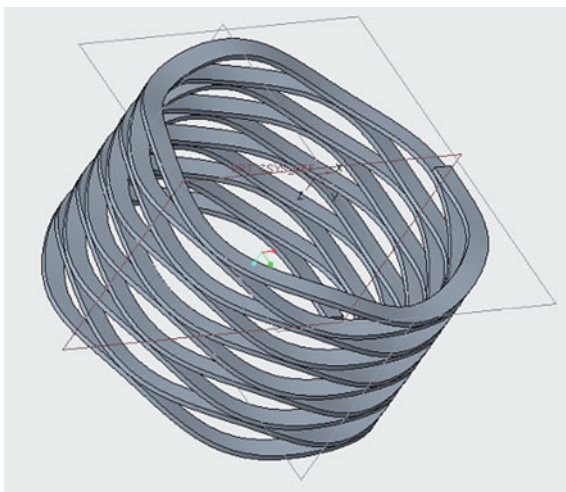


Table 1 Mechanical properties of helical spring and wave spring material [7]

Young's modulus	200GPa
Density	7850 kg/m ³
Yield stress	965 MPa
Poisson ratio	0.3

4 FEA Calculations

The FE model of both helical spring and wave spring is analysed in HyperWorks 2019 using linear and non-linear analysis respectively. Boundary conditions and load given as input are the same as used for theoretical calculations (Table 1).

A. For Helical Spring

Element type	CHEXA(Six Sided Solid Element) [10]
Element size	Element length: 1.346 mm Element cross section: 0.7936 mm × 0.7927 mm
Number of element	13,154
Number of nodes	16,893
Aspect ratio	3.09

The longitudinal deflection due to 100 N compressive load is 3.366 mm. The maximum deflection is at the top side of the spring where the load is applied and it decreases gradually from top to bottom side(Constraint side).

The Vonmises stress generated due to the compressive load shows maximum stress at the outer side of the helical spring (Figs. 6 and 7).

B. For Wave Spring

Element type	CHEXA(Six Sided Solid Element) [10]
Element size	Element length: 1.055 mm Element height: 0.4167 mm × 0.32 mm
Number of element	15,434
Number of nodes	27,028
Aspect ratio	3.60

The longitudinal deflection due to 100 N compressive load is 2.865 mm. The maximum deflection is at the top side of the spring where the load is applied and it gradually decreases as we move toward the bottom side (Constrained side).

The Vonmises stress generated is maximum at the contact points of the two waves crest and trough as the load is transferred through them from one wave ring to another (Figs. 8 and 9).

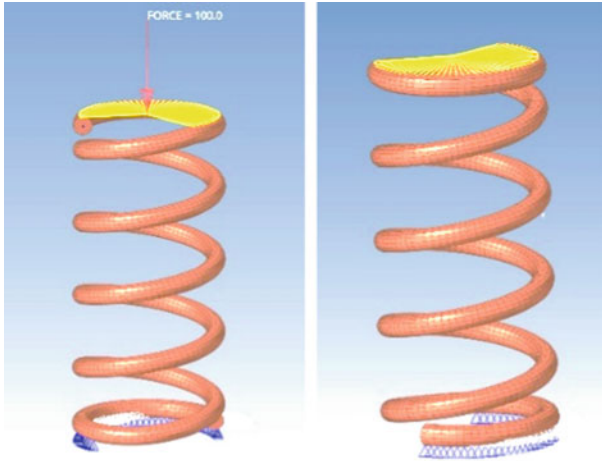


Fig. 6 FE model of Helical spring with load and boundary condition

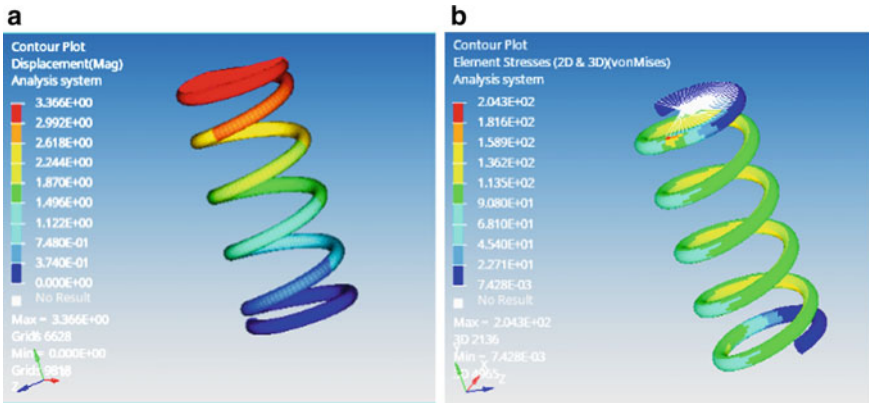


Fig. 7 a Deflection contour for the helical spring, b stress contour for the helical spring

5 Experimental Calculations

The Helical spring and Wave spring are subjected to the compression test on an industrial universal testing machine. ASTM A125 Standard is followed during the testing of the spring. Bottom side of the spring is constrained and top side of the spring is applied with the compressive load. The boundary conditions and applied load were kept the same as used for theoretical and FEA calculations (Figs. 10 and 11).

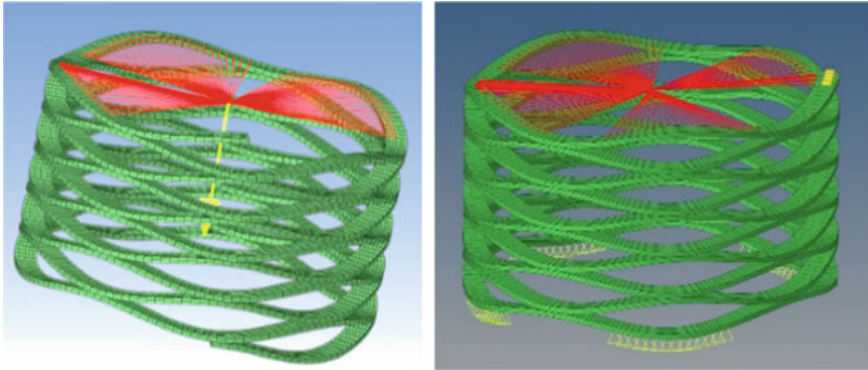


Fig. 8 FE model of wave spring with load and boundary condition

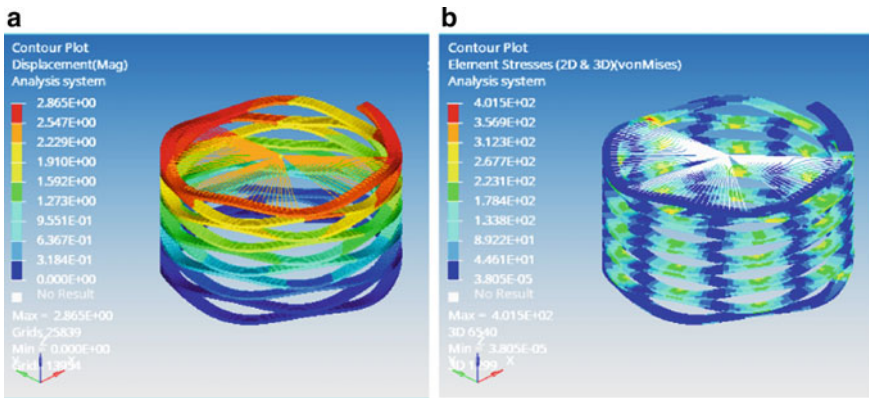


Fig. 9 **a** Contour diagram for wave spring showing deflection. **b** Contour diagram for wave spring showing stress generated

The following graphs were obtained from the universal testing machine. These graphs represent the load deformation relationship of both the spring under static loading of magnitude 100 N.

- A. **For Helical Spring** (Fig. 12)
- B. For Wave Spring (Fig. 13)

6 Results and Discussions

Readings and observations of all three phases of the experiment and recorded duly. These results are then compared with each other and the deviation percentage is calculated for both helical and wave springs.

Fig. 10 Experimental setup for helical spring

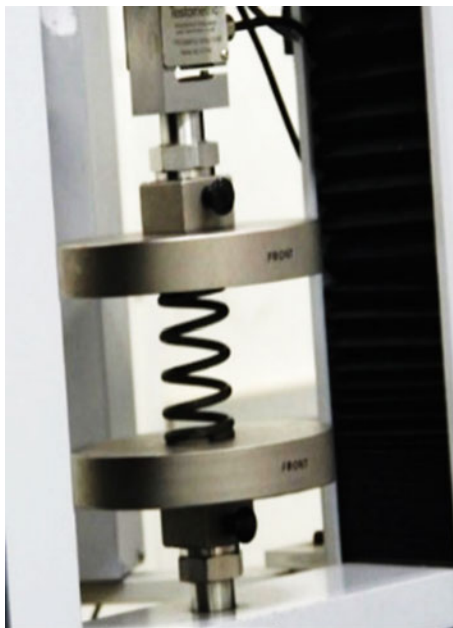
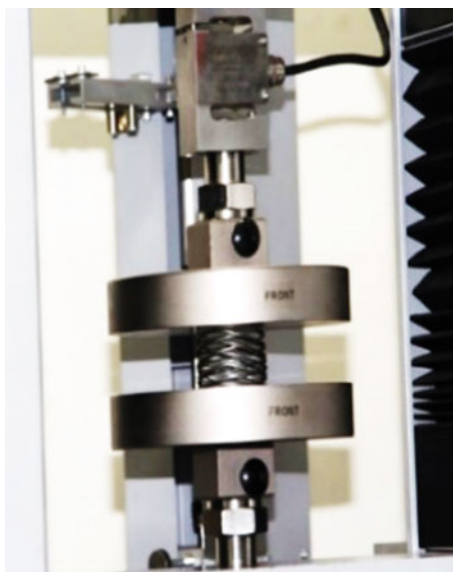


Fig. 11 Experimental setup for wave spring



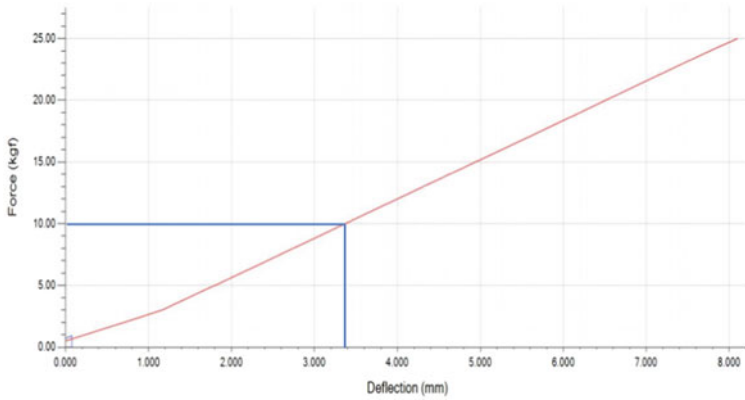


Fig. 12 Load deflection curve for a helical spring under static load

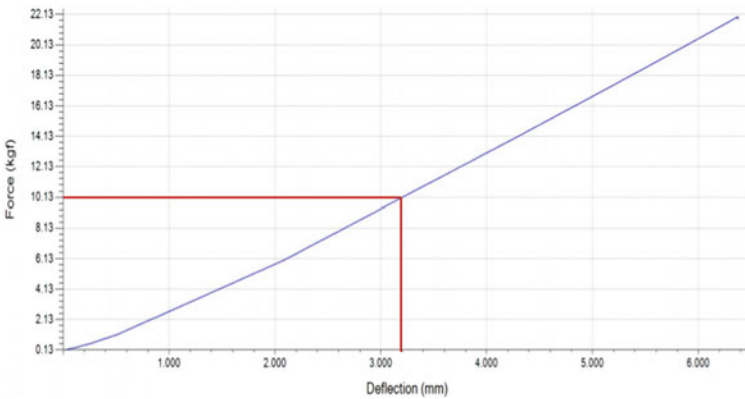


Fig. 13 Load deflection curve for a wave spring under static load

A. For Helical Spring

Observations for deflection undergone and stiffness of the helical spring is given in the Table 2:

Now we do the experimental validation of our results by comparing the experimental results with both theoretical and FEA results and calculating their individual deviation in percentage, as shown in the Tables 3 and 4:

As we can see that, the comparison of all the results has a deviation percentage less than or equal to 10%, and we can conclude that the observation readings for helical springs are correctly validated.

B. For Wave Spring

Observations for deflection undergone and stiffness of the wave spring are given in the Table 5:

Table 2 Observation for helical spring

Observations	Deflection undergone (δ) (mm)	Stiffness (k) (N/mm)	Stress (N/mm ²)
Theoretical value	3.53	28.28	86.81 (Shear)
FEA value	3.36	29.76	204.3 (Von mises)
Experimental value	3.38	29.58	N/A

Table 3 Comparison between experimental and theoretical results of helical spring

Comparison	Experimental results	Theoretical results	Deviation (%)
Deflection undergone (δ)	3.38 mm	3.53 mm	4.43
Stiffness (k)	29.58 N/mm	28.28 N/mm	4.39

Table 4 Comparison between experimental and FEA results of helical spring

Comparison	Experimental results	FEA results	Deviation (%)
Deflection undergone (δ)	3.38 mm	3.36 mm	0.59
Stiffness (k)	29.58 N/mm	29.76 N/mm	0.60

Table 5 Observations for wave spring

Observations	Deflection undergone (δ) (mm)	Stiffness (k) (mm)	Stress (N/mm ²)
Theoretical value	3.16	31.57	460.21 (Bending)
FEA value	2.90	34.96	401.5 (Von mises)
Experimental value	3.19	31.34	N/A

Now we do the experimental validation of our results by comparing the experimental results with both theoretical and FEA results and calculating their Deviation in percentage, as shown in the Tables 6 and 7:

As we can see that, the comparison of all the results has a deviation percentage less than or equal to 10%, we can conclude that the observation readings for wave springs are correctly validated.

Table 6 Comparison between experimental and theoretical results of wave spring

Comparison	Experimental results	Theoretical results	Deviation (%)
Deflection undergone (δ)	3.19 mm	3.16 mm	0.94
Stiffness (k)	31.34 N/mm	31.57 N/mm	0.73

Table 7 Comparison between experimental and FEA results of wave spring

Comparison	Experimental results	FEA results	Deviation (%)
Deflection undergone (δ)	3.19 mm	2.90 mm	9.09
Stiffness (k)	31.34 N/mm	34.48 N/mm	10.00

C. Stiffness Comparison of Both Springs

Percentage difference of the stiffness obtained experimentally for both helical and wave springs is given as:

$$\left(\frac{31.34 - 29.58}{\frac{31.34 + 29.58}{2}} \right) * 100 = \frac{1.76}{30.46} * 100 = 5.77\%$$

Hence, we can see that by analysing height difference for both the springs (80.5 mm for helical spring and 25 mm for wave spring), height of wave spring is less than that of helical spring by a factor of more than 3, however the stiffness of both the springs is approximately same with a difference percentage of a mere 5.77%.

7 Modal Analysis

Modal Analysis was performed in HyperWorks 2019 for both the springs. The one end (bottom side) of both spring is constrained and concentrated mass of 10.19 kg is applied at the top side of the springs. The Fundamental mode obtained for both the spring is longitudinal mode i.e. compression and extension of the spring (Figs. 14 and 15).

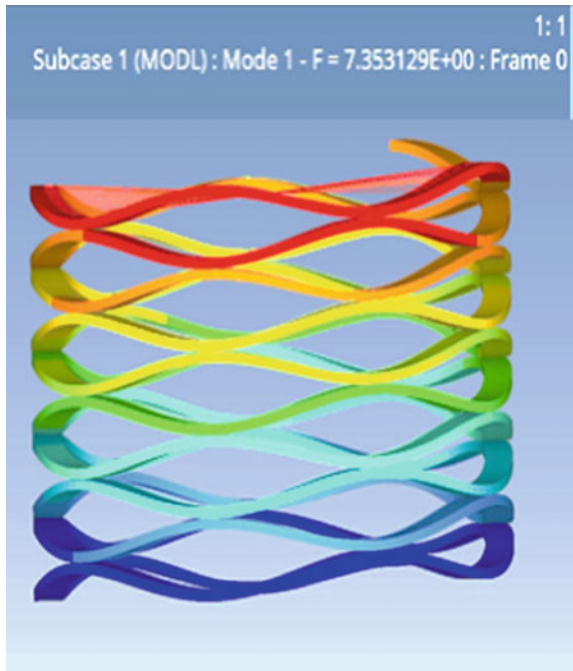
The frequency obtained for the fundamental mode is 7.16 Hz and 7.35 Hz for Helical spring and Wave spring respectively.

The Design frequency of the spring is 7 Hz so the deviation in FE Modal analysis is under 5%. This shows that the dimensions selected for both the springs are correct for our experiment.

Fig. 14 Modal analysis for helical spring showing frequency is calculated to be 7.16 Hz



Fig. 15 Modal analysis for wave spring showing frequency is calculated to be 7.35 Hz



8 Conclusions

Following conclusions can be made from the above study:

- The deflection and stiffness values for the helical spring and wave spring calculated theoretically, FEA experimentally are in good agreement with an error percentage less than 10% in all cases.
- The wave springs when used instead of helical springs help in reducing the size of the assembly by as much as 50% when used with helical springs.

9 Future Scope

Our main objective of conducting this experiment is to select a spring which can be used in our proposed compact vibration isolation system comprising of both spring and damper. Further development can be done using the wave springs and magnetorheological (MR) fluid-based damper to make a semi-active vibration isolation system where the damper will be of an active type which will change its damping properties corresponding to the road input.

Acknowledgements We thank Director SAC for his approval for publication, DD SRA, GD SRA and PIQAD Division Head for their support, valuable comments and feedbacks. Also, we extend our thanks to all the scientists/engineers and technicians/mechanics working in SAC-ISRO, Ahmedabad who helped by providing necessary information and guidance to successfully conduct this experiment.

References

1. Tang N, Lord CE, Sims ND, Rongong JA (2016) Experimental investigation and modelling of dynamic performance of wave springs. In: 11th International Conference on Advances in Engineering Mechanics
2. Muralidharan M, Aravinth R, Gafferkhan J, Gandhi R (2018) Comparative design and analysis of helical and wave spring. *Int J Eng Technol* 7:353–356
3. Pavani PNL, Prafulla BK, Rao RP, Srikanth S (2014) Design, modelling and structural analysis of wave springs. 3rd international conference on materials processing and characterization. *Procedia Mater Sci* 6:988–995
4. Bhandari VB (2010) Design of machine elements, 3rd edn. Tata McGraw Hill Education Private Limited, India
5. Smalley Wave Spring Design Handbook, Industrial Catalogue.
6. Singh SP, Sandhu APS, Singh J, Joneson E (2007) measurement and analysis of truck and rail shipping environment in India. *Packag Technol Sci* 20:381–392
7. Tapia-Gonzalez PE, Ledezma-Ramirez DF (2017) Experimental characterisation of dry friction isolators for shock and vibration. *J Low Freq Noise Vib Act Control* 36:83–95
8. Dragoni E (1988) A contribution to wave spring. *J Strain Anal Eng Des* 23(1988):145–153

9. Ying YU, Peng Y, Lan S, Zhou P (2013) Finite element analysis for wave spring of multi-disc wet clutch based on ANSYS. *Appl Mech Mater* 419:203–208
10. Gokhale NS, Deshpande SS, Bedekar SV, Thite AN (2020) *Practical finite element analysis*, 1st edn. Finite to Infinite Publications, India

Mechanical Properties Enrichment of Glass Fiber Epoxy by Sugarcane Baggage



Punita Kumari, Ashraf Alam, and Saahil

Abstract Recently the application of the natural filler was increased in order to avoid environmental issues. In this study, SBG (Sugarcane Baggage) was employed while fabrication of woven glass fiber composite. Regarding this vacuum assist resin infusion manufacturing (VARI) process was used to fabricate the composite. Three different weight percentages (5–15%) were used as filler in this study. Furthermore tensile and Charpy impact test was conducted on the specimen and compared with the original. The damage mode of the specimen was monitored through an acoustic emission sensor that was placed at the specimen while tensile testing. Four different damage modes were discovered through non-destructive testing that is matrix crack, debonding, delamination and fiber breakage.

Keywords Sugarcane baggage · Natural fiber · Damage mode · Non-destructive testing · Acoustic emission

1 Introduction

On the demand of light weight, corrosion resistance, fire resistance, high stiffness, toughness and long durability fiber reinforced polymer (FRP) is being used in aerospace, vehicle industry, wind turbine industry, medical, sports, defense gear

P. Kumari
School of Aeronautical Sciences, Hindustan University, Chennai, Tamilnadu 603103, India

A. Alam (✉)
Rekhi Centre of Excellence for the Science of Happiness, Indian Institute of Technology
Kharagpur, Kharagpur, India
e-mail: ashraf_alam@kgpian.iitkgp.ac.in

Saahil
School of Automotive Engineering, Wuhan University of Technology, 122 Luoshi Road,
Wuhan 430070, China

P. Kumari
School of Material Science and Engineering, Wuhan University of Technology, 122 Luoshi Road,
Wuhan 430070, China

(Bullet vest, combat helmet etc.) [1–8]. GFRP (glass fiber reinforced polymer) is used in doors, stabilizers of the aircraft and rockets fin. Car body, boat body and wind turbine blade are made by GFRP [8, 9]. In the case of synthetic fiber based composites, despite their usefulness in service, these are difficult to be recycled after designed service life. However, natural fiber based composites are environment friendly to a large extent. Environmental awareness and sustainability concept attracts researchers and scientists towards the utilization of natural fibers as reinforcement in polymer-based composites. Natural fiber reinforced composites are attracting researchers due to their lower cost, light weight, high strength to weight ratio, renewability, lower density and lower energy requirements for processing. Natural fibers in the composite industry usually refer to wood fiber and agro based leaf, seed and stem fibers. These fibers often contribute greatly to the structural performance of plant and when used in plastic composites can provide significant reinforcement. The stiffness and strength shortcomings of biocomposites can be overcome by structural configurations and better arrangement in a sense of placing the fibers in specific locations for the highest strength performance [4]. Natural fibers such as coconut shell, rice husk and teak wood are found to be the enactment of mechanical strength based upon weight percentage filler added into matrix and filler size [10]. Machining properties of pineapple as a natural filler were evaluated [11]. Sugarcane bagasse (SCB) is a waste product generated after the production of sugar and ethanol. It is organic type waste material. High quantity of SCB is produced by India among all [12]. About 9% of bagasse is used with alcohol (ethanol) production. Ethanol is environmentally friendly and this makes it more suitable for the replacement of fossil fuel. Ethanol is a very versatile material that is used in many chemical products as raw material. The selection of SCB was made on its lower fabricating costs and high quality ecofriendly material. It is easily obtainable from sugarcane. After the extraction of sugarcane juice the fibrous residue remains known as SCB. That is mainly used as burning material. Low caloric power makes it less efficient and generates less fumes or smoke during burning. Even though currently 85% of produce SCB is used as burning material but still an excess amount of it is generally dumped by the factories and ends up as excess SCB deposition around the landscape.

SCB can be categorised based upon cost, density, renewability and durability. Presently SCB is used as fuel, fertilizer, aggregate substituent and food for animals [10]. And large part of its usage in building or civil automobile applications [11, 12].

Acoustic emission (AE) type of non-destructive test is on line damage monitoring. It can predict damage mode such as fiber failure, matrix cracks etc. might be these major incident leads to catastrophic failure. AE sensor can read those failures while conducting health monitoring of the structure [13, 14].

There are several work reported on sugarcane bagasse as reinforcement in composite but very few works covered sugarcane's use as dust filler that enhances composite properties. Objective of the research work is to the assessment of mechanical properties enhancement of glass fiber reinforced composite with sugarcane bagasse fiber using tensile and charpy tests. The acoustic sensor was placed on the specimen while the tensile test in order to record damage mode.

2 Experimental Method

2.1 SBG Preparation

The SBG used in this experimental work was gathered from commercial storage where there was Sugarcane juice extracted from it through rolling and pressing and later dispose the left over sugarcane bagasse. After getting it the SBG was washed in running and clean water in order to eliminate any residual sugar. Then the washed SBG was poured into acetone solution to remove oil or grease. After cleaning SBG was dried under the sun for 2 days then it was dehydrated in the oven for 6–7 h at 50 °C. Once it was made sure there is water is evaporated from the SBG it was kept in a grinder to make it into dust particles. Later on, the SBG particle passed through sieves to make sure its size do not exceed 70 μm , dust particle also passes by a magnet installed chamber in order to remove any iron particles. Since SBG is hygroscopic material so it passes through a dehumidifier to remove any chance of humidity or water trapped in it.

2.2 Matrix Mixture

Epoxy LY556 and hardener HY951 were used to make the matrix mixture. The fiber resin ratio was 100: 60 was taken while epoxy and hardener 100:14 was used. First, the resin was measured then the SBG was added as per weight percentage (5, 10, and 15%) then the solution is mixed with a homogenizer. Homogenizer was used to blend the SBG in epoxy for 5 min. Thus the resin mixture was prepared.

2.3 Composite Plate Fabrication

E- Glass woven fiber mat (360 GSM) was used in the fabrication of composite. Vacuum assist resin infusion (VARI) method was used to fabricate the composite shown in Fig. 1. A total of 12 pieces of fiber mat was cut with a dimension of 500 \times 500 mm. A glass table was chosen as the fabrication mould. The table was cleaned with ethanol to remove any residual dust or grease. The fabrication region was marked on the table as per fiber mat dimension and that area was greased with wax (Spry) after once was deposited at the table the peel ply was stacked and fiber mats were stacked on it. Then again second peel play was stacked on it later the mesh mat was applied to the mesh and was placed to the uniform flow of the resin inside the fiber assembly system. Two pipes were placed inside fiber assembly one is used for vacuum and another one for resin flow. One pipe is connected to vacuum pump. The whole fiber system was covered with vacuum bag by double sided sealant tape. Once the mixture was ready it was impregnated into the fabrication setup. First, the pump

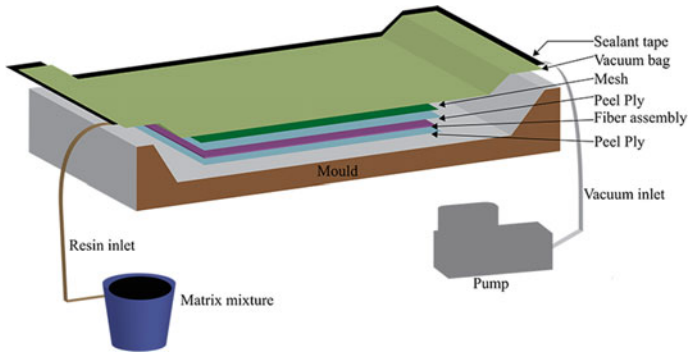


Fig. 1 VARI process

was on in order to create suction inside the vacuum bag. After that, the fabrication set was left idle for half an hour to make sure there is no leakage or any air trapped inside it. Meanwhile, the hardener was measured and mixed well in the resin solution. The bubble was developed in the resin mixture in process of the mixing to collapse this formed bubbles the resin mixture was kept inside the pressure vessel for 4 min. Now the prepared mixture is ready to insert into fabrication. Resin slowly impregnated in the fibers, it took 50–60 min when fibers fully poured by resin. The fabrication was left for 24–28 h at room temperature (27 °C) for the curing procedure [5–7]. After the curing the composite plate thickness was measured by Vernier caliper it was found to be 3 mm. After the curing composite plate was taken out from the specimen dimension was marked for charpy and tensile tests. For tensile test and charpy test the dimension of the specimen was marked 250 mm × 25 mm × 3 mm and 80 mm × 12 mm × 3 mm as per respective ASTM [15, 16] and cut it by a water jet cutting machine to avoid any properties changes of composites. For each type total of 5 samples were prepared so total of 30 specimens was cut down from the plate. After cutting the specimen it edges were rubbed with sand paper and later it was cleaned with acetone soaked cotton to remove residual dust (Fig. 2; Table 1).

3 Result and Discussion

3.1 Tensile Test

A UTM (universal testing machine) was employed with a capacity of 100KN to conduct tensile test. Once the specimen was prepared for testing it was put in the UTM jaw and the crosshead was maintained at 2 mm/min during the test. The AE sensor was mounted on the specimen in order to monitor the damage. Eight channel of AE was selected, and AE sensors are connected to a data acquisition device to record sensor generated data. Parametric and signal based technique was implemented in



Fig. 2 Composite plate

Table 1 Specimen identification

Specimen group	Test type	Specimen code	SBG weight percentage	Number of specimen
A	Tensile test	A1	5	5
		A2	10	5
		A3	15	5
B	Charpy test	A1	5	5
		A2	10	5
		A3	15	5

this research study. For tensile tests, 5 identical specimens were prepared and after the test, the average was noted. Tensile response of the specimen was plotted in form of curves that is load verse displacement and stress verse strain in Fig. 3. Figure 3 helps to acquire ultimate tensile strength, fiber elongation and modulus of elasticity developed in the specimen due to tensile loading. It was discovered that the adding weight percentage of the SBG filler was able to improve the tensile strength of the composite. And it was found maximum when filler weight percentage was 15%. This indicated that the SBG filler provides good bonding to the epoxy resin that

helps to enhance the tensile stress carrying capacity. Adding high SBG weight also demonstrated an increment in tensile load. Tensile strength readings can be vary with the crosshead speed. Fracture generated and propagation were also depended upon crosshead speed. In the stress strain curve it was shown the curve increased with the strain progressively and after achieving maximum stress amount the fiber brake with loud sound and fall extremely (Fig. 4).

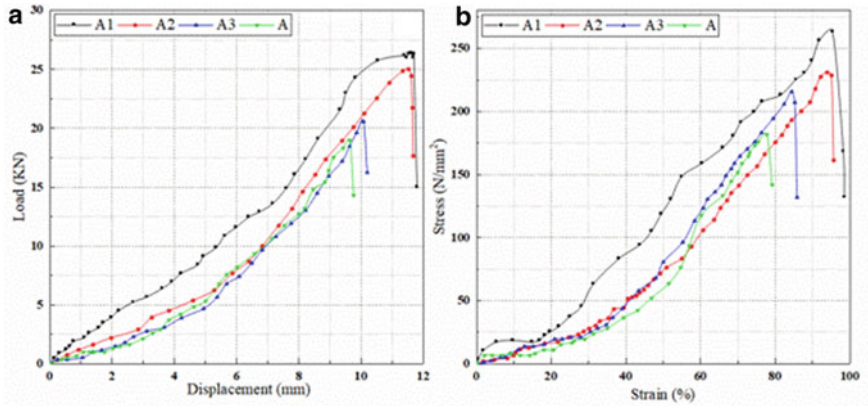
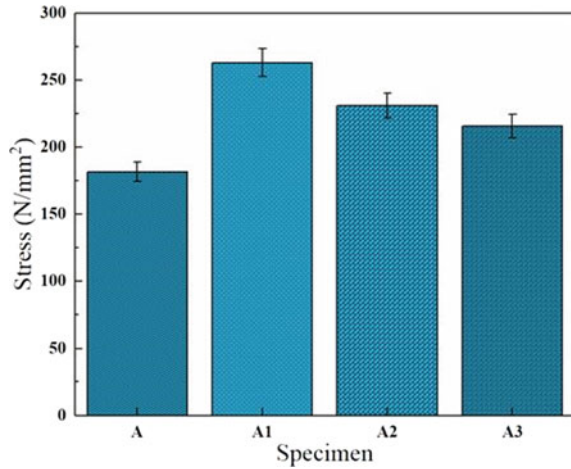


Fig. 3 Tensile test stress verse strain

Fig. 4 Bar graph



3.2 AE Results

Figure 5 displayed the AE sensor response when tensile test was carried out, it is an online damage monitoring procedure in that the mounted sensors record the data based upon damage type. These sensor data are stored in the form of frequency and displayed in 4 categories with the changing specimen behavior. This damage can be categorized as matrix cracks, debonding, delamination and fiber failure. Frequency bands 110–115 Hz, 120–122 Hz, 140–145 Hz and 250–255 Hz comes under matrix cracks, debonding, delamination and fiber failure respectively. When the frequency was between the ranges of 110–115 Hz the matrix cracks developed to the samples, it was detectable at the lowest frequency. The frequency with a range of 120–122 Hz denotes the debonding. Debonding referred to as macroscopic damage occurred between fibers sheets while microscopic damage between delamination is said to be delamination. The highest frequency 250–255 Hz is represented as fiber damage since it is the final type of failure so the last range of frequency assigns to it.

Figure 5 presents the AE response while tensile test of the glass fiber composite with different weight percentage of SBG. Figure 5 (A1), (A2) and (A3) explained the breaking behavior of the specimen A1, A2 and A3 respectively. When the SBG

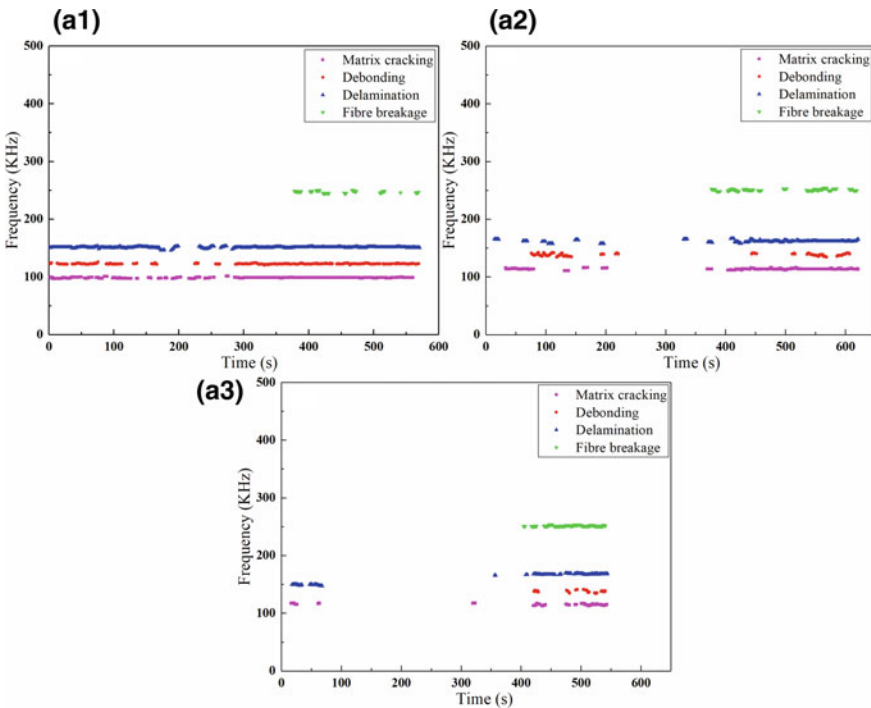


Fig. 5 AE response

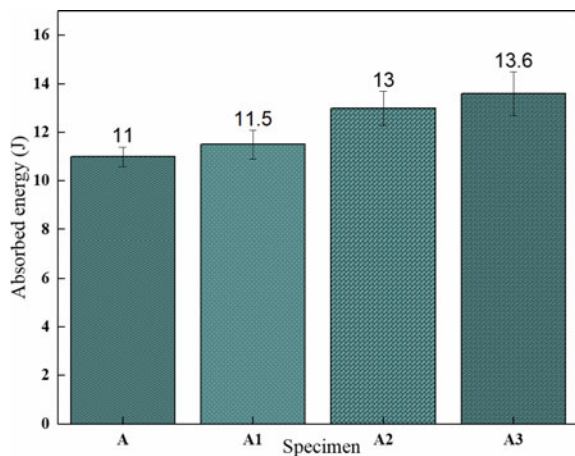
percentage was 5 there is continuous matrix cracks, debonding occurred to specimen that leads to delamination and finally the fiber breakage at the frequency 240–250 kHz. In the case of 10 weight percentage, the amount of matrix crack development has reduced including debonding and delamination whereas lesser fiber fracture was noticed. At 15 weight percentage of SBG, strong bonding was discovered through AE testing technique which means that the highest amount of addition of SBG capable to enhance the strength of the glass fiber composite but there is a high amount of fiber breakage was observed that implies the mixing of SBG should be within the limit.

3.3 Charpy Test

Charpy impact test was conducted to test the high rate resistance ability of the specimen. An impact test is a test for determining the energy absorbed in fracturing a test piece at high velocity. In other words, it is one object striking another object at a relatively high speed. The impact resistance of a part is, in many applications, a critical measure of service life. More importantly these days, it involves the perplexing problem of product safety and liability. The impact energies of the part can be expected to predict in its lifetime. A notch was marked at the center of each specimen before conducting the test then it was placed on the bench and clamped. The impact hammer was released from a certain height in order to achieve impact energy. The hammer hit the specimen and it breaks in the middle. The reading was noted down in order to calculate the energy absorbed by each specimen. The impact charpy test was carried out as per ASTM [16] (Fig. 6).

All specimens including the original were split into two fragments by a charpy hammer and it displayed the ruptured nature of the original and modified glass fiber

Fig. 6 Charpy test result



composite. This phenomenon occurred due to brittle behavior of composite. The original specimen demonstrated the highest brittle nature and absorb the least energy and fail soon while A1, A2 and A3 absorbed 11.5 J, 13 J and 13.6 J respectively. The high weight percentage of SBG and the high amount by the specimen was discovered. It means SBG cable to reduce the brittleness of the composite.

4 Conclusion

- The fabrication of the glass fiber composite modified with various weights of SBG through the VARI procedure was done. The mechanical strength of composite modified with SBG was evaluated.
- Highest amount of added SBG illustrated good result and was found capable to take high stress and load during tensile test addition performed very well.
- A.E results displayed there is less fiber delamination and failure occurred when SBG was 15% used. This test also confirms that the tensile test first cracks propagation and then fiber pull-out takes place to the specimen.
- Brittle and rigid behavior of specimen was tested and the modified one demonstrated better results compare to the original ones.

Credit Authorship Contribution Statement Punita Kumari Conceptualization, Data curation, Funding acquisition, Investigation, Methodology, Software, Validation, Visualization, Writing original draft, Writing -review & editing Ashraf Alam—Conceptualization, Formal analysis, Validation, review & editing Saahil -Investigation, Methodology, Software, Validation, Visualization, Writing original draft.

Conflicts of Interest No potential conflict of interest was reported by the authors in conducting this research.

References

1. Kumari P, Wang J (2018) Residual tensile strength of the multi-impacted scarf-repaired glass fiber-reinforced polymer (GFRP) composites. *Materials* 11(12):2351
2. Kumari P, Wang J (2019) Tensile after impact test of scarf-repaired composite laminates. *Arab J Sci Eng* 44(9):7677–7697
3. Kumari P, Alam A (2021) Influence of the impact position on scarf repair composite under low velocity impact: FEA investigation. *Mater Today: Proc* 38:3005–3013
4. Kumari P, Alam A (2021) Multi-impact on scarf repaired composite laminates: FE investigation. *Mater Today: Proc*
5. Kumari P, Alam A (2021) Analysis of the composite sample under low velocity multi-impact test: FEA investigation. In: *Advances in engineering materials*, pp 505–514
6. Kumari P, Alam A, Wang J (2021) Estimation of low velocity impact on the scarf repair GFRP composite: Experimental method. *Mater Today: Proc* 43:731–739

7. Kumari P, Alam A, Wang J, Sankar SS (2021) Tensile after impact response on the scarf repaired glass fiber reinforced polymer samples–Experimental approach. *Mater Today: Proc* 43:112–123
8. Jefferson AJ, Srinivasan SM, Arockiarajan A (2019) Effect of multiphase fiber system and stacking sequence on low-velocity impact and residual tensile behavior of glass/epoxy composite laminates. *Polym Compos* 40(4):1450–1462
9. Behnam S (2017) Nanomaterials as a filler in natural fiber reinforced composites. *J Nat Fibers*
10. Sajith S, Arumugam V, Dhakal HN (2017) Comparison on mechanical properties of lignocellulosic flour epoxy composites prepared by using coconut shell, rice husk and teakwood as fillers. *Polym Test* 58:60–69
11. Sumesh KR, Kanthavel K (2020) Abrasive water jet machining of Sisal/Pineapple epoxy hybrid composites with the addition of various fly ash filler. *Mater Res Expr* 7(3):035303
12. Guna V, Ilangovan M, Hu C, Venkatesh K, Reddy N (2019) Valorization of sugarcane bagasse by developing completely biodegradable composites for industrial applications. *Ind Crops Prod* 131:25–31
13. Ribeiro Filho SLM, Oliveira PR, Panzera TH, Scarpa F (2019) Impact of hybrid composites based on rubber tyres particles and sugarcane bagasse fibres. *Compos Part B: Eng* 159:157–164
14. Candido VS, da Silva ACR, Simonassi NT, da Luz FS, Monteiro SN (2017) Toughness of polyester matrix composites reinforced with sugarcane bagasse fibers evaluated by Charpy impact tests. *J Market Res* 6(4):334–338
15. 3039M ASfTMADD (2005) Standard test method for tensile properties of polymer matrix composite materials
16. ASTM Standard D 6110-97 (2002) Standard test methods for determining the Charpy impact resistance of notched specimens of plastics. In: *Annual book of ASTM standards* 8

A Neural Network Based Approach to Determine Chatter Stability in Milling for a Variable Pitch Cutter



Pritam Ghoshal

Abstract The aim of this paper is to investigate an artificial neural network-based approach to determine the chatter stability limit of a milling process with a variable pitch cutter. The variable pitch cutter provides an advantage over the uniform pitch cutter as it shows increased stability behavior in a small range of spindle speed and depth of cut. The training data for the neural network is obtained by time domain simulations for a given combination of cutting parameters like cutting coefficients, feed and machine dynamic parameters like stiffness and damping. This data is fed to the multi-layer perceptron neural network to solve a classification problem using the scaled conjugate gradient method. The network performance is compared for several network architectures and the best combination is chosen. Once trained, the neural network is able to predict the stability of any given cutting condition with an accuracy of 99%.

Keywords Neural network · Artificial intelligence · Milling · Variable pitch · Chatter stability · Time domain simulation

1 Introduction

One of the pioneering works in determining chatter stability of milling was done by Altintas and Budak [1] who developed a general formulation by considering the cutter and workpiece as a multi-degree of freedom system. The dynamics of this system were modelled using delay differential equations. As a further continuation of their work, they developed simple analytical models for face milling and peripheral milling [2]. Altintas [3] presented the frequency and discrete time domain chatter stability laws. Milling with variable pitch and variable helix tools has been analyzed by Sims et al. [4]. Comak and Budak [5] analyzed the dynamic stability of a variable pitch and helix cutter both in the frequency domain as well as using a semi-discretization method using multiple delays. Several other authors have worked on establishing

P. Ghoshal (✉)
Indian Institute of Technology Kanpur, Kalyanpur, Uttar Pradesh 208016, India
e-mail: pritam20@iitk.ac.in

chatter stability for irregular cutting tools namely Yusoff et al. [6] and Huang et al. [7]. Artificial neural networks have been previously used to predict chatter stability. Cherukuri et al. [8] applied a neural network approach to chatter stability in turning. The analytical stability limit was used to train a neural network which then predicted whether a cutting condition is stable or unstable. Lamraoui et al. [9] used artificial intelligence for chatter prediction in milling using radial basis function and multi-layer perceptron. Deng et al. [10] described a reliability analysis of a milling process with uncertainties using neural networks. Tran et al. [11] proposed a method of chatter detection in milling based on the scalogram of the continuous wavelet transformation and the deep convolutional neural network. All previous studies on the stability of the milling process using artificial neural networks (ANN) have been limited to milling cutters where the teeth are equally spaced. However, cutters with non-proportional spacing have been shown to have increased stability behavior in a certain regime due to interruption of regeneration of surface waviness. Such type of cutters is especially used where changing the spindle speed is inconvenient like in transfer lines or in applications where a high spindle speed will lead to tool wear and machinability issues. However, not all variable tooth spacing is accompanied by an increase in stability. The region which shows an increased stability behavior depends on the dynamics of the system, spacing between the teeth and speed of operation. This paper aims to determine the chatter stability limit of a milling process for a variable pitch cutter using ANN which may then be used to determine the stability for any given cutting condition. Several neural network architectures have been compared based on the number of hidden layers and neurons used to determine the stability boundary.

2 Background

Consider a milling cutter having radius r and N_t teeth, being used in a milling process with a depth of cut a mm and linear feed f mm/min. The cutter is rotating at a speed of Ω rpm. The feed per tooth is hence given by,

$$f_t = \frac{f}{\Omega N_t} \quad (1)$$

Let at any instant, the cutter has rotated by an angle φ . The cutter is said to be cutting, only when it is in contact with the workpiece. This happens when φ is between φ_s and φ_e , the start and exit angle which is defined by the cutter geometry and type of milling, that is up milling or down milling. More details about φ_s and φ_e can be found in [12]. Let k_n and k_t be the cutting force coefficients in the normal and tangential direction and b be the width of the cut. Then the cutting force given in these directions is given by

$$F_n = k_n b h F_t = k_t b h \quad (2)$$

where h is the instantaneous chip thickness. The cutting forces in the x and y directions can hence be found as,

$$F_x = F_t \cos\phi + F_n \sin\phi \quad (3)$$

and,

$$F_y = F_t \sin\phi - F_n \cos\phi \quad (4)$$

A brief overview of the time domain simulation of a milling problem with a constant pitch cutter is given below which is based on the formulation as given by Smith and Tlustý [13]. This formulation will later be modified for a variable pitch cutter.

Due to vibrations of the tool (assuming the workpiece to be rigid), wavy profiles are created on the original surface by the first tooth in contact. When the next tooth contacts the workpiece, it does not encounter the original surface, but the wavy surface left behind by the previous tooth. Thus, the instantaneous chip thickness depends not only upon the current vibration, but also on the profile left behind by the previous tooth. Thus, a feedback mechanism is produced. The chip thickness is measured along the surface normal. The normal direction changes as a function of the engagement angle ϕ . Projecting the vibrations in the x and y directions, in the direction of the normal, the following equation is obtained.

$$n = x \sin\phi - y \cos\phi \quad (5)$$

where $\phi = 6\Omega t$ and t is in seconds. The instantaneous chip thickness can thus be written as

$$h(t) = f_t \sin\phi + n(t - \tau) - n(t) \quad (6)$$

where f_t is the feed per tooth and τ is the tooth period in seconds and is given by

$$\tau = \frac{60}{\Omega N_t} \quad (7)$$

Here $n(t)$ is the normal direction vibration in the current pass and $n(t - \tau)$ that in the previous pass. Care must be taken to calculate $n(t - \tau)$ by considering whether the previous tooth was indeed cutting or not. Once the chip thickness is calculated, the cutting force in the x and y direction can be calculated using Eqs. (3) and (4). The equations of motion can be written as

$$m_x \ddot{x} + c_x \dot{x} + k_x x = F_x \quad (8)$$

and,

$$m_y \ddot{y} + c_y \dot{y} + k_y y = F_y \quad (9)$$

Here m_i , c_i , k_i are the mass, damping and stiffness in the i direction. If there is more than one degree of freedom in each direction, Eqs. (8) and (9) will become a system of equations represented in matrix form.

Assuming the initial displacement and velocity in both the x and y directions to be zero, the equations of motions can be solved for \ddot{x} and \ddot{y} iteratively, which can then be used to find the displacement and velocity for the subsequent time steps. One such iterative method is the Euler forward integration method, the algorithm for which states that,

$$\dot{x} = \dot{x} + \ddot{x}dt \quad \dot{y} = \dot{y} + \ddot{y}dt \quad (10)$$

and,

$$x = x + \dot{x}dt \quad y = y + \dot{y}dt \quad (11)$$

where dt is the small incremental time step. This completes the derivation of the time domain simulation algorithm for a constant pitch cutter. In the case of cutters with uniform teeth spacing, there is a periodic delay between two engagements. However, when the spacing is varied, this periodicity is interrupted. Hence, the first modification from the previous derivation is that τ is no longer constant. The second modification will be for the feed per tooth, which will now change with every tooth. Feed per tooth for each tooth each is given by,

$$f_t = \frac{\overline{f}_t \theta N_t}{360} \quad (12)$$

where \overline{f}_t is the mean feed per tooth and θ is the angle between the current and previous teeth and is different for each tooth. Rest of the derivation remains the same.

3 ANN Model

The training data is obtained by time domain simulations for several cutting conditions using the algorithm described in Sect. 2. Here it is considered that there are two modes each in the x and y directions. Data for both the modes is assumed to be as follows: $k_1 = 2 \times 10^7$ N/m, $f_{n1} = 800$ Hz, $\zeta_1 = 0.05$, $k_2 = 1.5 \times 10^7$ N/m, $f_{n2} = 1000$ Hz, $\zeta_2 = 0.03$, where f is the natural frequency and ζ is the damping ratio. The tangential and radial cutting coefficients are 520 N/mm² and 300 N/mm².

The cutter has 4 teeth which are placed at 95, 180 and 275 degrees from the first tooth. The radius of the cutter is such that the starting and exit angles are 0 and 66.4 degrees. The built-in neural net toolbox of MATLAB is used to construct the neural net architecture. There are two input features, the spindle speed, and the limiting depth of cut. So, the input layer has two nodes. A total of 19,200 data points are used to train and validate the ANN. The blue dots signify stable cutting conditions while the red dots represent unstable cutting conditions. The spindle speed is varied from 2000 to 6000 rpm and the depth of cut from 1 to 24 mm. Since the scale of both the features is different, first a feature scaling is performed using the min–max method to bring the input features within the range $[-1, 1]$. For the training data, the output is either 0 or 1 for unstable and stable points respectively. The normalized data is then randomly divided into three sets-training, validation and testing set in the ratio 70:15:15. So the training set has 13,440 data points, and the validation and test sets contain 2880 data points each as shown in Fig. 1.

The ANN consists of two hidden layers with seven neurons each as shown in Fig. 2. The input layer consists of two neurons corresponding to the limiting depth of cut and spindle speed. The output of the neural network is the probability $p(x)$

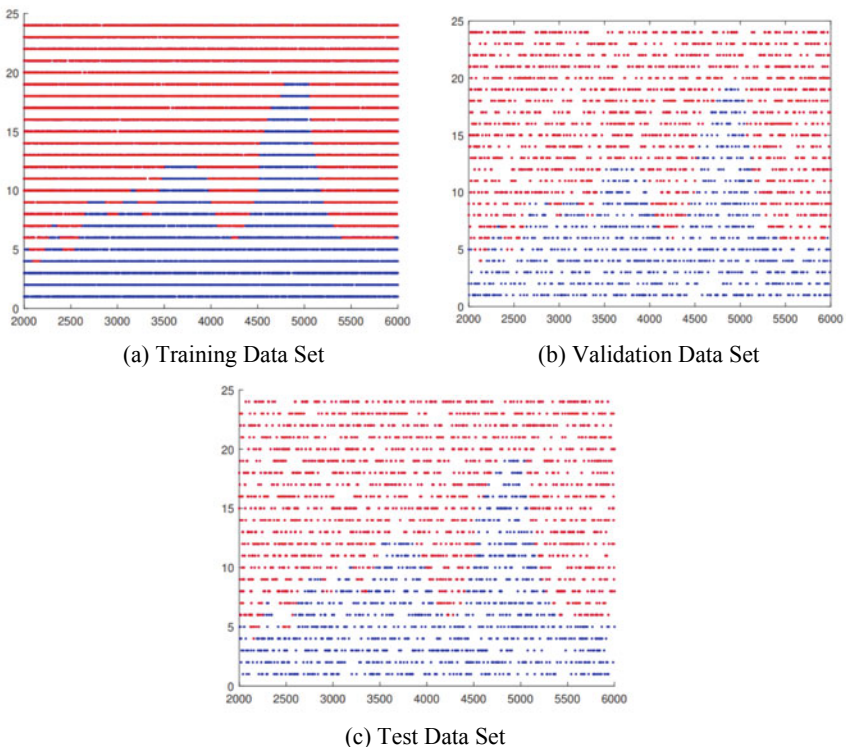


Fig. 1 Data set for the ANN

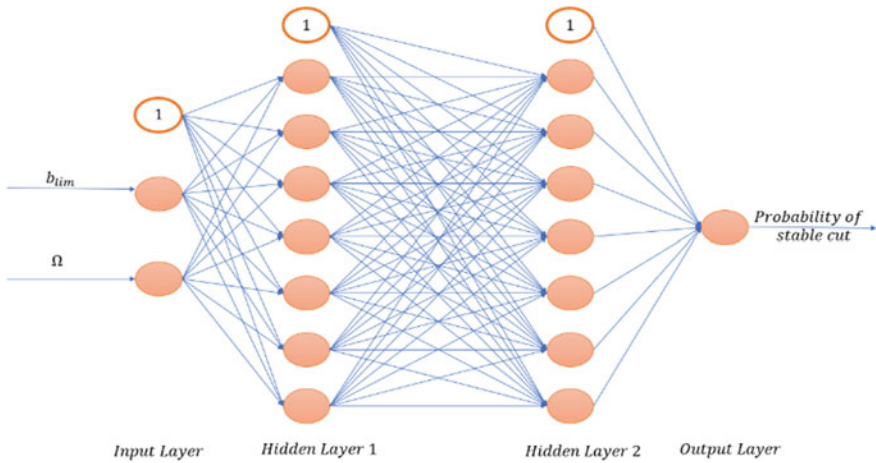


Fig. 2 The ANN architecture with 2 hidden layers and 7 node each

such that the conditions as defined by the input are stable. The probability is defined as

$$p(x) = \{Y = 1 | (\Omega, b_{lim})\} \tag{13}$$

If $p(x) \geq 0.5$, then the cutting conditions are stable, otherwise unstable. The activation function for the input and hidden layers has been taken as the hyperbolic tangent sigmoid function, while that for the output layer is taken as a purely linear function. The bias has been taken as one for both the input and hidden layers. The cross-entropy error function is used in this paper. However, there are other error functions available which might also be used. There are four stopping conditions for training. The first condition is when the number of epochs exceeds 500,000. The second condition is when the gradient (derivative with respect to the weights) reaches 10^{-6} . The third is when the error as evaluated by the error function is less than 0.001. The final condition is when the number of validation checks or the number of successive iterations for which the validation performance has failed to increase exceeds 6.

4 Results

The confusion matrix for the training, validation and test data is shown in Fig. 3. The target class represents the actual value while the output class represents the predicted value. 0 and 1 represent the chatter and stable case respectively. As can be seen in Fig. 3c, the ANN predicts 2863 (1787 true positives and 1076 true negatives) out

of the 2880 test data points accurately with an accuracy of 99.4% which is very accurate. Overall, the ANN predicts the data correctly with an accuracy of 99.7% as can be seen in Fig. 3d.

The network performance as evaluated by the cross-entropy function versus the epoch for the training, validation and test data is shown in Fig. 4. As can be seen, the error in the predicted output for the training data reduces with number of epochs and ultimately goes below 0.01. For the validation and test data, the curve starts rising upwards after a certain epoch which suggests over-fitting. Hence instead of running the algorithm till the error reaches below a certain value (which may lead to over-fitting), the algorithm is run up to 500,000 epochs. At this point the error in prediction for the training data is below 0.01 and, in the testing, and validation data is below 0.1 which is within an acceptable range.

The variation of the gradient with epochs is shown in Fig. 5. As can be seen the gradient has a decreasing trend on average with number of iterations which means the error function is approaching its minimum. The gradient after 500,000 iterations was 0.000249 which signifies that the algorithm has stopped very close to the minimum.

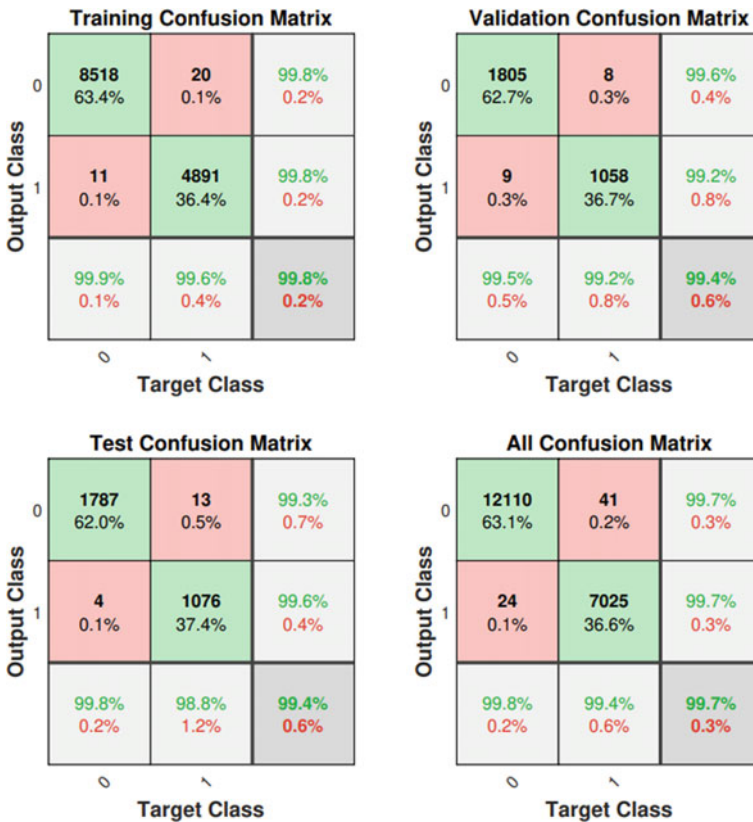


Fig. 3 Confusion matrix

Fig. 4 ANN performance plot

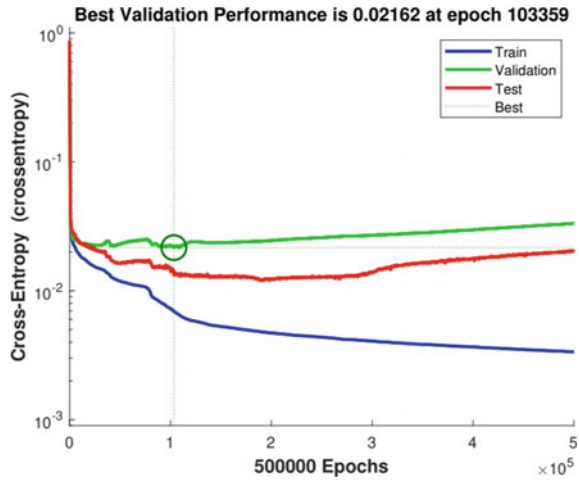
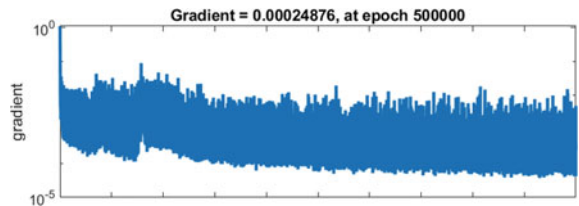


Fig. 5 Variation of gradient with epochs



The error histogram for the training, validation and testing data is shown in Fig. 6. The x axis represents the error in the prediction while the y axis represents the number of samples which are in the same error range. The error ranges from -0.95 to 0.95 which has been divided into 20 ranges or bins. The width of each bin is thus $(0.95 + 0.95)/20 = 0.095$. It can be seen that most of the sample data lies within a small range of error from $(0.0499 - 0.0950/2) = 0.0024$ to $(0.0499 + 0.0950/2) = 0.0974$. Almost 18,000 of the total 19,200 points have been predicted with an error of less than 0.05 which suggests that the classification problem has been solved very accurately.

The receiver operating characteristic (ROC) curve is shown in Fig. 7. The ROC is a measure of the performance of a binary classifier and is created by plotting the true positive rate versus the false positive rate. The more each curve hugs the top and left edge of the graph, the better the classifier. As can be seen, the curves for all three data sets-training, validation, and testing are almost along the edges which signifies a very good prediction of stability. Hence from all these measures, it can be concluded that the ANN is able to predict the stability of a given cutting condition very accurately.

The decision boundary as obtained by the ANN is shown in Fig. 8. It is a pretty accurate representation of the stability boundary as obtained from the time domain simulation. It is also evident from Fig. 8, that there is a region around 4000 rpm to 4600 rpm where the stability has increased as compared to the uniform pitch

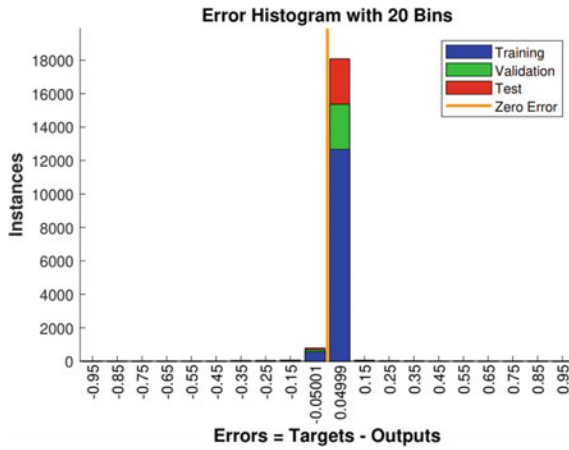


Fig. 6 Error histogram

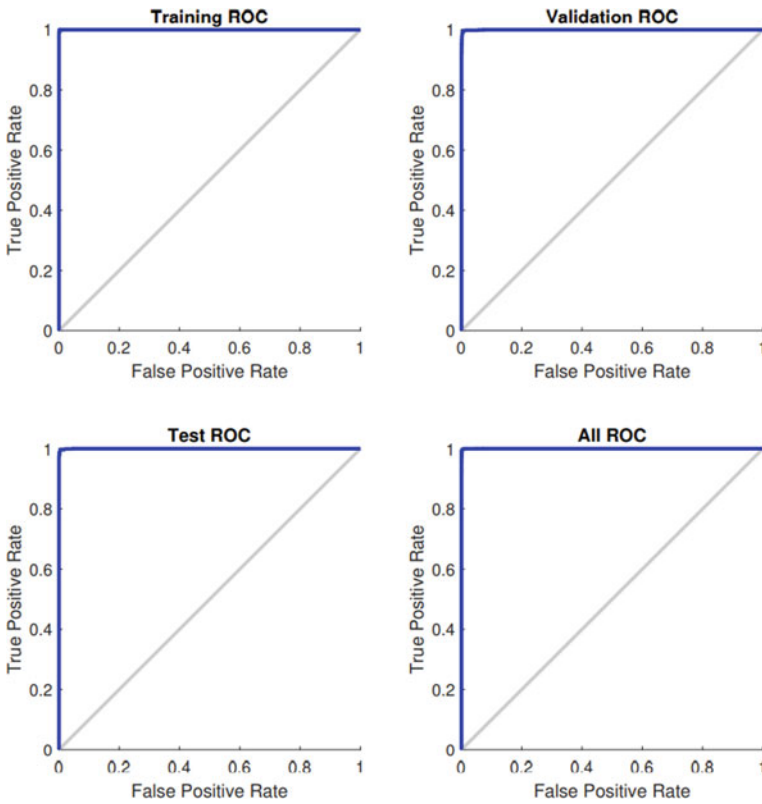
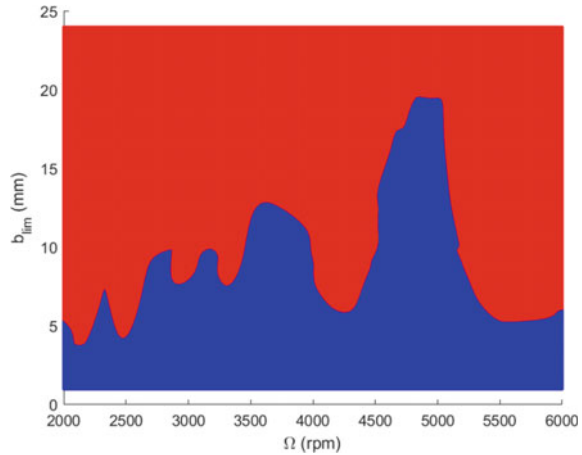


Fig. 7 Receiver operating characteristics

Fig. 8 Stability limit as predicted by ANN



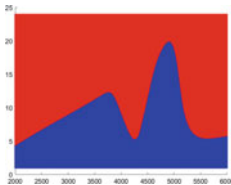
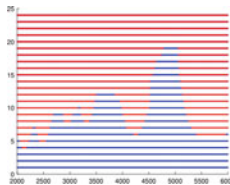
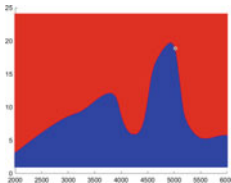
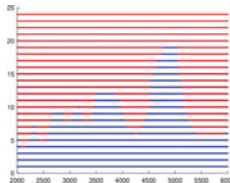
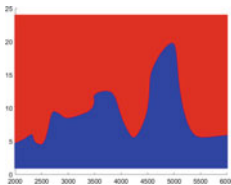
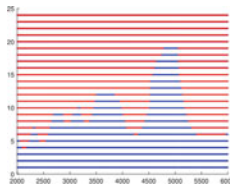
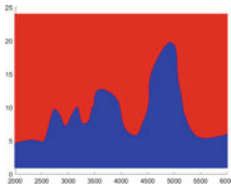
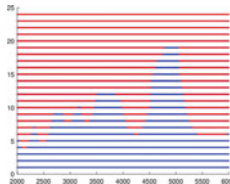
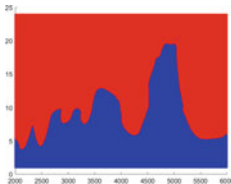
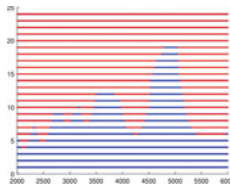
cutter, which is in line with the time domain simulation predictions. To give some perspective, the stability limit at 4000 rpm for a uniform pitch cutter is around 4.6 mm, for that of a variable pitch cutter in the configuration considered in this paper is 10 mm while that predicted by ANN is around 9.8 mm. The stability limit at 4600 rpm for a uniform pitch cutter is around 7 mm, for that of a variable pitch cutter is 16 mm while that predicted by ANN is around 16.2 mm.

The sensitivity of the decision boundary on the network architecture has been investigated. The decision boundary has been plotted for several combinations of layers and neurons. Some such combinations are shown in Table 1. The first column represents the network architecture. The second column shows the decision boundary as obtained from the ANN and the third column shows the original decision boundary obtained from time domain simulation. As can be seen, for less number of neurons, although the increase in stability around 4000 rpm is predicted, the ANN misses out on the smaller lobes. However, on increasing the number of neurons, the ANN is able to predict the stability lobes very closely.

5 Conclusion

This paper aims to apply a neural network-based approach to milling chatter stability analysis for a cutter with variable pitch. The ANN predicts that for the cutting parameters and machine dynamics considered in this paper, there is a small regime around 4000 rpm to 4600 rpm where improved stability behavior can be obtained which confirms the predictions of the time domain simulations. For a smaller number of neurons in the hidden layer, the ANN is not able to predict stability near the smaller lobes very accurately. On increasing the number of nodes, even the smaller lobes are taken into account. The ANN with two hidden layers and seven neurons each is able to predict the stability with an accuracy of about 99%. Once trained, this network

Table 1 Comparison of sensitivity of decision boundary to ANN architecture

ANN architecture	ANN decision boundary	Time domain simulation
2 layers 3 neurons		
2 layers 4 neurons		
2 layers 5 neurons		
2 layers 6 neurons		
2 layers 7 neurons		

can be used to predict the stability for any given cutting condition for the parameters considered in this paper without performing a complex time domain simulation and observing the behavior of the displacements and forces.

6 Future Scope

The data in this paper has been generated using time domain simulations. An improvement over this would be to generate the data from actual experiments itself for a wide combination of cutting coefficients, material and machine dynamics. The data thus obtained, could be then used to train a much larger neural network. The input layer in this case, would not only consist of the spindle speed and depth of cut, but also several other parameters like feed, cutting coefficients, machine stiffness and damping, number of modes etc. The trained network thus obtained can then be used to predict chatter stability in milling on any machine for any material workpiece combination. Improved stability behavior may also be obtained using a helical tooth that has a varying angle of helix along the axis or a cutter that has a different angle of the helix for each tooth. Such cases may also be investigated in the future using ANN.

References

1. Budak E, Altintas Y (1998) Analytical prediction of chatter stability in milling—part I: general formulation
2. Budak E, Altintas Y (1998) Analytical prediction of chatter stability in milling—part II: application of the general formulation to common milling systems
3. Altintas Y, Stépán G, Merdol D, Dombóvári Z (2008) Chatter stability of milling in frequency and discrete time domain. *CIRP J Manuf Sci Technol* 1(1):35–44
4. Sims ND, Mann B, Huyanan S (2008) Analytical prediction of chatter stability for variable pitch and variable helix milling tools. *J Sound Vib* 317(3–5):664–686
5. Comak A, Budak E (2017) Modeling dynamics and stability of variable pitch and helix milling tools for development of a design method to maximize chatter stability. *Precis Eng* 47:459–468
6. Yusoff AR, Mansor MH, Hussain HC, Abidin MAZ (2014) Analytical chatter stability prediction for irregular types of milling tools. *Mater Sci Forum* 773:420–426. Trans Tech Publications Ltd.
7. Huang P, Li J, Sun J, Ge M (2012) Milling force vibration analysis in highspeed-milling titanium alloy using variable pitch angle mill. *Int J Adv Manuf Technol* 58(1–4):153–160
8. Cherukuri H, Perez-Bernabeu E, Selles MA, Schmitz TL (2019) A neural network approach for chatter prediction in turning. *Proc Manuf* 34:885–892
9. Lamraoui M, Barakat M, Thomas M, Badaoui ME (2015) Chatter detection in milling machines by neural network classification and feature selection. *J Vib Control* 21(7):1251–1266
10. Deng C, Miao J, Ma Y, Wei B, Feng Y (2020) Reliability analysis of chatter stability for milling process system with uncertainties based on neural network and fourth moment method. *Int J Prod Res* 58(9):2732–2750
11. Tran MQ, Liu MK, Tran QV (2020) Milling chatter detection using scalogram and deep convolutional neural network. *Int J Adv Manuf Technol* 107(3):1505–1516
12. Schmitz TL, Smith KS (2014) *Machining dynamics*. Birkhauser
13. Smith S, Tlustý J (1991) An overview of modeling and simulation of the milling process. *J Eng Ind* 113(2):169

Effect of Chromium on Mechanical and Corrosion Behaviour of Ferrous Metal Matrix Composites by Using Powder Metallurgy Route



K. R. Varadaraj, Sanjay Kumar, H. R. Vitala, M. K. Ravishankar, and B. P. Dileep

Abstract In this present research work effect of chromium in ferrous material by using the powder metallurgy technique is been studied in detail. Chromium is added to iron matrix in various proportions of 2%Cr, 4%Cr, 6%Cr, and 8%Cr and the remaining is Fe powder. First challenge was to produce these metal matrix composites by using the powder metallurgy technique, we also added zinc stearate as a binder and die releasing agent. The compaction load is optimized to 160KN by trial-and-error method to get a healthy specimen and the required density is achieved (Mahajan et al. in Indian J Sci Technol 8:101–105, 2015). These compacted green specimens were sintered at 12,000 C to make them hard and useable shape. Once this Fe–Cr metal matrix composite is successfully prepared by using the powder metallurgy technique these composites were tested for Vickers Hardness number and corrosion behaviour and tested under an optical microscope to study on microstructure of the prepared composites (Gurcan and Baker in Wear 188:185–191, 1995). During these tests, it showed that the purest iron specimen produced at 160 KN load and sintered at 12,000 C showed a hardness of 126HV against a 100HV of 6% of Cr in the Fe matrix, that clearly shows that Cr is not contributing much to the hardness of the composites (Yih and Chung in Int J Powder Metall (1986) 31(4):335–340, 1995). Corrosion tests on these sample show that adding Cr to Fe matrix will definitely delay the corrosion to a good extent and microstructure studies revealed that chromium reinforcement in the iron matrix is uniformly distributed and no internal defects are found (Saheb in ARPN J Eng Appl Sci 6:41–46, 2011).

K. R. Varadaraj

School of Mechanical Engineering, REVA University, Bengaluru 560064, India

S. Kumar · H. R. Vitala

Department of Mechanical Engineering, SJBIT, Bengaluru 560060, India

M. K. Ravishankar

Department of Mechanical Engineering, PES University, Electronic City Campus, Bengaluru, India

B. P. Dileep (✉)

Department of Mechanical Engineering, Amrita School of Engineering, Amrita Vishwa Vidyapeetham, Bengaluru 560035, India

e-mail: bp_dileep@blr.amrita.edu

Keywords Metal matrix composites · Ferrous materials · Hardness · Corrosion · Powder metallurgy

1 Introduction

Composite materials have been in use for centuries. The composites when compared to a monolithic metal, have different properties and can be tailored to a specific requirement. These composites show high strength to weight ratio while also providing higher stiffness. The composite materials also possess good fatigue resistance, corrosion resistance, resistance to thermal expansion, exceptional optical and magnetic properties etc., There are numerous applications that demand a unique combination of properties that cannot be met with conventional materials [5]. The present trend is to get light weight for ease of handling, reduced space and reduction in parts of an assembly along with aesthetic appearance. Factors like this propel modern designers to develop better composite materials to enable large scale production [6].

2 Powder Production

2.1 Selection of Powders

Composition of Iron and chromium has been selected as matrix and reinforcement material respectively. This MMC (Metal Matrix Composite) was fabricated by using the powder metallurgy technique. Chromium particles (0%, 2%, 4%, 6% and 8% by weight) were reinforced into Iron using Zinc stearate to reduce friction all along the walls of the die and the punch [7]. Zinc stearate also has a secondary function as a binder.

2.2 Mixing of Powders

The Iron and Chromium powders were mixed together before compaction to ensure uniform distribution. Zinc stearate was also used to ensure that the powder does not stick to the walls of die and punch, also reducing the friction between them during compaction [8]. These three were mixed by tumbling action and then transferred to a die which was used for compaction. Different combinations of specimens were prepared by using the design of experiments, where different percentages of reinforcements were used. Five different specimens were prepared 0%, 2%, 4%, 6% and 8% by weight of Cr [9] (Fig. 1).

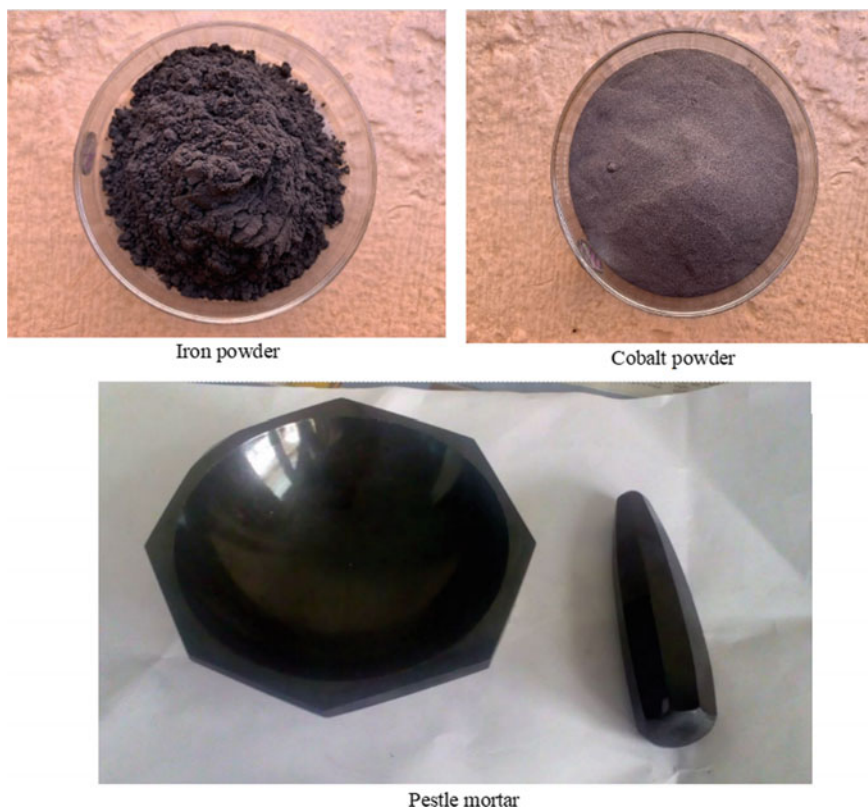


Fig. 1 Matrix, reinforcement and pestle mortar

2.3 *Compaction*

Compaction is the process where pressure is applied to the metal powder in a die to take the shape of the die there by increasing the density of the material. The tool was kept vertically with the punch moving coaxially with the die hole. The powders then were compacted and ejected from the die cavity to obtain the green specimen (Compacted specimen) (Fig. 2).

Premixed and precalculated amounts of powders were compacted as mentioned below.

1. The die was rammed properly before placing the die to ensure powder particles does not stick to the walls of the die cavity.
2. Then the die was placed vertically below the cross head and ensured that it was placed coaxially to the cross head, to ensure non breaking of the punch.
3. The load was then applied slowly using UTM. The amount of load applied depends on the specifications of the die used and the composition of the material used. The load used here is 160 KN for all the compositions.

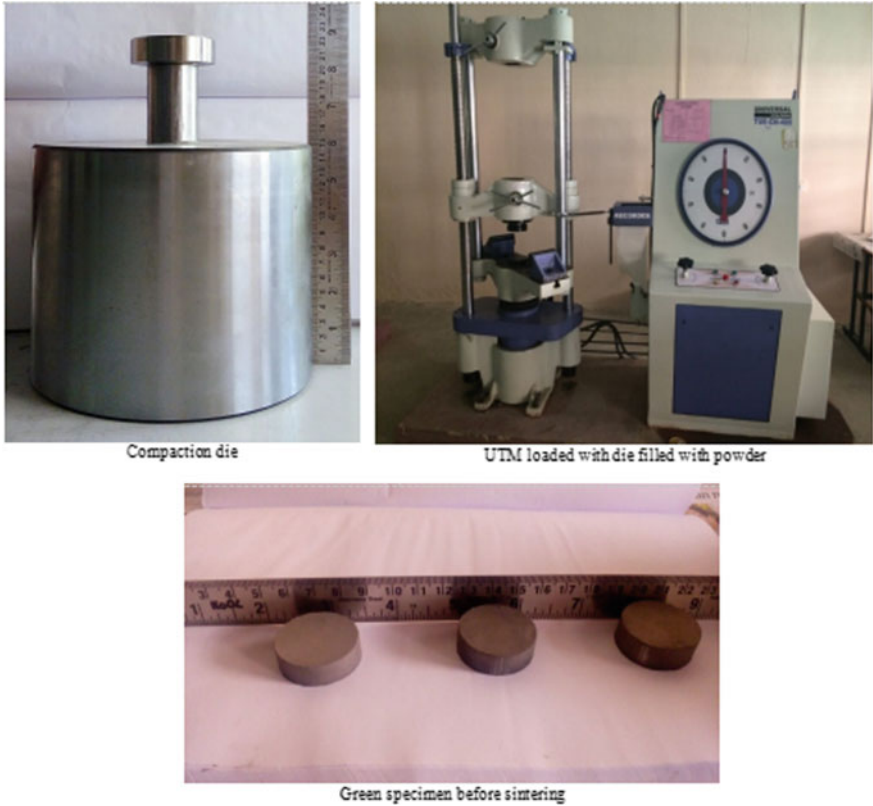


Fig. 2 Compaction process

4. After unloading by moving the cross head away from die and the specimen is removed from the die.
5. Different loads applied will vary the density of the specimen obtained and could be an important parameter to be considered while preparing specimens for a specific application.
6. These specimens thus prepared are then sent for sintering (Fig. 3).

2.4 Sintering

The Specimens are cooled down to room temperature before placing inside the muffle furnace. The green specimens cooled are then transferred into the SEMCO muffle furnace. The temperature is raised to 1200 °C and cooled back to room temperature completing the sintering process [10]. But there are many ways of cooling down the specimen but the process adopted was furnace cooling. As Iron has always been tending to get oxidized more even at room temperature [11], care has to be taken

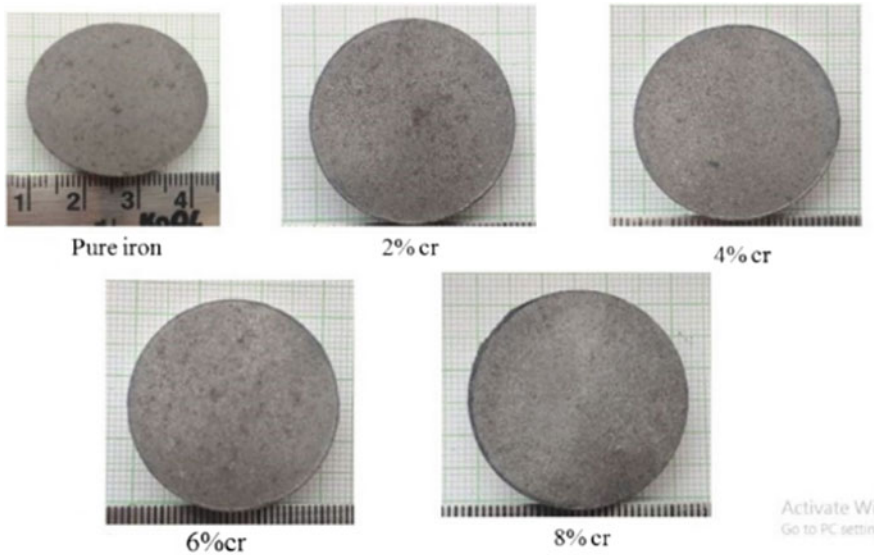


Fig. 3 Green specimens

so that the exposure of specimens to atmospheric air is minimal. Once the furnace comes back to room temperature the specimens are taken out and further machining operations are carried out [12].

3 Mechanical Testing

3.1 Hardness Test

The hardness test consists of applying a fixed amount of force and using a specific indenter. The smaller indentation indicates harder material and a larger indentation indicated less hardness. The measure of the depth of indentation or area of the indentation is a direct measure of the Indentation hardness value [13]. The Vickers hardness test starts with creating indentation on the test material by using a right pyramid shaped diamond indenter with a square base and 136 degrees angles between the faces. Applied load varying from 1 to 100 kgf. Generally, the test load is applied on the specimen for a duration of 10 to 15 s [14]. Two diagonals of the indentations are measured by using a micrometre after the load is removed from the specimen, and the average value of measured indentation is considered for future calculations to determine the hardness of the specimens undergone hardness testing [15].

Fig. 4 Sintered specimens

3.2 Corrosion Resistance

Corrosion resistance is described as the ability of a material (particularly a metal) to withstand damage caused by oxidation or other chemical reactions. It is measured in millimeters per year and is expressed as a corrosion rate [16]. These corrosion resistance measurements are taken in a specific environment under specific operating conditions, such as strain, temperature, and fluid velocity [17]. Different processes, such as cathode protection, coating, plating, and applying a corrosion inhibitor, can be used to improve a metal's corrosion resistance [18] (Fig. 4).

3.3 Microstructural Study

Microstructure is a term used to describe the small-scale structure of a material, which is described as the structure of a required surface of the material as revealed by a microscope at a magnification of greater than 25X. Physical properties such as strength, toughness, ductility, hardness, corrosion resistance, high/low temperature behaviour, and wear resistance can all be affected by a material's microstructure. These properties, in turn, decide how these materials are used in industry. Microstructure at sizes too small for optical microscopes to see.

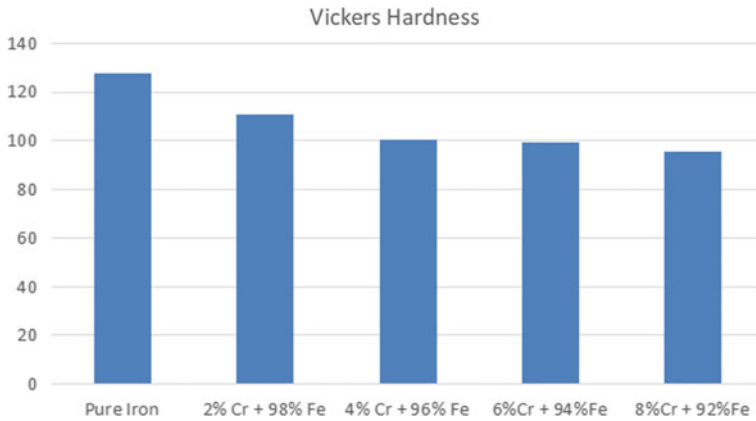
4 Results and Discussion

4.1 Vickers Hardness Values

Microstructure is a term used to describe the small-scale structure of a material, which is described as the structure of a required surface of the material as revealed

Table 1 Vickers hardness number

Composition	HV
Pure iron	127.6
2% Cr + 98% Fe	73.6
4% Cr + 96% Fe	100.3
6%Cr + 94%Fe	99.3
8%Cr + 92%Fe	95.3

**Fig. 5** Vickers hardness variations for different specimens

by a microscope at a magnification of greater than 25X. Physical properties such as strength, toughness, ductility, hardness, corrosion resistance, high/low temperature behaviour, and wear resistance can all be affected by a material's microstructure. These properties, in turn, decide how these materials are used in industry. Microstructure at sizes too small for optical microscopes to see (Table 1; Fig. 5).

4.2 Microstructure

The microstructure was studied under an optical metallurgical microscope where the specimens were initially belt polished using 120, 220, 400 and 600 emery papers then buffed using aluminum and finally washed using 2% nitol. In Fig. 6, irregular grains are observed in microstructural studies which are appreciable and which suggest the presence of Cr.

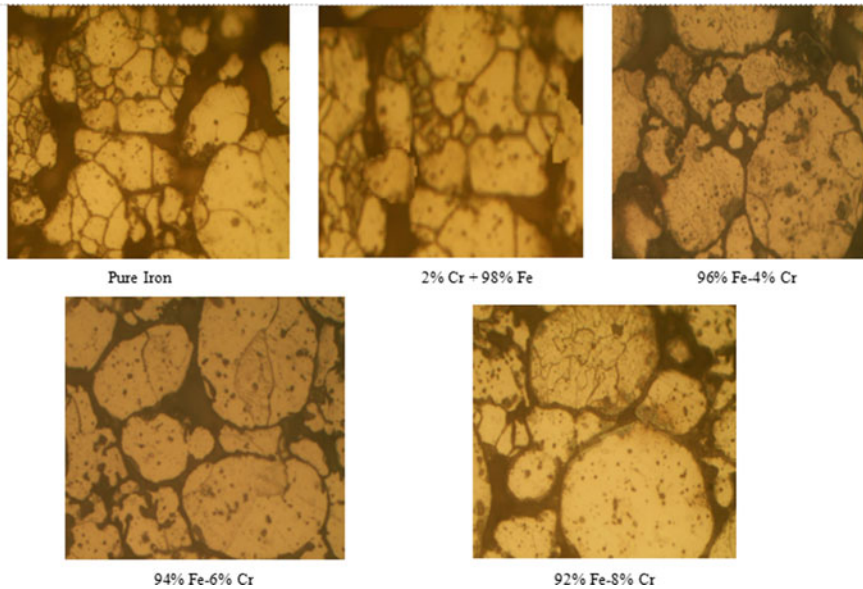


Fig. 6 Microstructure of all the specimens

4.3 Salt Spray Test

Salt spray test was conducted with a 5% concentration of NaCl sprayed on it at a test temperature of 34–36 °C for a duration of 48 h. The test volume collected is 1.80 ml/hr/80sq cm. The pH of the collected sample was found to be 6.48. The observations were carried out at two intervals 24 h apart. It was observed that after 24 h no rust was observed while at 48 h red rust was observed on all the samples. The samples of Iron showed comparatively larger rust particles than any other sample. It was also observed that corrosion resistance increases as the composition of Cr increases up to 6% and after that, it reaches saturation point for 8% Cr composition.

4.4 Tafel Plots

The tafel plots schematically represented below are the results of the corrosion resistance test that can be interpreted for information such as: Rate of pitting, Passivity and Corrosion susceptibility. With these figures the corrosion current (the rate of flow of ions is identified) can be used to compute the rate of corrosion. The plot together with the equation can be very useful in depicting the life span of materials in various industries (Fig. 7).

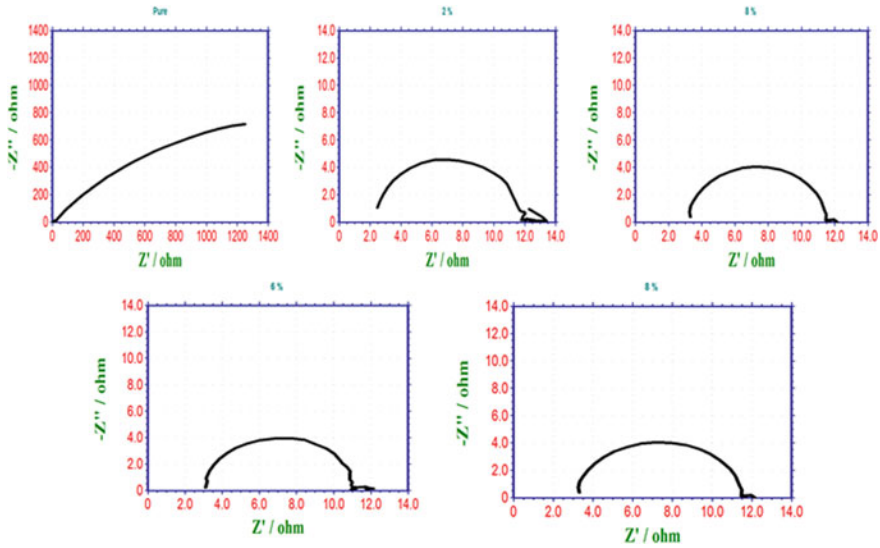


Fig. 7 Tafel plots

5 Conclusion

The Fe–Cr MMC's Specimens were successfully fabricated using Powder Metallurgy Technique. Zinc stearate has been shown to be a good solid binder while also serving as friction reducing agent between the die wall and the plunger. With the addition of Cr hardness decreases because of the low density of chromium when compared to the density of pure Fe. And reached saturation at about 6% Cr beyond which there was no appreciable decrease in the hardness value. The microstructure studies showed irregular grains which are appreciable suggesting the presence of Cr in Fe. Pure Fe showed higher rusting compared to other specimens with 6 and 8% Cr showing less rusting, indicating the saturation point lying at about 6% Cr.

References

1. Mahajan G, Karve N, Patil U, Kuppan P, Venkatesan K (2015) Analysis of microstructure, hardness and wear of Al-SiC-TiB₂ hybrid metal matrix composite. *Indian J Sci Technol* 8(2):101–105
2. Gurcan AB, Baker TN (1995) Wear behaviour of AA6061 aluminium alloy and its composites. *Wear* 188(1–2):185–191
3. Yih P, Chung DL (1995) Powder metallurgy fabrication of metal matrix composites using coated fillers. *Int J Powder Metall* (1986) 31(4):335–340
4. Saheb DA (2011) Aluminum silicon carbide and aluminum graphite particulate composites. *ARNP J Eng Appl Sci* 6(10):41–46

5. Ozden S, Ekici R, Nair F (2007) Investigation of impact behaviour of aluminium based SiC particle reinforced metal–matrix composites. *Compos A Appl Sci Manuf* 38(2):484–494
6. Debnath S, Oo Z, Rahman M, Maleque M, Tan C (2012) Physio-mechanical properties of aluminium metal matrix composites reinforced with Al₂O₃ and SiC. *Int J Eng Appl Sci* 6:288–291
7. Bayraktar E, Katundi D (2010) Development of a new aluminium matrix composite reinforced with iron oxide (Fe). *J Achiev Mater Manuf Eng* 38(1)
8. Bayraktar E, Masounave J, Caplain R, Bathias C (2008) Manufacturing and damage mechanisms in metal matrix composites. *J Achiev Mater Manuf Eng* 31(2):294–300
9. Ravi Kumar V, Dileep BP, Vital HR (2017) Tribological and mechanical characterization of Al-Ni-SiC metal matrix composites. In: AIP conference proceedings 1859, 020020
10. Abbass MK, Hassan KS, Alwan AS (2015) Study of corrosion resistance of aluminum alloy 6061/SiC composites in 3.5% NaCl solution. *Int J Mater, Mech Manuf* 3(1):31–35
11. Włodarczyk-Fligier A, Adamiak M, Dobrzański LA (2010) Corrosion resistance of the sintered composite materials with the EN AW-AlCu4Mg1 (a) alloy matrix reinforced with ceramic particles. *J Achiev Mater Manuf Eng* 42(1–2):120–126
12. Kumar A, Swamy RP (2011) Experiments on Al6061, fly ash and E glass fiber reinforced hybrid metal matrix composites. *ARPN J Eng Sci* 6:135–156
13. Dinesh Kumar DK, Agnihotri G, Purohit R (2013) Properties and characterization of Al-Al₂O₃ composites processed powder metallurgy routes. *Int J Latest Trends Eng Technol* 2
14. Dileep BP, Kumar VR, Prashanth M, Phanibhushana MV (2014) Effect of Zinc coating on mechanical behavior of Al 7075. *Appl Mech Mater* 592:255–259
15. Kumar SS, Suresh AV, Nagamadhu M, Vitala HR, Dileep BP (2019) Optimization of drilling parameters on Alkaline treated jute fiber sandwich material. *Int J Recent Technol Eng* 8
16. Kumar VR, Dileep BP, Kumar SM, Phanibhushana MV (2017) Effect of metal coatings on mechanical properties of aluminium alloy. *AIP Conf Proc* 1859:020037
17. Dileep BP, Sridhar BR (2018) A investigation on mechanical and metallurgical properties of steel EN24 and SiC MMCs. *Int J Mech Prod Eng Res Dev* 8:189–194
18. Nair AK, Kalmadi A, Kumar N, Dileep BP (2021) Investigation on mechanical properties of aluminum-boron carbide metal matrix composites. In: *Recent advances in smart manufacturing and materials*, pp 213–221

Study of Effect of Protrusions on Cones in Hypersonic Flow



V. C. Mithun Chandrakumar and S. R. Nagaraja

Abstract Protrusions are the discontinuities on the surface. It can be sheet joints or control surfaces that cause protrusion. In low speed flow, the boundary layer thickness is higher so that protrusion has a small effect compared to high speeds which have a thin boundary layer. In hypersonic flow, even a small protrusion can cause a severe increment in heat load. As the height and geometry of the protrusion change the effect in the flow field also changes. Heat flux due to protrusion depends on height, shape and inlet conditions. The maximum heat flux occurs on the vertical surface of the protrusion. The maximum heat flux in front of the protrusion depends on the height of the protrusion. The flow separation distance in front of the protrusion is about 3–4 times the protrusion height.

Keywords Hypersonic flow · Protrusions · Separation length · Heat flux

1 Introduction

Aerodynamic vehicle requires maximum fuel volume. For providing this the piping, instrumentation etc. are placed on the exterior of the vehicle, which creates discontinuities on the surface. Also, the presence of control surfaces, cable protection systems and rivets sheet joints add to these discontinuities. These discontinuities can be protrusions or cavities. At high speeds, the effect of these discontinuities are predominant than lower speeds. These discontinuities will increase the heat and pressure loads due to flow separation. Lighthill et al. [1] have explained the mechanism of flow separation in sub-sonic and supersonic flows in the presence of protrusions on flat plates. A flat plate and cone were tested in a hypersonic flow by Kumar et al. [2, 3]. The cone model used in the experiment was fabricated by Duralumin 2014 with a half angle of 20° (similar to the nose of the Space Capsule Recovery Experiment model of ISRO) and a base diameter of 130 mm. It is 178.5 mm long along the axis. The experiment was conducted for different protrusion heights such as 3, 5 and 8 mm.

V. C. M. Chandrakumar · S. R. Nagaraja (✉)

Department of Mechanical Engineering, Amrita School of Engineering, Amrita Vishwa Vidyapeetham, Bengaluru, India
e-mail: sr_nagaraja@blr.amrita.edu

The protuberance was of trapezoidal planform with 21 mm width at the front and 40 mm at back. It was observed that there exists a complicated recirculation region near the protrusion and the flow wrap around it in a horse shoe fashion, creating a hot spot due to the vortices. Kumar et al. [3] have experimentally studied flow dynamics protrusions on flat plates. The protrusion angles used are 60° , 90° and 120° . They have concluded that in the presence of protrusions the boundary layer lifts off from the surface of the plate. This separation distance is about 4–8 times the height of it. The hottest point was formed at the front of the protrusion rather than the side of it. For a low speed flow, the boundary layer thickness is more compared to the protrusion height so the effect of this is negligible. But in a high speed (hypersonic) flow, the boundary layer is very thin so even a small discontinuity can cause a severe increment in drag and heat. Nair et al. [4] have studied the flow dynamics of hypersonic flow over three dimensional forward facing steps on flat plates. They have used different deflection angles in Mach 8 flow. They have reported that for unseparated flow the protrusion height has very little effect, whereas for separated flow the surface heating was higher. Estruch et al. [5] have done an experimental study on protrusions using a hypersonic gun tunnel with free stream Mach numbers of 8.2 and 12.3, which states that the height of the protrusion is less dependent on surface heating when the boundary layer ahead of the protrusion is unseparated. But in separated cases the heat flux is more for long protrusions than for short ones. Value of heat flux is depending on freestream conditions, height of protrusion and deflection angle of protrusion. Micro Vortex Generator (MGV) is used as a sub boundary layer protrusion by Lu [6]. Complex flow field around MGV is visualized. It is reported that hairpin vortices are formed by the confluence of two primary vortices formed on either side of the MGV. Price et al. [7] have studied flow separation over fin type protrusions in turbulent flows. King et al. [8] have studied the effect of protuberance shape and orientation on space shuttle orbiters. Ramaswamy et al. [9] have studied the effect of cylindrical protuberances on surface heat transfer. They have considered both laminar and turbulent boundary layers. They have reported that, in the wake region a series of high and low heat transfer streaks. Sharief et al. [10] have studied the effect of the shape of protrusion and bluntness of the cone on the pressure and heat flux over the protrusion. They have studied triangular and hexagonal protrusions in hypersonic flow for freestream Mach numbers of 6, 8 and 10. Akshay et al. [11] have done a steady state analysis of the flow field around pin protrusions on blunt bodies in Mach 8 flow. They have compared pressure and heat flux variations with and without pin protrusions. It is reported that peak heat flux occurs on the protrusion in all cases except for the case of short protrusion for which the height of the protrusion is 0.1 times the diameter.

In this paper, the effect of protrusion height on the separation length, pressure and surface heat flux on a conical model in hypersonic flow is reported. The freestream conditions and angle of attack are constant.

2 Computational Methodology

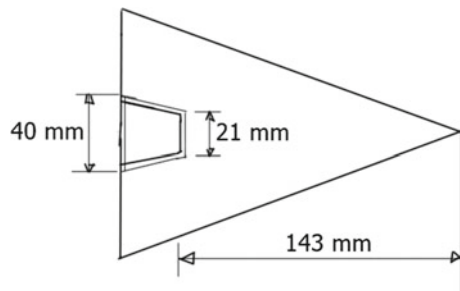
The present analysis is done using ANSYS Fluent software. The geometry of the 3 dimensional conical model is shown in Fig. 1. The cone has a base diameter of 130 mm and a height of 178.5 mm. The trapezoidal protrusion is placed at a distance of 143 mm. The enclosure used is of the same shape as that of the conical model. This reduces the number of elements required. The computational model consists of nearly 1,700,000 elements. An additional inflation was created near the body boundary for improving efficiency. There are 5 inflation layers with a growth rate of 1.2. The Y+ on the surface of the protrusion is around 2.0. Fluid used was air which was considered as an ideal gas and viscosity variation is incorporated using the Sutherlands model. Among the three faces, both inlet and outlet were made as pressure far field, and the body was named as wall-body. In the solution model, the formulation was implicit and the flux type was Roe-FDS. In spatial discretization, the gradient used was Least squares cell based and second order upwind. The Courant number used was 0.5. The calculations were done in density based model which is generally used to model compressible flows. The turbulence is modelled using two equation K- ε model. In this model, the two transport variables are used to represent turbulence. These variables are turbulent kinetic energy k and turbulent dissipation ε. Variable k represents the energy in turbulence and ε represents the scale of turbulence. The equations solved are the continuity, momentum and energy equations. They are as follows.

$$\frac{\partial p}{\partial t} + \nabla \cdot (\rho u) = 0 \tag{1}$$

$$\rho \frac{\partial u}{\partial t} + \rho(u \cdot \nabla)u = \nabla \cdot [-pI + \tau] + F \tag{2}$$

$$\rho C_p \left(\frac{\partial y}{\partial x} + (u \cdot \nabla)T \right) = -(\nabla \cdot q) + \tau : S - \frac{T}{\rho} \frac{\partial y}{\partial x} \left(\frac{\partial y}{\partial x} + (u \cdot \nabla)p \right) + \emptyset \tag{3}$$

Fig. 1 Computational model



where ρu is momentum density, p is pressure, T is temperature, C_p is specific heat, q is heat flux.

3 Results and Discussions

The simulations were done for free stream Mach number of 5.7, pressure 2051 Pa and temperature 148.1 K. The wall temperature of the body is 300 K. These conditions are similar to the experimental conditions used by Kumar et al. [3]. Three trapezoidal protrusions with 4 mm, 6 mm and 8 mm height are considered. The size of the protrusion is as shown in Fig. 1. In supersonic/hypersonic flows ahead of the protrusion the boundary layer thickness increases due to a positive pressure gradient and separates ahead of the protrusion. As there is a discontinuity in the flow two shocks are visible, lip shock and separation shock. These are as shown in Fig. 2. Due to the separation shock, the flow at the upper part of the protrusion will flow over it and the lower part will enter the recirculation zone developed immediately in front of the protrusion (Fig. 3) and a horse shoe vortex is created in front of the protrusion. This causes an increase in heat flux near the foot of the protrusion and thereby creating a hot spot. The pressure and heat flux are noted on the surface of the cone.

The flow separation length in front of the protrusion can be estimated by different methods like measuring surface pressure or heat flux in front of the protrusion or using shadowgraph or schlieren images. The surface pressure rapidly increases just ahead of the separation point. After it reaches the first peak, there is a pressure plateau where the pressure remains almost constant. There is a slight decrease of pressure before it starts rapidly increasing nearer to the protrusion. The surface pressure profile is as shown in Figs. 4 and 5 and is similar to the results reported by Earl A Prince et al. [8]. The rapid increase in pressure is more pronounced in supersonic and hypersonic

Fig. 2 The lip shock and separation shock

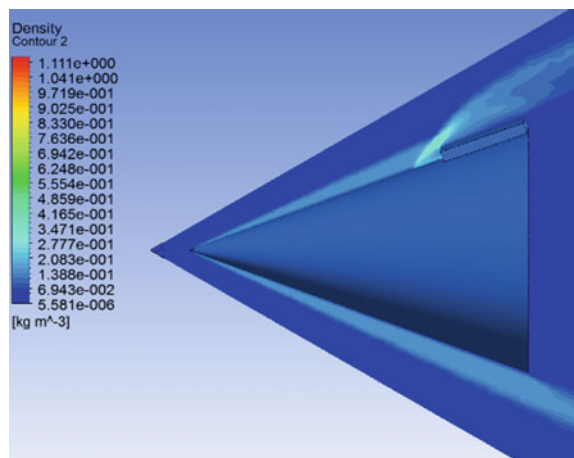


Fig. 3 Recirculation zone in front of protrusion

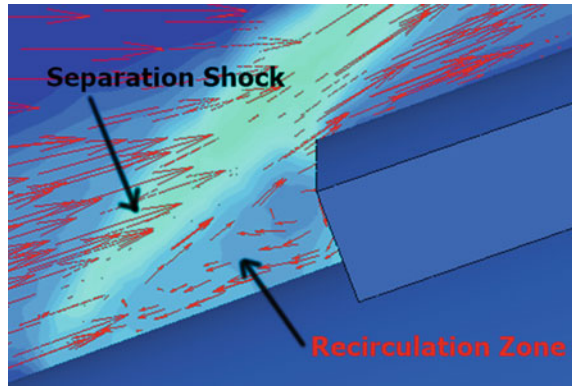
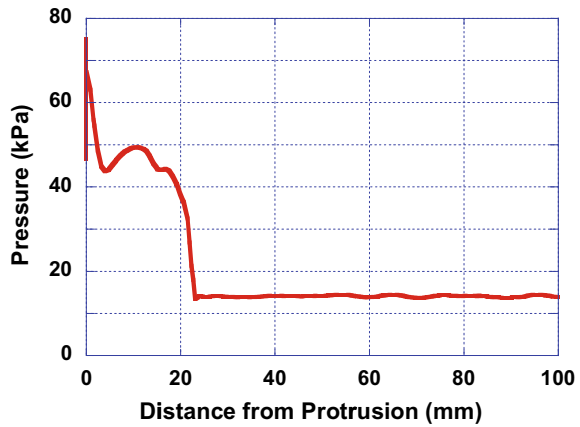


Fig. 4 Surface pressure ahead of 6 mm protrusion



flows compared to subsonic flows, where the pressure rise is slow. The separation point is the pressure inflection point as shown.

Figures 6 and 7 show the variation of the surface heat flux in front of the protrusion. The point at which the flow separates can also be determined using heat flux plots. The separation point for 8 mm protrusion is as shown in Fig. 6. The heat flux on the face of the protrusion is shown in Fig. 8. The surface of the protrusion is subjected to severe heat loads. The maximum heat flux occurs just below the top face of the protrusion. The point at which flow separates depends on the height of the protrusion. The distance of the separation point from the foot of the protrusion is 14 mm, 20.5 mm and 25.5 mm respectively for 4 mm, 6 mm and 8 mm height protrusions.

Fig. 5 Surface pressure ahead of 8 mm protrusion

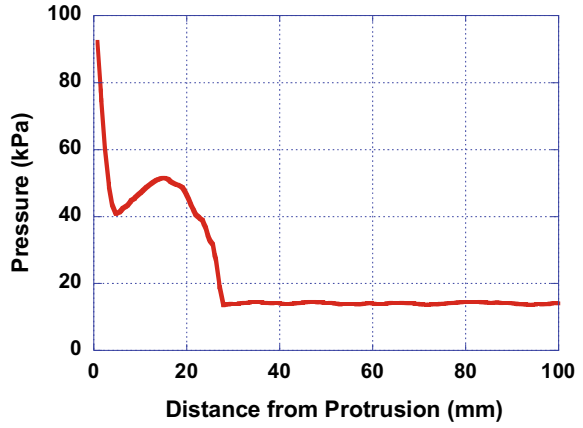


Fig. 6 Surface heat flux ahead of 8 mm protrusion

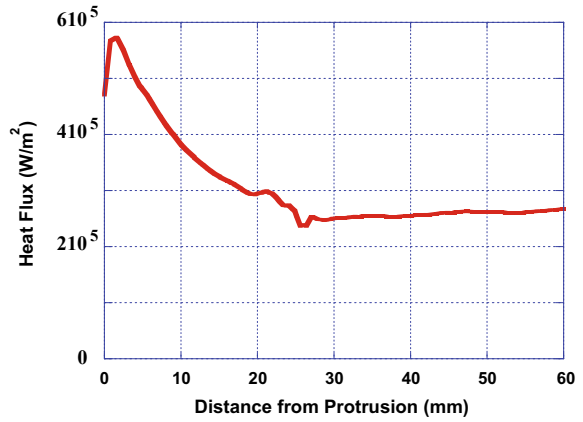


Fig. 7 Surface heat flux ahead of 6 mm protrusion

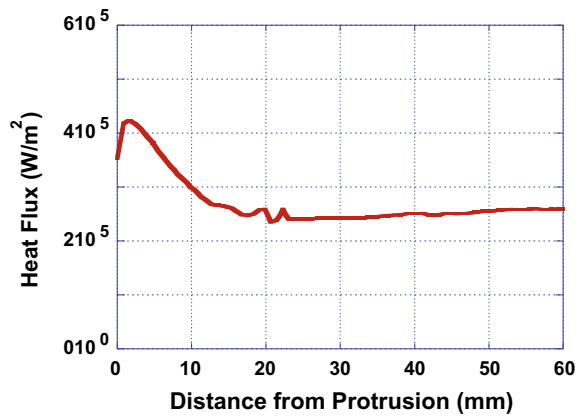
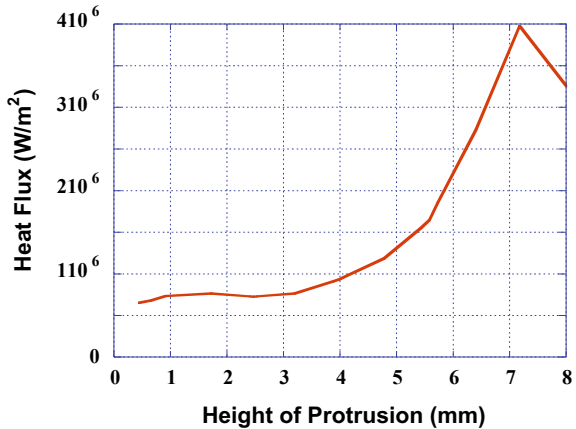


Fig. 8 Heat flux on the face of 8 mm protrusion



4 Conclusions

The height is an important parameter for protrusions in high speed flows. As the height increases the maximum heat flux in front of the protrusion also increases. If the height is increased by just 2 mm, the increment of heat flux at the foot is 35%. This rate of increase will reduce as we move away from the foot of the protrusion. For a given protrusion the maximum temperature and hence max heat flux occurs on a vertical face. The separation distance is varying between 3 and 4 times the height of the protrusion. As the hotspot is near to the base of the protrusion, the temperature near to base will be always high. Temperature will reduce when moving from the base to separation shock along the surface of the cone.

References

1. Lighthill MJ (1953) On boundary layers and upstream influence, part I: a comparison between subsonic and supersonic flows. *Proc R Soc A* 217(1130):344–357
2. Kumar CS, Singh T, Reddy KPJ (2014) Investigation of the separated region ahead of three-dimensional protuberances on plates and cones in hypersonic flows with laminar boundary layers. *Phys Fluids* 26(12):126101
3. Kumar CS, Reddy KPJ (2013) Experimental investigation of heat fluxes in the vicinity of protuberances on a flat plate at hypersonic speeds. *J Heat Transf* 135(12):121701
4. Nair MA, Nagaraja SR (2016) Simulation and analysis of protrusions on flat plate at hypersonic speeds. *Indian J Sci Technol* 9(45)
5. Estruch D, MacManus DG, Stollery JL, Lawson NJ, Garry KP (2010) Hypersonic interference heating in the vicinity of surface protuberances. *Exp Fluids* 49:683–699
6. Lu FK (2015) Visualization of supersonic flow around a sharp-edged, sub-boundary-layer protuberance. *J Visual* 18(4):619–629
7. Price EA Jr, Robert L St, Jr (1967) Investigation of turbulent separated flows in the vicinity of fin type protuberances at supersonic Mach numbers. NASA Technical note TN D-3804

8. King RA, Berry SA, Kegerise MA (2008) Effect of protuberance shape and orientation on space shuttle orbiter boundary-layer transition, NASA/TM2008215103
9. Ramaswamy DP, Schrijer FFJ, Avallone F (2018) Experimental investigation of the effect of a surface protuberance on the surface heat transfer in a high speed boundary layer. In: 5th international conference on experimental fluid mechanics ICEFM Munich, Munich, Germany
10. Sharief SN, Nagaraja SR (2019) December. Analysis on a blunt cone with protrusion in hypersonic flow. In AIP conference proceedings 2200, 020067
11. Akshay N, Nagaraja SR (2021) Analysis of hypersonic flow over pin protrusions on a blunt body. In Recent advances in sustainable technologies, pp 293–302

Design and Analysis of Multifacility Splint for Children with Congenital Clubfoot Deformities



Mahavir Kantilal Beldar, Aditya Kumar Manethia, Mallika Joka, and Ayush Murarka

Abstract Congenital Talipes Equinovarus (CTEV) or commonly known as clubfoot is a type of deformity present at birth. This deformity involves the baby's foot twisted out of shape or position. Under clubfoot, the tissues which connect the muscles to the bone (tendons) are short than usual. The deformity may be in one or both feet and is curable easily, even without surgery. Clubfoot usually makes it hard to walk normally, so doctors suggest treating it soon after birth. It can be treated by both methods surgically and non-surgically. As the surgical method is very painful, mostly non-surgical methods are used. As a baby's bones and joints are incredibly soft and flexible, non-surgical methods can be used in the first week after birth. The existing treatment options include Casting (Poinsettia method), Surgery and Splints. In this research, the focus is on analysing already existing static and dynamic splints by modelling and simulations, studying their mechanism and effect on patients and developing a splint that can be used as a static as well as a dynamic splint and reducing its cost (Mayoclinic, Clubfoot, <https://www.mayoclinic.org/diseases-conditions/clubfoot/symptoms-causes/syc-20350860>, 2019).

Keywords Clubfoot · Dynamic and static splints · CAD model · Splint analysis

1 Introduction

Clubfoot is such a deformity which is seen in children during the birth itself and it can be recognized as the foot is out of shape and twisted in an unnatural way sometimes out of position as well. This is also known as a congenital orthopaedic disorder or CTEV as shown in Fig. 1. The actual cause of this deformity may not be known exactly but there were many theories that have been looked upon like genetic

M. K. Beldar (✉)

Research Scholar, Department of Mechanical Engineering, College of Engineering, Pune 411005, India

e-mail: mkb18.mech@coep.ac.in

A. K. Manethia · M. Joka · A. Murarka

Department of Mechanical Engineering, Bharati Vidyapeeth (Deemed to Be University), College of Engineering, Pune 411043, India

Fig. 1 CTEV (congenital talipes equinovarus) [2]



disorders or mutations in the genes, etc. Its shape may be deformed for all the angles and shape may look opposite to a regular foot of a human baby.

This deformity is treated by surgical and non-surgical methods. Non-surgical methods are applied in two phases:

1. **Corrective phase**—In this method, using the Ponseti method the physical look of the foot is corrected.
2. **Maintenance phase**—In this phase, a foot abduction brace also called FAB is used to keep from relapse [1].

This deformity affects the main bone structure of the foot of the baby. There are many terms like cavus which is the deformity in which the foot turns to the inside of the original position similarly to varus in which the hindfoot is affected and turns in unnatural direction. At the position of the subtalar joint, the foot is fixed like a horse or an equine.

Usually in this deformity, the foot is affected in only one foot instead of two and can be easily brought back to its first shape by methods like Ponseti technique, etc. [1]. As per the survey conducted, parents also prefer the physiotherapy or massage time to time to get the foot back to its original shape or position. The deformity is classified into two types namely, structural and postural.

In the structural deformity, the foot of the baby and the joint or hinge are affected and motions of the same are not comfortable.

In the postural deformity, the muscles that are present in the foot of the child are affected and they may not cause proper functioning of the foot. The bone in this case affected is negligible [1].

1.1 Treatments for CTEV Deformation

The major problem with clubfoot is that tendons (bone) are shortened on the inside of the leg and have an unusual shape. Also, the Achilles tendon is tightened which causes difficulties in foot movements. If this deformity is left untreated, then the affected person may never walk properly on their ankles and on the sides of their feet.

In Infant, clubfoot may appear as follows:

1. Upper part of the foot may be twisted inward and downward.
2. The calf muscles are underdeveloped.
3. If one foot is affected, then it is usually shorter than the other foot at the heel.
4. In the worst case, the foot may be upside down.

Following are the few treatments used for CTEV:

1. **Postural:** It is self-resolving or self-healing, and in some cases, physiotherapy intervention for stretching and stimulation to the feet is also helpful and gives particularly satisfactory results also, e.g., The Ponseti Clubfoot Treatment (Casting) [3].

There are two types of the Ponseti method namely Pre-Ponseti and Post-Ponseti methods which have been in practice.

- (a) In the first phase, there is the casting of the foot in its proper shape so that the shape that is desired may be regained (like a fracture of the bone); this cast helps in the manipulation of the foot's angle and the shaping of the same. There is a procedure called as tenotomy in which there is mild surgery involved to correct the angle of the foot of the child.
 - (b) In the second phase, our splint comes into action as it helps in avoiding the relapse of the foot to its deformed shape. It helps in avoiding the recurrence of the foot and wastage of treatment.
2. **Structural:** On requirement with the help of minimal surgery and casting, manipulation in the foot is done. In most serious cases, surgery may be preferred. This surgery is then followed by maintenance with special boots and bar/splint till 3–4 years of age, e.g., clubfoot surgery [4].

Static Orthoses: As the static name implies, these splints do not allow any active motion. It provides rigid support in stable fractures and inflammatory conditions of tendons and soft tissue.

Dynamic Orthoses: These splints do allow the motion. These types of orthoses are used primarily to help the movement of weak muscles and to augment the motion of joints.

1.2 Problems with Existing Clubfoot Splints

There are different types of splints and abduction braces available in the market but most of them are very heavy and costly. The other thing is that the brace length and abduction angle are also not adjustable. After the literature review, the following things are found as shown in Fig. 2:

1. Most of the research that has been done till now is mostly related to the static splints and has limited knowledge about them.
2. The materials that are used in these splints are limited and the manufacturing procedures are also costly.
3. The current dynamic splint studies are concentrated on shoe design and not on the brace design. Also, dorsiflexion and plantar flexion parameters are not considered while designing the braces.
4. As the shoe material and padding are discussed only a few times, there is a possibility of discomfort.
5. As seen below in Fig. 2, as the shoe is not comfortable and there is no motion of the feet in the static splint, there is bruising and skin rupturing [2].

The dynamic splints that are now present in the market have more emphasis on the shoe rather than on the brace of the splint. In the existing splints, only abduction angle is usually considered for the splint design. Whereas the dorsiflexion and plantar flexion angles are not inculcated in the same. If dorsiflexion and plantar flexion angles are not considered in a splint, then the comfort of the foot for the child is compromised and the child may face severe bruising and skin ruptures.



Fig. 2 Existing braces in market [3]

Also, without the proper design, there may be relapses of the deformity and may hurt the baby as it grows up. This can be avoided with the help of a proper design and justification of the design with optimization.

As there are no such splints in the market that have both facility of static and dynamic splints in it, our objective is to design such a splint that has both features so that the parents do not have to buy or utilize different splints according to the need. In this splint, it is planned to integrate both. This splint will also be an effort to reduce the cost by more than half.

2 Methodology and Techniques

To make a dynamic brace for unilateral and bilateral clubfoot deformities, the following objectives are considered as shown in Fig. 3:

1. To study the present splints, present in the market, and find the drawbacks of the same to optimize it.
2. To prepare the new and optimized design of the splint (CAD model) with integrated dorsiflexion (10°), plantar flexion and degree of abduction.
3. Conducting the analysis of the splint by keeping in mind all necessary factors and conducting force analysis of the dynamic splint using Ansys which includes Stress, Strain and Displacement Analysis and Factor of Safety Simulation.
4. Optimization of weight and cost and improve sturdiness and effectiveness of dynamic splint by changing the material and development using design for additive manufacturing approach.

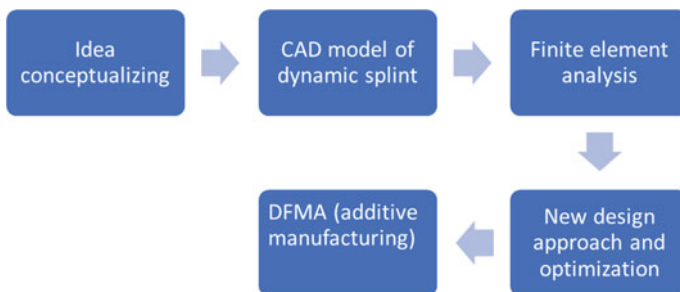


Fig. 3 Flowchart of the splint design procedure

2.1 Design of Dynamic Splint Components and Specifications

1. **CAD Modelling of new dynamic splint**—CAD Model Design of new dynamic splint is done using solid works software, and FEA analysis/orthotic analysis is done by Ansys by keeping in mind rotational deformities like dorsiflexion, plantar flexion, Degrees of Abduction and Force Analysis.
2. **The New Design Method**—The design of the splint is done using the solid works software and optimizing it for max output.
3. **Finite Element Analysis**—For this study, ANSYS software is used. With the help of solid elements topology, the geometry is meshed. The brace is checked for mesh independency by performing a mesh convergence analysis. The weight of the child and age group as shown in Table 1 are considered for analysis.
4. **Dynamic Plantar Pressure Distribution**—All the splints that are developed are static and hence all the angles must be included, and pressure distribution must be made so that the bearer is comfortable and not irritating to the child.
5. **Optimization of Splint**—Optimization of splint consists of optimizing weight and cost and improving the effectiveness of dynamic splint by changing the material to polycarbonate and development using design for 3d printing for the manufacturing process [3].
6. **Dynamic Splint Construction**—The dynamic splint is manufactured using two processes casting for the aluminium rod and the 3d printing technique for the polycarbonate shoe mounting and the plates so that it is cost-efficient and easy.

Above is the weight chart of the child which is used for force analysis for the splints under different conditions.

Table 1 Weight chart of the child with age up to 12 months [5]

Age in months	Boy (kg)	Girl (kg)
0	2.5–4.3	2.4–4.2
1	3.4–5.7	3.2–5.4
2	4.4–7.0	4.0–6.5
3	5.1–7.9	4.6–7.4
4	5.6–8.6	5.1–8.1
5	6.1–9.2	5.5–8.7
6	6.4–9.7	5.8–9.2
7	6.7–10.2	6.1–9.6
8	7.0–10.5	6.3–10
9	7.2–10.9	6.6–10.4
10	7.5–11.2	6.8–10.7
11	7.4–11.5	7.0–11.0
12	7.8–11.8	7.1–11.3

2.2 Conceptual CAD Model Design of Dynamic Splint

For manufacturing a splint for a child, two sets of measurements are considered which are as follows:

1. **Foot size of Child's feet**—On a white paper sheet, outline of the child's foot is marked and it is measured in centimetres. Distance between longest toe to heel is considered as foot size as shown in Table 2.
2. **Shoulder width of Child**—It is measured with the help of measuring tape by holding it between the tip of two acromia on either side. It is also recorded in centimetres [4].

In this study for calculation, we assumed a 70° angle between the metal bar and shoe part, and with the help of Table 2, we took the prescribed length of the bar as 250 mm and that too for 80 to 140 mm foot sizes.

3 CAD Model of Dynamic Splint

As per the market requirements and needs, the following dynamic splint is designed. In the Fig. 4, exploded view of the new splint CAD model is shown.

To design the 3D components and assembly, solid works software is used. There are four components mainly two rods, shoe plates and shoe mountings as shown in Figs. 4, 5, and 6.

The length of the rod is variable between 230 and 350 mm according to the size of the feet (100–140 mm). The sides of the bar are to be connected with the dynamic links holding the shoe braces at 70° for the affected leg and 30° for the unaffected leg. Shoe plates are connected with dynamic links adjusting plantarflexion angle from $1-10^\circ$ [6].

Table 2 Prescribed bar length for clubfoot [5]

Foot size (mm)	Prescribed bar length (mm)
60	237.5
70	250
80	262.5
90	275
100	287.5
110	300
120	312.5
130	325
140	350

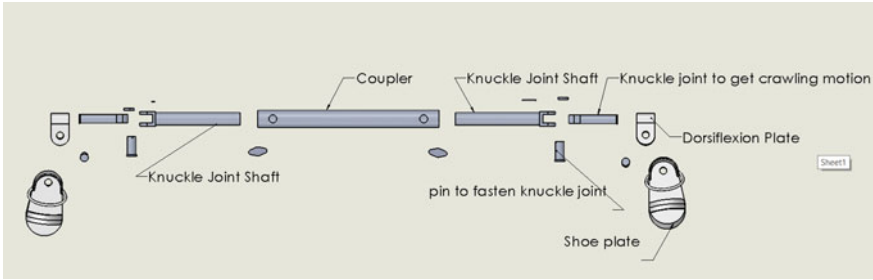


Fig. 4 Components of the splint

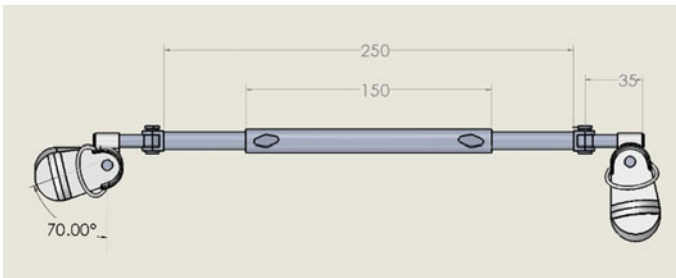
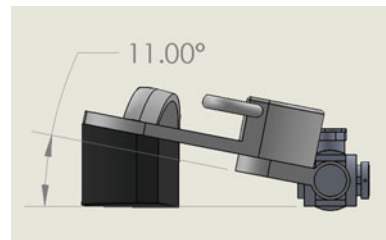


Fig. 5 Length adjustment and abduction angles

Fig. 6 Dorsiflexion angle



4 Materials Selected for Splint Components

- The material used for Rod extension and mounting is aluminium alloy 5052 H 32 as it is easily available, lightweight, cheap and easy to machine [5].
- The material used for Shoe plate and mounting is polycarbonate as it is very lightweight and cheap. And it is more adjustable and can bear a load of up to 10–12 kg.
- The material used for shoe cushion is silicon padding as it is extremely comfortable and does not irritate the skin of feet [7].
- The material used for the heel is silicon rubber so that while standing also there is no hindrance and easy motion is possible [8].

5 Experimentation Procedure-Observations and FEA Analysis of the Splint

5.1 Results of Foot Plate Deformation

For calculation of shaft diameter, maximum shear stress theory was selected and used the data from Tables 3 and 4. The maximum and minimum weight of the baby are considered and calculated the outer and inner diameter in both cases.

Table 3 Results of deformation in the splint at various loads and brace lengths

Sr. No	Parameters		Output	Conditions
	Load applied (weight of the child kg)	Length of the splint (mm)	Deformation (mm)	Direction of applied force
1	2.5	230	0.556	Upwards (during crawling motion)
	2.5	230	0.635	Downwards (weight)
2	2.5	328	0.650	Upwards (during crawling motion)
	2.5	328	0.648	Downwards (weight)
3	12	328	0.5448	Upwards (during crawling motion)
	12	328	0.5412	Downwards (weight)
4	12	230	0.2207	Upwards (during crawling motion)
	12	230	0.221	Downwards (weight)

Table 4 Aluminium alloy 5052 H 32 for the rod [6]

Property	Value	Units
Elastic modulus	70,000	N/mm ²
Poisson’s ratio	0.33	N/A
Shear modulus	25,900	N/mm ²
Mass density	2680	kg/m ³
Tensile strength	230	N/mm ²
Yield strength	195	N/mm ²
Thermal expansion coefficient	2.38e–005	/K

- For maximum Weight (12 kg), $D_o = 13.35 \text{ mm} \approx 14 \text{ mm}$, $D_i = 8.68 \text{ mm} \approx 10 \text{ mm}$. $t = 2 \text{ mm}$.
- Likewise, for minimum weight (2.5 kg), $D_o = 6.67 \text{ mm} \approx 7 \text{ mm}$, $D_i = 4.55 \text{ mm} \approx 5 \text{ mm}$.

5.2 Static Structural Analysis of Splint

To perform deformation analysis, Ansys software is used, and different loads were considered to test the bearing capacity of the splint. As per the analysis data provided in Table 3 which contains different loads and factors which are considered while performing the analysis.

At every load which is considered almost the same deformation can be seen after analysis which is shown in Figs. 7 and 8. On an average deformation in the splint is 0.0002209 m (minimum) and 0.00054124 m (maximum). The Ansys simulation results are shown in Figs. 9 and 10.

From the above calculation and analysis, it is concluded that the material selected and the mechanism designed work perfectly.

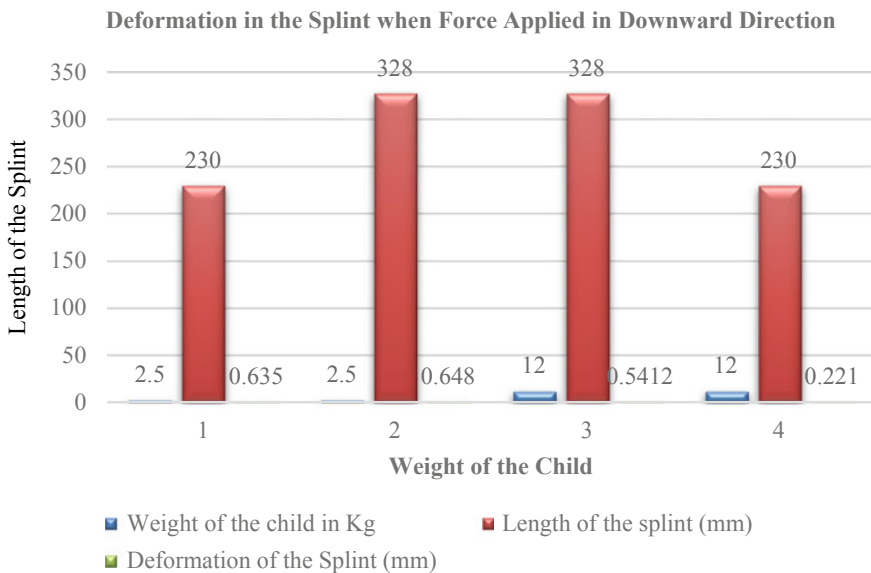


Fig. 7 Deformation in the splint when force applied in downward direction

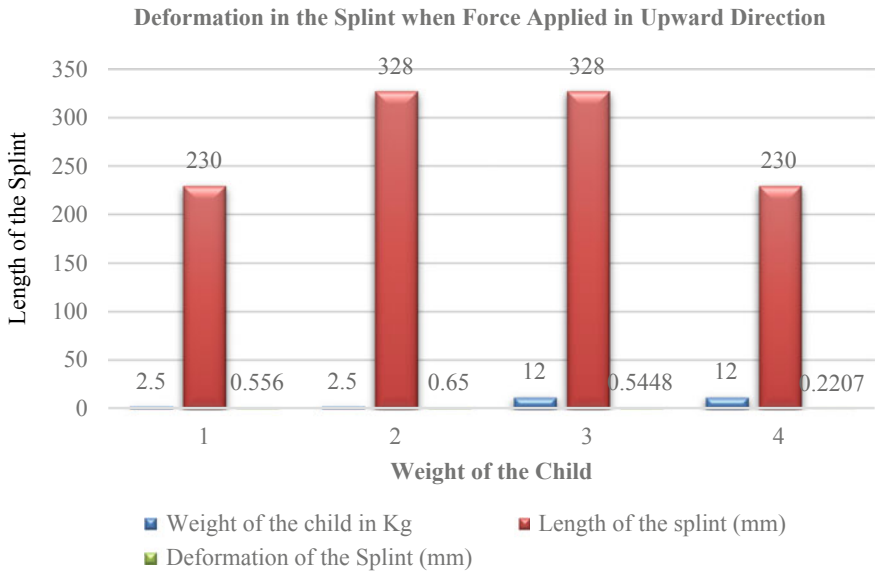


Fig. 8 Deformation in the splint when force applied in upward direction

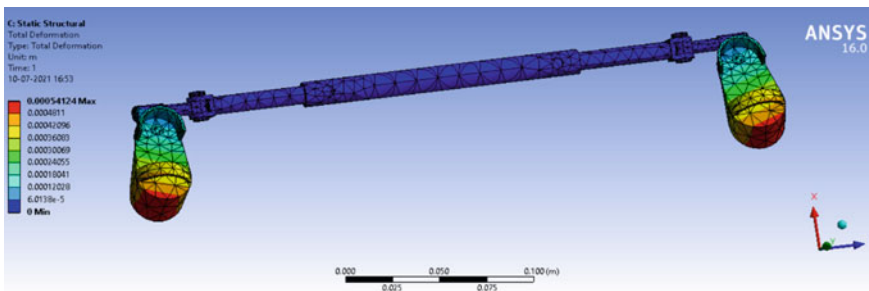


Fig. 9 FEA Analysis of the splint with maximum force and maximum brace length

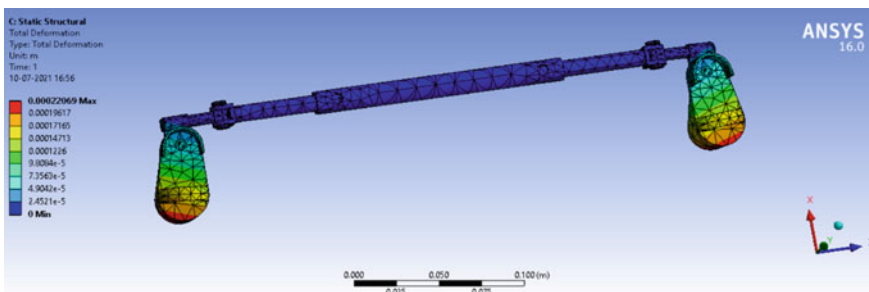


Fig. 10 FEA Analysis of the splint with minimum force and minimum brace length



Fig. 11 Fabricated dynamic splint sample

5.3 Manufacturing of Splint

The dynamic splint is fabricated as a sample splint on basis of the CAD model and its results from the calculation as shown in Fig. 11. The proposed design is found to be accurate and can be produced with the actual materials and exact dimensions.

6 Conclusion and Future Scope

In this project, maximum input was given for designing the new dynamic splint. Many elements like crawling motion with the split for children are provided with the knuckle joint. Similarly, the inclusion of dorsiflexion and plantar flexion angles are provided with the plate. With their added provisions, there will be most comfort to the child's feet and it will surely help to cure this disease without further complications.

The material used in this splint is Al alloy which has aircraft range industrial usage and has corrosion resistance which helps even if the child wears it frequently, the splint will not be damaged. The overall weight of the splint is also drastically reduced and is much more comfortable for the child. Considering all these factors, it is concluded that the dynamic splint is a useful medical equipment for children born with clubfoot deformity and curing becomes easier too without any repercussions.

References

1. Felman A (2018) Everything you need to know about clubfoot. <https://www.medicalnewstoday.com/articles/183991>
2. Alves C (2019) Bracing in clubfoot: do we know enough?. <https://www.ncbi.nlm.nih.gov/pmc/articles/PMC6598043/>

3. Savonen B (2019) https://hal.archives-ouvertes.fr/hal-02111344/file/Open-Source_Three-Dimensional_Printable.pdf
4. Agarwal A (2017) Is the same brace fit for all? The length of abduction bar in Steenbeek foot abduction brace for Indian children—a pilot study. <https://www.ncbi.nlm.nih.gov/pmc/articles/PMC6349614/>
5. Kammardi PK (2014) Compliance monitored clubfoot brace “PADMAPADA”©. https://link.springer.com/chapter/10.1007/978-81-322-2229-3_47
6. Agarwal A, Kumar A, Sharyar A, Mishra M (2016) The dynamicity of Steenbeek foot abduction brace for clubfoot in dorsiflexion and pronation: a pilot study. <https://journals.sagepub.com/doi/abs/10.1177/1938640016640894>
7. PhysioSunit How to use silicone heel cup for pain-free heel. <https://physiosunit.com/heel-pain-use-silicon-heel-pads-for-pain-free-walking/>
8. MayoClinic (2019) Clubfoot. <https://www.mayoclinic.org/diseases-conditions/clubfoot/symptoms-causes/syc-20350860>

Experimental Validation of End Effector Position and Orientation for a 5 DoF Robotic Manipulator



Uday R. Walke, Raunak V. Wasnik, Rohit M. Pal, Ashutosh S. Borkar, Parag M. Kowe, Aniket R. Buchunde, Palak N. Ukey, and Vinit Gupta

Abstract In this work, experimental validation of position and orientation equations is carried out on a prototype of five degree of freedom robotic manipulator. The experimental setup is fabricated in-house to study the spatial properties of a manipulator and validate the equations obtained from the Denavit–Hartenberg parameters. The results obtained show that for a specific set of theta values, the end effector position and orientation represented by the Cartesian co-ordinate system matches closely both for the mathematical model as well as experimental data. The slight deviation observed may be attributed to fabrication and experimental error.

Keywords Degree of freedom · Robotic manipulator · Position · Orientation · Denavit–Hartenberg notation

1 Introduction

Robots are widely used nowadays for automation of industrial operations as well as for difficult working conditions such as underground mining, sea bed mining and space exploration [1, 2]. The mechanical design of a robotic manipulator is dominated by kinematic and dynamic analysis [3–5]. The kinematic analysis mainly focuses on the determination of position and orientation at different joints and end effector depending on individual joint and link parameters [6–8]. In the past few decades, researchers have carried out extensive studies on the representation of position and

U. R. Walke · R. V. Wasnik · R. M. Pal · A. S. Borkar · P. M. Kowe · A. R. Buchunde · P. N. Ukey · V. Gupta (✉)
S.B. Jain Institute of Technology, Management and Research, Nagpur, India
e-mail: guptavinit1988@gmail.com

U. R. Walke
e-mail: udaywalke.me@sbjit.edu.in

R. V. Wasnik
e-mail: raunakwasnik.me@sbjit.edu.in

A. S. Borkar
e-mail: ashutoshborkar.me@sbjit.edu.in

orientation. The Denavit–Hartenberg (DH) notations are widely used for specifying link and joint parameters for a serial manipulator [1–3].

Forward kinematic analysis is carried out to work out the position and orientation of the end effector based on link lengths and joint angles [1, 2]. The resulting transformation matrix consists of a position vector and parameters corresponding to normal, sliding and approach vectors for the representation of orientation [1, 2]. At the same time, if the final position of the wrist or end effector is known along with link lengths, the inverse kinematic approach is utilized to analyze the joint angles [1, 6–8].

This work focuses on experimental validation of position and orientation matrix obtained by DH notations using a prototype of five degree of freedom robotic manipulator. Such experimental validation is rarely available in the literature and helps toward a better understanding of kinematic equations for a serial manipulator derived via the Denavit–Hartenberg approach. Section 2 gives the details of the fabricated setup and methodology, Sect. 3 highlights the results and discussion and Sect. 4 presents important conclusions.

2 Fabrication and Methodology

2.1 Fabrication

The serial manipulator shown in Fig. 1 is a representation of five degree of freedom robotic manipulator. It is fabricated using wooden material and the main purpose of this fabrication is to experimentally validate the analytical values for kinematic analysis. Two of the joints are twisting joints, one at the waist and the other at the wrist. The remaining three joints are revolute, i.e. one each at the shoulder, elbow and wrist. Angular scales are mounted on each joint to provide joint angles. The waist joint can provide an angular movement of 180° whereas all revolute joints are capable to rotate to 90° . The twisting joint at the wrist provides an angular movement of 360° .

Link d_1 , between waist and shoulder joint, is 431 mm, link $a_2 = 285$ mm (between shoulder and elbow joint), link a_3 (between elbow and wrist joint) is 297 mm and link d_5 , i.e. from the wrist joint to end effector length is 292 mm. Home position is defined as a position in which links a_2 and a_3 are collinear and perpendicular to links d_1 and d_5 , with the end effector facing in the downward direction.

2.2 Methodology

The angles are set to a particular value at each of the joints and the position of the center point of the end effector (representational) is measured. Graph paper is placed

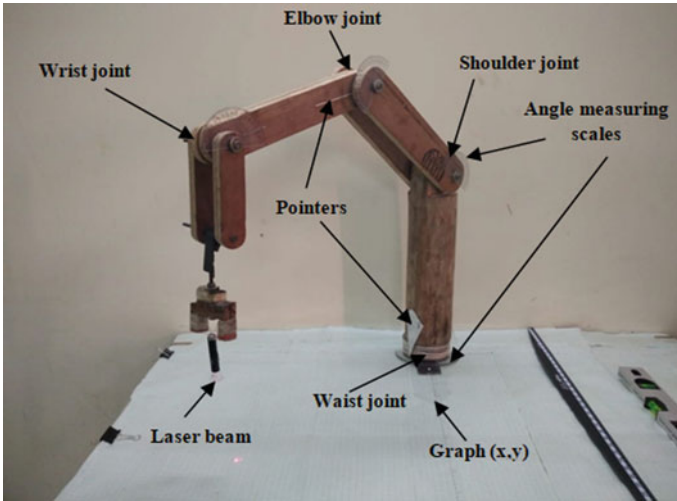


Fig. 1 Prototype of 5 DoF robotic manipulator

on the top of the table on which the manipulator is mounted for recording x and y co-ordinate whereas z co-ordinate is measured using a meter rule. Orientation of the end effector is measured by measuring the angle of approach, sliding and normal direction with positive x-, y- and z-axes. A bubble leveler is used to ensure proper level at each of the final theta configurations.

Mathematically, the transformation matrix (position and orientation) is represented by

$$\begin{bmatrix} n_x & s_x & a_x & q_x \\ n_y & s_y & a_y & q_y \\ n_z & s_z & a_z & q_z \\ 0 & 0 & 0 & 1 \end{bmatrix} \tag{1}$$

Here, *n*, *s* and *a* represent components of normal, sliding and approach vectors along x, y and z directions. The components of position vectors along three Cartesian directions are represented by *q_x*, *q_y* and *q_z*. Analytically, the transformation matrix is obtained for serial manipulators by the Denavit–Hartenberg approach. This transformation matrix relates joints with each other and to the base as well as the end effector of the robot kinematically. It is through this transformation matrix that the final position and orientation of the end effector can be analyzed once the link lengths and joint angles are known and vice-versa.

So, for a five degree of freedom serial manipulator, the final transformation matrix is given as [1, 2] follows:

$$T_{base}^{end\ effector} = \begin{bmatrix} c_1c_{234}c_5 + s_1s_5 - c_1c_{234}s_5 + s_1c_5 - c_1s_{234} & c_1(a_2c_2 + a_3c_{23} - d_5s_{234}) \\ s_1c_{234}c_5 - c_1s_5 - s_1c_{234}s_5 - c_1c_5 - s_1s_{234} & s_1(a_2c_2 + a_3c_{23} - d_5s_{234}) \\ -s_{234}c_5 & s_{234}s_5 & -c_{234} & d_1 - a_2s_2 - a_3s_{23} - d_5c_{234} \\ 0 & 0 & 0 & 1 \end{bmatrix} \quad (2)$$

In Eq. (2), c_1 signifies $\cos(\theta_1)$ and likewise. Similarly, s_{234} stands for $\sin(\theta_2 + \theta_3 + \theta_4)$. d_1, a_2, a_3 and d_5 signify link length corresponding to waist, shoulder, elbow and wrist. Equation 2 is solved in MATLAB® and the result is validated against experimental data.

3 Results and Discussion

3.1 Variation in Position

Experimental data is measured at five points for variation in each joint angle and the corresponding variation in the position co-ordinate of the end effector (considered at its center). This is then validated with the values obtained from the mathematical model and corresponding equations after being solved in MATLAB®. Figure 2a, b represents the variation in the x and y component of the position vector (center of the end effector to the origin of base), i.e. q_x and q_y with varying θ_1 (twisting angle at waist joint). Here, θ_1 is varied between 0 and 180° keeping all other joint angles set to zero degree.

It is observed that the analytical results map closely with experimental results. q_x varies gradually from 582 mm, i.e. $a_2 + a_3$ to the same magnitude on the negative x-axis with θ_1 varying between 0 and 180°. Likewise, q_y starts varying from zero

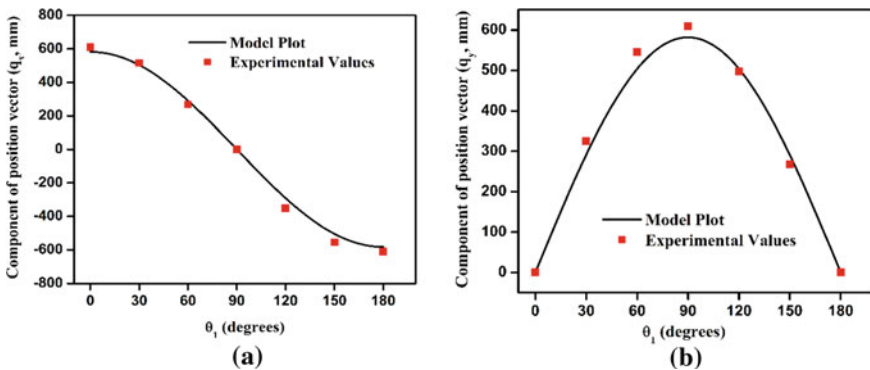


Fig. 2 a and b Variation of q_x and q_y with θ_1 (model vs experimental results)

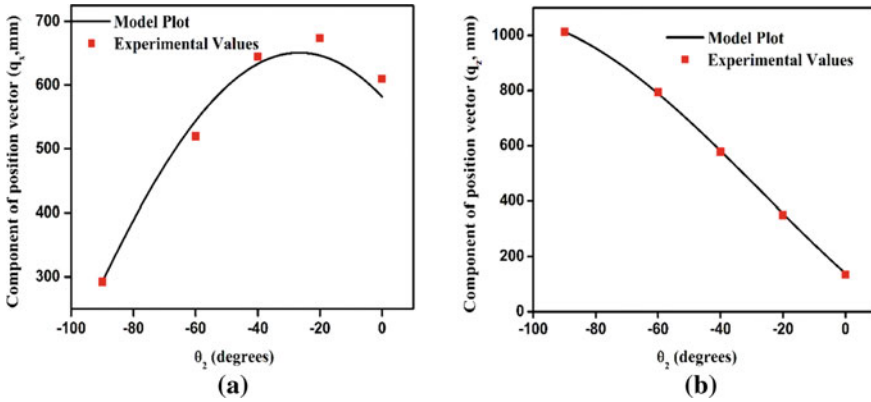


Fig. 3 a and b Variation of q_x and q_z with θ_2 (model vs experimental results)

to reach 582 mm ($a_2 + a_3$ length) at maximum corresponding to 90° twisting at the waist joint. The calculated values from the prototype are in line with the model values for the same shoulder angles.

Figure 3a, b shows the variation of q_x and q_z (position co-ordinates) with θ_2 . All other joint angles are kept constant at zero degrees. The results in experimental observations are consistent with that obtained by the mathematical model. When θ_2 varies from 0 to 90° (directed upwards), z co-ordinate changes from $d_1 - d_5$ to $d_1 + a_2 + a_3$. Similarly, x co-ordinate changes from $a_2 + a_3$ to d_5 .

Figure 4a, b gives the corresponding variation with θ_3 . It is seen that with change in θ_3 from 0 to 90° , q_x changes from $a_2 + a_3$ to $a_2 + d_5$. Likewise, q_z changes from $d_1 - d_5$ to $d_1 + a_3$. The findings from the model and experimental analysis are consistent. Some errors in the data may be attributed to fabrication and experimental errors. Similarly, Fig. 5a, b gives the trend with variation in θ_4 . In this, x co-ordinate varies from $a_2 + a_3$ to $a_2 + a_3 + d_5$ and y co-ordinate changes from $d_1 - d_5$ to d_1 . Therefore, the model obtained by the DH approach maps well the actual values for position changes with respect to variation in joint angles.

3.2 Variation in Orientation

Orientation is mainly dominated by the wrist angles of a serial manipulator. Correct position and orientation both are crucial to the optimum performance of any robotic manipulator. Table 1 presents the angle corresponding to the normal vector (n_x, n_y, n_z), sliding vector (s_x, s_y, s_z) and approach vector (a_x, a_y, a_z) from the mathematical model and experimental data for three sets of readings corresponding to different orientations of the end effector.

It is observed that the values obtained by mathematical models and experiments map closely to each other. However, a slight deviation in readings may be attributed

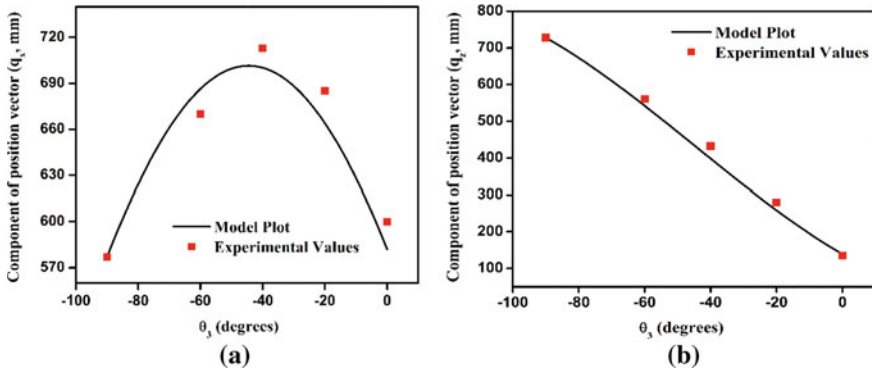


Fig. 4 a and b Variation of q_x and q_z with θ_3 (model vs experimental results)

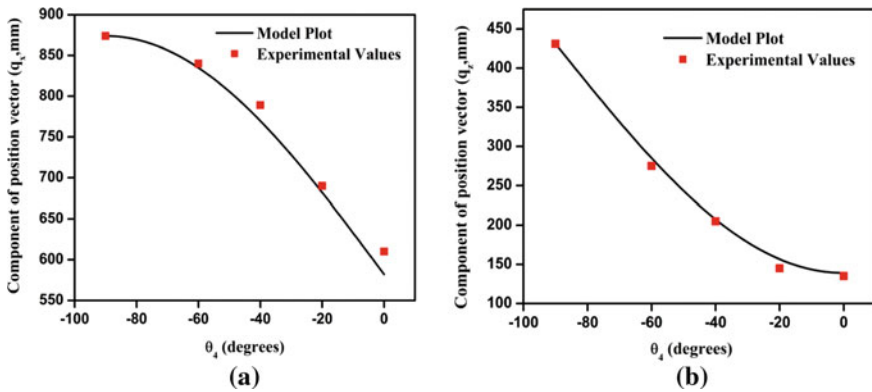


Fig. 5 a and b Variation of q_x and q_z with θ_4 (model vs experimental results)

to errors mainly contributed by laboratory-made mechanical linkages. It is thereby established that the mathematical model for kinematic analysis of a serial manipulator via DH approach can be used to study a wide range of problems involving changes in position and orientation.

4 Conclusions

The above-reported work focuses on experimental validation of the mathematical model for kinematic analysis of a five degree of freedom robot. The mathematical model is based on the Denavit–Hartenberg algorithm for kinematic analysis of serial manipulators. A wooden prototype is fabricated for experimentation and experimental results for both position and orientation show close mapping with the results

Table 1 Readings corresponding to normal, sliding and approach vector for mathematical model and experimental data

Orientation study	Home position (all theta values are set to zero)				$\theta_1 = 50, \theta_2 = -40, \theta_3 = 50, \theta_4 = -40, \theta_5 = 120$				$\theta_1 = 45, \theta_2 = -40, \theta_3 = -40, \theta_4 = 22, \theta_5 = -9, \theta_6 = 120$			
	Model (angle)	Experimental (angle)	Error (%)	Model (angle)	Experimental (angle)	Error (%)	Model (angle)	Experimental (angle)	Error (%)	Model (angle)	Experimental (angle)	Error (%)
Alpha nx	0	0	0	56.17	55	2.08	72.7	70	3.71			
Alpha ny	90	90	0	48.44	47	2.97	158.03	155	1.92			
Alpha nz	90	90	0	60	58	3.33	103.12	100	3.03			
Alpha sx	90	90	0	40	40	0	154.05	154	0.03			
Alpha sy	180	180	0	50	50	0	101.07	100	1.06			
Alpha sz	90	90	0	90	90	0	113.08	110	2.72			
Alpha ax	90	90	0	71.25	70	1.75	71.27	70	1.78			
Alpha ay	90	90	0	67.48	65	3.67	71.27	70	1.78			
Alpha az	180	180	0	150	150	0	153	150	1.96			

obtained from the mathematical model. This work paves the way to a better understanding of kinematic equations for robotic manipulators. The work can be further extended to the kinematic analysis of different similar mechanisms.

References

1. Pratihari DK (2017) Fundamentals of robotics. Narosa Publications
2. Ashokan T NPTEL video lectures on introduction to robotics. IIT Madras
3. Shah J, Rattan SS, Nakra BC (2013) End-effector position analysis using forward kinematics for 5 DOF PravaK robot arm. *Int J Robot Autom* 2:112–116
4. Upadhyay M, Gadhavi B, Chauhan M (2013) Forward kinematic analysis of an eight D.O.F. serial robotic manipulator. In: International conference on innovations in automation and mechatronics engineering, pp 124–129
5. Bingul Z, Ertunc HM, Oysu C (2005) Comparison of inverse kinematics solutions using neural network for 6R robot manipulator with offset. In: ICSC congress on computational intelligence methods and applications. IEEE Explore
6. Manjaree S, Nakra BC, Agrawal V (2015) Comparative analysis of kinematics of 5-DOF industrial robotic manipulator. *Acta Mech* 9:229–240
7. Shabeeb AH, Mohammed LA (2014) Forward analysis of 5 DOF robot manipulator and position placement problem for industrial applications. *Eng Technol J* 32:617–628
8. Hussein MT, Gafer AS, Fadhel EZ (2020) Robot manipulator inverse kinematics using adaptive neuro-fuzzy inference system. *J Eng Sci Technol* 15:1984–1998

Effect of Printing Parameters on Tensile Strength of 3D Printed PLA + Carbon Fiber Samples—A Taguchi Approach



T. S. Sachit, Mukul Ramnirajan Saini, and D. Vinaykumar

Abstract The influencing parameters like infill density, infill pattern, nozzle temperature and layer height on tensile strength of carbon fiber-reinforced Poly(lactic acid) (PLA) samples were investigated. PLA along with carbon fiber composite filament is used as a printing material owing to its excellent structural properties. Fused Deposition Modeling (FDM) technique is employed in the present investigation due to its simplicity. Fused Filament Fabrication (FFF) is one of the simplest and most cost-effective printing techniques in the Additive manufacturing process. The different printing parameters are used to develop the tensile samples as per Taguchi's design of experiments. A L16 orthogonal array was selected from the set of levels and factors in the present investigation. The tensile specimens were printed as per the ASTM D638 testing standard. It has been observed from the results that the most influencing parameter on tensile strength is infill density, and infill pattern layer thickness is having very less influence on tensile strength followed by nozzle temperature. The maximum tensile strength of 61.83 MPa is obtained at a line pattern with 90% of infill density with a layer thickness of 0.05 mm printed with a nozzle temperature of 210 °C.

Keywords Additive manufacturing · FDM · PLA · Tensile strength · Taguchi method · ANOVA

T. S. Sachit (✉) · M. R. Saini · D. Vinaykumar
Department of Mechanical Engineering, Symbiosis Institute of Technology (SIT), Symbiosis International (Deemed) University (SIU), Lavale, Pune, Maharashtra 412115, India
e-mail: sachi017@gmail.com

M. R. Saini
e-mail: saini.ramnirajan.mtech2019@sitpune.edu.in

D. Vinaykumar
e-mail: vinynie@gmail.com

1 Introduction

In recent years, AM (Additive Manufacturing) technology has been used in many industries especially in the field of medical sector [1]. FDM is considered to be one of the easily accessible and cost-effective methods of 3D printing as compared to stereolithography (SLA) and selective laser sintering (SLS) methods [2]. In the past few years, there is a rapid growth in the 3D printer market due to increased demand for the desktop customized machines [3]. Likewise, the demand for the polymers for printing in the form of filaments is also increased. Different Filament materials like polylactic acid (PLA), polyacrylonitrile butadiene styrene (ABS), Polycarbonate (PC) and Polyetheretherketone (PEEK) are the mainly used filament materials in FDM. Despite this variety, the majority of the applications use PLA material because of its environmental compatibility and biodegradability and also it emits less dangerous ultra-fine particles than ABS [4]. Many research articles report that the parts made by ABS start delaminating during printing. Thus, the parts made by PLA show less shrinkage and no local stresses developed and thereby show good mechanical properties. Tymrak et al. [3] reported that the mean tensile strength of the samples was 28.5 MPa and 56.6 MPa for ABS and PLA, respectively. Normally all desktop-level FDM 3D printers use the filament diameters of 1.75 and 2.85 mm. The printing parameters decide the quality of the product in the FDM method. It is very important to define certain printing parameters to obtain the effective product during the FDM method [5]. The process characteristics decide the mechanical properties of the parts by showing explicit anisotropy due to layer deposition of the fine threads of molten polymer material. In most of the studies, the print orientation and layer thickness were selected as the most influencing parameters.

The development in the additive manufacturing technology is accompanied by filler materials in the thermoplastic filaments. The various filler materials such as short fibers like glass fibers, carbon fibers, carbon nanotubes and natural fibers were reinforced with polymer filaments [6–8]. Over the past five years, several companies started to fabricate composite parts commonly known as continuous fiber additive manufacturing (CF-AM) [9], where the continuous fibers are reinforced together in the thermoplastic materials which act as a matrix material. This process shows significant improvement in the mechanical properties of the printed parts [10]. Chacon et al. [11] conducted an extensive mechanical and bending test to access the effect of layer orientation, layer thickness and fiber volume content. Dickson et al. [12] used different types of fibers to understand the effect of reinforcement on tensile and flexural behavior of the 3D printed specimens under different process characteristics. Al Abadi et al. [13] investigated the elastic properties of the composite structures. Three different types of Fiber-reinforced materials were used in the study. They finally concluded that the level of reinforcements and their orientation have a major effect on the structural performance of the composite parts.

The objective of the paper is to study the tensile properties of the carbon fiber-reinforced PLA samples developed by using the FDM process with different print

parameters. The tensile strength of the developed samples was tested under a tensile testing machine and the results obtained are discussed in the result section.

2 Experimental Method

The Taguchi Design of Experiment was employed to identify the most influencing parameters and the optimal conditions on the tensile properties [14]. From the literature, the four most influencing factors and four levels were chosen for the current study. The infill pattern, infill density, nozzle temperature and layer thickness are chosen as the common influencing factors. The details of the parameters and the levels are listed in Table 1.

From the above data, the Taguchi L16 orthogonal array was designed by using MINITAB software [15]. All the 16 tensile test specimens were prepared as per the Taguchi design combinations. Total of 16 experiments were carried out with different combinations. The details of the test combinations and the tensile test results were shown in Table 2. All the tensile test specimens were prepared as per the ASTM D-638 standard [16]. The 2D drawing of the test specimen was shown in Fig. 1.

All the tensile test specimens were printed under FDM-based 3D printer (Dreamer). Figure 2a, b shows the printing process of tensile test specimens using the Dreamer printer. Each specimen was printed with different print parameters like infill pattern, infill density, nozzle temperature and layer thickness [15].

Once the tensile test specimens were prepared, they were tested under computerized twin screw Universal Testing Machine VFD (Vector Model) as shown in Fig. 3. Figure 4 shows the UTM contains speed variation between 0.5 and 800 mm/min and the maximum load capacity of 700 kg.

All the tensile test specimens were tested under UTM and recorded changes in length, cross section area and modulus of elasticity, and the ultimate tensile strength of each specimen was calculated and listed in Table 2. The ANOVA was conducted by taking print parameters as factors and ultimate tensile strength as a response [11].

From the test result, it was observed that specimen 12 shows the maximum ultimate tensile strength of 61.83 MPa with 90% infill density, line pattern, 210 °C nozzle temperature and 0.05 mm layer thickness. Specimen 8 shows the next best result of 55.37 MPa of ultimate tensile strength with 90% infill density, triangular pattern with 220 °C of extruder temperature and 0.1 mm of layer thickness. From the results, it

Table 1 Print parameters and levels

Parameters/levels	I	II	III	IV
Infill pattern (A)	Hexagonal	Triangular	Line	3D infill
Infill density (B)	60%	70%	80%	90%
Temperature (C)	200 °C	210 °C	220 °C	230 °C
Layer height (D)	0.05 mm	0.1 mm	0.15 mm	0.2 mm

Table 2 Tensile test results as per the Taguchi L16 array

Sr. No	Infill pattern	Infill density (%)	Temperature (°C)	Layer thickness (mm)	Ultimate tensile strength (MPa)
1	Hexagonal	60	200	0.05	29.807
2	Hexagonal	70	210	0.1	41.268
3	Hexagonal	80	220	0.15	51.88
4	Hexagonal	90	230	0.2	54.096
5	Triangular	60	210	0.15	37.731
6	Triangular	70	200	0.2	42.824
7	Triangular	80	230	0.05	54.002
8	Triangular	90	220	0.1	55.37
9	Line	60	220	0.2	41.551
10	Line	70	230	0.15	45.135
11	Line	80	200	0.1	53.719
12	Line	90	210	0.05	61.831
13	3D infill	60	230	0.1	30.42
14	3D infill	70	220	0.05	31.835
15	3D infill	80	210	0.2	43.485
16	3D infill	90	200	0.15	31.364

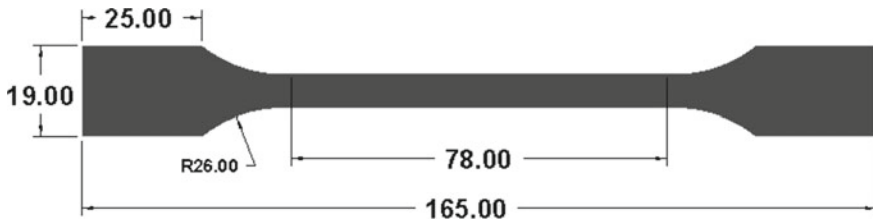


Fig. 1 2D CAD model of the tensile test specimen (all dimensions are in mm)



Fig. 2 a and b Dreamer FDM 3D printer. Tensile test specimen printing process

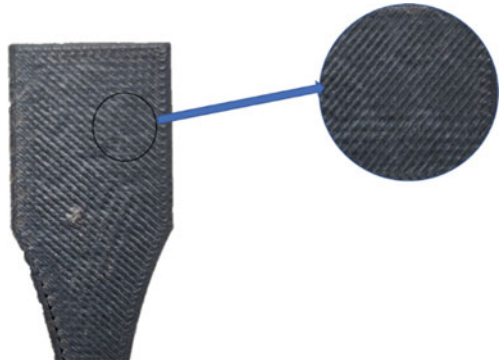
Fig. 3 The tensile specimens



Fig. 4 Computerized tensile testing machine



Fig. 5 3D printed specimen with exploded view of the surface



was observed that infill density shows a significant influence on the tensile properties of the printed specimens. Also, it was observed from the result that a large increase in the tensile strength when the infill density increases from 70 to 80%. But that trend was not observed in 80 to 90% of infill density models. Also, it was observed that there was a strong adhesive bonding between the layers when printed under optimum extrusion temperature [17]. But when increase in temperature results, the material becomes more brittle and breaks easily. The tensile strength result obtained at 200 °C and at 220 °C can be observed from the result Table 2.

3 Results and Discussion

Experimental data were used to analyze the influencing factors on the tensile strength of the developed specimens. ANOVA was used to understand the response of each variable and it was listed in Table 3. The effect plot of each parameter is shown in Fig. 6.

From Table 3, it was observed that the factors which show more influencing parameter on tensile strength were considered with p values less than 0.05. From the

Table 3 ANOVA result of ultimate tensile strength

Source	DOF	Seq. SS	Adj. SS	Adj. MS	F	P	Percentage
Infill pattern	3	598.74	598.74	199.58	12.84	0.032	38.51
Infill density	3	749.46	749.46	249.82	16.07	0.024	48.20
Temperature	3	120.56	120.56	40.19	2.59	0.228	7.75
Layer thickness	3	39.23	39.23	13.08	0.84	0.555	2.52
Error	3	46.63	46.63	15.54			2.99
Total	15	1554.62					100

$$S = 3.94233 \text{ R-Sq.} = 97.00\% \text{ R-Sq. (adj.)} = 85.00\%$$

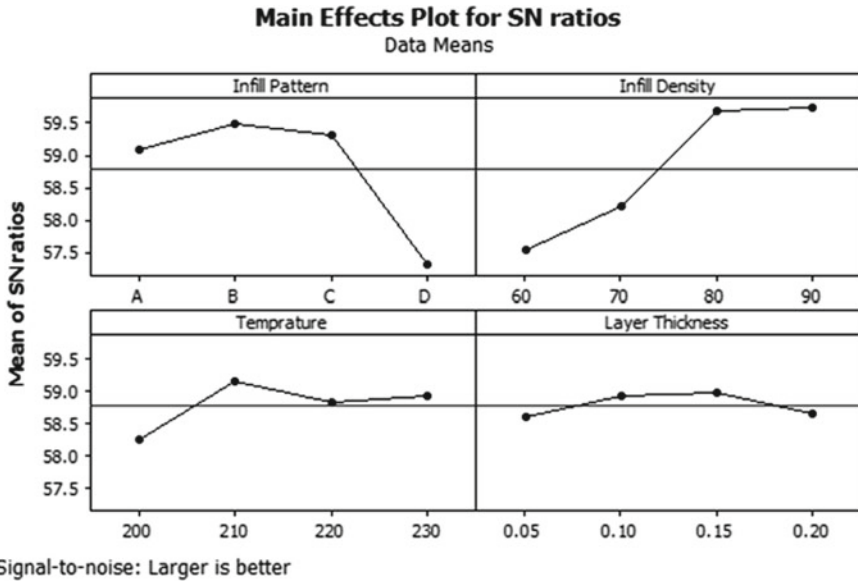


Fig. 6 SN ratio plot of different parameters

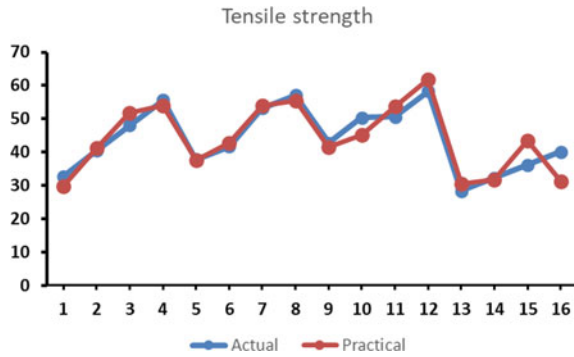
results, the most influencing factor in tensile strength was infill density with 48.20% followed by an infill pattern of 38.51%. Nozzle temperature shows very less influence on tensile strength of 7.75%. Layer thickness shows a very negligible percentage of influence on tensile strength. SN ratio response of each printing parameter and their levels were analyzed by using the “larger is the better” concept. It was observed that the Triangular infill pattern shows a better performance on tensile strength as compared with other patterns. 3D infill shows very less influence on the tensile strength of the specimens. 60% Infill density shows very less effect on tensile strength as compared to 80 and 90%. Nozzle temperature shows very less influence when compared to other parameters. 210 °C showed good results as compared to other sets of temperature. Layer thickness shows a negligible influence on tensile strength, and we can see very less variation in signal-to-noise ratio values. The R square value obtained was above 95% confident level [18].

Table 4 shows the SN ratio response of all parameters along with their levels. From the table, it was observed that the infill density shows the better response among all the other parameters, and it was ranked as one followed by the infill pattern. The infill pattern was ranked second and it shows considerable response on the output of the result. Temperature and Layer thickness show a negligible amount of response on the output, so they ranked as third and fourth. All the responses were recorded by setting Larger is the better option.

Table 4 Response table for signal-to-noise ratios (larger is better)

Level	Infill pattern	Infill density	Temperature	Layer thickness
1	32.69	30.76	31.66	32.5
2	33.42	32.02	33.11	32.86
3	33.97	34.08	32.9	32.21
4	30.6	33.82	33.02	33.11
Delta	3.32	3.37	1.45	0.9
Rank	2	1	3	4

Fig. 7 Validation of regression model results versus experimental results



3.1 Regression Analysis

The Linear regression model was developed by using Minitab software by considering all the dependent variables. Equation 1 shows the regression equation for the tensile strength. The validation of the regression model developed was done by comparing the regression model results with actual experimental results. The variation of regression results and actual experimental results was shown in Fig. 7. After comparison, it was observed that the nominal error value was obtained and that was well within 5%.

$$\sigma_{UT} = -32.3096 - 2.6883A + 0.5787B + 0.185345C - 0.612D \quad (1)$$

4 Conclusion

Finally, the following conclusions were drawn from the present investigation.

Carbon fiber-reinforced PLA samples were successfully developed by using the FDM technique. The tensile strength of the developed samples is mainly depending

on the different print parameters. Infill Density and infill pattern show the majority of the influence on the tensile strength of the developed samples. Nozzle temperature and layer thickness show very less influence on tensile strength. The results obtained by the regression model were successfully correlated with the experimental results. The errors obtained during correlation were less than 5%. So that the model generated and the parameters chosen were more suitable for the current study. The results obtained are taken as a reference, and further studies on the compression and torsion behavior of the printed specimen can be done using other optimization techniques.

Further studies should focus on the tensile and compression strength of different binding particles like graphene particles in the filament and by varying its percentage.

References

1. Leite M, Fernandes J, Deus AM, Reis L, Vaz MF (2018) Study of the influence of 3D printing parameters on the mechanical properties of PLA. In: 3rd international conference on progress in additive manufacturing
2. Kuznetsov VE, Solonin AN, Urzhumtsev OD, Schilling R, Tavitov AG (2018) Strength of PLA components fabricated with fused deposition technology using a desktop 3D printer as a function of geometrical parameters of the process. *Polymers* 10(3):313
3. Tymrak BM, Kreiger M, Pearce JM (2014) Mechanical properties of components fabricated with open-source 3-D printers under realistic environmental conditions. *Mater Des* 58:242–246
4. Stephens B, Azimi P, El Orch Z, Ramos T (2013) Ultrafine particle emissions from desktop 3D printers. *Atmos Environ* 79:334–339
5. Wittbrodt B, Pearce JM (2015) The effects of PLA color on material properties of 3-D printed components. *Addit Manuf* 8:110–116
6. Ferreira I, Madureira R, Villa S, de Jesus A, Machado M, Alves JL (2020) Machinability of PA12 and short fibre–reinforced PA12 materials produced by fused filament fabrication. *Int J Adv Manuf Technol* 107(1):885–903
7. Ivey M, Melenka GW, Carey JP, Ayranci C (2017) Characterizing short-fiber-reinforced composites produced using additive manufacturing. *Adv Manuf: Polym Compos Sci* 3(3):81–91
8. Zandi MD, Jerez-Mesa R, Lluma-Fuentes J, Jorba-Peiro J, Travieso-Rodríguez JA (2020) Study of the manufacturing process effects of fused filament fabrication and injection molding on tensile properties of composite PLA-wood parts. *Int J Adv Manuf Technol* 108:1725–1735
9. Parmiggiani A, Prato M, Pizzorni M (2021) Effect of the fiber orientation on the tensile and flexural behavior of continuous carbon fiber composites made via fused filament fabrication. *Int J Adv Manuf Technol* 114(7):2085–2101
10. Singh S, Ramakrishna S, Berto F (2020) 3D printing of polymer composites: a short review. *Mater Des Process Commun* 2(2):97–102
11. Chacón JM, Caminero MA, Núñez PJ, García-Plaza E, García-Moreno I, Reverte JM (2019) Additive manufacturing of continuous fibre reinforced thermoplastic composites using fused deposition modelling: effect of process parameters on mechanical properties. *Compos Sci Technol* 181:107688
12. Dickson AN, Barry JN, McDonnell KA, Dowling DP (2017) Fabrication of continuous carbon, glass and Kevlar fibre reinforced polymer composites using additive manufacturing. *Addit Manuf* 16:146–152
13. Al Abadi H, Thai HT, Paton-Cole V, Patel VI (2018) Elastic properties of 3D printed fibre-reinforced structures. *Compos Struct* 193:8–18

14. Sachit TS, Kumar DV, Keshavamurthy R, Kumar GP (2021) Mechanical and tribological investigation on Al LM4/TiC composite fabricated through bottom pouring method. *Mater Today: Proc* 43:2909–2914
15. Sachit TS, Mohan N (2019) Wear rate optimization of tungsten carbide (WC) nano particles reinforced aluminum LM4 alloy composites using Taguchi techniques. *Mater Res Express* 6(6):066564
16. ASTM D638 - 14 Standard test method for tensile properties of plastics. <https://www.astm.org/Standards/D638>. Accessed 11 Aug 2021
17. Sood AK, Ohdar RK, Mahapatra SS (2012) Experimental investigation and empirical modelling of FDM process for compressive strength improvement. *J Adv Res* 3(1):81–90
18. Narayana YV, Reddy NP (2019) Influence of process parameters on tensile strength of additive manufactured PLA parts using Taguchi method. *Int J Recent Technol Eng* 8(3):7635–7639

Modelling of Manganese and Nickel Transfer in Terms of Flux Ingredients in SAW



Brijpal Singh and Narender Singh

Abstract This study has been done to make a model of Mn and Ni transfer in terms of flux ingredients in submerged arc welding (SAW). The high Mn and Ni are desired in steel up to a certain extent. As it has an impact on the properties of the joint. However, beyond a certain increase, the tensile strength of the joint and ultimate strength of the welds are decreased. Elements transfer to the weld can be governed by the type and constituents of flux and wire composition. This can be done for getting the desirable properties. This study uses the twenty fluxes which are designed by using RSM. The properties of the welds are ensured by the composition of the welds. The flux and consumables also decide the weld metal properties. To study the effect of flux constituents on elements transfer during SAW, the welding parameters have been made constant in this study. The mathematical modelling of manganese and nickel transfer to the weld can predict the weld chemistry, and the desired weld metal properties can be obtained.

Keywords Multi-objective optimization · SAW · Fluxes · UTS · Impact strength

1 Introduction

In SAW, the joint is prepared by the heat produced by the submerged arc which is created by the short-circuiting between the consumable wire electrode and the metal to be joined. In SAW, the electric spark remains submerged and is hidden under the flux layer. In this welding, high-quality joint is made as it gives more protection from the atmospheric gases. So in this welding, no gas for shielding is used. The flux is of granular form and is stored in waterproof containers. For supplying the flux, usually a hopper is attached to the machine as a large quantity of flux is used in this

B. Singh (✉) · N. Singh

Department of Applied Sciences, Maharaja Surajmal Institute of Technology, Janak-Puri, New Delhi 110058, India

e-mail: brijpal.singh@msit.in

N. Singh

e-mail: narender_singh@msit.in

welding. This welding is used for joining pressure vessels, pipes and shipbuilding. The appearance and quality of the joint are very good [1–3]. The desired mechanical properties in the joint such as shock absorbing capacity, elongation and load-bearing capacity can be controlled by the selecting the proper flux and wire composition in combination with the welding parameters. All these parameters affect the elements transferred to the welds and the transferred elements decide the weld metal properties. The ductility and UTS of the weld both should be high. The composition which decides the chemistry of the weld can be decided by the exchange of elements during the slag metal reactions. The process parameters voltage, current and travelling speed also show an important effect on elements transfer. The movement of elements may be either from slag to weld or vice versa [4–7].

The constituents of flux are supposed to be an important factor for getting desired properties in the welds. Flux basically decides the arc stability, quality and properties in welded joints. The strength of the weld metal joint and other properties may be decided by elements that have been added to the weld from the flux in SAW. The weld metal properties may be improved by the transfer of C, Si, Mn, Ni, sulphur and phosphorus.

The weld manganese has an important effect on hardness and UTS. It may increase the hardness initially but further addition of Mn may affect the ductility. The manganese in the weld may get transferred from the flux, wire or from both. The toughness of the weld and ductility both show proportionality in the joints. If impact strength is increased, ductility is improved [8]. High Mn in the weld may work as a deoxidizer. The ratio of Mn/S should be high in order to decrease the weld oxygen content [9].

The ductility is also affected by the atmospheric gas present like oxygen, nitrogen and hydrogen Nitrogen in the atmosphere reacts with the weld and forms nitrides which are hard and it may lower the weld ductility [10].

2 Experimental Procedure

Fluxes were designed by using a central composite design and RSM which has been given in Table 1. The equilibrium diagrams of steels were used for designing the base fluxes $\text{CaO-SiO}_2\text{-Al}_2\text{O}_3$. The basic fluxes were decided to have the proportion as 7:10:2. CaF_2 , ferromanganese and nickel oxide were mixed between (2 and 8%) of the basic fluxes. These were added to the flux to see the transfer of elements in SAW. The main elements which were studied during this study were carbon, silicon, manganese, sulphur and nickel. The measured responses which were considered to study are impact strength, elongation and UTS. Table 2 shows the three additive factors and low, mid and high levels of these additives. Twenty fluxes were made by agglomeration technique and Beads were deposited on the plate. The process parameters voltage, current and travel speed were not varied in this experiment. Table 3 depicts the composition of consumable wire and the plate to be welded. The lathe machine was used for making the tensile test specimens and tensometer

Table 1 Design matrix

S. No.	CaF ₂ % (A)	FeMn % (B)	NiO % (C)
1	8.0	2.0	2.0
2	5.0	8.0	5.0
3	8.0	2.0	8.0
4	2.0	2.0	2.0
5	5.0	5.0	5.0
6	5.0	5.0	5.0
7	8.0	8.0	8.0
8	5.0	5.0	5.0
9	5.0	5.0	5.0
10	8.0	5.0	5.0
11	5.0	5.0	8.0
12	2.0	2.0	8.0
13	5.0	5.0	5.0
14	5.0	5.0	5.0
15	8.0	8.0	2.0
16	2.0	5.0	5.0
17	5.0	5.0	5.0
18	5.0	5.0	2.0
19	2.0	8.0	8.0
20	2.0	8.0	2.0

machine was used for making the tensile test specimen. Table 4 shows the mechanical properties such as ultimate tensile strength and percentage elongation. It also depicts the transfer of elements to the welds. The tested samples for tensile and impact strength and prepared fluxes have been depicted in Figs. 1 and 2. The following equation was used for finding the quantity of Mn and Ni transfer during SAW.

Table 2 Additives

Input	Added substances	Level-I	Level-II	Level-III
1 (A)	Calcium fluoride (CaF ₂)	2.0	5.0	8.0
2 (B)	Ferromanganese (FeMn)	2.0	5.0	8.0
3 (C)	Nickel oxide (NiO)	2.0	5.0	8.0

Table 3 The composition of wire and used plate

Composition	C %	Si %	Mn %	S %	P %	Ni %
Plate comp.	0.03	0.07	0.34	0.017	0.022	–
Wire comp.	0.11	0.09	0.45	0.021	0.021	–

Table 4 Measured responses

Flux	CaF ₂ %	FeMn %	NiO %	Mn %	Ni %	Ultimate tensile strength	Percentage elongation
						MPa	%
1	8	2	2	0.17	0.177	270.0	19.76
2	5	8	5	0.37	0.702	318.0	13.20
3	8	2	8	0.23	0.544	320.2	26.16
4	2	2	2	0.17	0.374	189.8	7.00
5	5	5	5	0.35	0.388	300.0	10.00
6	5	5	5	0.31	0.25	320.0	9.80
7	8	8	8	0.38	0.477	190.7	8.86
8	5	5	5	0.34	0.27	284.7	10.33
9	5	2	5	0.34	0.474	280.1	11.41
10	8	5	5	0.42	0.744	292.6	21.03
11	5	5	8	0.15	1.33	240	6.90
12	2	2	8	0.57	0.44	175.7	5.82
13	5	5	5	0.38	0.32	330.9	10.10
14	5	5	5	0.34	0.32	326.5	16.2
15	8	8	2	0.24	0.054	351.0	9.20
16	2	5	5	0.25	0.344	152.3	15.65
17	5	5	5	0.5	0.452	319.5	15.60
18	5	5	2	0.29	0.366	351	7.87
19	2	8	8	0.33	0.502	128.8	13.25
20	2	8	2	0.33	0.288	319.5	13.68

Fig. 1 Photograph of tested sample for tensile and impact strength



Fig. 2 Prepared fluxes

The Δ transferred quantity of manganese and nickel has been calculated as follows:

Measured delta quantity = Analysed composition – Expected composition.

The predicted or anticipated composition was found from the formula as depicted in relation 1.

$$\text{Expected - composition} = \frac{\text{dilution} * \text{baseplatecomp.} + (100 - \text{dilution}) * \text{wire comp.}}{100} \quad (1)$$

3 Result and Analysis

The ANOVA results for the transfer of manganese to the welds are depicted in Table 5. The F-value of the model is 7.354, which shows that the model may be significant. The “Prob > F” is 0.003, which is less than 0.05. The ANOVA Table shows that NiO is the only factor that has a significant effect on Mn transfer to the weld. However, besides this individual factor, the interaction factors AB, BC and AC are also having a significant effect on heat-affected areas. The quadratic terms A² and B² are too significant. The MRC value of the quadratic model is found to be 0.694. This means that 69.4% of the variance is in the model. This value indicates that this variation in the model can be understood by the independent variables and hence this model is strong enough in predicting heat-affected areas of the weld. The “pred. R-Squared” is near to the value of “Adj. R-Squared”. The lack of fit in the model should be insignificant relative to pure error and it shows that the model is good. The predicted Mn transfer equation is given in Eq. 2.

Table 5 Analysis of variance for manganese transfer

ANOVA for weld Mn transfer in SAW						
Analysis of variance table [partial sum of squares—type III]						
Source	Sum of squares	DF	Mean square	F-value	p-value	
					Prob > F	
Model	0.124	4	0.031	7.354	0.003	Significant
C-Nio	0.086	1	0.086	20.381	0.001	Significant
AB	0.036	1	0.036	8.487	0.012	Significant
AC	0.025	1	0.025	5.875	0.031	Significant
A ²	0.035	1	0.035	8.167	0.014	Significant
Residual	0.055	13	0.004			
Lack of fit	0.032	8	0.004	0.883	0.584	Not significant
Pure error	0.023	5	0.005			
Cor total	0.180	17				

Standard deviation	0.065	R ²	0.694
Mean	0.332	Adjusted R ²	0.599
Cof variance %	19.581	Predicted R ²	0.449
PRESS	0.099	Adequate precision	10.658

$$Mn = 0.37 + 0.11 * C + 0.0748 * A * B - 0.062 * A * C - 0.090 * A^2 \tag{2}$$

Figure 3 shows the combined influence of CaF₂ and FeMn on Mn transfer to the weld joint. It shows that with increasing both A and B factors, the Mn transfer is decreased. The weld Mn content is affected by CaF₂. As the CaF₂ content in the flux is increased, more manganese may go to the slag and the percentage of Mn content in the weld may be low. The reduction in weld Mn may also be due to the evaporation of manganese. The weld manganese percentage may be higher as more FeMn is added. The interaction effect of Calcium fluoride and nickel oxide on Mn transfer is depicted in Fig. 4. It shows that with increasing both the input factors the weld Mn is increased. With an increase of NiO content in the flux, the manganese in the joint may increase. The reason behind this may be low oxygen availability in the joint.

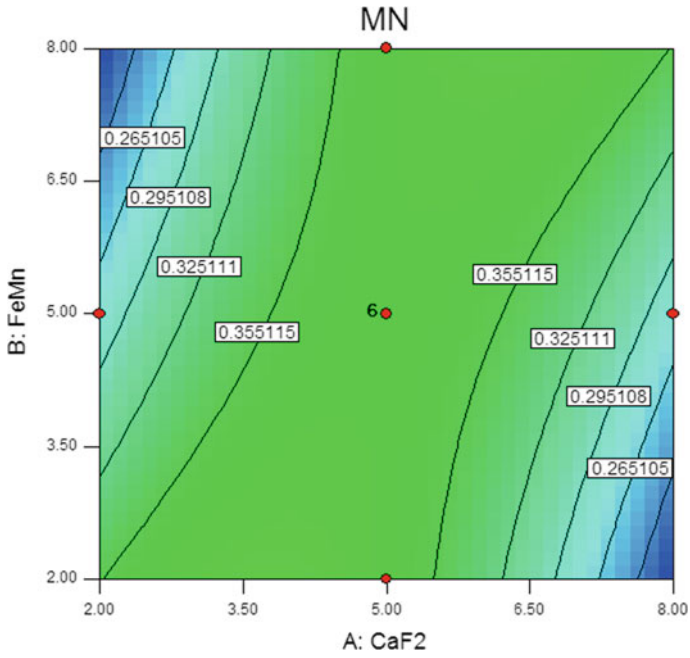


Fig. 3 Interaction effect of CaF₂ and FeMn on Mn transfer

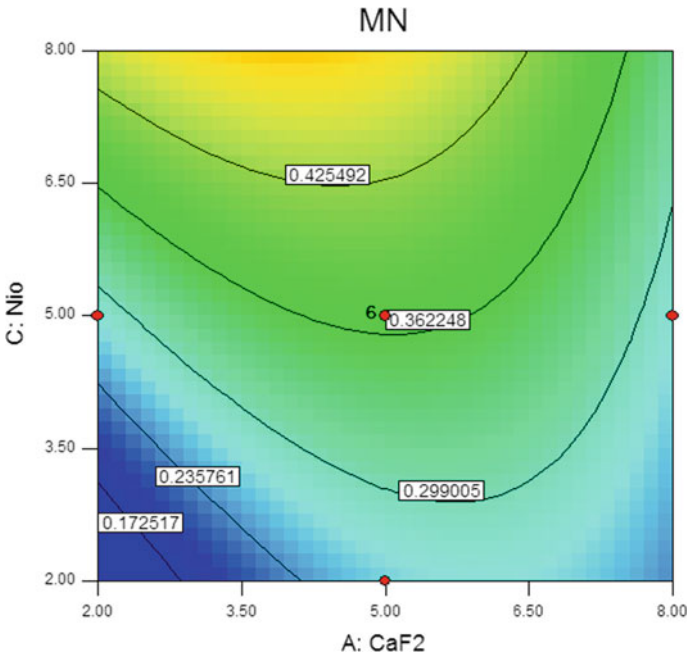


Fig. 4 Combined effect of CaF₂ and NiO on Mn transfer

4 Correlation of Mn and Ni Contents with UTS and Elongation

The correlation of UTS with manganese has been shown in Fig. 5. It shows that after increasing to a certain limit, the tensile strength is reduced. The optimized value of Mn may lie between 0.35 and 0.39%. This can be seen from Fig. 5. The basic reason for this increase may be solid solution hardening as Mn promotes this to a certain extent. Further increasing Mn in the weld reduces the tensile strength. The UTS is also affected by the other elements such as the presence of carbon in the welds. The optimal balance of carbon and Mn is desirable for good impact strength. Figure 6 reveals that there is a reduction in percentage elongation with high Mn content. The metallurgical reactions and dilution reactions are important in SAW. These two reactions may affect the weld manganese transfer. These reactions are very important in SAW as during the welding the temperature may be very high. The equilibrium condition may not exist because of this high temperature. So the elements transfer cannot be predicted only by equilibrium conditions. The above equations are also equally important. These reactions may decide the transfer of elements to the welds. The ultimate tensile strength of the weld is also reduced by increasing Nickel content [11]. This may be due to the microsegregation of manganese at the grain boundary Fig. 7. The correlation with Ni and elongation has been given in Fig. 8 and it reveals that after some decrease in elongation, it is further increased with increasing Mn transfer.

Standard deviation	0.27	R ²	0.2434
Mean	0.49	Adj R ²	0.2014
Coefficient of variation %	55.27	Pred R ²	0.0566
PRESS	1.61	Adequate precision	4.8130

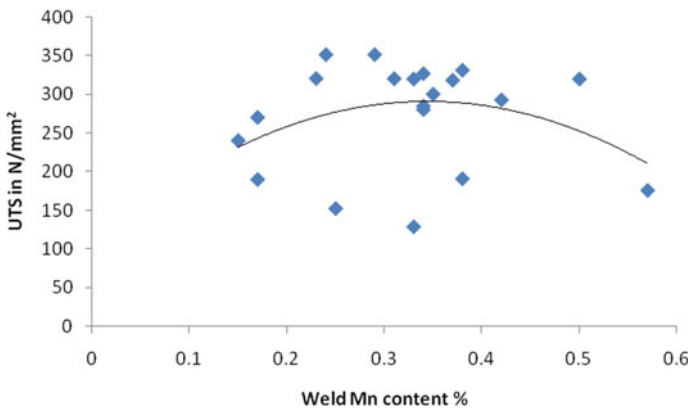


Fig. 5 Ultimate tensile strength versus weld Mn percentage

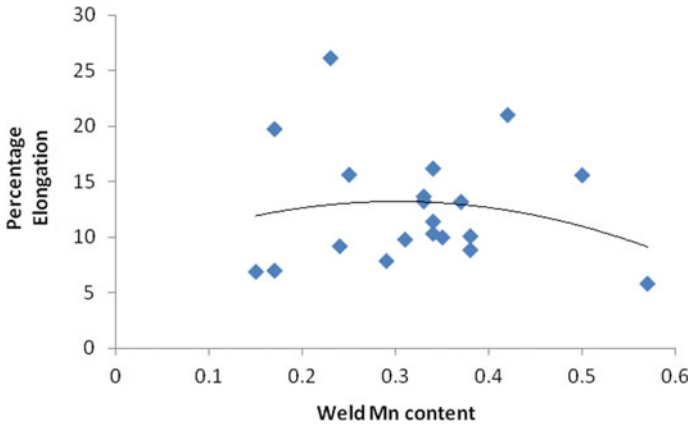


Fig. 6 Elongation versus weld Mn percentage

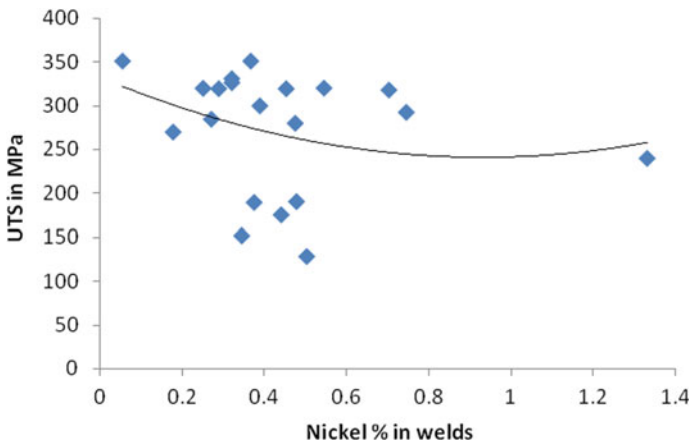


Fig. 7 Graph of nickel with ultimate strength

The ANOVA results for transfer of Ni transfer in the welds are given in Table 6. The obtained value of 5.79 shows that the model is effective. The “Prob > F” is 0.0271, which is less than 0.05. The ANOVA Table shows that NiO is the only factor that has a significant effect on nickel transfer. The “predicted R²” is also in reach or with the “Adjusted R-Squared”. The model shows an insignificant lack of fit with relative to pure error, and it is assumed satisfactory for a good model. The found model for Manganese transfer is given in Eq. 3.

$$Ni = -0.1450 + 0.0680 * NiO \tag{3}$$

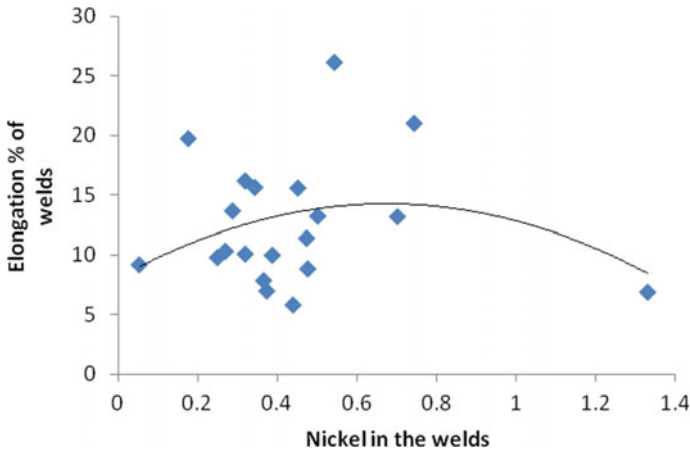


Fig. 8 Correlation of Ni with elongation of welds

Table 6 ANOVA results for Ni transfer

ANOVA for response surface reduced linear model						
Analysis of variance table [partial sum of squares—type III]						
Source	Sum of squares	Degree of freedom	M.S	F-value	p-value Prob. > F	
Model	0.416	1	0.416	5.7913	0.0271	Significant
C-Nio factor	0.42	1	0.416	5.7913	0.0271	
Residual	1.293	18	0.072			
Lack of fit	0.785	13	0.060	0.5944	0.792	Not significant
Pure error	0.508	5	0.102			
Correction total	1.7096	19				

5 Conclusions

From the experimental work, the following conclusions can be made:

1. Mathematical modelling can predict the weld Mn and Ni transfer in terms of flux ingredients.
2. The UTS and elongation of welds are affected by the transfer of Mn and Nickel in the weld.
3. For increasing UTS in the weld, low content of nickel is desired as UTS is reduced with increasing nickel content.

References

1. Parmar RS (1992) *Welding processes technology*. Khanna publisher, New Delhi
2. Murgan N, Gunaraj V (2005) Prediction and control of weld bead geometry and shape relationship in submerged arc welding of pipes. *J Mater Process Technol* 168:478–487
3. Hould Croft PT (1989) *Submerged arc welding*, 2nd edn. Abington publishing, Cambridge, England
4. Kanjilal P, Pal TK, Majumdar SK (2005) Combined effect of flux and welding parameters on chemical composition and mechanical properties of submerged arc weld metal. *J Mater Process Technol* 171(2):223–231
5. Kanjilal P, Pal TK, Majumdar SK (2007) Prediction of element transfer in submerged arc welding. *Weld J* 46:135–146
6. Kanjilal P, Pal TK, Majumdar SK (2006) Prediction of acicular ferrite from flux ingredients in submerged arc welds metals from C-Mn-Steel. *ISIJ Int* 45:876–885
7. Palm JH (1972) Technical note on how fluxes determine the metallurgical properties of SAW. *Weld Res Suppl* 358–360
8. Modi OP, Deshmukh ND, Mandal DP, Jha AK, Egenswaran AH (2001) Effect of interlamellar spacing on the mechanical properties of 0.65 % carbon steel. *Mater Charact* 46:347–352
9. Grong O, Siewart TA, Martins GP, Olson DL (1986) A model for silicon manganese deoxidation of steel weld metals. *Metall Trans* 17(10):1797–1807
10. Potapov NN (1993) Oxygen effect on low alloy steel weld metal properties. *Weld Res Suppl* 367–370
11. Burck PA, Indacochea JE, Olson DL (1990) Effects of welding flux additions on 4340 steel weld metal composition. *Weld J* 69(3):115–122